TECHNISCHE UNIVERSITÄT MÜNCHEN

Lehrstuhl für Aerodynamik und Strömungsmechanik

Analysis and Control of Shock-Wave/Turbulent Boundary-Layer Interactions on Rigid and Flexible Walls

Vito Pasquariello

Vollständiger Abdruck der von der Fakultät für Maschinenwesen der Technischen Universität München zur Erlangung des akademischen Grades eines

Doktor-Ingenieurs

genehmigten Dissertation.

Vorsitzender: Prof. Dr.-Ing. habil. Oskar J. Haidn
Prüfer der Dissertation: 1. Prof. Dr.-Ing. habil. Nikolaus A. Adams
2. Prof. Dr.-Ing. habil. Stefan Hickel
Delft University of Technology, The Netherlands

Die Dissertation wurde am 06.04.2017 bei der Technischen Universität München eingereicht und durch die Fakultät für Maschinenwesen am 15.12.2017 angenommen.

Vito Pasquariello
Gebsattelstraße 6
81541 München
Germany

vito.pasquariello@gmail.com

Released   March 16, 2018
Typesetting   LaTeX

ABSTRACT

Shock-wave/turbulent boundary-layer interactions (SWBLI) occur in many technical applications and have been an active research field for more than sixty years. While mean-flow properties of the interaction are well understood and documented in the literature, a general consensus on the physical origin of low-frequency unsteady effects associated to the shock/bubble system is still not reached. In this work, a numerical framework is developed which allows for high-fidelity large-eddy simulations (LES) of SWBLI on flexible walls. Implicit LES is used to investigate the dynamics of weak and strong impinging SWBLI at low and high Reynolds numbers on rigid and flexible walls.

The in-house flow solver INCA operates on Cartesian grids and employs a cut-cell immersed boundary method for representing embedded geometries. The method has been extended for coupling with finite-element based structural solvers through a loosely-coupled approach within a classical Dirichlet-Neumann partitioning. The resulting fluid-structure interaction algorithm has been validated for shock-loaded structures and proven accurate in predicting large and complex deformations.

Low-Reynolds-number SWBLI studies on rigid walls are conducted to verify the LES capabilities of the flow solver in predicting mean-flow properties and unsteady effects. A passive flow control device is proposed, which is able to shift the high-energy low-frequency pressure fluctuations to higher frequencies, while at the same time mitigating shock dynamics and reducing turbulence intensity across the interaction.

Unprecedented LES of strong SWBLI at considerably higher Reynolds numbers are validated with recent experiments and thoroughly analyzed with respect to unsteady effects. Clear evidence of the existence of Görtler-like vortices emerging in the reattachment region is found, which, in contrast to many previous investigations, are not locked at a specific spanwise location, but rather undergo a slow meandering motion coupled to the separation-bubble dynamics. Support is given by a sparsity-promoting dynamic mode decomposition which reveals streamwise streaks at low frequencies that could be linked to footprints of Görtler-like vortices. A new instability mechanism responsible for low-frequency unsteadiness is postulated, in which unsteady Görtler-like vortices act as a source for continuous (coherent) forcing on the separation-shock-system dynamics.

A two-way coupled SWBLI is studied, which matches recent experiments of a fast-pitching shock generator whose incident shock induces a transient load on a flexible wall. Results indicate a mainly unidirectional coupling, in which the SWBLI passively adapts to the structural deformation (as superimposed on a transient mean) without significant influence on the panel response. Panel oscillations induce compression and expansion waves in the flow, while at the same time amplifying separation-shock dynamics.

Danksagung

TABLE OF CONTENTS

Nomenclature

2D   Two-Dimensional

3D   Three-Dimensional

AER   Institute of Aerodynamics and Fluid Mechanics

ALDM   Adaptive Local Deconvolution Method

ALE   Arbitrary Lagrangian Eulerian

CFD   Computational Fluid Dynamics

CFL   Courant-Friedrichs-Lewy

DEM   Discrete Element Method

DFG   Deutsche Forschungsgemeinschaft

DLR   German Aerospace Center

DNS   Direct Numerical Simulation

FE   Finite Element

FEM   Finite Element Method

FSI   Fluid-Structure Interaction

FSS   Free Shock Separation

FV   Finite Volume

FVM   Finite Volume Method

GPU   Graphics Processing Unit

IBM   Immersed Boundary Method

ILES   Implicit Large-Eddy Simulation

LCO   Limit-Cycle Oscillation

LES	Large-Eddy Simulation
LNM	Institute for Computational Mechanics
NASA	National Aeronautics and Space Administration
NPR	Nozzle Pressure Ratio
PIV	Particle Image Velocimetry
RANS	Reynolds-Averaged Navier-Stokes
RMS	Root Mean Square
ROM	Reduced-Order Model(ing)
RSS	Restricted Shock Separation
SFB-TR40	Sonderforschungsbereich Transregio 40
SGS	Subgrid Scale
SPDMD	Sparsity-Promoting Dynamic Mode Decomposition
SSME	Space Shuttle Main Engine
SWBLI	Shock-Wave/Turbulent Boundary-Layer Interaction
TBL	Turbulent Boundary Layer
TIC	Truncated Ideal Contoured
TKE	Turbulent Kinetic Energy
TOP	Thrust-Optimized Parabolic
TUM	Technische Universität München

1. INTRODUCTION

This thesis summarizes my work as a Research Assistant at the Institute of Aerodynamics and Fluid Mechanics at the Technische Universität München (TUM). During the past four and a half years I have been working in the field of compressible flow, more precisely on the numerical simulation of shock-wave/turbulent boundary-layer interactions (SWBLI) and the development of fluid-structure interaction (FSI) algorithms in the context of cut-cell based immersed boundary methods (IBM).

The thesis is structured as follows: In Chapter 1, a brief introduction to SWBLI is given in the context of rocket nozzles, with special emphasis on the generation of side loads and the well-known low-frequency phenomenon of the reflected shock. The chapter is concluded by summarizing the objectives of this thesis. In Chapter 2 the numerical model is presented, including the governing equations for fluid and solid, a short description of the FSI framework, and an introduction to large-eddy simulations (LES). Chapter 3 provides the main accomplishments of the present thesis. A state-of-the-art in literature is given for each section together with a short summary for each publication. Concluding remarks are given in Chapter 4. A full list of publications (either peer-reviewed journal publications, book sections or conference papers) is provided in Appendix A and selected main publications can be found in Appendix B.

1.1. MOTIVATION

As part of the DFG SFB-TR40 project (*Deutsche Forschungsgemeinschaft: Sonderforschungsbereich Transregio 40*) with its main objective to investigate "*Fundamental Technologies for the Development of Future Space-Transport-System Components under High Thermal and Mechanical Loads*", the primary goal of subproject D4 (*Fluid-Structure Interaction in Rocket Nozzles*) was, amongst others, to investigate shock-induced boundary-layer separation at high Reynolds number for rigid and flexible surrogate nozzle geometries using high-fidelity LES. During the second funding period of the SFB-TR40, main project partners were the *Institute for Computational Mechanics* (LNM, TUM) to jointly develop coupling methods for fluid and structural solvers, and the *German Aerospace Center* (DLR, Cologne, subproject D6), who provided reference experiments for validation purposes.

Rocket nozzles have the simple task to produce thrust according to Newton's second law by accelerating the stagnant combustion gas to high supersonic speed. The total thrust F[1] can be expressed as

$$F = \dot{m}u_e + (p_e - p_\infty)A_e \,, \tag{1.1}$$

where $\dot{m}$ is the mass flow, u_e the exit velocity of the supersonic jet, p_e the exit pressure, A_e the nozzle exit area, and p_∞ the ambient pressure of the nozzle. Optimum thrust is achieved for an ideally expanded flow, i.e., when the nozzle exit pressure equals the ambient pressure $p_e = p_\infty$. This ideal flow state, however, may only be achieved throughout ascent when using a variable nozzle geometry by either changing the throat area A_t or A_e, thus continuously adapting the expansion ratio $\epsilon = A_e/A_t$ (note that u_e directly depends on ϵ). Since this results in a complex mechanical task with additional weight penalties, present-day rocket engineering still relies on conventional bell-shaped nozzles with a fixed ϵ (Östlund and Muhammad-Klingmann, 2005). As a consequence, the rocket nozzle operates in off-design conditions ($p_e \neq p_\infty$) for most of the time during its flight trajectory with induced performance losses: overexpansion ($p_e < p_\infty$) as well as underexpansion ($p_e > p_\infty$) are possible flow states characterized by the formation of shock and expansion waves around the exhaust plume, respectively. While the latter is considered as unproblematic from a rocket's stability point of view, high overexpansion ($p_e \ll 0.5\,p_\infty$, according to Frey (2001)) may lead to internal flow separation which constitutes the basis for the generation of off-axis loads, or so-called side loads. This poses a limitation to the target of generating high vacuum thrust (i.e., good efficiency at high altitudes), since it would result in large-area ratio nozzles ($\epsilon \uparrow$) operating in a highly-overexpanded state at sea level and low altitudes. As a compromise, today's rocket nozzles (Vulcain, Space Shuttle Main Engine (SSME), J-2S) are usually designed in such a way that a high degree of underexpansion at high altitude and thus performance loss is accepted (moderate ϵ), thereby minimizing the risk of flow separation and the generation of side loads at sea level for a full-flowing nozzle. However, the transient start of a rocket nozzle, until a full-flowing state is reached, always implies overexpanded conditions and thus internal flow separation (Frey, 2001). A typical start-up process of the SSME is shown in Fig. 1.1. An asymmetric separation line can be seen in the first frame, which is unsteady in nature. It

---

[1] Often the specific impulse $I_{sp} = F/\dot{m}$ is given to measure the efficiency of a rocket engine.

Figure 1.1.: Transient start-up of the SSME. Courtesy of NASA.

is continuously forced towards the nozzle exit as the nozzle pressure ratio ($NPR = p_c/p_\infty$, p_c denotes the combustion chamber stagnation pressure) increases, until the nozzle is finally full-flowing (third frame) and a Mach disk is formed in the exhaust plume. During the first and second frame a significant bending of the nozzle around its throat can be observed together with an ovalization of the structure. Improving prediction capabilities of numerical tools with respect to flow separation and resulting nozzle loads during liftoff would potentially allow for designs with higher ϵ and thus higher vacuum performance.
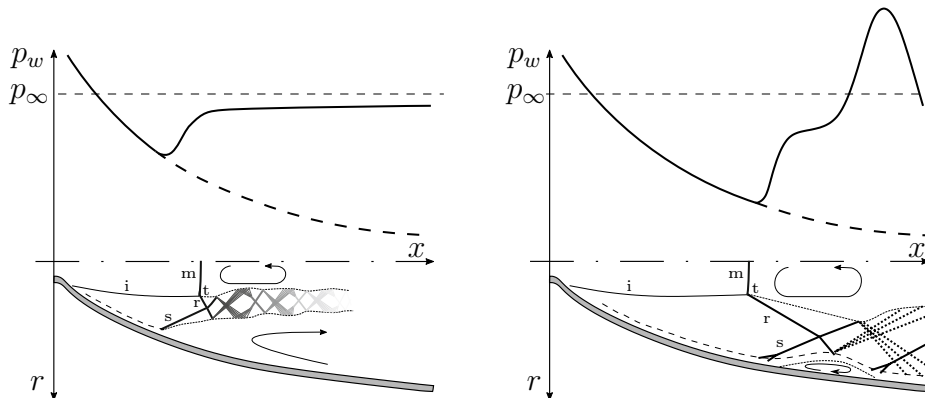
Figure 1.2.: Schematic representation of FSS (left) and RSS (right) inside a TOP nozzle during transient start-up. Figure partially reproduced from Frey (2001) and Baars and Tinney (2013).

The nozzle contour directly determines the internal flow field and in turn controls the flow-separation and side-load behavior, which is especially important for first-stage nozzles with an operating range from sea level to high altitudes (Frey, 2001; Östlund, 2002; Östlund and Muhammad-Klingmann, 2005). For thrust-optimized parabolic (TOP) nozzles[2], such as the Vulcain, J-2S and SSME, the wall-curvature abruptly changes between the circular throat and the parabolic nozzle extension, which consequently leads to the generation of an internal shock[3]. In such nozzles, two different separation patterns resulting from SWBLI can be observed for highly-overexpanded states, see also Fig. 1.2, which shows free shock separation (FSS) and restricted shock separation (RSS), where

---

[2] TOP nozzles are often used because of their high thrust-to-mass ratio.

[3] Note that this is not the case for truncated ideal contoured (TIC) nozzles, or so-called TICTOP nozzles. The latter is a recent nozzle contouring concept developed by Frey et al. (2016).

the latter is a distinct characteristic of TOP nozzles. FSS typically occurs at low NPR where the nozzle flow fully separates from the wall. The associated pressure distribution departs from the ideal expansion (dashed line in Fig. 1.2) and is characterized by a strong adverse pressure gradient in the proximity of the separation shock. Further downstream, below the detached supersonic plume, a subsonic recirculating region develops with an associated weak pressure increase up to the nozzle exit ($p_e < p_\infty$). The separation shock (s) interacts with a reflected shock (r), which originates from the triple point (t) where the Mach disk (m), the internal shock (i) and the reflected shock (r) coincide. A further increase in NPR shifts the separation shock downstream of the Mach disk (see right side of Fig. 1.2) and augments the outward radial momentum induced by the reflected shock, which eventually leads to reattachment of the supersonic plume (see also the momentum-balance considerations given in Frey (2001)). FSS transitioned to RSS, a flow separation pattern, which has been first observed during cold-flow subscale tests of the J-2S engine (Nave and Coffey, 1973). In this configuration, a restricted separation bubble forms and is attached to the nozzle wall[4]. While the initial wall-pressure distribution up to the pressure-plateau bears similarities to the FSS, flow reattachment provokes the formation of a reattachment shock with increased wall-pressure levels beyond ambient conditions ($p > p_\infty$). Upon further increasing the NPR, the separation bubble is pushed towards the nozzle exit and periodically opens/closes to the ambient flow while triggering a re-transition from RSS to FSS. This phenomenon, which is known as the end-effect, lasts until the nozzle is finally flowing full.

Side loads occur whenever the integrated pressure along the nozzle wall results in an off-axis component, which, due to the axisymmetric nozzle design, can consequently only result whenever asymmetric flow effects or deformations occur. One may distinguish between three main sources identified for the generation of lateral forces, see also Östlund and Muhammad-Klingmann (2005) for a review: (i) pressure fluctuations amplified by/inherent to SWBLI and separation-shock unsteadiness, (ii) transition of separation patterns (FSS ⟷ RSS), and (iii) aeroelastic interaction between flow-induced pressure fluctuations and mechanical eigenmodes (mainly the pendulum and bending mode) of the nozzle. The separation line for both FSS and RSS is unsteady and follows low-frequent shock motions, which consequently leads to an asymmetric pressure distribution and thus induces lateral forces. Distinct side-load peaks in TOP nozzles are observed whenever the separation pattern transitions from FSS to RSS (and vice-versa), a phenomenon which usually does not occur synchronously in circumferential direction (Frey, 2001; Hagemann et al., 2002; Östlund and Muhammad-Klingmann, 2005; Verma et al., 2006; Ruf et al., 2009). According to Fig. 1.2, different pressure distributions in FSS/RSS state occur along with a significantly shifted separation location. With respect to aeroelastic instabilities, Brown et al. (2002) conducted full-scale and sub-scale nozzle experiments and found evidence of a self-excited vibration loop between the structural ovalization mode and flow separation. Given that SWBLI is a common characteristic of all described side-load mechanisms, the following section provides a brief introduction to this topic with a focus on unsteady aspects related to reflected-shock unsteadiness.

---

[4] Depending on the initial shock strengths, multiple annular separation bubbles may develop, resulting from wave reflections at the shear layer.

1.2. Shock-wave/turbulent boundary-layer interaction

Besides playing an important role for the performance and structural integrity of rocket nozzles, SWBLI occur in a wide range of practical flow devices, including, e.g. , turbomachine cascades, supersonic air intakes, and hypersonic vehicles. For more than sixty years SWBLI has been an active research field still offering open questions, in particular regarding unsteady effects of the interaction with mean boundary-layer separation (Dolling, 2001). Figure 1.3 shows a numerical schlieren image obtained from a LES of an impinging SWBLI. The case of an oblique shock impinging on a flat plate is historically the least well studied configuration, but shares similarities with the most considered compression ramp or forward-facing step flow. When comparing the resulting flow topology in Fig. 1.3 to the one resulting from a RSS as shown in Fig. 1.2, one can directly identify strong similarities. As such, the case of an impinging SWBLI serves as a characteristic nozzle surrogate with respect to RSS and is used by researchers to gain deeper insights into side-loads generating mechanisms related to unsteady wall-pressure fluctuations induced by the separation shock.

Figure 1.3.: Numerical schlieren image from a LES showing contours of the density gradient magnitude $|\nabla \rho|$ for an impinging SWBLI at $Ma = 3$ and $Re_\delta \approx 2 \cdot 10^5$.

For a strong incident shock, as is the case in Fig. 1.3, the turbulent boundary layer (TBL) cannot sustain the adverse pressure gradient and consequently separates. Separation takes place upstream of the nominal inviscid impingement point, since pressure waves induced by the incident shock are convected upstream through the subsonic part of the TBL. This upstream influence leads to a thickening of the TBL, which results in the generation of compression waves within the supersonic part of the TBL. These waves coalesce to the so-called reflected/separation shock (Délery, 1985). Reflected and incident shock intersect[5] and continue traveling as transmitted shocks, while the latter one is being reflected at the sonic line as an expansion fan. Experimental as well as numerical investigations confirm the concept of *free interaction*, which states that the initial part of interaction, i.e. , the compression at separation as well as the pressure plateau, solely depends on the incoming flow state and neither on the source of separation nor on the downstream geometry (Délery and Marvin, 1986; Chapman et al., 1958). A detached turbulent shear layer originates from the separation shock foot. It follows the initial inclination of the separated flow region, is being deflected towards the wall through the expansion fan, and is finally reattaching further downstream along with the formation of

---

[5] In this case well outside the TBL due to a very strong incident shock.

compression waves which coalesce into the reattachment shock. Turbulence is strongly and anisotropically amplified across the SWBLI, with high levels typically located along the detached shear layer, the reflected shock and the incident shock tip (Adams, 2000; Pirozzoli and Grasso, 2006; Pasquariello et al., 2014). Downstream of the interaction region the TBL progressively returns to an equilibrium state on a length scale of $\mathcal{O}(10)$ TBL thicknesses δ_0 with respect to first and second order statistical moments (Shahab, 2006; Pirozzoli and Grasso, 2006).

1.2.1. Low-frequency unsteadiness

SWBLI characteristics with respect to mean-flow properties are well understood and documented in the literature. For SWBLI with mean-flow separation, however, a complex dynamical system with a broad range of involved temporal and spatial scales develops, with still unexplained low frequencies that keep SWBLI being an active research field. The terminology *low frequency* refers to unsteady motions of the reflected shock which are typically one to two orders of magnitude lower than the characteristic frequency U_0/δ_0 (freestream velocity/TBL thickness) of integral scales within the incoming TBL. These shock motions result in unsteady loads (pressure and friction forces) which may couple to free vibration modes of the structure, and potentially result in failure due to fatigue (Dolling, 2001; Délery and Dussauge, 2009). Kistler (1964) was the first to provide high-frequency measurements of the fluctuating wall pressure within the interaction region of a forward-facing step flow. His measurements indicate a low-frequency high-amplitude loading of the underlying structure close to the separation point. Since then, numerical and experimental studies provided theories related to *upstream* or *downstream mechanisms* to explain the unsteadiness of the reflected shock, see also the review paper by Clemens and Narayanaswamy (2014) for an extensive summary.

Upstream mechanisms make flow phenomena or events in the upstream TBL responsible for the observed shock unsteadiness, e.g., through bursting events of the incoming TBL (Andreopoulos and Muck, 1987; Erengil and Dolling, 1993; Adams, 2000). Although the shock directly responds to such upstream pressure fluctuations, it rather results in a high-frequency smaller-scale jitter motion unable to explain the large-scale low-frequency oscillations. A low-frequency thickening/thinning of the TBL may be linked to upstream/downstream motions of the shock as proposed by Ünalmis and Dolling (1994), and later verified by Beresh et al. (2002) and Hou et al. (2003) through an inspection of conditionally-averaged velocity profiles obtained through particle image velocimetry (PIV). Employing time-resolved PIV on a streamwise-spanwise plane, Ganapathisubramani et al. (2009) found low-velocity coherent structures of $50\,\delta_0$ length upstream of their compression-ramp flow. The authors expressed a strong correlation between these so-called *superstructures* and an instantaneous separation-line surrogate. Wu and Martín (2008), however, did not find such a correlation when using the true separation point defined through the zero skin-friction coefficient in their simulation. Tomographic PIV measurements by Humble et al. (2009) revealed a high-frequency small-amplitude spanwise wrinkling of the shock as a result of an interaction with upstream coherent structures.

Downstream mechanisms link the separation shock motion to dynamics of the downstream separation bubble. Dolling and Erengil (1991) and Thomas et al. (1994) were probably the first (and later also Dupont et al. (2006)) to show that wall-pressure fluctuations measured in the proximity of the reflected shock foot and close to reattachment are correlated at low frequencies, with a phase shift indicating a periodic contraction/expansion of the separation bubble. Piponniau et al. (2009) as well as Wu and Martín (2008) proposed a self-sustaining process based on an entrainment/recharge mechanism involving the detached shear layer, the separation bubble and the shock system. An acoustic feedback mechanism provoked by acoustic disturbances, which are generated at the incident shock tip and subsequently travel upstream to feed the separation point oscillations, similar to Rossiter modes in cavity flows, has been proposed by Pirozzoli and Grasso (2006). A proof of possibly upstream-traveling acoustic waves within the separation bubble has been reported by Touber and Sandham (2009), who performed LES of the impinging SWBLI experiment by Dupont et al. (2006). They provided a linear stability analysis of the mean flow and linked a two-dimensional (2D), zero-frequency, globally unstable mode to the low-frequency unsteadiness. The same authors (Touber and Sandham, 2011) later derived a stochastic ordinary differential equation for the reflected-shock low-frequency motions. The final expression is similar to the one postulated by Plotkin (1975) and describes the unsteadiness as an intrinsic low-pass filtering property of the SWBLI, which selectively amplifies any kind of low-frequency content (being coherent or incoherent, originating from upstream or downstream) in the flow.

1.2.2. Numerical simulation of SWBLI

Computational Fluid Dynamics (CFD) is a valuable method for predicting fluid flows by numerically approximating mathematical models of physical systems. The *Navier-Stokes equations* comprise a set of partial differential equations (see also Chapter 2) which fully account for the temporal and spatial evolution of laminar and turbulent flows. Typical applications usually involve turbulent flows, which are characterized by eddies of widely varying spatial scales. Large, energy-rich eddies correlate with the characteristic length L of the flow problem, whereas small (Kolmogorov) scales depend on kinematic viscosity ν and dissipation ε through $l_\eta = (\nu^3/\varepsilon)^{0.25}$. Since the ratio of largest to smallest turbulent scales increases with increasing Reynolds number by a factor of $\mathrm{Re}^{3/4}$, where $\mathrm{Re} = U_0 L/\nu$, resolving all occurring eddies may result in an intractable task. This becomes even more obvious when considering all three spatial directions, since the computational cost with respect to grid cells then scales with $\mathrm{Re}^{9/4}$. When further accounting for a time-resolved simulation, the total cost of a fully-resolving simulation scales with $\mathrm{Re}^{11/4}$. Although such an approach, which is referred to as *direct numerical simulation* (DNS), is computationally expensive and thus intractable for typical industrial applications, it is a powerful research tool for investigating simple turbulent flows at moderate Reynolds numbers (Pope, 2000). Depending on the degree of approximation with respect to modelled flow scales, one can differentiate between *large-eddy simulations* (LES) and *Reynolds-averaged Navier-Stokes* (RANS) simulations. While for the latter all turbulent scales are modelled which consequently implies greater dependencies of the results with respect to the chosen turbulence model, LES resolve the energy-rich large scales and only model small (subgrid) scales.

The RANS approach is still the most frequently used modeling technique in industry due to its low computational cost, but increasing computational power and especially the use of *graphics processing units* (GPU) may pave the path for LES in this context. The reader is referred to Anderson (1995) and Ferziger and Perić (2008) for a detailed introduction to CFD. A comprehensive introduction on LES of incompressible flows can be found in Sagaut (2006) and for compressible flows in Garnier et al. (2009).

Numerical simulation of SWBLI is a challenging task, especially when considering turbulent interactions with strong mean-flow separation. Knight and Degrez (1998) assessed the capabilities of RANS methods in predicting[6] 2D/3D laminar/turbulent SWBLI for the configurations involving a single fin, a double fin, and a hollow cylinder flare. The authors found that RANS simulations allow for an accurate prediction of laminar interactions, while they usually fail in predicting the skin-friction and heat-transfer distribution for strong turbulent SWBLI. Flow unsteadiness is not captured by steady RANS solutions, which is a dominant flow feature in strong interactions with a significant impact on mean flow quantities (Dolling, 2001). Further inaccuracies result from the use of a single length scale in eddy-viscosity models or the application of wall functions. Knight and Degrez (1998) state that "it appears necessary to develop large eddy simulation solvers, as only LES models will allow us to predict the fluctuating pressure and heat transfer loads which can be very significant in shock wave/boundary layer interactions.". Four years later, Knight et al. (2002) reassessed advances in CFD prediction of SWBLI. They included DNS and LES results that became available in the meantime, which reveal enhanced prediction capabilities of turbulent SWBLI over RANS. However, they also found discrepancies due to possibly different Reynolds numbers in experiment and simulation. This let them to conclude that DNS and LES of SWBLI are needed at Reynolds numbers corresponding to the experiment. Morgan et al. (2013) investigated modeling errors in RANS simulations employing eddy-viscosity and Reynolds-stress-transport based turbulence closures for the simulation of impinging SWBLI at different Reynolds numbers and shock strengths. As a *surrogate-truth model* they utilized a database of well-resolved LES. Results indicate a significant overestimation of the separation length when using low-order RANS models, similar to previous observations made by Pirozzoli et al. (2009). Both turbulence closure approaches misrepresent the turbulent kinetic energy (TKE) within the interaction region, which mainly stems from the failure to account for effects of turbulent transport within the detached shear layer. By further investigating invariants of the anisotropy tensor, the authors identified a missing one-component turbulence state for both RANS approaches in the upstream near-wall TBL that is present in the LES results and which subsequently lifts up to follow the initial inclination of the shear layer.

---

[6] With respect to the general flow field, mean and fluctuating aerodynamic and thermal loads.

1.3. Objectives

The introduction highlighted the necessity of high-fidelity LES for the simulation of turbulent SWBLI, especially when considering strong interactions with significant mean-flow separation. The goal of this thesis is to develop a numerical toolbox capable of simulating high-Reynolds-number SWBLI coupled to flexible walls by means of LES. Wall-resolved LES will be used to investigate the dynamics of weak and strong impinging SWBLI at low and high Reynolds number, including rigid and flexible walls. The main objectives of this thesis are summarized as follows:

  i. As a starting point, wall-resolved LES are conducted for weak interactions at low Reynolds number. Besides addressing the LES capability and accuracy in predicting mean-flow as well as unsteady properties of the interaction, a new passive flow-control method is proposed for impinging SWBLI. Particular emphasis is put on the control efficiency with respect to unsteady effects associated to reflected-shock oscillations.

 ii. The finite-volume (FV) based compressible flow solver INCA[7] operates on Cartesian grids and utilizes a cut-cell based IBM for representing embedded geometries. At the beginning of this thesis project, the algorithm could only handle stationary interfaces or rigid body motions. In this work, a coupling framework for compressible FSI is developed, in which the cut-cell based IBM is coupled to the finite-element (FE) based structural solver BACI[8], as well as to the open source structural solver CalculiX[9]. The loosely coupled partitioned framework is validated for mainly shock-loaded structures undergoing large and complex deformations.

iii. The LES approach is validated for strong SWBLI at unprecedented high Reynolds number. For this purpose, a direct comparison with experimental results is performed.

 iv. The long-time integrated LES database is used to analyze low-frequency aspects of the high-Reynolds-number SWBLI in detail. Besides investigating filtered three-dimensional flow fields and power spectral densities of wall-pressure probes, a modal reduction technique by means of dynamic mode decomposition, applied to spanwise-averaged as well as wall-plane snapshots, is used.

  v. With the developed numerical toolbox, the first two-way coupled LES of a turbulent SWBLI on an elastic panel is performed. The reference experiment has been developed within the SFB-TR40 and consists of a fast-pitching wedge, whose impinging shock wave interacts with a flexible baseplate.

---

[7] INCA is a general-purpose multi-physics CFD solver for high-fidelity DNS and LES developed at the Institute of Aerodynamics and Fluid Mechanics (AER, TUM) and at the Faculty of Aerospace Engineering (Technische Universiteit Delft), see also `www.inca-cfd.org` for details.

[8] BACI is the multi-physics research code of the Institute for Computational Mechanics (LNM, TUM) and is mainly based on the finite element method, see also `www.lnm.mw.tum.de` for details.

[9] CalculiX is an open source three-dimensional (3D) structural FE solver developed by employees of MTU Aero Engines AG (Munich), see also `www.calculix.de` for details.

2. Physical model and numerical approach

In the following chapter the governing equations for fluid and solid are summarized. The numerical approach is briefly discussed and focuses on the FV based cut-cell IBM. Details can be found in Pasquariello et al. (2016), see also Appendix B.2.

2.1. Governing equations

The computational domain $\Omega = \Omega_\mathsf{F} \cup \Omega_\mathsf{S}$ is divided into non-overlapping fluid Ω_F and solid Ω_S subdomains, which share a conjoined interface $\Gamma = \Omega_\mathsf{F} \cap \Omega_\mathsf{S}$ and whose normal vector $\mathbf{n}^\Gamma$ points from the solid into the fluid domain. In the following, subscripts F and S are used whenever a distinction between both subdomains is necessary.

Fluid

The three-dimensional, compressible Navier-Stokes equations in conservative form are considered

$$\frac{\partial \mathbf{w}}{\partial t} + \nabla \cdot \mathbf{K}(\mathbf{w}) = 0 \quad \text{in } \Omega_\mathsf{F} \, . \tag{2.1}$$

Therein, the state vector $\mathbf{w} = [\rho_\mathsf{F}, \rho_\mathsf{F} u_1, \rho_\mathsf{F} u_2, \rho_\mathsf{F} u_3, E]^\mathsf{T}$ comprises the conserved variables density ρ_F, momentum $\rho_\mathsf{F}\mathbf{u}$ and total energy E. The flux tensor $\mathbf{K}(\mathbf{w}) = [\mathbf{k}^1, \mathbf{k}^2, \mathbf{k}^3]^\mathsf{T}$

may be decomposed into an inviscid (hyperbolic) part $\mathbf{F} = [\mathbf{f}^1, \mathbf{f}^2, \mathbf{f}^3]^\mathsf{T}$ and a viscous contribution $\mathbf{D} = [\mathbf{d}^1, \mathbf{d}^2, \mathbf{d}^3]^\mathsf{T}$, following

$$
\mathbf{k}^i\left(\mathbf{w}\right) = \mathbf{f}^i\left(\mathbf{w}\right) + \mathbf{d}^i\left(\mathbf{w}\right) =
\begin{bmatrix}
\rho_\mathsf{F} u_i \\
\rho_\mathsf{F} u_1 u_i + \delta_{i1} p \\
\rho_\mathsf{F} u_2 u_i + \delta_{i2} p \\
\rho_\mathsf{F} u_3 u_i + \delta_{i3} p \\
u_i\left(E + p\right)
\end{bmatrix}
-
\begin{bmatrix}
0 \\
\tau_{i1} \\
\tau_{i2} \\
\tau_{i3} \\
u_k \tau_{ik} - q_i
\end{bmatrix}.
\tag{2.2}
$$

The viscous stress tensor τ_{ij} for a Newtonian fluid reads

$$
\tau_{ij} = \mu_\mathsf{F}\left(\frac{\partial u_i}{\partial x_j} + \frac{\partial u_j}{\partial x_i}\right) + \lambda_\mathsf{F}\frac{\partial u_k}{\partial x_k}\delta_{ij}\,,
\tag{2.3}
$$

where the first Lamé parameter λ_F is related to the dynamic viscosity μ_F through Stoke's hypothesis, i.e., $\lambda_\mathsf{F} = -2/3\,\mu_\mathsf{F}$. The heat flux due to conduction is evaluated according to Fourier's law

$$
q_i = -\kappa_\mathsf{F}\frac{\partial T}{\partial x_i}\,,
\tag{2.4}
$$

with κ_F denoting the coefficient of thermal conductivity. In this work air is considered and modeled as a perfect gas with a specific-heat ratio of $\gamma = 1.4$ and a specific gas constant of $\mathcal{R} = 287.05\,\mathsf{J/(kg\,K)}$. Pressure p and temperature T are given by the ideal-gas equation of state

$$
p = \rho_\mathsf{F}\mathcal{R}T\,,
\tag{2.5}
$$

and the definition of total energy

$$
E = \frac{p}{\gamma - 1} + \frac{1}{2}\rho_\mathsf{F} u_i u_i\,.
\tag{2.6}
$$

Temperature dependence of dynamic viscosity μ_F and thermal conductivity κ_F is modeled through Sutherland's law and assuming a constant Prandtl number,

$$
\mu_\mathsf{F} = \mu_{\mathsf{F},ref}\frac{T_{ref} + C}{T + C}\left(\frac{T}{T_{ref}}\right)^{1.5}\,, \qquad \kappa_\mathsf{F} = \frac{\gamma\mathcal{R}}{(\gamma - 1)Pr}\mu_\mathsf{F}\,,
\tag{2.7}
$$

with $Pr = 0.72$, $T_{ref} = 293.15\,\mathsf{K}$, $C = 122\,\mathsf{K}$ and $\mu_{\mathsf{F},ref} = 18.21 \cdot 10^{-6}\,\mathsf{Pa\,s}$.

SOLID

The local form of the balance of linear momentum governs the structural subdomain

$$
\rho_{\mathsf{S};0}\frac{\partial^2 \mathbf{d}}{\partial t^2} = \nabla_0 \cdot (\mathbf{F} \cdot \mathbf{S}) + \hat{\mathbf{b}}_0 \quad \text{in } \Omega_\mathsf{S}\,,
\tag{2.8}
$$

and describes an equilibrium between the forces of inertia, internal and external forces with respect to the undeformed structural domain Ω_S. Therein, $\mathbf{d}$ denotes the vector of unknown displacements, $\rho_{\mathsf{S};0}$ the structural material density, $\nabla_0 \cdot (\cdot)$ the material divergence operator, and $\hat{\mathbf{b}}_0$ external (known) material body forces. Internal forces are

calculated through the first Piola-Kirchhoff stress tensor $\mathbf{P} = \mathbf{F} \cdot \mathbf{S}$, which itself depends on the deformation gradient tensor $\mathbf{F}$ and the second Piola-Kirchhoff stress tensor $\mathbf{S}$. Stresses are determined with the help of a constitutive equation, which in this work is given by a hyperelastic Saint Venant-Kirchhoff material model. Its strain energy density function Ψ is given as

$$\Psi(\mathbf{E}) = \mu_\mathsf{S}\mathbf{E} : \mathbf{E} + \frac{1}{2}\lambda_\mathsf{S}\left(\mathbf{E} : \mathbf{I}\right)^2 , \tag{2.9}$$

where λ_S and μ_S denote the Lamé constants, $\mathbf{I}$ the second-order identity tensor and $\mathbf{E}$ the Green-Lagrange strain tensor. The latter is defined as

$$\mathbf{E} = \frac{1}{2}\left(\mathbf{F}^\mathsf{T} \cdot \mathbf{F} - \mathbf{I}\right) . \tag{2.10}$$

The second Piola-Kirchhoff stress tensor $\mathbf{S}$ is derived from Eq. (2.9) through

$$\mathbf{S} = \frac{\partial \Psi}{\partial \mathbf{E}} . \tag{2.11}$$

For later reference the Cauchy stress tensor $\boldsymbol{\sigma}_\mathsf{S}$, or in the literature often called the *true stress tensor*, is introduced by

$$\boldsymbol{\sigma}_\mathsf{S} = \frac{1}{J}\mathbf{P} \cdot \mathbf{F}^\mathsf{T} , \tag{2.12}$$

in which J is the Jacobian. The boundary of the structural domain, $\partial\Omega_\mathsf{S}$, is decomposed into pairwise disjoint segments following

$$\partial\Omega_\mathsf{S} = \Gamma_{\mathsf{S};\mathsf{D}} \cup \Gamma_{\mathsf{S};\mathsf{N}} \cup \Gamma . \tag{2.13}$$

Displacements $\hat{\mathbf{d}}$ are prescribed on the Dirichlet boundary $\Gamma_{\mathsf{S};\mathsf{D}}$, whereas tractions $\hat{\mathbf{t}}_0 = \mathbf{P} \cdot \mathbf{n}_0$ are given on the Neumann segment $\Gamma_{\mathsf{S};\mathsf{N}}$. In the latter case, $\mathbf{n}_0$ denotes the normal vector in material configuration.

FLUID–SOLID INTERFACE CONDITIONS

The integrity between the domains Ω_F and Ω_S is established by imposing dynamic and kinematic coupling conditions at the conjoined interface Γ. Dynamic equilibrium requires the tractions to be equal, i.e.

$$\boldsymbol{\sigma}_\mathsf{F}^\Gamma \cdot \mathbf{n}^\Gamma = \boldsymbol{\sigma}_\mathsf{S}^\Gamma \cdot \mathbf{n}^\Gamma . \tag{2.14}$$

The Cauchy stress tensor $\boldsymbol{\sigma}_\mathsf{S}$ is given by Eq. (2.12). The fluid stress tensor $\boldsymbol{\sigma}_\mathsf{F} = -p\mathbf{I} + \boldsymbol{\tau}$ comprises normal (inviscid) and tangential (viscous) stresses, where the latter are given by Eq. (2.3). A kinematic no-slip boundary condition is imposed

$$\mathbf{u}^\Gamma = \frac{\partial \mathbf{d}^\Gamma}{\partial t} , \tag{2.15}$$

which reduces to matching normal velocities in the case of an inviscid flow

$$\mathbf{u}^\Gamma \cdot \mathbf{n}^\Gamma = \frac{\partial \mathbf{d}^\Gamma}{\partial t} \cdot \mathbf{n}^\Gamma . \tag{2.16}$$

2.2. Numerical approach

In this section the numerical approach for fluid and solid domains, as well as the coupling between both subdomains is briefly discussed. For a detailed discussion refer to Örley et al. (2015) and Pasquariello et al. (2016). In Pasquariello et al. (2016) (see also Appendix B.2), the coupling framework is presented in full length. With respect to the finite element method (FEM), the reader is referred to Zienkiewicz and Taylor (2000a,b) and Dhondt (2004). Details about the implicit LES model used in this work can be found in Hickel et al. (2006, 2014).

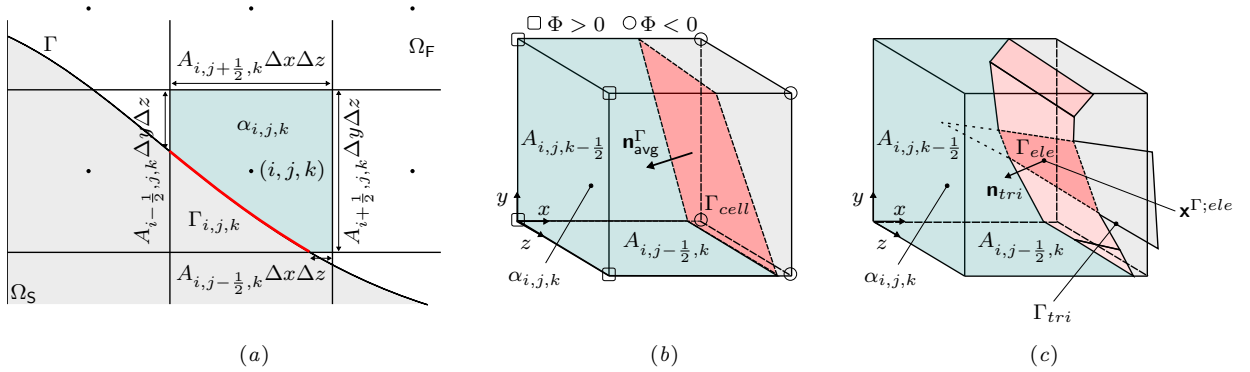### Fluid: Finite volume cut-cell immersed boundary method

Figure 2.1.: (a) Two-dimensional sketch of a cut-cell. (b) Cut-algorithm based on a level-set field $\mathbf{\Phi}$ and (c) on intersection with a triangulated surface. Figures partially reproduced from Örley et al. (2015) and Pasquariello et al. (2016).

The flow solver INCA operates on Cartesian grids and employs the finite volume method (FVM) for solving the Navier-Stokes equations. In Fig. 2.1(a), a two-dimensional sketch of a cut-cell is shown. Considering the computational cell $\Omega_{i,j,k}$ and a single time step $\Delta t = t^{n+1} - t^n$, the integral form of Eq. (2.1) after applying the Gauss theorem reads

$$\int_{t^n}^{t^{n+1}} \int_{\Omega_{i,j,k} \cap \Omega_{\mathsf{F}}} \frac{\partial \mathbf{w}}{\partial t} \, \mathrm{d}V \, \mathrm{d}t + \int_{t^n}^{t^{n+1}} \int_{\partial(\Omega_{i,j,k} \cap \Omega_{\mathsf{F}})} \mathbf{K}(\mathbf{w}) \cdot \mathbf{n} \, \mathrm{d}S \, \mathrm{d}t = 0 \,. \tag{2.17}$$

Therein, $\partial(\Omega_{i,j,k} \cap \Omega_{\mathsf{F}})$ denotes the fluid wetted surface of $\Omega_{i,j,k}$, and $\mathrm{d}V$, $\mathrm{d}S$ the infinitesimal volume and surface element, respectively. Considering a volume average of the conserved variables,

$$\mathbf{w}_{i,j,k} = \frac{1}{\alpha_{i,j,k} V_{i,j,k}} \int_{\Omega_{i,j,k} \cap \Omega_{\mathsf{F}}} \mathbf{w} \, \mathrm{d}x \, \mathrm{d}y \, \mathrm{d}z, \tag{2.18}$$

and applying a simple forward Euler time integration scheme[1] results in the discrete form

---

[1] This is equivalent to one sub-step of the explicit third-order Runge-Kutta scheme of Gottlieb and Shu (1998) used in this work.
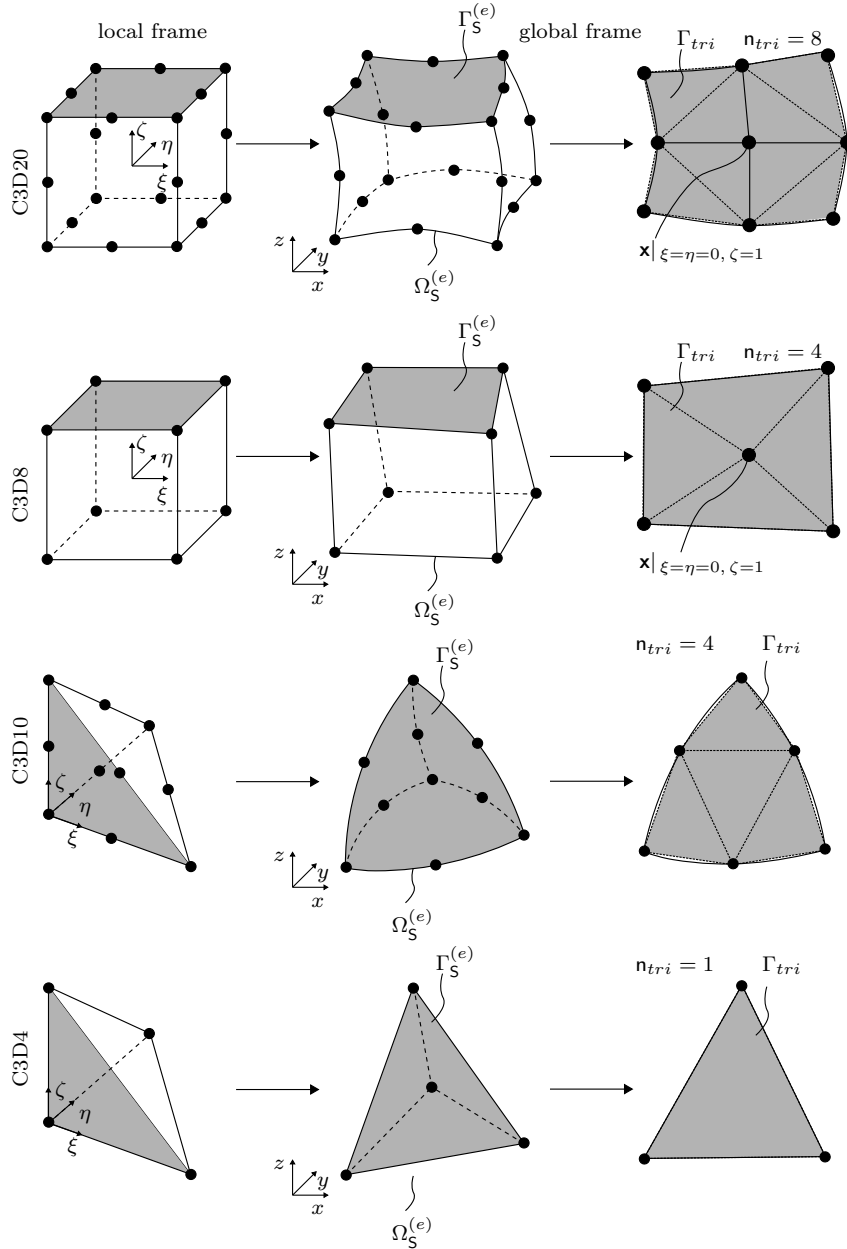
Figure 2.2.: Triangulation of fluid-wetted structural surface elements $\Gamma_\mathsf{S}^{(e)}$, exemplarily shown for different structural elements $\Omega_\mathsf{S}^{(e)}$ as treated by the FSI framework. Γ_{tri} is used by the cut-algorithm for computing cut-cells and related geometric quantities. From top to bottom: Quadractic (C3D20) and linear (C3D8) brick element, quadratic (C3D10) and linear (C3D4) tetrahedral element. Naming convention adopted from Dhondt (2016).

of Eq. (2.17)

$$
\begin{aligned}
\alpha_{i,j,k}^{n+1}\mathbf{w}_{i,j,k}^{n+1} = \alpha_{i,j,k}^{n}\mathbf{w}_{i,j,k}^{n} &+ \frac{\Delta t}{\Delta x_i}\left[A_{i-\frac{1}{2},j,k}^{n}\mathbf{k}_{i-\frac{1}{2},j,k}^{1,n} - A_{i+\frac{1}{2},j,k}^{n}\mathbf{k}_{i+\frac{1}{2},j,k}^{1,n}\right]\\
&+ \frac{\Delta t}{\Delta y_j}\left[A_{i,j-\frac{1}{2},k}^{n}\mathbf{k}_{i,j-\frac{1}{2},k}^{2,n} - A_{i,j+\frac{1}{2},k}^{n}\mathbf{k}_{i,j+\frac{1}{2},k}^{2,n}\right]\\
&+ \frac{\Delta t}{\Delta z_k}\left[A_{i,j,k-\frac{1}{2}}^{n}\mathbf{k}_{i,j,k-\frac{1}{2}}^{3,n} - A_{i,j,k+\frac{1}{2}}^{n}\mathbf{k}_{i,j,k+\frac{1}{2}}^{3,n}\right]\\
&+ \frac{\Delta t}{V_{i,j,k}}\boldsymbol{\chi}_{i,j,k}\,.
\end{aligned}
\tag{2.19}
$$

Therein, $V_{i,j,k} = \Delta x_i \Delta y_i \Delta z_i$ denotes the total volume of cell $\Omega_{i,j,k}$ and $0 \leq \alpha_{i,j,k}$, $A \leq 1$ correspond to the fluid volume fraction and the effective fluid wetted cell face aperture, respectively. The face-averaged numerical fluxes across regular cell faces in the x, y and z direction are denoted as $\mathbf{k}^1$, $\mathbf{k}^2$ and $\mathbf{k}^3$, respectively. In cut-cells, i.e. fluid cells $\Omega_{i,j,k}$ for which $0 < \alpha_{i,j,k} < 1$ holds, the flux across the interface $\Gamma_{i,j,k} = \Gamma \cap \Omega_{i,j,k}$ is especially accounted for through an interface exchange term $\boldsymbol{\chi}_{i,j,k}$. Geometric quantities of a cut-cell directly depend on the structural interface $\Gamma_{i,j,k}$ and are needed by the cut-cell IBM, see also Eq. (2.19). Traditional algorithms based on the level-set method approximate the interface through a single plane[2], i.e. $\Gamma_{i,j,k} \approx \Gamma_{cell}$, see Fig. 2.1($b$). As shown by Örley et al. (2015), this piecewise linear approximation of Γ may produce spurious pressure oscillations when dealing with moving objects in weakly compressible flows. These numerical artifacts originate from a discontinuous evolution of fluid volume fractions near sharp corners or edges in general, where the curvature radius is of the order of the local fluid grid size. A solution to overcome these problems is to use a more accurate representation of the structural interface Γ within the computational fluid mesh. The so-called cut-element IBM, see Örley et al. (2015) for details, recovers sub-cell interface resolution by considering a set of cut-elements $\Gamma_{ele} = \Gamma_{tri} \cap \Omega_{i,j,k}$ in a single fluid cell, see Fig. 2.1(c). A cut-cell may consist of several cut-elements, i.e. $\Gamma_{i,j,k} \approx \sum_{ele} \Gamma_{ele}$, which result from the intersection of individual structural interface triangles Γ_{tri} with a fluid cell. For this purpose, each fluid-wetted structural surface elements $\Gamma_{\mathsf{S}}^{(e)}$ is triangulated as shown exemplarily in Fig. 2.2 for linear (quadratic) hexahedral (tetrahedral) elements. The fluid volume fraction $\alpha_{i,j,k}$ is subsequently computed through a sub-tetrahedralization of the fluid volume, whereas face apertures such as $A_{i,j,k-\frac{1}{2}}$ are calculated using a sub-triangulation of the cell faces.

The interface exchange term $\boldsymbol{\chi}_{i,j,k}$ in Eq. (2.19) models the interaction between fluid and solid in the cut-cell framework. Accounting for possibly multiple cut-elements within a single cut-cell, the exchange term within the computational cell $\Omega_{i,j,k}$ can be written as

$$
\boldsymbol{\chi}_{i,j,k} = \sum_{ele}\boldsymbol{\chi}_{ele} = \sum_{ele}\left(\boldsymbol{\chi}_{ele}^{p} + \boldsymbol{\chi}_{ele}^{\nu} + \boldsymbol{\chi}_{ele}^{ht}\right)\,.
\tag{2.20}
$$

The interface fluxes include the fluid stresses and the resulting work due to pressure $\boldsymbol{\chi}_{ele}^{p}$ and viscous effects $\boldsymbol{\chi}_{ele}^{\nu}$, as well as heat transfer effects $\boldsymbol{\chi}_{ele}^{ht}$. The pressure term

---

[2] The level-set field may be calculated based on a search algorithm that finds the closest distance to the interface. After interpolating the level-set cell values to the cell vertices, a marching cubes algorithm (Lorensen and Cline, 1987) can be used to reconstruct the single planar interface.

χ_{ele}^{p} requires the interface pressure $\mathsf{p}_{ele}^{\Gamma}$ at the cut-element face centroid $\mathbf{x}^{\Gamma;ele}$, which is obtained by solving a symmetric face-normal Riemann problem $\mathcal{R}\left(\mathbf{w}_{i,j,k}, \mathbf{u}^{\Gamma;ele}\right) = 0$ (Pasquariello et al., 2016). Both the viscous χ_{ele}^{ν} and heat transfer χ_{ele}^{ht} contributions require the evaluation of flow gradients at $\mathbf{x}^{\Gamma;ele}$. The most simple (but less accurate) way is to use a bi-linear (tri-linear) interpolation in 2D (3D), see Meyer et al. (2010). However, this approach may suffer from spurious oscillations in the flow solution resulting from mesh irregularities or the inclusion of small cut-cells in the reconstruction process (Berger et al., 2012; Pasquariello et al., 2013). An extension to higher-order interpolation based on a weighted least-squares interpolation, which overcomes these drawbacks, is given in Pasquariello et al. (2013). For more details on the evaluation of the individual contributions, the reader is referred to Meyer et al. (2010), Pasquariello et al. (2013), Örley et al. (2015) and Pasquariello et al. (2016).

In the cut-cell IBM, non-cut fluid cells in the solid part Ω_{S} of the computational domain Ω near the interface Γ contain ghost fluid states for imposing boundary conditions at the interface without requiring a modification of interpolation stencils in the FV reconstruction scheme. In this work, the ghost-cell methodology as proposed by Mittal et al. (2008) for incompressible flows, extended to stationary and moving boundary compressible cut-cell methods is used (Pasquariello et al., 2013, 2016).

A drawback of cut-cell methods is the so-called *small-cell problem*, which can lead to numerical instability or require excessively small time steps due to the presence of very small cut-cells. In this work a stabilization method based on a conservative mixing procedure is used (Hu et al., 2006; Meyer et al., 2010; Örley et al., 2015).

SOLID: FINITE ELEMENT METHOD

The structural problem is solved with the FEM. Starting point is the weak (integral) form of the balance equation, which is obtained by calculating weighted residuals of Eq. (2.8) with virtual displacements $\delta\mathbf{d}$. Subsequent integration over Ω_{S} and application of the Gauss theorem leads to

$$\int_{\Omega_{\mathsf{S}}} \left(\rho_{\mathsf{S};0}\ddot{\mathbf{d}} \cdot \delta\mathbf{d} + \mathbf{S} : \delta\mathbf{E} - \hat{\mathbf{b}}_0 \cdot \delta\mathbf{d} \right) \mathrm{d}V_0 - \int_{\Gamma_{\mathsf{S};\mathsf{N}}} \hat{\mathbf{t}}_0 \cdot \delta\mathbf{d} \, \mathrm{d}A_0 - \delta\mathcal{W}_{\mathsf{S}}^{\Gamma} = \mathbf{0} \, . \qquad (2.21)$$

Therein, $\mathrm{d}V_0$ and $\mathrm{d}A_0$ denote infinitesimal volume and surface elements, respectively, $\delta\mathcal{W}_{\mathsf{S}}^{\Gamma}$ represents the virtual work at the additional FSI interface, and $\delta\mathbf{E}$ results from the variation of the Green-Lagrange strain tensor, Eq. (2.10), to

$$\delta\mathbf{E} = \frac{1}{2}\left[(\nabla_0\delta\mathbf{d})^{\mathsf{T}} \cdot \mathbf{F} + \mathbf{F}^{\mathsf{T}} \cdot \nabla_0\delta\mathbf{d} \right] \, . \qquad (2.22)$$

In this work Eq. (2.21) is discretized in space with the FEM. The structural domain Ω_{S} is decomposed into n^e solid elements $\Omega_{\mathsf{S}}^{(e)}$ with associated standard shape functions for approximating the displacement field. Assembling the contributions of all elements $\Omega_{\mathsf{S}}^{(e)}$ and assuming virtual displacements $\delta\mathbf{d}$ to be arbitrary leads to the semi-discrete weak

form of the balance equation,

$$\mathbf{M}\ddot{\mathbf{d}} + \mathbf{f}_{\mathsf{S;int}}(\mathbf{d}) - \mathbf{f}_{\mathsf{S;ext}}(\mathbf{d}) - \mathbf{f}_{\mathsf{S}}^{\Gamma} = \mathbf{0}\,, \qquad (2.23)$$

where $\mathbf{M}$ denotes the mass matrix and $\ddot{\mathbf{d}}$, $\mathbf{d}$ are the discrete acceleration and displacement vectors, respectively. The discrete force vectors can be split into internal $\mathbf{f}_{\mathsf{S;int}}$, external $\mathbf{f}_{\mathsf{S;ext}}$ and interface $\mathbf{f}_{\mathsf{S}}^{\Gamma}$ forces, where the latter results from fluid tractions exerted on the FSI interface. The above equation needs to be discretized in time. Depending on the structural solver used, this is done by employing the generalized trapezoidal rule (or one-step-Θ method) for BACI, whereas the Hilber-Hughes-Taylor α-method (Hilber et al., 1977) is used for CalculiX. The fully discretized balance equation describes a set of nonlinear algebraic equations which is solved iteratively with the Newton-Raphson method.
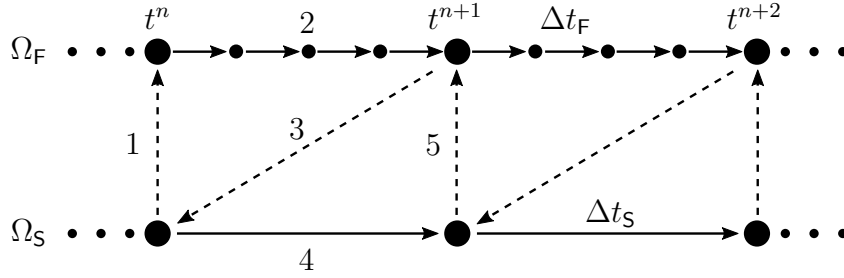

Figure 2.3.: Staggered coupling algorithm with optional subcycling in the fluid.

Coupling framework

The fluid Ω_{F} and structural Ω_{S} subdomains are loosely coupled by means of a conventional serial staggered algorithm (Farhat et al., 1995) which follows the classical Dirichlet-Neumann partitioning, see Fig. 2.3. In this approach, the fluid takes the Neumann part by imposing its tractions on the FSI interface Γ, whereas the solid defines kinematic constraints (displacements and velocities) in the sense of a Dirichlet boundary condition. The main steps to advance the coupled system from time level t^n to $t^{n+1} = t^n + \Delta t$ are:

1. Transfer structural interface displacements $\mathbf{d}^{\Gamma;n}$ and velocities $\dot{\mathbf{d}}^{\Gamma;n}$ at time t^n to the flow solver, which act as a Dirichlet boundary condition. The new interface position is used to update the cut-cells and related geometric properties on the fluid side. The cut-element algorithm is applied on the triangulated structural interface which comprises several interface triangles Γ_{tri}, see Fig. 2.1(c) and Fig. 2.2.

2. Advance the fluid system, Eq. (2.19), in time from $t^n \to t^{n+1}$. Subcycling ($n_{\mathsf{F/S}} = \frac{\Delta t_{\mathsf{S}}}{\Delta t_{\mathsf{F}}} > 1$) may be optionally used to increase computational efficiency by computing several fluid steps $n_{\mathsf{F/S}}$ before updating the structure[3]. The interface exchange term, Eq. (2.20), as well as the ghost-cell methodology use given structural velocities $\dot{\mathbf{d}}^{\Gamma;n}$ at time level t^n. This information is required at the cut-element face centroids $\mathbf{x}^{\Gamma;ele}$.

---

[3] In this case the structural interface displacements are evenly distributed among all subcycles. Fluid interface tractions may be optionally averaged or instantly transferred to the structure.

Consequently, an interpolation procedure is needed to transfer solid velocities to the fluid interface.

3. Transfer the fluid interface tractions $\boldsymbol{\sigma}_{\mathsf{F}}^{\Gamma;n+1} \cdot \mathbf{n}^{\Gamma;n}$ to the structural solver. An interpolation procedure is needed to transfer fluid forces to the solid interface.

4. Advance the structural system, Eq. (2.23), in time. The projected fluid interface loads $\mathbf{f}_{\mathsf{S}}^{\Gamma}$ at time level t^{n+1} act as additional Neumann boundary condition on the solid.

5. Proceed to the next time step.

The staggering procedure introduces a one time-step lag between both subdomains with respect to the displacement continuity, which consequently results in a first-order in time, $\mathcal{O}(\Delta t)$, coupling scheme (Farhat et al., 1995).

The use of a cut-cell IBM inevitably leads to non-matching interface grids and thus requires interpolation methods for the load and motion transfer as highlighted in the above algorithm (steps 2. and 3.). A Mortar method has been developed for coupling with the structural solver BACI, see also Pasquariello et al. (2016) for details. When using CalculiX as FE solver, a simple but efficient projection-based interpolation method based on the FE shape functions is used (Farhat et al., 1998). Recently, Thari et al. (2017) has shown that the latter approach leads to accurate results when applied to the test cases presented in Pasquariello et al. (2016). A more detailed literature overview of existing interpolation methods for non-matching grids is given in Section 3.2.

Implicit large-eddy simulation by ALDM

LES exploit a spatial scale-separation approach: the largest most-energetic turbulent structures are fully resolved on the computational grid, whereas the unresolved smaller scales are modeled. Following Kolmogorov's isotropy hypothesis, small eddies are less dependent on the geometry, i.e. they tend to be more isotropic and consequently more universal than large scales, which in turn corroborates the LES modeling approach. Numerically solving the Navier-Stokes equations implicitly generates a scale separation through the use of a computational grid of finite spacing[4] and through the numerical discretization of continuous operators. The latter describes the interference between numerical errors and *represented non-resolved scales* (Garnier et al., 2009). Mathematically, this separation in scales is equivalent to the convolution of the governing equations with a filter kernel, which yields the filtered Navier-Stokes equations (Leonard, 1975). Filtering the nonlinear terms of the Navier-Stokes equations results in unclosed subgrid scale (SGS) tensors which need to be modeled. It is common practice to consider spatial filtering only and assume that all relevant temporal scales are resolved by choosing a sufficiently small time step (Adams et al., 2004).

One may differentiate between *explicit* and *implicit* SGS models. For the former, one considers the filtered Navier-Stokes equations, adds explicit model terms to account for SGS effects and subsequently discretizes the resulting system of equations. The underlying

---

[4] No wavenumber larger than the Nyquist wavenumber of the underlying grid, $\xi = \pi/\Delta$, can be resolved.

basic assumption is that turbulence model and artificial numerical dissipation do not interfere, which in general is not true. Several studies in the literature (Vreman et al., 1995; Kravchenko and Moin, 1997) have shown that even high-order centered discretizations can have truncation errors whose magnitude is in the order of corrsponding SGS terms and hence lead to unpredictable consequences regarding the solution accuracy. Implicit LES (ILES) approaches, on the other hand, exploit this mutual interference by solving the unmodified conservation laws in such a way, that the numerical truncation error acts as a SGS model, thus avoiding explicit computations of model terms (Adams et al., 2004).

The *Adaptive Local Deconvolution Method* (ALDM) constitutes a general framework for ILES and has been developed for incompressible (Adams et al., 2004; Hickel et al., 2006) and compressible turbulence (Hickel et al., 2014). ALDM is a nonlinear FV scheme which incorporates the fundamental elements of explicit SGS modeling in LES, i.e., filtering and deconvolution, through cell-averaging and reconstruction in the FVM. It operates on the discretization of the convective fluxes with its main building blocks being (i) an adaptive local deconvolution operator that returns an approximation of the unfiltered solution at cell faces, (ii) a numerical flux function that operates on the reconstructed solution, and (iii) a numerical integration scheme to compute face-averaged fluxes. Local reconstruction of the unfiltered solution is obtained from a solution-adaptive convex combination of Harten-type deconvolution polynomials. Since the computational cost of a multi-dimensional FV scheme is strongly dictated by this reconstruction step, Hickel and Adams (2007) proposed a simplified ALDM with one Gauss point per cell face, which is also used in this work. The discretization of the hyperbolic flux $\mathbf{F}$ in Eq. (2.2) is mainly responsible for the SGS effects and is consequently manipulated by the ALDM[5]. Secondary regularization is provided by a modified Lax-Friedrichs flux function which is composed of the physical Navier-Stokes flux and a (dissipative) regularization tensor. The dissipation tensor is locally modified near shock waves to ensure essentially non-oscillatory solutions at strong discontinuities. The free parameters that result from the the reconstruction step, $\{\boldsymbol{\alpha}, \boldsymbol{\gamma}\}$, as well as those that originate from the secondary regularization within the numerical flux function, $\{\boldsymbol{\sigma}\}$, are used to tailor the spatial truncation error of the FV scheme. The deconvolution parameters $\{\boldsymbol{\alpha}, \boldsymbol{\gamma}\}$ were determined by Hickel et al. (2006) for incompressible homogeneous turbulence by applying an evolutionary optimization algorithm with a cost function that minimizes the difference between spectral numerical viscosity and eddy viscosity based on the *Eddy Damped Quasi Normal Markovian* theory (Lesieur et al., 2005). The secondary regularization parameters $\{\boldsymbol{\sigma}\}$ are used to adjust the low-wavenumber plateau of the spectral eddy viscosity and diffusivity, see Hickel et al. (2014) for details. To compensate overestimated SGS dissipation in wall-bounded flows, the dissipative weight $\sigma^{\rho u}$ of the numerical flux function is reduced by means of an additional wall-damping functional (Hickel and Adams, 2007). In this work, a damping functional based on the coherent structures model of Kobayashi (2005) is used.

---

[5] The truncation error of the diffusive flux may also be considered as done by Zandonade et al. (2004). However, its influence on the results should be negligible when considering LES of high-Reynolds-number flows, where the grid cutoff is typically located within the inertial range. Consequently, in this work, the viscous flux $\mathbf{D}$ in Eq. (2.2) is discretized by a second-order central-difference scheme.

3. ACCOMPLISHMENTS

This chapter summarizes the main contributions of this thesis including a short literature overview of the current state-of-the-art in research. Support is given by selected publications which can be found in Appendix B.

3.1. FLOW CONTROL OF SWBLI

SWBLI with mean-flow separation impose increased mean and fluctuating pressure loads as well as thermal loads on the underlying structure and affect the vehicle performance in terms of increased viscous and wave drag (Dolling, 2001). Furthermore, unsteady effects associated to low-frequency modulations of the separation bubble and reflected shock impose limitations to the choice of materials and may degrade structural integrity, e.g., by the occurrence of buffeting. In supersonic engine inlets, where the flow deceleration is accomplished through a complex system of oblique shocks, SWBLI may even lead to the hazardous effect of engine unstart, in which the shock system propagates upstream out of the inlet duct. The unstart process itself may be initiated by blockage effects induced by SWBLI with mean-flow separation (Wagner et al., 2009). Flow control gained increased research interest in the past decades and is applied to mitigate the aforementioned detrimental effects associated to SWBLI.

Flow control can be generally classified into *active* or *passive* types, depending on whether the control device needs to be powered or not. A further distinction can be made based on the control purpose, thereby distinguishing between *boundary-layer control*, aiming at

reducing shock-induced separation which is the prime performance degradation mechanism in supersonic engine inlets, and *shock control*, tending to reduce stagnation pressure losses (wave drag) which plays a crucial role for transonic airfoils (Babinsky and Ogawa, 2008).

Boundary-layer control increases the stiffness of the upstream boundary layer, hence making it less susceptible against shock-induced separation. This can be accomplished, e.g., through tangential blowing, suction, wall-cooling or the use of (micro-)vortex generators upstream of the SWBLI (Délery, 1985). All of these control methods have in common that they additionally supply momentum to the near-wall flow prior to the interaction, which results in a reduced separation length.

Reducing the wave drag for transonic applications demands for shock-control techniques. This is mainly accomplished by smearing strong normal shocks into λ-type structures. Since the overall stagnation pressure drop is smaller for multiple weaker shocks compared to a single normal shock of the same overall pressure jump, shock control reduces total shock losses and thus wave drag (Babinsky and Ogawa, 2008). Smearing the shock wave is performed by deflecting the flow outside the boundary layer, either through the use of 2D/3D-contoured bumps or by placing a cavity with a porous plate underneath the interaction region. For a more detailed overview of existing control methods refer to Délery (1985), Viswanath (1988) and Stanewsky et al. (1997, 2002).

In his experiments, McCormick (1993) found that the use of micro-vortex generators significantly reduce shock-induced separation (at the expense of higher total pressure loss), while the passive cavity concept substantially reduces wave drag through a more isentropic compression (at the expense of increased boundary-layer losses downstream). Further experimental studies for this control type can be found in the work of Blinde (2008), Verma et al. (2012), Bo et al. (2012), Giepman et al. (2014) and Verma and Chidambaranathan (2015). Souverein and Debiève (2010) and Verma and Manisankar (2012) studied the influence of Air Jet Vortex Generators (AJVGs) placed in a row upstream of the interaction for an impinging and compression-ramp SWBLI, respectively. Similar to conventional vortex generators, AJVGs energize the incoming TBL through the formation of counter-rotating streamwise vortices. Souverein and Debiève (2010) reported a significant increase of the shock frequency by about 50 % as a direct consequence of the smaller recirculation bubble. Verma and Manisankar (2012) found a reduction of the peak rms value of shock-foot pressure fluctuations by an order of magnitude for air jets with a pitch angle of 90°.

Lee (2009) and Ghosh (2010) conducted LES of impinging SWBLI controlled by micro-vortex generators. They observed a three-dimensional modification of the reversed-flow region with a net reduction in separation length and improved TBL characteristics downstream of the interaction region. Recently, Bisek et al. (2013) applied LES to a plasma-based control mechanism for a 24° compression ramp SWBLI at Ma = 2.25, and proved the concept to be able to significantly reduce the mean separation length by more than 75 % which consequently reduced the low-frequency content. Given the lack of available high-fidelity numerical studies (LES/DNS) of SWBLI control aiming at mitigating reflected-shock unsteadiness, the following work proposes a new passive control device and analyzes low-frequency modulations in detail.

V. Pasquariello, M. Grilli, S. Hickel and N. A. Adams (2014)
Large-eddy simulation of passive shock-wave/boundary-layer interaction control
International Journal of Heat and Fluid Flow, **49**, 116-127

In this paper (Pasquariello et al., 2014), a passive flow-control technique for the interaction of an oblique shock with a TBL is numerically investigated in the context of boundary-layer control by means of wall-resolved LES. Besides the evaluation of control efficiency in terms of mean-flow modulation, the analysis focuses on the potential of the newly proposed control mechanism in alleviating unsteady aspects of the interaction associated to low-frequency shock dynamics.

The SWBLI considered for control is an oblique shock impinging on a flat-plate TBL, where the shock itself is generated by a 8.8° wedge at a freestream Mach number of $Ma = 2.3$. The Reynolds number based on the incoming TBL thickness is $Re_{\delta_0} = 60.5 \cdot 10^3$ and the adverse pressure gradient imposed by the incident shock is strong enough to provoke a fully separated mean-flow region. The proposed control device combines full-span suction inside the separation bubble and blowing upstream of the interaction region by a pressure feedback through a duct embedded in the wall which provokes a natural recirculating flow similar to control mechanisms involving porous surfaces, mesoflaps or streamwise slots (McCormick, 1993; Stanewsky et al., 1997; Srinivasan et al., 2006). Three different suction locations are investigated while keeping the injection position constant.

Wall-resolved LES are conducted with the use of the ALDM (Hickel et al., 2006, 2014) for physically consistent subgrid scale turbulence modeling. Special attention is paid to the correct prescription of turbulent inflow boundary conditions which do not artificially correlate with low-frequency shock motions. For this purpose, a digital filter based boundary condition is used (Klein et al., 2003).

Results imply that suction applied within the recirculation zone significantly alters turbulence evolution in this region. Specifically, suction acting in the region of the inclined detached shear layer strongly increases turbulence production through a deflection towards the discrete suction slot, whereas a reduced turbulence intensity is observed for suction applied in the rear part of the separation bubble. With respect to the reflected-shock dynamics, the analysis of wall-pressure spectra indicates a shift of the high-energy low-frequency content to higher frequencies for all control configurations, a finding which is in accordance with the reduction in bubble mass and the concept of a quasi-constant Strouhal number (Piponniau et al., 2009; Souverein and Debiève, 2010). Furthermore, unsteady wall-pressure loads induced by the separation shock foot are remarkably reduced in case of suction acting close to the reattachment point. For this configuration, a stabilizing effect with respect to the flapping motion of the incident shock tip as well as for the reflected shock dynamics is observed.

Initial work on this topic was already done in my Diploma thesis (Pasquariello, 2012), where I developed the simulation setup in the in-house code INCA and performed preliminary numerical simulations. Thereafter, I performed additional numerical simulations including grid generation for different control configurations, extended the post-processing and analysis of the simulation data, and wrote the manuscript for the publication.

3.2. FSI modeling in compressible flow

Compressible FSI phenomena appear in a wide field of applications including, e.g., non-linear aeroelasticy of wings (flutter calculations, limit cycle oscillations), shock-induced deformations of rocket nozzles, parachute dynamics, airfoil buffeting and acoustic problems in general.

Solving FSI problems demands for tracking the time-varying FSI interface within the fluid domain, for which two main approaches can be distinguished. Arbitrary Lagrangian Eulerian (ALE) methods (Donea et al., 1982; Farhat et al., 1995) involve a mesh-evolution algorithm that distorts the CFD mesh with the FSI interface, thus ensuring a body-fitted grid at all times which simplifies the treatment of wall-boundary conditions. However, problems arise when dealing with complex and in general large solid displacements or structures undergoing topological changes as for crack propagation, making the ALE method unfeasible in such applications. IBM (Peskin, 1972; Mittal and Iaccarino, 2005), on the other side, alleviate the aforementioned problems and significantly simplify the CFD mesh generation by considering a fixed (Eulerian) background mesh in which the wet structural boundary surface is embedded and tracked through, e.g., geometric algorithms (Wang et al., 2012; Örley et al., 2015). IBM based on a continuous forcing or ghost-cell approach suffer from spurious loss or production of mass, momentum and energy at the interface (Mittal and Iaccarino, 2005), and as such may pose particular problems for long-time integrated LES which employ coarse grids and rely on accurate flow solutions near walls. Furthermore, capturing shocks accurately relies on conservation properties. Cartesian cut-cell methods (Clarke et al., 1986; Ye et al., 1999; Grilli et al., 2009; Örley et al., 2015) recover conservation by reshaping the FV cells cut by the interface to locally fit the wet boundary surface in a sharp manner. A drawback often related to such methods, however, is that the fluid volume fraction of cut-cells may become arbitrary small and thus lead to numerical instability with explicit time integration schemes. Stability can be recovered by cell-merging (Ye et al., 1999), cell-linking (Kirkpatrick et al., 2003) or flux-redistribution techniques (Colella et al., 2006; Hu et al., 2006).

FSI algorithms may be generally classified as monolithic or partitioned. While monolithic approaches are numerically robust since a single system of equations is solved including the full information of the coupled problem, partitioned algorithms solve the different disciplines in a sequential or parallel way and thus offer an efficient coupling of different specialized single-field solvers (Felippa et al., 2001). Partitioned algorithms can be further classified as loosely or strongly coupled, which refers to whether the coupling conditions are satisfied exactly at each time step, or not. Loosely coupled approaches are often used in the field of aeroelasticity (Farhat and Lesoinne, 2000; Farhat et al., 2006) and compressible flows in general (Cirak et al., 2007; Karagiozis et al., 2011), where the added mass effect (Causin et al., 2005) is often negligible due to low fluid-solid density ratios.

Transmission conditions at the common FSI interface ensure the integrity of both subdomains and require, e.g., fluid and solid tractions to be in equilibrium. While this results in a trivial load transfer in case of matching discretizations, non-matching interfaces, e.g. due to different resolution requirements in the different physical fields or when using a cut-cell IBM, require accurate interpolation techniques. A detailed review of existing

coupling methods for non-matching meshes is given by Farhat et al. (1998) and de Boer et al. (2007). The target interpolation method should be accurate, conservative (in the sense of total forces and virtual work) and computationally efficient. Conservation of virtual work requires the same interpolation strategy to be used for both the transfer of fluid forces to the structure as well as for the transfer of solid displacements (and velocities) to the fluid. Farhat et al. (1998) proposed a simple projection-based interpolation algorithm based on the FE shape functions, which has shown to outperform classical non-conservative consistent approaches when applied to the aeroelastic response of a wing in a transonic airstream. However, problems arise if the fluid interface elements are larger than the structural ones. As a consequence there may be some solid elements that do not receive a fluid force contribution, hence leading to a deteriorated load transfer. This problem can be alleviated by using more Gauss points in a fluid cell for approximating the fluid stress tensor at the interface, i.e. subdividing the element face into smaller elements. Note that this is equivalent to the case when using a cut-cell based IBM with sub-cell resolution. In contrast to the aforementioned techniques, weighted residual methods introduce Lagrange multipliers as additional interface variables with the aim to enforce the transmission conditions in a weak sense. As such, Mortar methods have become a popular and accurate method often used for FSI problems and mesh tying in fluid flow (Klöppel et al., 2011; Ehrl et al., 2014). Often at the expense of computational efficiency, Mortar methods have the great advantage that the introduced interface error of the coupled problem is not worse than the local fluid and structure discretization error Farhat et al. (1998). Computational efficiency can be recovered when using discontinuous Mortar elements for the Lagrange multipliers, avoiding the need for solving a possibly large linear system (Pasquariello et al., 2016). For aeroelastic FSI problems, where the fluid surface mesh is often much finer than the structural interface mesh, projection- and Mortar-based interpolation methods are found to be equally accurate (Farhat et al., 1998). Note that for a cut-cell IBM the transfer of the structural motion to the fluid system is implicitly accounted for by the cut-algorithm which is triggered in each time step, hence no further interpolation procedure is needed.

In the recent years FSI algorithms in the context of IBM have become a popular and appealing alternative to conventional ALE-based approaches, especially when it comes to large solid displacements and fracturing structures. Cirak et al. (2007) and Deiterding et al. (2008) developed a level-set-based FSI approach for simulating shock- and detonation-loaded thin-walled structures. A Lagrangian Kirchhoff-Love thin-shell solver with fracture capabilities is coupled to an Eulerian compressible flow solver using a ghost-cell approach for representing the immersed boundary. The method, however, causes a diffusion of the interface with a staircase approximation and results in an overall non-conservative scheme. Wang et al. (2011) proposed to solve a FSI half Riemann problem for the evaluation of convective fluxes on a surrogate interface embedded in the FV-based fluid solver, resulting in an algorithm which is able to handle thin and possibly cracking structures (Wang et al., 2015), however, again at the expense of loss of conservation properties. Furthermore, the surrogate interface introduces a first-order geometric spatial error in the numerical flux computation across the interface. The procedure is extended by a ghost-cell method in case of viscous flow to allow for the computation of flow gradients at the interface (Farhat and Lakshminarayan, 2014). Recently, Puscas et al. (2015b)

presented a conservative coupling method between an inviscid compressible fluid and a deformable structure undergoing large displacements. A cut-cell FV-based IBM is used for representing the embedded boundary, while the structure is discretized by the discrete element method (DEM). DEM is a particle-based method, in which particles interact through forces and torques while being governed by the classical equations of mechanics. Cracking structures can be naturally treated with DEM by breaking links between particles (Puscas et al., 2015a).

Computational efficiency is a crucial aspect when dealing with FSI simulations. Often mixed time integration schemes are used for fluid (explicit) and structure (implicit). This may be motivated by the fact that existing solvers have to be reused, or by physical aspects such as low-frequency dynamics of the structure in aeroelastic applications that are most efficiently solved when using an implicit scheme and LES of turbulent flows for which explicit time marching schemes are generally employed. In such cases the fluid solver usually requires a smaller time step which is restricted by the *Courant-Friedrichs-Lewy* (CFL) condition of the underlying explicit scheme. In order to resolve the possibly different timescales of both physical fields and increase the overall efficiency of the FSI simulation, subcycling within the fluid part can be employed (Farhat et al., 1995). Another strategy to reduce the time-cost of the coupled simulation is to replace the most likely FE-based structural solver by a reduced-order model (ROM), see Mignolet et al. (2013). Based on repeated linearizations of the structural balance equations, Thari et al. (2017) recently proposed an adaptive ROM for the solid that is able to overcome drawbacks related to classical ROM approaches with respect to FSI simulations involving large deformations. It can be seen as a natural extension of the work presented in the following publication (Pasquariello et al., 2016).

Given the objective to study SWBLI coupled to flexible panels, the original cut-cell IBM available in the flow solver INCA is extended for coupling with a FE structural solver. The focus of the following study lies on the accurate prediction of shock-loaded structures undergoing large and complex deformations. To the best of the authors knowledge, a coupling framework for compressible FSI between a FV-based cut-cell IBM and a FE structural solver is yet missing in the literature.

V. Pasquariello, G. Hammerl, F. Örley, S. Hickel, C. Danowski, A. Popp, W. A. Wall and N. A. Adams (2016)
A cut-cell finite volume – finite element coupling approach for fluid-structure interaction in compressible flow

The flow solver INCA used in this work operates on Cartesian grids and makes use of a cut-cell based IBM for representing complex geometries, which is limited to stationary boundaries or rigid body motions (Grilli et al., 2009; Örley et al., 2015).

In this work (Pasquariello et al., 2016), the original IBM is extended to treat deformable structures by coupling the FV-based flow solver INCA to the FE-based structural solver BACI through a loosely coupled approach within a classical Dirichlet-Neumann partitioning. The interface motion within the Eulerian flow solver is accounted for by means of a conservative cut-cell IBM which guarantees sub-cell resolution by considering individual cut-elements within a single fluid cell (Örley et al., 2015). To the best of the authors knowledge, this is the first time that a compressible cut-cell IBM for the fluid has been coupled to a nonlinear structural solver based on the FEM.

The use of a cut-cell method inevitably leads to non-matching discretizations at the conjoined FSI interface. In this work a Mortar method is chosen to guarantee a conservative load transfer. Efficiency is retained by using piecewise constant ansatz functions for interpolating the fluid state as well as for the Lagrange multipliers on each cut-element, which leads to the inversion of a diagonal matrix for the evaluation of the discrete projection operator.

The proposed coupling framework is tested and validated with two-dimensional FSI problems involving rigid and deformable shock-loaded structures undergoing large deformations. The first FSI problem involves the simple interaction of a light-weight cylinder with a Ma = 3 shock wave, for which the method correctly predicts the cylinder trajectory as well as the resulting shock patterns when compared to available data in the literature. Furthermore, the aeroelastic instability of a thin plate structure subjected to supersonic flow is studied. The method correctly predicts the onset of panel flutter and shows an accurate oscillation-free wall-pressure distribution. Giordano et al. (2005) proposed a FSI experiment consisting of a cantilever panel subjected to a shock tube flow. Excellent agreement is observed with respect to the time evolution of the panel tip displacement. A comparison in terms of schlieren images qualitatively confirms identical flow characteristics between experiment and simulation without any notable time lag. Finally, to demonstrate the capabilities of the FSI algorithm to handle three-dimensional complex deformations, a newly proposed FSI test case involving a flexible inflated thin shell interacting with a Ma = 1.21 shock wave is investigated.

My contribution to this work was the development and the implementation of the cut-cell based FSI algorithm in the in-house code INCA. I tested and validated the algorithms, performed the numerical simulations including grid generation on the fluid side, conducted major parts of the post-processing and wrote major parts of the manuscript for the publication.

3.3. Strong SWBLI at high Reynolds number

The dynamics of SWBLI mainly depend, amongst other parameters, on the Reynolds number of the flow as well as on the degree of TBL separation. Considering low- and high-Reynolds-number interactions (where the distinction may be roughly set at $\text{Re}_\delta \approx 1 \cdot 10^5$ according to Délery (1985)), the near-wall flow is either dominated by viscous ($\text{Re}_\delta \downarrow$) or inertia ($\text{Re}_\delta \uparrow$) effects, which has a direct consequence on the separation-shock dynamics and the associated wall-pressure signal in this region. High-Reynolds-number compression corner experiments (Dolling and Murphy, 1983; Dolling and Or, 1985) have shown that the wall-pressure signal in this region is highly intermittent and reflects the inviscid pressure jump across the oscillating shock. In low-Reynolds-number flows, the separation-shock foot does not penetrate as deeply into the TBL as it does in the high-Reynolds-number case: Increased viscous effects diffuse the reflected shock into a compression fan with a broader range of involved frequencies and attenuated shock intermittency (Ringuette et al., 2009). High-Reynolds-number effects are well documented (both experimentally and numerically) for compression corner flows, but so far have not been thoroughly studied numerically for impinging SWBLI.

The origin of the low-frequency unsteadiness is often debated in the literature to be found within the upstream TBL (*upstream mechanism*) or within the interaction itself (*downstream mechanism*), i.e. downstream of the reflected shock. Based on conflicting observations in many studies, Clemens and Narayanaswamy (2009) and Souverein et al. (2010) argued that probably both mechanisms are always at play, however, with a weighting function depending on the separation state of the SWBLI. While the reflected shock motion might be primarily influenced by upstream events (e.g. superstructures, bursting events, thickening/thinning of the incoming TBL) in case of weakly separated flow (i.e. $L_{sep} \leq 2\,\delta_0$), the authors argue that strong SWBLI are most probably dominated by downstream mechanisms inherent to the shock/bubble system itself (Clemens and Narayanaswamy, 2014).

The following study extends the available numerical database for impinging SWBLI by a high-Reynolds-number case with strong flow separation. So far, DNS (Pirozzoli and Grasso, 2006; Priebe et al., 2009) or LES studies (Touber and Sandham, 2009; Pirozzoli et al., 2010; Hadjadj, 2012; Agostini et al., 2012; Aubard et al., 2013; Morgan et al., 2013; Pasquariello et al., 2014; Nichols et al., 2016) mainly concentrated on weak interactions (with respect to the absence of a distinct pressure plateau) and/or low Reynolds numbers typically below $\text{Re}_{\delta_0} \approx 60 \cdot 10^3$. Furthermore, a direct comparison of low-frequency characteristics between simulation and experiment is rarely found in the literature due to insufficient integration time of the numerical data.

V. Pasquariello, S. Hickel and N. A. Adams (2017)
Unsteady effects of strong shock-wave/boundary-layer interaction at high Reynolds number
Journal of Fluid Mechanics, **823**, 617-657

In this work (Pasquariello et al., 2017), unprecedented LES results of a high-Reynolds-number impinging SWBLI with strong mean-flow separation are presented with focus on unsteady effects. The flow configuration matches recent experiments by Daub et al. (2015a) for the interaction of a $Ma = 3$ TBL with a wedge-induced impinging shock that nominally deflects the flow by $19.6°$ and leads to a separated mean-flow region with a length of $L_{sep} = 15.5\,\delta_0$. The Reynolds number of $Re_{\delta_0} \approx 2 \cdot 10^5$ is significantly higher than in previous LES studies and requires a computational grid with $363 \cdot 10^6$ cells for an accurate and grid-converged prediction of SWBLI characteristics.

LES results agree with experimental wall-pressure measurements, with both datasets exhibiting the distinct pressure plateau representative of a strong SWBLI. An analysis of filtered three-dimensional flow fields showed clear evidence of counter-rotating streamwise vortices originating near the bubble apex, similar to Görtler-like vortices often identified in compression corner configurations (Loginov et al., 2006; Grilli et al., 2013). In this impinging SWBLI, however, these vortices are not locked at a specific spanwise location, but rather undergo a slow meandering motion coupled to the separation bubble dynamics.

A very long integration time of the LES database of $3805\,\delta_0/U_0$ allowed for an accurate analysis of low-frequency SWBLI dynamics. Spectral analysis of numerical and experimental separation-shock wall-pressure signals agree and highlight a broadband unsteadiness centered around a non-dimensional low frequency of $St_{L_{sep}} = 0.04$, consistent with experimental findings by Dussauge et al. (2006). The high Reynolds number of the flow results in a strongly intermittent wall-pressure signal with $95\,\%$ fluctuation intensity residing in frequencies below $1\,U_0/L_{sep}$. Statistical moments such as kurtosis and skewness, as well as probability density functions, reflect the same behavior and agree with previous experimental observations (Dolling and Murphy, 1983; Dolling and Or, 1985).

Sparsity-promoting dynamic mode decomposition (SPDMD) of spanwise-averaged data and wall-plane snapshots is used to relate global flow phenomena to characteristic frequencies found by the locally-confined wall-pressure spectra. SPDMD identified two types of robust and dynamically important modes: (i) low-frequency modes ($St_{L_{sep}} \approx 0.04$) that yield a classical and well-known breathing motion of the separation bubble and (ii) medium-frequency modes ($St_{L_{sep}} \approx 0.5$) that are of convective nature and describe shear-layer vortices and radiated Mach waves responsible for reflected- and reattachment-shock corrugation. SPDMD of the two-dimensional skin-friction coefficient identified streamwise streaks at low frequencies. These streaks could be linked to footprints of Görtler-like vortices that cause a superimposed large-scale flapping of the reattachment line, and which may constitute a new physical mechanism responsible for low-frequency unsteadiness.

My contribution to this work was the development of the simulation setup and the implementation in the in-house code INCA. I tested and validated the algorithms, performed the numerical simulations including grid generation and post-processing, and wrote the manuscript for the publication.

3.4. SWBLI on flexible walls

The previous sections presented prerequisites needed for studying SWBLI on flexible surfaces, i.e. in summary: (i) development and validation of an accurate coupling framework for the prediction of mainly shock-loaded structures, (ii) validation of the LES capabilities of the flow solver INCA for the simulation of SWBLI along rigid panels at low and high Reynolds numbers and (iii) detailed investigation of the low-frequency phenomenon.

In this section the focus lies on the coupling of SWBLI and flexible surfaces, a phenomenon often discussed in the context of side loads generated in rocket nozzles (Östlund and Muhammad-Klingmann, 2005) and in lightweight flexible structures of air-breathing hypersonic cruise vehicles (Eason and Spottswood, 2013). For the former, the magnitude of these loads may be large enough to fail interfacing components as well as the complete nozzle, while the time-dependent pressure fluctuations may incite aeroelastic instabilities (Brown et al., 2002).

One of the first experiments related to SWBLI and flexible panels goes back to the early work of Maestrello and Linden (1971). A TBL (Ma = 3.0, $\mathrm{Re}_\delta \approx 487 \cdot 10^3$) and an impinging shock wave ($\vartheta = 15°$) interact with a titanium test panel which is brazed on all four sides. Besides the fact that the panel response is more intense in the presence of a shock than when solely excited by the TBL, they conjectured through an analysis of broad-band space-time correlations of panel displacements that separation-shock oscillations might set up waves on the panel moving in opposite direction. Similarly, Spottswood et al. (2012, 2013) investigated the impact of a SWBLI (Ma = 2.0, $\vartheta = 8°$) on the dynamic response of an aircraft-like fully-clamped panel. They applied conventional measurements of surface pressure and panel displacements as well as novel optical techniques such as pressure-sensitive paint and digital image correlation. Depending on the shock-impingement location a completely different panel response was observed with significantly increased displacement amplitudes when compared to the no-shock case. Willems et al. (2013) studied a similar case of an impinging shock at Ma = 3.0 ($\mathrm{Re}_\delta \approx 200 \cdot 10^3$) interacting with a steel-panel clamped only in streamwise direction to the frame with two rows of rivets at each side. The aim was to provide a sufficiently two-dimensional reference experiment which could be used for validation of numerical simulations. However, three-dimensional effects, mainly due to the finite-span shock generator and panel, have been observed and complicated the use of high-fidelity LES which often rely on periodic boundary conditions across the span. They also applied RANS simulations to the rigid panel configuration and found a strong sensitivity of the results with respect to the chosen turbulence model and to the dimension of the setup (2D or 3D). The experimental FSI data confirmed a big static deflection of the panel with a small dynamic component. Associated frequencies range between $50 - 2000\,\mathrm{Hz}$ and correspond to normal modes of the deflected panel. However, they did not find any prominent frequency in the schlieren pictures or pressure spectrum which could be linked to the panel motion. Daub et al. (2015b) refined the experimental design by replacing the finite-span shock generator through a full-span wedge mounted on a revolvable shaft, which, with respect to the flow, lead to a fully two-dimensional SWBLI accessible for LES (see also Daub et al. (2015a) and Pasquariello et al. (2017)).

Only a limited number of numerical studies that deals with SWBLI coupled to flexible

panels is available in the literature. Gogulapati et al. (2014) performed FSI simulations based on the experiments of Spottswood et al. (2012, 2013). They applied a CFD surrogate based on a RANS database for the mean flow that is augmented by unsteady terms using local piston theory to account for the vibrating panel, as well as a semi-empirical model to evaluate the TBL loads. The fluid model is coupled to a ROM and a commercial FEM-based structural solver in an explicit, i.e. loosely, way. Results indicate a good agreement between experiment and simulation with respect to static deflections and mean pressure distributions. However, the dynamic response of the panel was grossly underestimated. Uncertainties with respect to the modeling of SWBLI, amongst experimental uncertainties, are made responsible for the observed discrepancies between simulation and experiment. Visbal (2012) studied the influence of an impinging oblique shock on panel-flutter characteristics in the inviscid regime by coupling a compressible flow solver to the nonlinear von Kármán plate equations. Weak shocks lead to a stiffening of the panel, thereby eliminating standard panel flutter which would be present in the absence of a shock. At higher shock strengths the panel response resulted in limit-cycle oscillations (LCO) with increased oscillation amplitudes and frequencies for a fixed dynamic pressure. Further, the critical dynamic pressure (for which LCO is observed the first time) decreases with increasing shock strength, from which the authors conclude a new aeroelastic instability to be present resulting from the complex interaction of the shock system with panel flexural modes. Recently, Visbal (2014) and Boyer et al. (2016) extended the studies to viscous laminar flows and observed non-periodic self-excited oscillations of the panel when considering laminar interactions, involving multiple discrete frequencies together with a traveling disturbance.

The aforementioned numerical studies are limited in the sense that low-order CFD models are applied to model SWBLI, or in the sense that only inviscid/laminar interactions have been considered. When dealing with turbulent interactions, however, LES or DNS approaches are necessary to correctly predict the unsteadiness inherent to SWBLI. Östlund and Muhammad-Klingmann (2005) state that "it appears necessary to move toward large eddy simulations (LES). This perspective is not unique for separated nozzle flow; Knight and Degrez (1998) reached the same conclusion in their review of generic SWBLI test cases."

To the authors knowledge, the only available LES study of a turbulent SWBLI coupled to a flexible panel is the one by Pasquariello et al. (2015), see also Appendix B.4, which is the numerical counterpart of the experimental study published in Daub et al. (2015b). The setup has been developed within the SFB-TR40 and provides a FSI validation experiment related to SWBLI in the context of over-expanded rocket nozzles (Daub et al., 2014). It consists of a wedge mounted on a shaft that spans the complete wind-tunnel width. The shock generator is pitched from initially 0° deflection angle to a final value of 17.5° within approximately 15 ms, thus inducing a time-varying load on the flexible panel with significant boundary-layer separation. Note that this configurations bears similarities with start-up transients of rocket nozzles for which the NPR continuously changes, see also recent experimental studies by Baars et al. (2015).

FSI results by Pasquariello et al. (2015) reveal a large static deflection of the panel on the order of the local TBL thickness, which has been found to be in excellent agreement with

experimental data. Numerical results indicate a clear coupling between first-mode panel oscillations and increased separation shock motions, however, in the sense of a mainly unidirectional coupling: The SWBLI passively adapts to the structural deformation (as superimposed on a transient mean) without significantly influencing the panel response itself, see also Daub et al. (2015b). The panel motion provokes the formation of compression and expansion waves in the flow at a frequency matching the first eigenmode. An analysis of resolved mean Reynolds shear stress clearly indicates an increased unsteadiness of the shock system when compared to a rigid wall. The dynamics of the panel in terms of oscillation frequency and damping differs from the experimental measurements. Several reasons may be responsible for the observed discrepancies: (i) numerical uncertainties related to the modeling of the panel mounting, (ii) cavity effects which lead to a stiffening of the system are not fully incorporated and (iii) undesirable damping effects caused by sealing materials between panel and frame in spanwise direction.

Recent investigations by Hammerl et al. (2016) have shown that the softening of the elastic panel mounting due to the rivets can be accurately modeled through an elastic support including linear springs, a strategy which has been used in the FSI simulations of Pasquariello et al. (2015). With respect to the dynamic response, however, further effects have to be included in order to match the experimental eigenfrequencies of the panel. Additional rotational springs (tuned through experimental measurements at very-low ambient pressure) included at both ends of the panel as well as incorporating cavity effects resulted in a panel surrogate that matches the free vibration modes of the structure. However, the experimental and numerical studies presented in Hammerl et al. (2016) so far only considered a characterization of the panel in an undeflected state with superimposed small oscillations, hence assuming only linear effects to be present. This does not match the real FSI experiment for which a mean static deflection on the order of the TBL thickness and large oscillation amplitudes may necessitate the inclusion of nonlinear boundary conditions. Furthermore, strong damping effects, as observed in Daub et al. (2015b), are not captured by the panel surrogate and thus still constitute a significant uncertainty in the numerical model. On the other hand, the experimental setup needs further refinement: Small-amplitude low-frequency oscillations of the shock generator persist after pitching, thus exacerbating to differentiate between intrinsic and imposed low-frequency effects of the interaction.

In conclusion, the coupled LES study presented in Pasquariello et al. (2015) and the subsequent detailed analysis of the panel mounting in Hammerl et al. (2016) have revealed the complexity in accurately modeling the flexible wall within the FE structural solver. Undesirable effects are present in the experiment which strongly influence the panel response and to a lesser extent the imposed incident shock. The coupling algorithm, however, has proven robust and successful in simulating SWBLI on flexible walls, irrespective of the aforementioned experimental and numerical uncertainties. A redesign of the experiment which focuses on an improved panel mounting with reduced cavity and damping effects, as well as mitigated post-pitch shock-generator oscillations is desirable in order to limit disturbance variables which complicate a meaningful analysis.

4. CONCLUSION

Shock-wave/turbulent boundary-layer interactions (SWBLI) occur in a wide range of technical applications, such as overexpanded rocket nozzles, turbomachine cascades, supersonic air intakes, and high-speed vehicles in general. Their impact on system performance and structural integrity can be severe, mainly due to increased (unsteady) mechanical and thermal loads occurring in the interaction region. SWBLI with mean-flow separation form a complex dynamical system involving a broad range of temporal and spatial scales, which may couple to free vibration modes of the structure and potentially result in failure due to fatigue. While mean-flow properties of SWBLI are well understood and documented in the literature, research in the past sixty years has focused on low-frequency unsteady effects associated to the shock/bubble system, however, without providing a general consensus on the origin of reflected shock oscillations.

So far, high-fidelity numerical studies of SWBLI in terms of large-eddy simulations (LES) or direct numerical simulations (DNS) exist only for considerably weak interactions and/or low Reynolds numbers. Furthermore, structural rigidity is always assumed. The main focus of the present thesis was thus to develop a numerical toolbox capable of simulating SWBLI coupled to flexible walls, and to extend the available numerical database for high-Reynolds-number impinging SWBLI by a case with strong flow separation from wall-resolved long-time integrated LES.

Starting point has been the LES of a weak SWBLI at a low Reynolds number of $Re_{\delta_0} = 60.5 \cdot 10^3$, which was used to verify the LES capabilities in predicting mean-flow properties and unsteady effects of the interaction. The configuration consists of an impinging shock generated by an 8.8° wedge at a freestream Mach number of $Ma = 2.3$, which interacts

with a flat-plate turbulent boundary layer (TBL). A passive flow control device consisting of full-span suction inside the separation bubble and blowing upstream of the interaction region by a pressure feedback duct embedded in the wall has been proposed, which is able to shift the high-energy low-frequency pressure fluctuations to higher frequencies. In total, three different control devices have been investigated which differ in the location of the suction slot. While all configurations reduced the amount of separated flow, only suction acting in the rear part of the separation bubble favors a reduction in turbulence intensity across the interaction region and mitigated shock dynamics.

The flow solver used in this work operates on Cartesian grids and employs a cut-cell immersed boundary method (IBM) for representing embedded geometries. At the beginning of this thesis project, however, only stationary boundaries or rigid body motions could be treated by the algorithm. As a necessary step towards the final goal of simulating SWBLI on flexible walls, the method has been extended for coupling with finite-element (FE) based structural solvers, which, to the authors knowledge, is being done for the first time with respect to a cut-cell IBM. It has been demonstrated through a detailed validation that the loosely coupled approach following the classical Dirichlet-Neumann partitioning is accurate in simulating mainly shock-loaded structures undergoing large and complex deformations. Test cases comprised the interaction of a light-weight cylinder with a $Ma = 3$ shock wave, the aeroelastic instability of a thin plate structure subjected to supersonic flow (panel flutter), a cantilever panel placed in a $Ma = 1.21$ shock tube flow, and a shock-loaded flexible inflated thin shell undergoing strong buckling.

One major contribution has been the detailed analysis of an impinging SWBLI simulation at unprecedented high Reynolds number ($Re_{\delta_0} \approx 2 \cdot 10^5$) by means of wall-resolved long-time integrated LES. The flow configuration mimics recent experiments of a $Ma = 3$ TBL interacting with a wedge-induced impinging shock that nominally deflects the flow by $19.6°$ and leads to a massively separated mean-flow region of length $L_{sep} = 15.5\,\delta_0$. LES results agree with experimental measurements in terms of mean wall pressure, with both datasets reflecting the distinct pressure plateau within the separation bubble representative of a strong SWBLI. Similar to compression corner configurations, an analysis of filtered three-dimensional flow fields showed clear evidence of counter-rotating streamwise vortices originating in the proximity of the bubble apex. The Görtler number evaluated on a sample streamline revealed high values within the reattachment region that last over a significantly long streamwise distance of $11\,\delta_0$ while exceeding classical stability criteria in laminar flow. In contrast to many studies available in the literature, these Görtler-like vortices are not locked at a specific spanwise location, but rather undergo a slow meandering motion coupled to the separation-bubble dynamics. Power spectral densities of numerical and experimental separation-shock wall-pressure signals agree well and predict the broadband unsteadiness typically centered around $St_{L_{sep}} = 0.04$. Consistent with previous experimental observations, high-Reynolds-number effects allow the separation shock to penetrate deeply into the TBL, leaving a strongly intermittent footprint on the wall-pressure signal with $95\,\%$ fluctuation intensity residing in frequencies below $1\,U_0/L_{sep}$. This effect is also reflected by the probability density function which is highly left-skewed at the onset of interaction. Sparsity-promoting dynamic mode decomposition (SPDMD) was proven suitable in identifying robust and dynamically important modes, whose frequencies support the spectral analysis. While low-frequency modes ($St_{L_{sep}} \approx 0.04$) yield a

classical breathing motion of the separation bubble, convective medium-frequency modes ($St_{L_{sep}} \approx 0.5$) involve shear-layer vortices whose radiated Mach waves are found to be responsible for reflected- and reattachment-shock corrugation. Wall-plane low-frequency modes revealed streamwise streaks which could be linked to footprints of Görtler-like vortices, and which are responsible for a large-scale flapping of the reattachment line. From the above analysis, a new instability mechanism responsible for low-frequency unsteadiness has been postulated, in which unsteady Görtler-like vortices might act as a source for continuous forcing of the intrinsic separation-shock-system dynamics. This holds for SWBLI featuring significant streamline curvature, thus allowing centrifugal instabilities to arise. In case of impinging SWBLI, the curvature directly depends on the dividing streamline (and thus shock strength) and is not a geometric feature as in the case of compression corner studies. Consequently, a strong interaction is necessary for Görtler-like vortices to develop in impinging SWBLI.

With verification of LES capabilities for the simulation of strong SWBLI at high Reynolds number and the FSI framework capable of treating shock-loaded structures undergoing large deformations, the final application of a two-way coupled SWBLI on a flexible wall could be tackled. To the authors knowledge, this is the first LES of a turbulent SWBLI coupled to a nonlinear structure. The experiment consists of a fast-pitching shock generator whose incident shock induces a transient load on the panel and provokes significant boundary-layer separation. Results have shown a large static deflection of the panel on the order of the TBL thickness, which was found to be in excellent agreement with experimental measurements. Numerical results indicate a mainly unidirectional coupling, i.e., the SWBLI passively adapts to the structural deformation (as superimposed on a transient mean) without significantly influencing the panel response, which itself is dictated by its first eigenmode and is responsible for the formation of compression and expansion waves in the flow. Discrepancies between experiment and simulation have been found in terms of oscillation frequency and damping of the panel response. They could be mainly linked to (i) numerical and experimental uncertainties with respect to the panel mounting, (ii) undesirable damping effects caused by sealing materials in the experiment and (iii) cavity-induced stiffening effects which have not been included in the structural model. Furthermore, small-amplitude low-frequency oscillations of the shock generator persist after pitching, thus exacerbating to differentiate between intrinsic and imposed dynamics of the coupled SWBLI. These uncertainties demand for a redesign of the experiment with the goal to reduce disturbance variables which so far complicate a meaningful analysis.

The numerical toolbox developed in this thesis provides a complete framework for studying SWBLI coupled to flexible surfaces in detail, with each discipline validated thouroughly. The current state provides a starting point for future studies which may focus on the influence of turbulent SWBLI on panel flutter characteristics, a research field, which so far is only addressed numerically for inviscid and laminar interactions.

A. LIST OF PUBLICATIONS

A.1. PEER-REVIEWED JOURNAL PUBLICATIONS

- **V. Pasquariello**, M. Grilli, S. Hickel and N. A. Adams (2014). Large-eddy simulation of passive shock-wave/boundary-layer interaction control. *International Journal of Heat and Fluid Flow*, **49**, 116-127.

- G. Castiglioni, J. A. Domaradzki, **V. Pasquariello**, S. Hickel and M. Grilli (2014). Numerical simulations of separated flows at moderate Reynolds numbers appropriate for turbine blades and unmanned aero vehicles. *International Journal of Heat and Fluid Flow*, **49**, 91-99.

- F. Örley, **V. Pasquariello**, S. Hickel and N. A. Adams (2015). Cut-element based immersed boundary method for moving geometries in compressible liquid flows with cavitation. *Journal of Computational Physics*, **283**, 1-22.

- **V. Pasquariello**, G. Hammerl, F. Örley, S. Hickel, C. Danowski, A. Popp, W. A. Wall and N. A. Adams (2016). A cut-cell finite volume – finite element coupling approach for fluid–structure interaction in compressible flow. *Journal of Computational Physics*, **307**, 670-695.

- **V. Pasquariello**, S. Hickel and N. A. Adams (2017). Unsteady effects of strong shock-wave/boundary-layer interaction at high Reynolds number. *Journal of Fluid Mechanics*, **823**, 617-657.

- T. Kaller, **V. Pasquariello**, S. Hickel and N. A. Adams (2018). Turbulent flow through a high aspect ratio cooling duct with asymmetric wall heating. *Journal of Fluid Mechanics*, under review.

A.2. Book sections and e-prints

- **V. Pasquariello**, S. Hickel and N. A. Adams (2016). Shock-wave/turbulent boundary-layer interaction over a flexible panel. In *High Performance Computing in Science and Engineering*; S. Wagner, A. Bode, H. Brüchle and M. Brehm (Eds.), Verlag der Bayerischen Akademie der Wissenschaften. ISBN 978-3-9816675-1-6.

- A. Thari, **V. Pasquariello**, N. Aage and S. Hickel (2017). Adaptive Reduced-Order Modeling for Non-Linear Fluid-Structure Interaction. *ArXiv e-prints*, arXiv:1702.04332.

A.3. Conferences

- **V. Pasquariello**, J. Matheis, M. Grilli and S. Hickel (2013). Large-eddy simulation of passive shock-wave/boundary-layer interaction control. *8th International Symposium On Turbulence and Shear Flow Phenomena*, August 28 - 30, 2013, Poitiers, France.

- **V. Pasquariello**, S. Hickel, N. A. Adams, G. Hammerl, W. A. Wall, D. Daub, S. Willems and A. Gülhan (2015). Coupled simulation of shock-wave/turbulent boundary-layer interaction over a flexible panel. *6th European Conference for Aeronautics and Space Sciences*, June 29 - July 3, 2015, Kraków, Poland.

- **V. Pasquariello**, F. Örley, S. Hickel and N. A. Adams (2016). Cut-Element Immersed Boundary Method for Moving Geometries and Fluid-Structure Interaction. *87th Annual Meeting of the International Association of Applied Mathematics and Mechanics*, March 7 - 11, 2016, Braunschweig, Germany.

- **V. Pasquariello**, S. Hickel and N. A. Adams (2016). Large-Eddy Simulation of Strong Shock-Wave/Turbulent Boundary-Layer Interaction at $Re_\Theta = 14000$. *24th International Congress of Theoretical and Applied Mechanics*, August 21 - 26, 2016, Montréal, Canada.

B. Selected publications

Here, the main publications are attached.

B.1. Large-eddy simulation of passive shock-wave/boundary-layer interaction control

This Agreement between Vito Pasquariello ("You") and Elsevier ("Elsevier") consists of your license details and the terms and conditions provided by Elsevier and Copyright Clearance Center.

License Number	4073710811930
License date	
Licensed Content Publisher	Elsevier
Licensed Content Publication	International Journal of Heat and Fluid Flow
Licensed Content Title	Large-eddy simulation of passive shock-wave/boundary-layer interaction control
Licensed Content Author	Vito Pasquariello,Muzio Grilli,Stefan Hickel,Nikolaus A. Adams
Licensed Content Date	October 2014
Licensed Content Volume	49
Licensed Content Issue	n/a
Licensed Content Pages	12
Start Page	116
End Page	127
Type of Use	reuse in a thesis/dissertation
Portion	full article
Format	both print and electronic
Are you the author of this Elsevier article?	Yes
Will you be translating?	No
Order reference number	
Title of your thesis/dissertation	Analysis and Control of Shock-Wave/Turbulent Boundary-Layer Interactions on Rigid and Flexible Walls
Expected completion date	Apr 2017
Estimated size (number of pages)	150
Elsevier VAT number	GB 494 6272 12
Requestor Location	Vito Pasquariello Boltzmannstrasse 15 Technische Universität München
	Garching bei München, 85748 Germany Attn: Vito Pasquariello
Publisher Tax ID	GB 494 6272 12
Total	0.00 EUR
Terms and Conditions	

INTRODUCTION

established by Copyright Clearance Center, Inc. ("CCC"), at the time that you opened your Rightslink account and that are available at any time at http://myaccount.copyright.com).

GENERAL TERMS

2. Elsevier hereby grants you permission to reproduce the aforementioned material subject to the terms and conditions indicated.

3. Acknowledgement: If any part of the material to be used (for example, figures) has appeared in our publication with credit or acknowledgement to another source, permission must also be sought from that source. If such permission is not obtained then that material may not be included in your publication/copies. Suitable acknowledgement to the source must be made, either as a footnote or in a reference list at the end of your publication, as follows:

"Reprinted from Publication title, Vol /edition number, Author(s), Title of article / title of chapter, Pages No., Copyright (Year), with permission from Elsevier [OR APPLICABLE SOCIETY COPYRIGHT OWNER]." Also Lancet special credit - "Reprinted from The Lancet, Vol. number, Author(s), Title of article, Pages No., Copyright (Year), with permission from Elsevier."

4. Reproduction of this material is confined to the purpose and/or media for which permission is hereby given.

5. Altering/Modifying Material: Not Permitted. However figures and illustrations may be altered/adapted minimally to serve your work. Any other abbreviations, additions, deletions and/or any other alterations shall be made only with prior written authorization of Elsevier Ltd. (Please contact Elsevier at permissions@elsevier.com). No modifications can be made to any Lancet figures/tables and they must be reproduced in full.

6. If the permission fee for the requested use of our material is waived in this instance, please be advised that your future requests for Elsevier materials may attract a fee.

7. Reservation of Rights: Publisher reserves all rights not specifically granted in the combination of (i) the license details provided by you and accepted in the course of this licensing transaction, (ii) these terms and conditions and (iii) CCC's Billing and Payment terms and conditions.

8. License Contingent Upon Payment: While you may exercise the rights licensed immediately upon issuance of the license at the end of the licensing process for the transaction, provided that you have disclosed complete and accurate details of your proposed use, no license is finally effective unless and until full payment is received from you (either by publisher or by CCC) as provided in CCC's Billing and Payment terms and conditions. If full payment is not received on a timely basis, then any license preliminarily granted shall be deemed automatically revoked and shall be void as if never granted. Further, in the event that you breach any of these terms and conditions or any of CCC's Billing and Payment terms and conditions, the license is automatically revoked and shall be void as if never granted. Use of materials as described in a revoked license, as well as any use of the materials beyond the scope of an unrevoked license, may constitute copyright infringement and publisher reserves the right to take any and all action to protect its copyright in the materials.

9. Warranties: Publisher makes no representations or warranties with respect to the licensed material.

10. Indemnity: You hereby indemnify and agree to hold harmless publisher and CCC, and their respective officers, directors, employees and agents, from and against any and all claims arising out of your use of the licensed material other than as specifically authorized pursuant to this license.

11. No Transfer of License: This license is personal to you and may not be sublicensed, assigned, or transferred by you to any other person without publisher's written permission.

12. No Amendment Except in Writing: This license may not be amended except in a writing signed by both parties (or, in the case of publisher, by CCC on publisher's behalf).

13. Objection to Contrary Terms: Publisher hereby objects to any terms contained in any purchase order, acknowledgment, check endorsement or other writing prepared by you, which terms are inconsistent with these terms and conditions or CCC's Billing and Payment terms and conditions. These terms and conditions, together with CCC's Billing and Payment terms and conditions (which are incorporated herein), comprise the entire agreement between you and publisher (and CCC) concerning this licensing transaction. In the event of

42

any conflict between your obligations established by these terms and conditions and those established by CCC's Billing and Payment terms and conditions, these terms and conditions shall control.

14. Revocation: Elsevier or Copyright Clearance Center may deny the permissions described in this License at their sole discretion, for any reason or no reason, with a full refund payable to you. Notice of such denial will be made using the contact information provided by you. Failure to receive such notice will not alter or invalidate the denial. In no event will Elsevier or Copyright Clearance Center be responsible or liable for any costs, expenses or damage incurred by you as a result of a denial of your permission request, other than a refund of the amount(s) paid by you to Elsevier and/or Copyright Clearance Center for denied permissions.

LIMITED LICENSE

The following terms and conditions apply only to specific license types:

15. **Translation**: This permission is granted for non-exclusive world **English** rights only unless your license was granted for translation rights. If you licensed translation rights you may only translate this content into the languages you requested. A professional translator must perform all translations and reproduce the content word for word preserving the integrity of the article.

16. **Posting licensed content on any Website**: The following terms and conditions apply as follows: Licensing material from an Elsevier journal: All content posted to the web site must maintain the copyright information line on the bottom of each image; A hyper-text must be included to the Homepage of the journal from which you are licensing at http://www.sciencedirect.com/science/journal/xxxxx or the Elsevier homepage for books at http://www.elsevier.com; Central Storage: This license does not include permission for a scanned version of the material to be stored in a central repository such as that provided by Heron/XanEdu.

Licensing material from an Elsevier book: A hyper-text link must be included to the Elsevier homepage at http://www.elsevier.com . All content posted to the web site must maintain the copyright information line on the bottom of each image.

Posting licensed content on Electronic reserve: In addition to the above the following clauses are applicable: The web site must be password-protected and made available only to bona fide students registered on a relevant course. This permission is granted for 1 year only. You may obtain a new license for future website posting.

17. **For journal authors:** the following clauses are applicable in addition to the above:
Preprints:
A preprint is an author's own write-up of research results and analysis, it has not been peer-reviewed, nor has it had any other value added to it by a publisher (such as formatting, copyright, technical enhancement etc.).

Authors can share their preprints anywhere at any time. Preprints should not be added to or enhanced in any way in order to appear more like, or to substitute for, the final versions of articles however authors can update their preprints on arXiv or RePEc with their Accepted Author Manuscript (see below).

If accepted for publication, we encourage authors to link from the preprint to their formal publication via its DOI. Millions of researchers have access to the formal publications on ScienceDirect, and so links will help users to find, access, cite and use the best available version. Please note that Cell Press, The Lancet and some society-owned have different preprint policies. Information on these policies is available on the journal homepage.

Accepted Author Manuscripts: An accepted author manuscript is the manuscript of an article that has been accepted for publication and which typically includes author-incorporated changes suggested during submission, peer review and editor-author communications.

Authors can share their accepted author manuscript:

- immediately
    - via their non-commercial person homepage or blog
    - by updating a preprint in arXiv or RePEc with the accepted manuscript

- via their research institute or institutional repository for internal institutional uses or as part of an invitation-only research collaboration work-group
- directly by providing copies to their students or to research collaborators for their personal use
- for private scholarly sharing as part of an invitation-only work group on commercial sites with which Elsevier has an agreement
  - After the embargo period
    - via non-commercial hosting platforms such as their institutional repository
    - via commercial sites with which Elsevier has an agreement

In all cases accepted manuscripts should:

- link to the formal publication via its DOI
- bear a CC-BY-NC-ND license - this is easy to do
- if aggregated with other manuscripts, for example in a repository or other site, be shared in alignment with our hosting policy not be added to or enhanced in any way to appear more like, or to substitute for, the published journal article.

Published journal article (JPA): A published journal article (PJA) is the definitive final record of published research that appears or will appear in the journal and embodies all value-adding publishing activities including peer review co-ordination, copy-editing, formatting, (if relevant) pagination and online enrichment.
Policies for sharing publishing journal articles differ for subscription and gold open access articles:
Subscription Articles: If you are an author, please share a link to your article rather than the full-text. Millions of researchers have access to the formal publications on ScienceDirect, and so links will help your users to find, access, cite, and use the best available version.
Theses and dissertations which contain embedded PJAs as part of the formal submission can be posted publicly by the awarding institution with DOI links back to the formal publications on ScienceDirect.
If you are affiliated with a library that subscribes to ScienceDirect you have additional private sharing rights for others' research accessed under that agreement. This includes use for classroom teaching and internal training at the institution (including use in course packs and courseware programs), and inclusion of the article for grant funding purposes.
Gold Open Access Articles: May be shared according to the author-selected end-user license and should contain a CrossMark logo, the end user license, and a DOI link to the formal publication on ScienceDirect.
Please refer to Elsevier's posting policy for further information.
18. **For book authors** the following clauses are applicable in addition to the above:
Authors are permitted to place a brief summary of their work online only. You are not allowed to download and post the published electronic version of your chapter, nor may you scan the printed edition to create an electronic version. **Posting to a repository:** Authors are permitted to post a summary of their chapter only in their institution's repository.
19. **Thesis/Dissertation**: If your license is for use in a thesis/dissertation your thesis may be submitted to your institution in either print or electronic form. Should your thesis be published commercially, please reapply for permission. These requirements include permission for the Library and Archives of Canada to supply single copies, on demand, of the complete thesis and include permission for Proquest/UMI to supply single copies, on demand, of the complete thesis. Should your thesis be published commercially, please reapply for permission. Theses and dissertations which contain embedded PJAs as part of the formal submission can be posted publicly by the awarding institution with DOI links back to the formal publications on ScienceDirect.

Elsevier Open Access Terms and Conditions
You can publish open access with Elsevier in hundreds of open access journals or in nearly 2000 established subscription journals that support open access publishing. Permitted third party re-use of these open access articles is defined by the author's choice of Creative Commons user license. See our open access license policy for more information.

Terms & Conditions applicable to all Open Access articles published with Elsevier:
Any reuse of the article must not represent the author as endorsing the adaptation of the article nor should the article be modified in such a way as to damage the author's honour or reputation. If any changes have been made, such changes must be clearly indicated.
The author(s) must be appropriately credited and we ask that you include the end user license and a DOI link to the formal publication on ScienceDirect.
If any part of the material to be used (for example, figures) has appeared in our publication with credit or acknowledgement to another source it is the responsibility of the user to ensure their reuse complies with the terms and conditions determined by the rights holder.
Additional Terms & Conditions applicable to each Creative Commons user license:
CC BY: The CC-BY license allows users to copy, to create extracts, abstracts and new works from the Article, to alter and revise the Article and to make commercial use of the Article (including reuse and/or resale of the Article by commercial entities), provided the user gives appropriate credit (with a link to the formal publication through the relevant DOI), provides a link to the license, indicates if changes were made and the licensor is not represented as endorsing the use made of the work. The full details of the license are available at http://creativecommons.org/licenses/by/4.0.
CC BY NC SA: The CC BY-NC-SA license allows users to copy, to create extracts, abstracts and new works from the Article, to alter and revise the Article, provided this is not done for commercial purposes, and that the user gives appropriate credit (with a link to the formal publication through the relevant DOI), provides a link to the license, indicates if changes were made and the licensor is not represented as endorsing the use made of the work. Further, any new works must be made available on the same conditions. The full details of the license are available at http://creativecommons.org/licenses/by-nc-sa/4.0.
CC BY NC ND: The CC BY-NC-ND license allows users to copy and distribute the Article, provided this is not done for commercial purposes and further does not permit distribution of the Article if it is changed or edited in any way, and provided the user gives appropriate credit (with a link to the formal publication through the relevant DOI), provides a link to the license, and that the licensor is not represented as endorsing the use made of the work. The full details of the license are available at http://creativecommons.org/licenses/by-nc-nd/4.0.
Any commercial reuse of Open Access articles published with a CC BY NC SA or CC BY NC ND license requires permission from Elsevier and will be subject to a fee.
Commercial reuse includes:

- Associating advertising with the full text of the Article
- Charging fees for document delivery or access
- Article aggregation
- Systematic distribution via e-mail lists or share buttons

Posting or linking by commercial companies for use by customers of those companies.

20. **Other Conditions**:

v1.9

Questions? customercare@copyright.com or +1-855-239-3415 (toll free in the US) or +1-978-646-2777.

CrossMark
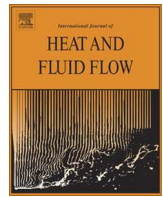
Large-eddy simulation of passive shock-wave/boundary-layer interaction control

Vito Pasquariello *, Muzio Grilli, Stefan Hickel, Nikolaus A. Adams

Lehrstuhl für Aerodynamik und Strömungsmechanik, Technische Universität München, D-85748 Garching, Germany

ARTICLE INFO

ABSTRACT

We investigate a passive flow-control technique for the interaction of an oblique shock generated by an $8.8°$ wedge with a turbulent boundary-layer at a free-stream Mach number of $Ma_\infty = 2.3$ and a Reynolds number based on the incoming boundary-layer thickness of $Re_{\delta_0} = 60.5 \times 10^3$ by means of large-eddy simulation (LES). The compressible Navier–Stokes equations in conservative form are solved using the adaptive local deconvolution method (ALDM) for physically consistent subgrid scale modeling. Emphasis is placed on the correct description of turbulent inflow boundary conditions, which do not artificially force low-frequency periodic motion of the reflected shock. The control configuration combines suction inside the separation zone and blowing upstream of the interaction region by a pressure feedback through a duct embedded in the wall. We vary the suction location within the recirculation zone while the injection position is kept constant. Suction reduces the size of the separation zone with strongest effect when applied in the rear part of the separation bubble. The analysis of wall-pressure spectra reveals that all control configurations shift the high-energy low-frequency range to higher frequencies, while the energy level is significantly reduced only if suction acts in the rear part of the separated zone. In that case also turbulence production within the interaction region is significantly reduced as a consequence of mitigated reflected shock dynamics and near-wall flow acceleration.

© 2014 Elsevier Inc. All rights reserved.

1. Introduction

Shock-wave/boundary-layer interactions (SWBLI) frequently occur in flows of technological interest, such as supersonic air intakes, turbomachine cascades, helicopter blades, supersonic nozzles and launch vehicles in general. SWBLI can critically affect the vehicle or machine performance in several ways. The adverse pressure gradient acting on the flow strongly retards the boundary-layer, eventually leading to separation if the imposed pressure gradient is strong enough (Délery and Dussauge, 2009).

A schematic of the basic interaction type studied in this work is shown in Fig. 1. The adverse pressure gradient imposed by the incident shock C_1 is large enough to cause separation of the boundary-layer. Separation takes place well ahead of the inviscid impingement x_{imp}. The upstream propagation of the pressure gradient within the subsonic part of the turbulent boundary-layer (TBL) induces compression waves in the supersonic part of the TBL, which coalesce to the reflected shock C_2. The reflected shock intersects the incident shock at point I and the original shocks continue traveling as the transmitted shocks C_3 and C_4, respectively. The

shock C_4 penetrates into the separated shear layer, curves due to the local Mach number variation and finally reflects at the sonic line as an expansion fan. Pirozzoli and Grasso (2006) found from their direct numerical simulation (DNS) of an impinging shock on a $Ma = 2.25$ TBL that the formation of the detached shear layer is primarily responsible for turbulence amplification. The separated shear layer follows the inclination of the initial part of the separation bubble, while being deflected towards the wall due to the expansion fan and finally reattaching further downstream. The compression waves associated with reattachment merge to form the reattachment shock C_5. Downstream of the SWBLI the TBL recovers an equilibrium state.

Until the 1950s SWBLI have been described as a steady process, which nowadays is known to be incorrect when shock-induced separation occurs. As stated by Dolling (2001), the interaction region is the main source of maximum mean and fluctuating pressure levels as well as thermal loads. Turbulence production is enhanced in the vicinity of the mean separation location which in turn increases viscous dissipation in this region (Délery and Dussauge, 2009). The low-frequency unsteadiness of the reflected shock is a crucial aspect with regard to the choice of materials concerning supersonic engine-inlets, since it is a main contribution to failure due to fatigue (Pirozzoli et al., 2010).

---

* Corresponding author. Tel.: +49 89 289 16121.
E-mail address: vito.pasquariello@tum.de (V. Pasquariello).

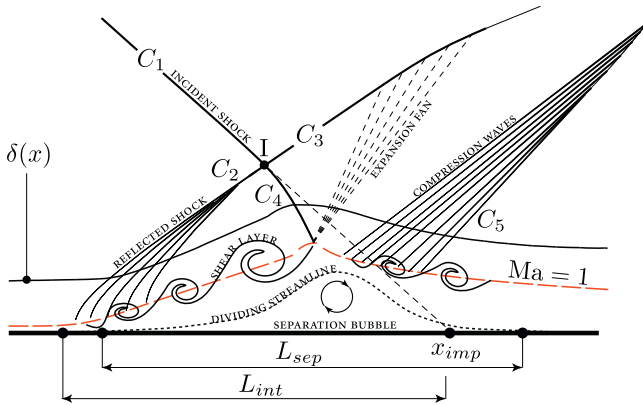**Fig. 1.** Schematic of the oblique shock/boundary-layer interaction with mean separation.

Several experiments Dolling and Bogdonoff (1981), Beresh et al. (2002), Dupont et al. (2006), Ganapathisubramani et al. (2007) and numerical investigations by means of direct numerical simulations Adams (2000), Pirozzoli and Grasso (2006), Wu and Martín (2007), Priebe and Martín (2012) and large-eddy simulations Loginov et al. (2006), Touber and Sandham (2009b), Pirozzoli et al. (2010), Grilli et al. (2012, 2013) unanimously confirmed the existence of such low-frequency motions, which typically reveal themselves by a "breathing" motion of the separation bubble, accompanied by an oscillatory movement of the reflected shock. The nomenclature "low-frequency" emphasizes the fact that the characteristic frequency of the incoming TBL is approximately two or three orders of magnitude higher than the one related to the shock unsteadiness. Touber and Sandham (2011) have shown that the separation acts as a broadband amplifier, imposing additional problems for vehicles with SWBLI since upstream distrubances get amplified through the shock system which in turn probably decrease the vehicles performance.

On this account research is motivated with the goal to identify suitable control mechanisms that reduce pressure and heat loads due to unsteady SWBLI, see Délery (1985). One can distinguish between *boundary-layer control* mechanisms, which aim at reducing shock-induced separation, and *shock control* mechanisms, which reduce stagnation pressure losses. Délery (1985) and Viswanath (1988) report a great number of suitable boundary-layer control methods such as tangential blowing upstream of the interaction region, suction within the separation bubble, wall-cooling and vortex generators. These techniques all have in common that they reduce the separation length by additionally supplying momentum to the near-wall flow, hence making the incoming TBL less susceptible against an adverse pressure gradient. Souverein and Debiève (2010) investigated the influence of Air Jet Vortex Generators (AJVGs) placed in a row upstream of the interaction region for an impinging SWBLI at $M = 2.3$ and $9.5°$ deflection angle, consistent with the flow conditions at IUSTI ("Institution Universitaire des Systèmes Thermiques Industriels, Marseille", Doerffer et al. (2011)), and reported a significant reduction of the recirculation zone both in length and height due to the enhanced mixing process initiated through the generation of counter-rotating vortexes. Moreover, the characteristic frequency associated with the reflected shock increases by about 50%, which is an important finding concerning practical control applications. Experimental studies McCormick (1993) and Blinde (2008) and numerical simulations Lee (2009) and Ghosh (2010) for the control technique involving structural vortex generators both revealed a significant reduction of the shock-induced separation, accompanied by an improvement of the boundary-layer characteristics
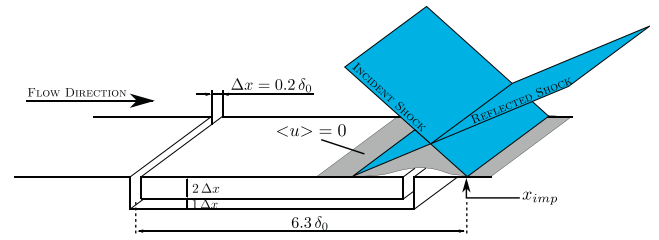
downstream of the interaction region. A recent numerical study performed by Bisek et al. (2012) for a control strategy resembling a magnetically-driven gliding-arc discharge model has shown, that besides a substantial reduction of separation length up to 75%, the low-frequency content from wall-pressure spectra can be removed.

The current work is motivated by the control configurations reported by McCormick (1993) and Fulker (1999), where a pressure feedback is generated downstream and upstream of the shock impingement region. For this purpose a porous surface with a common plenum beneath it was placed in the region of the shock impingement. A natural recirculating flow is generated, bleeding boundary layer flow from the high-pressure to the low-pressure side. In order to have better control on the effect of the precise location of suction and blowing, we replace the porous surface and cavity by a duct, see Fig. 2. The duct spans the entire spanwise domain extent, which leads to a quasi two-dimensional control configuration. The main objective of this paper is to evaluate the influence of the applied control technique on mean flow properties, turbulence structure within the interaction region and unsteady shock dynamics by analysing results from implicit large-eddy simulations. Details of the flow configuration are given in Section 2 and the underlying numerical approach is described in Section 3. Numerical results are presented and analysed in Section 4. Conclusions are drawn in Section 5.

Fig. 2. Schematic of the considered control method. Blue planes: reflected shock system. Grey Surface: 2D sketch of the recirculation region. (For interpretation of the references to color in this figure legend, the reader is referred to the web version of this article.)

2. Flow configuration

The basic SWBLI topology studied in this work is the case of an oblique shock impinging on a flat plate boundary-layer. The resulting flow pattern is shown in Fig. 3. The shock is generated by a $8.8°$ wedge at a freestream Mach number of $Ma_\infty = 2.3$ and the Reynolds number based on the inlet boundary-layer thickness is $Re_{\delta_0} = 60.5 \times 10^3$. Stagnation temperature and pressure are $T_0 = 300$ K and $p_0 = 0.5$ bar. Table 1 summarizes the flow
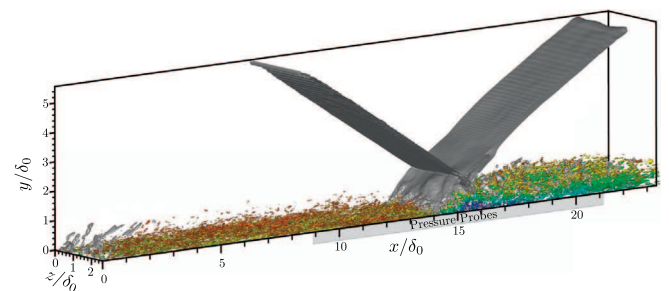

Fig. 3. Illustration of the computational domain together with isocontours of pressure gradient magnitude (gray) and Q-criterion (colored by local streamwise velocity). (For interpretation of the references to color in this figure legend, the reader is referred to the web version of this article.)

47

Table 1
Flow parameters.

Flow parameters	
M_∞	2.3
Θ	8.8°
T_0	300 (K)
p_0	0.5 (bar)
Re_{δ_0}	60524
δ_0 [a]	11.35 (mm)
δ_0^r [b]	13.46 (mm)

[a] Evaluated at the domain inlet.
[b] Evaluated at a reference plane at $x/\delta_0 = 11.7$.

Table 2
Numerical details of all cases studied.

Case	NC	CA	CB	CC
Statistics acquisition				
Runtime[a] TU_∞/δ_0^r	1113	945	929	1004
Timestep $\Delta t U_\infty/\delta_0^r \cdot 10^{-3}$	1.5	0.9	0.9	0.9
Sampling rate[b] $\Delta t U_\infty/\delta_0^r$	0.01	0.01	0.01	0.01
Number of FTT	56	48	47	51
LF-Analysis				
Sampling rate[c] $\Delta t U_\infty/\delta_0^r$	0.045	0.026	0.026	0.026
$St_{min} = f_{min}\delta_0^r/U_\infty$	0.001	0.001	0.001	0.001
$St_{max} = f_{max}\delta_0^r/U_\infty$	11	19	19	19

[a] Excluding a start-up transient of 5 FTT.
[b] Sampling time for the post-processing based on collected snapshots.
[c] Mean sampling time for the wall-pressure probes.

conditions. Throughout this study we will use the boundary-layer thickness either evaluated at the domain inlet $\delta_0 = 11.35$ mm or at a reference plane $\delta_0^r = 13.46$ mm located upstream of the interaction region at $x/\delta_0 = 11.7$ as reference length. The boundary-layer thickness is calculated based on the distance from the wall where 99% of the mean free-stream velocity U_∞ is reached.

The computational domain is rectangular with dimensions $23.39\delta_0 \times 5.57\delta_0 \times 2.62\delta_0$ and is discretized with $560 \times 190 \times 130$ cells in streamwise, wall-normal and spanwise directions, respectively. This leads to a grid resolution of $\triangle x^+ = 30, \triangle y_{min}^+ = 1.2, \triangle z^+ = 15$ at the reference plane. In the wall-normal direction hyperbolic grid stretching is used with a stretching factor of $\beta_y = 5.0$

$$y(j) = L_y \cdot \frac{\sinh\left(\frac{\beta_y \cdot (j-1)}{N_y - 1}\right)}{\sinh(\beta_y)}, \tag{1}$$

where j denotes the individual grid point, L_y the domain height and N_y the total number of cells in wall-normal direction.

For the low-frequency analysis presented later, 10,387 equally spaced pressure probes ($\triangle/\delta_0^r \approx 0.05$) have been placed both in stream- and spanwise direction along the wall within the region indicated in Fig. 3.

Fig. 2 shows a schematic of the basic control method used in this work together with the main geometry parameters. In total three parameter sets have been investigated, for which the suction location within the separated zone is varied while the injection position is kept fix. Intuitively, vertical injection perturbs the incoming TBL, followed by a relaxation process before the interaction region is reached. For this reason the injection is located well upstream of the nominal inviscid impingement point. Fig. 4 shows the average normalized wall-pressure distribution for the baseline configuration without control, referred to as NC in the following, together with the bubble topology represented through the
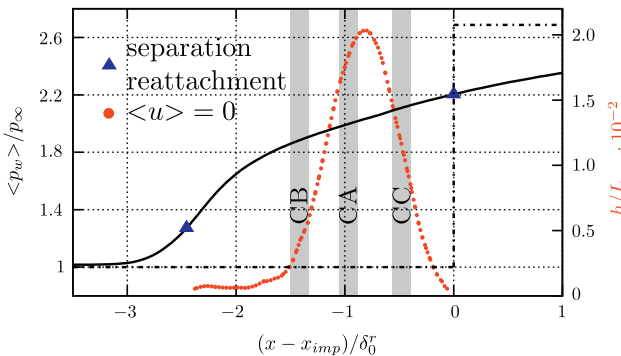
$\langle u \rangle/U_\infty = 0$ iso-line (●). Grey shaded rectangles represent three different suction locations under investigation. With CA we denote the case where suction is applied near the maximum bubble height and for the cases CB and CC the suction slot is shifted $0.3\delta_0$ upstream and downstream, respectively.

3. Numerical approach

We solve the three-dimensional compressible Navier–Stokes equations in conservative form

$$\partial_t \mathbf{U} + \nabla \cdot \mathbf{F}(\mathbf{U}) + \nabla \cdot \mathbf{D}(\mathbf{U}) = 0, \tag{2}$$

with the state vector $\mathbf{U} = [\rho, \rho u_1, \rho u_2, \rho u_3, E]$ consisting of: density ρ, momentum ρu_i and total energy E. In the above equation the total flux is split into an inviscid part

$$\mathbf{F}_i(\mathbf{U}) = [u_i\rho, u_i\rho u_1 + \delta_{i1}p, u_i\rho u_2 + \delta_{i2}p, u_i\rho u_3 + \delta_{i3}p, u_i(E+p)], \tag{3}$$

and a viscous contribution

$$\mathbf{D}_i(\mathbf{U}) = [0, -\tau_{i1}, -\tau_{i2}, -\tau_{i3}, u_k\tau_{ik} + q_i], \tag{4}$$

where u_i is the velocity vector and τ_{ij} the viscous stress tensor, which according to the Stokes hypothesis for a Newtonian fluid is

$$\tau_{ij} = \mu(T)\big(\partial_j u_i + \partial_i u_j - 2/3\delta_{ij}\partial_k u_k\big). \tag{5}$$

The heat fluxes q_i due to conduction follow from the Fourier law

$$q_i = -\kappa(T)\partial_i T. \tag{6}$$

The above equations are solved in non-dimensional form where the normalization process reads

$$u_i = u_i^\star/U_\infty^\star, \quad \rho = \rho^\star/\rho_\infty^\star, \quad T = T^\star/T_\infty^\star, \quad p$$
$$= p^\star/(\rho_\infty^\star U_\infty^{\star 2}), \quad E = E^\star/(\rho_\infty^\star U_\infty^{\star 2}), \quad x_i = x_i^\star/\delta^\star, \quad t$$
$$= t^\star U_\infty^\star/\delta^\star, \tag{7}$$

and variables marked with a star ($\star$) represent dimensional quantities. The governing flow parameters are the Reynolds number Re, the Prandtl number Pr, the Mach number Ma and the specific-heat ratio γ. We consider a perfect gas with a constant Prandtl number of Pr = 0.72 and specific-heat ratio of $\gamma = 1.4$. Pressure p and temperature T are determined by the non-dimensional ideal-gas equation of state

$$p = \frac{1}{\gamma \mathrm{Ma}^2}\rho T, \tag{8}$$

and the definition of total energy E

$$E = \frac{p}{\gamma - 1} + \frac{1}{2}\rho u_i u_i. \tag{9}$$

Fig. 4. Average normalized wall-pressure distribution and zero streamwise velocity iso-line for the uncontrolled reference configuration NC. Investigated suction locations are indicated by CA, CB and CC. Triangles (▲) denote separation and reattachment pressure levels, respectively.

Temperature dependence of dynamic viscosity $\mu(T)$ and thermal conductivity $\kappa(T)$ are modeled through the Sutherland law

$$\mu(T) = \frac{1}{Re} T^{1.5} \frac{1+C}{T+C} \quad \text{with} \quad C = \frac{S}{T^{\star}_{\infty}}, \quad S = 110.4K$$

$$\kappa(T) = \frac{1}{(\gamma-1)Ma^2 Pr} \mu(T). \tag{10}$$

The compressible Navier–Stokes equations are solved using the Adaptive Local Deconvolution Method (ALDM) for the discretization of the convective fluxes Hickel et al. (2006) and Hickel and Larsson (2009). ALDM is a nonlinear finite volume method that provides a physically consistent subgrid-scale turbulence model for implicit LES. Employing a shock sensor to detect discontinuities and switch on the shock-dissipation mechanism, ALDM can capture shock waves while smooth waves and turbulence are propagated accurately without excessive numerical dissipation. The diffusive fluxes are discretized using a 2nd order central difference scheme, and a 3rd order Runge Kutta scheme is used for the time integration.

At the domain inlet a Digital Filter (DF) based boundary condition is used (Touber and Sandham, 2009b), for which first and second order statistical moments have been obtained through a precursor temporal boundary-layer simulation under the same flow conditions. The shock is introduced at the top of the domain by imposing a jump in the flow variables that satisfies the Rankine–Hugoniot relations. The nominal inviscid impingement point at the wall is $x_{imp} = 16.7\delta_0$. At the outlet, linear extrapolation of all flow variables is used. The wall is modeled as isothermal with the temperature fixed to its nominal adiabatic value $T_w/T_\infty = 1 + r\frac{\gamma-1}{2}M^2_\infty = 2.065$, which corresponds to a recovery factor of $r = 1$. Periodic boundary conditions are used in the spanwise direction. Statistical quantities have been obtained by averaging instantaneous three-dimensional flow fields in time and spanwise direction after an initial transient of $5L_x/U_\infty$; see Table 2 for details. In the following Reynolds averages will be denoted as $\langle \cdots \rangle / \overline{\cdots}$ and Favre averages as $\widetilde{\cdots}$.

4. Results and discussion

4.1. Incoming turbulent boundary-layer

According to Grilli et al. (2013), the spatial extent of the separation bubble in SWBLI is highly sensitive on the level of turbulence in the incoming TBL. Thus, before the influence of each control configuration on the SWBLI is addressed, the main incoming boundary-layer properties will be discussed. The van-Driest transformed mean-velocity profile together with the RMS of Reynolds stresses in Morkovin scaling at $x/\delta_0 = 13.1$ are presented in Fig. 5(a)/(b) and compared with DNS data of Pirozzoli and Bernardini (2011) for identical friction Reynolds number $Re_\tau = 900$. Note that the DNS has a slightly different Mach number of $Ma_\infty = 2.0 \, (Ma_{\infty,LES} = 2.3)$ and a lower local Reynolds number of $Re_\delta = 55,170 \, (Re_{\delta,LES} = 73,756)$. The velocity profile is in good agreement with the logarithmic law of the wall and the DNS data, with small differences in the wake region due to higher Reynolds number. The Reynolds stresses are in good agreement with the DNS data in the near-wall region, while larger deviations occur in the logarithmic and wake region.

For further validation, the incompressible skin friction distribution $\langle C_{f_i} \rangle$, obtained from the van-Driest II transformation (van Driest, 1956), is compared to algebraic incompressible relations, various DNS and experimental data for a wide range of Mach numbers; see Fig. 6(a). Reported incompressible skin friction formulas by Kármán-Schoenherr and Blasius are adopted from Hopkins and Inouye (1971) and the relation by Smits is adopted from
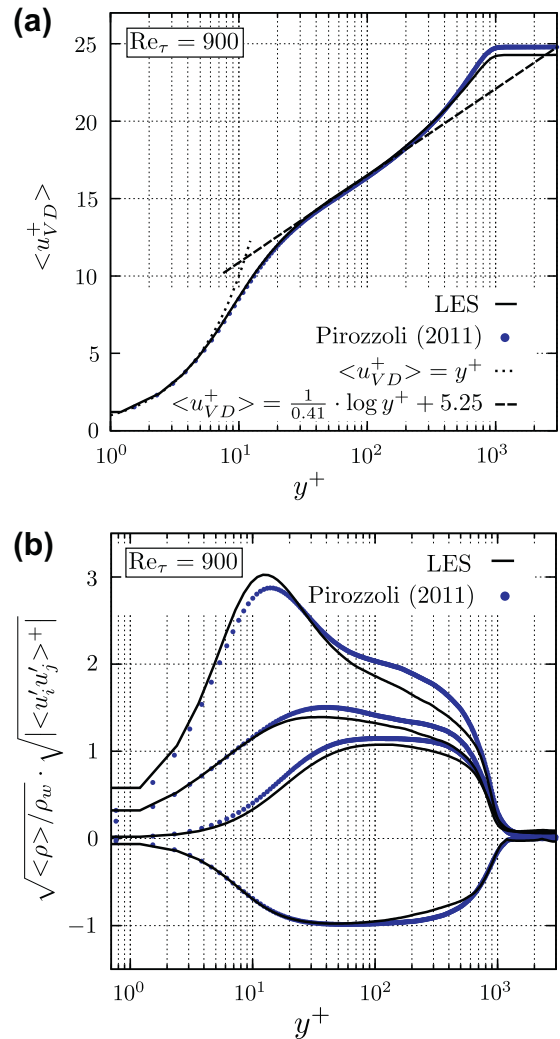
Fig. 5. Incoming boundary-layer: (a) van-Driest transformed mean-velocity profile. (b) RMS of Reynolds stresses with density scaling at $Re_\tau = 900$.

Smits et al. (1983). The computed incompressible skin friction coefficient (——) is in good agreement with the reported empirical relations. Autocorrelation functions in spanwise direction, evaluated at the streamwise position $x/\delta_0 = 11.7$ and wall-normal distance $y/\delta_0 = 0.1$, are reported in Fig. 6(b). The figure shows that all flow variables are sufficiently decorrelated over a distance equal to half of the spanwise domain extent. We conclude that the domain is sufficiently large and that the turbulence structure is not affected by the periodic boundary conditions. In the same figure, also the streamwise evolution of the autocorrelation functions for $y/\delta_0 = 0.1$ is illustrated. It is important to note, that the DF inflow technique does not introduce any spurious low-frequency forcing and does not interfere with the reflected shock dynamics investigated in this study.

Finally, Fig. 7 reports the turbulence kinetic energy (TKE) budgets together with the anisotropy invariant map (AIM) evaluated at the reference station $x/\delta_0 = 11.7$. The transport equation for the mean TKE $k = 1/2\widetilde{u''_i u''_j}$ for a compressible flow can be written as

$$\frac{\partial \overline{\rho}k}{\partial t} = C + T + P + D + \Pi - \varepsilon + M = 0, \tag{11}$$

where the single budgets on the right hand side are the contributions due to convection C $(-\partial_{xj}[\overline{\rho}\tilde{u}_j k])$, turbulent transport T
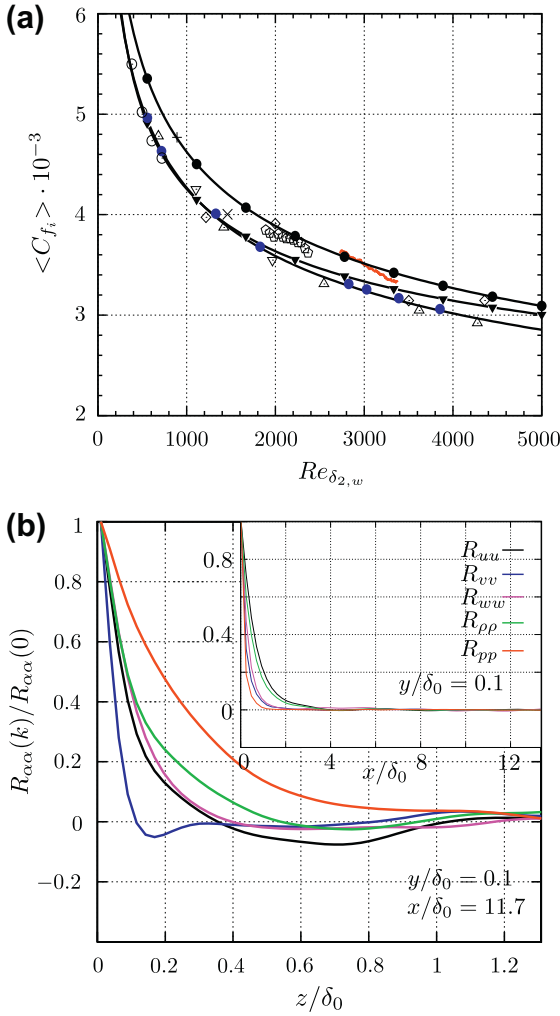
49

(a)

(b)

Fig. 6. Incoming boundary-layer: (a) Incompressible skin friction evolution. (−•−) Blasius; (−▼−) Kàrmàn-Schoenherr; (−) Smits; (—) Present LES; (○) Pirozzoli and Grasso (2004), (●) Pirozzoli and Bernardini (2011), (⊙) Komminaho and Skote (2002), △ Schlatter and Örlü (2010), (▽) Simens et al. (2009), (◇) CAT5301 AGARD 223, (+) Guarini et al. (2000), (×) Maeder et al. (2001). (b) Two-point autocorrelation functions.

(a)

(b)

Fig. 7. (a) Turbulent kinetic energy transport equation evaluated at $x/\delta_0 = 11.7$. Individual budgets are normalized by $\rho_w u_\tau^4/v_w$. (b) Reynolds stress anisotropy invariant map evaluated at $x/\delta_0 = 11.7$. Black bullets • represent the wall and boundary-layer edge locations, respectively. The wall-normal distance is represented through the colorbar and normalized by the local boundary-layer thickness δ_x. (For interpretation of the references to color in this figure legend, the reader is referred to the web version of this article.)

$(-\partial_{x_j}[1/2\overline{\rho}\widetilde{u_i''u_i''} + \overline{p'u_i'}\delta_{ij}])$, production P $(-\overline{\rho}\widetilde{u_i''u_j''}\partial_{x_j}\tilde{u}_i)$, viscous diffusion D $(\partial_{x_j}[\overline{\tau_{ij}'u_i''}])$, pressure-dilatation Π $(\overline{p'\partial_{x_i}u_i''})$, viscous dissipation ε $(\overline{\tau_{ij}'\partial_{x_j}u_i''})$ and compressible mass flux M $(\overline{u_i''}[\partial_{x_j}\overline{\tau}_{ij} - \partial_{x_i}\overline{p}])$. For a detailed discussion of the single terms refer to e.g. Shahab et al. (2011). Consistent with observations for a canonical boundary-layer flow, production and dissipation are balanced over a large part of the boundary-layer starting from $y^+ > 40$ in the logarithmic layer (Pope, 2000). In the viscous sublayer ($y^+ < 5$) the main contributions are due to viscous diffusion, transporting kinetic energy all the way to the wall, and viscous dissipation, whereas contributions due to convection are negligible small. The production peak is observed within the buffer layer at $y^+ = 10$, where the excess energy produced cannot be balanced by viscous dissipation, but is transported away by turbulent transport.

Following the work of Lumley (1978), the second II_b and third III_b invariant of the anisotropic Reynolds stress tensor $b_{ij} = \widetilde{u_i''u_j''}/2k - 1/3\ \delta_{ij}$ provide a representative description of the turbulent state. Each vertex in the (III_b, II_b) map, also known as the "Lumley triangle", constitutes a special turbulence state, see Fig. 7(b) for details. A two-component turbulence state is found for the near-wall flow, with highest anisotropy in the buffer layer
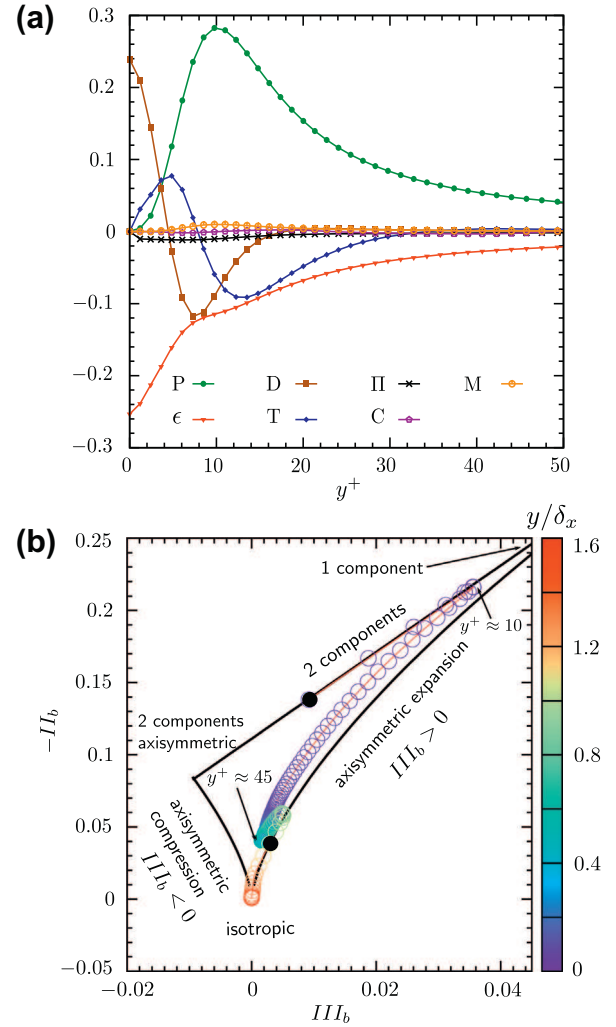
($y^+ \approx 10$). Within the buffer layer the path turns and follows the limit of axisymmetric expansion while gradually returning to an isotropic state in the outer layer.

4.2. Baseline SWBLI – NC

The mean skin-friction evolution in the direct vicinity of the interaction region is shown in Fig. 8(a). Due to the adverse pressure gradient imposed on the turbulent boundary-layer, the flow is decelerated and forms a recirculation zone as indicated by the change of sign in $\langle C_f \rangle$. The mean separation length for the baseline configuration is $L_{sep} = 2.46\delta_0^r$. The corresponding wall-pressure evolution is shown in Fig. 4. The pressure increase associated with the impinging shock is felt approximately $3\delta_0^r$ before the theoretical inviscid impingement location x_{imp}. This effect is known as the upstream influence mechanism (Délery, 1985). Black triangles denote the separation and reattachment pressure levels. The bubble topology, analyzed through the $\langle u \rangle/U_\infty = 0$ iso-line in Fig. 4, reveals a very shallow separation zone with an aspect ratio of $L_{sep}/h_{max} = 50$, consistent with numerical simulations performed
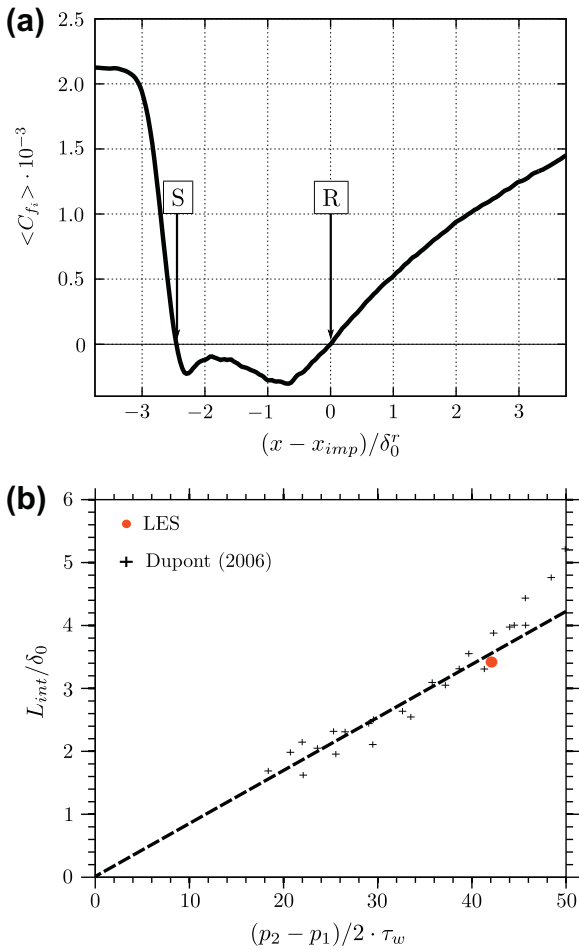
(a)

(b)

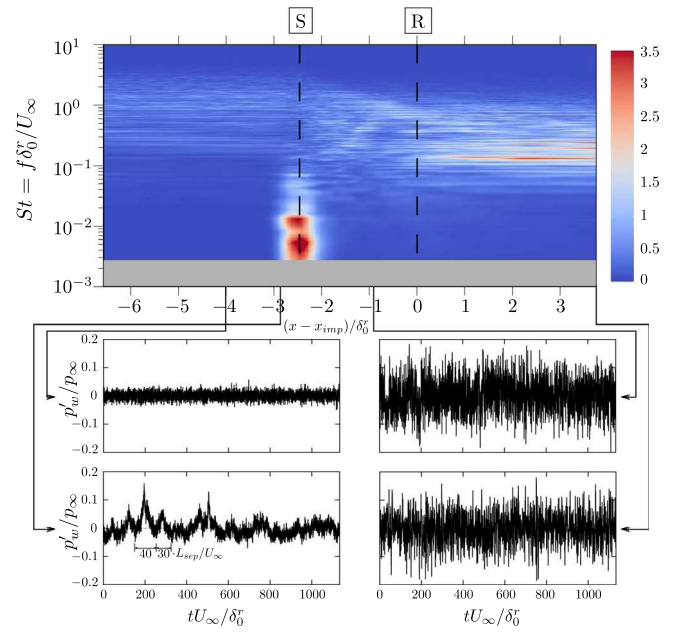**Fig. 8.** Mean-flow statistics: skin friction evolution and interaction length.

Fig. 9. Weighted power spectral density (PSD) of spanwise-averaged wall-pressure signals for the baseline configuration and selected pressure signals. Contour: $f \cdot \mathrm{PSD}(f)/\int f \cdot \mathrm{PSD}(f)\mathrm{d}f$.

with 50% overlap using Hamming windows. The most upstream wall-pressure variance signal shows no significant pressure variation, indicating the undisturbed turbulent boundary-layer. Considering the next probe, which is located in the proximity of the mean reflected shock foot, distinctive pressure peaks associated with the back and forth motion of the reflected shock can be identified. Dussauge et al. (2006) found typical Strouhal numbers based on the separation length ranging between $St_{L_{sep}} = 0.02, \ldots, 0.05$ for different flow geometries and upstream conditions. Associated
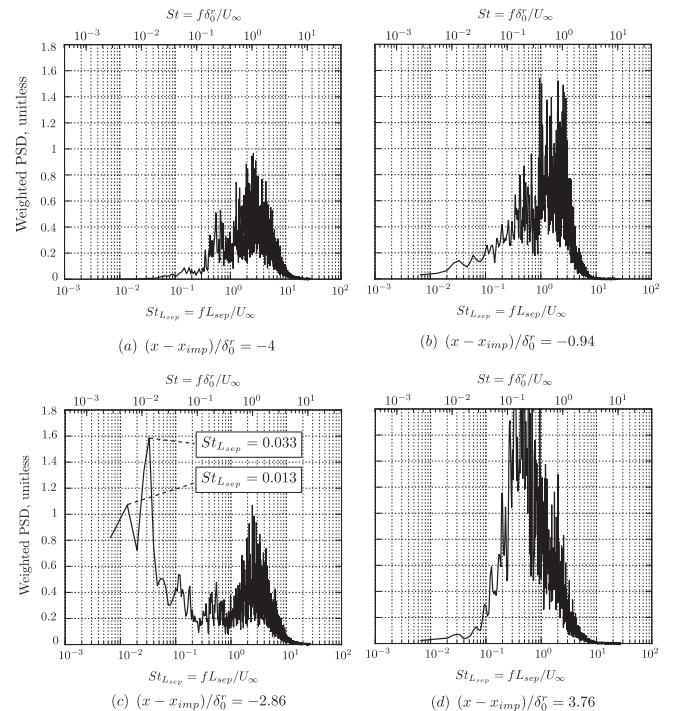
by Touber and Sandham (2009a) for the IUSTI case. Dupont et al. (2006) proposed a linear relationship for weak interactions between the interaction length L_{int} and the pressure jump across the impinging shock wave $(p_2 - p_1)$ normalized by the upstream boundary-layer thickness δ_0 and wall shear stress τ_w, respectively. In this study we define the distance between the mean reflected shock foot position (obtained through linear extrapolation to the wall) and x_{imp} as the interaction length L_{int}, as done by Dupont et al. (2006). Fig. 8(b) shows the experimental data together with the value for the current LES ($\bullet$), confirming the expected linear relationship.

In the following we analyze the Power Spectral Densities (PSD) of wall-pressure probes in order to address unsteady aspects related to reflected shock dynamics. Pressure signals have been recorded at a mean sampling time interval of $0.045\delta_0^r/U_\infty$ and cover a total timespan of $1113\delta_0^r/U_\infty$; see Table 2 for details. This leads to a maximum resolvable Strouhal number of $St_{max} \approx 11$ and a minimum resolvable Strouhal number of $St_{min} \approx 0.001$, which means that the current LES is well able to capture the expected low-frequency unsteadiness. In Fig. 9 we report the wall-pressure spectrum together with the full evolution of pressure fluctuations evaluated at four selected streamwise locations. Moreover, mean separation ⓢ and reattachment ⓡ positions are indicated. In order to emphasize the frequencies that contribute most, we show contours of the premultiplied PSD normalized by the integrated PSD over a given frequency range, i.e., $f \cdot \mathrm{PSD}(f)/\int f \cdot \mathrm{PSD}(f)\mathrm{d}f$. The spectra have been obtained with the Welch algorithm by splitting the time-signal in eight segments

Fig. 10. Weighted power spectral density (PSD) associated to pressure variance signals reported in Fig. 9.

51

time scales of $tU_\infty/L_{sep} = 20, \ldots, 50$ could be found in the current LES as indicated in Fig. 9. Further downstream, distinct peaks are no longer visible, however, the amplitude of the pressure fluctuations has increased significantly as a consequence of turbulence amplification over the shock. The PSD spectrum in Fig. 9 clearly shows the broadband peak associated with the characteristic frequency of the energetic scales in the undisturbed TBL, being U_∞/δ_0^r. The energy peak shifts towards significantly lower frequencies in the vicinity of the mean separation location and moves back again to higher frequencies downstream of the interaction zone. Due to the thickening of the boundary-layer past the shock system, the new PSD peak is located at lower Strouhal numbers. Fig. 10 reports weighted PSDs related to the wall-pressure signals shown in Fig. 9. It is important to note that no energetically significant low-frequencies have been introduced by the inflow technique used for the current LES, hence allowing to state that the SWBLI dynamics are not artificially influenced by upstream events. Based on the mean separation length a Strouhal number of $St_{L_{sep}} = fL_{sep}/U_\infty = 0.03$ is found for the low-frequency shock motion. This finding is consistent with experimental values documented in Dupont et al. (2006). Based on this characteristic frequency a total number of 15 low-frequency cycles (LFC) are captured within the available integration time.

4.3. Control configurations

In this section, we provide a cross-comparison between the uncontrolled baseline case NC and the three control configurations CA, CB and CC. A general impression of the effect of flow control is given in Figs. 11 and 12, where contour plots of the instantaneous and time-averaged temperature distribution within the *x*–*y*
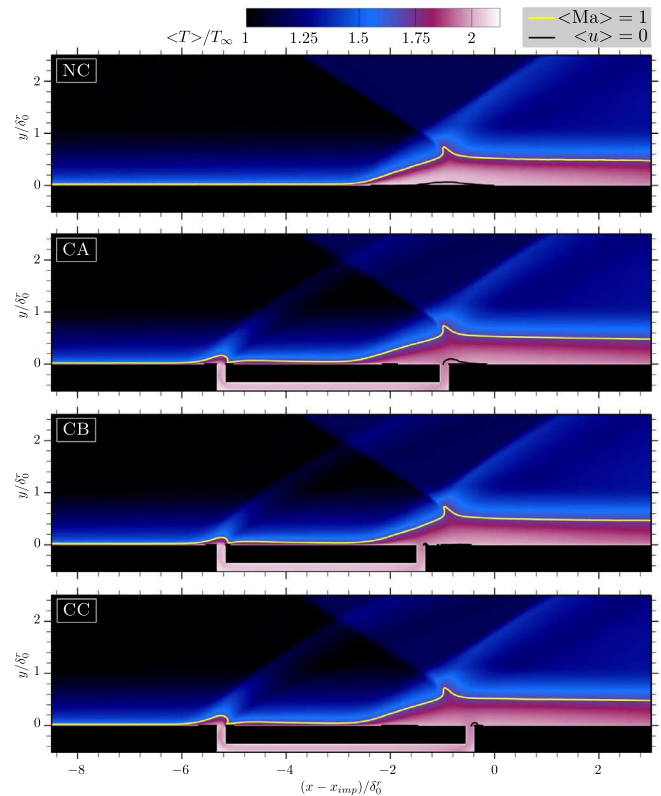

Fig. 12. Time-averaged temperature distribution $\langle T \rangle/T_\infty$ in $x - y$ mid-plane with $\langle Ma \rangle = 1$ isoline in yellow and $\langle u \rangle = 0$ isoline in black for all configurations studied.
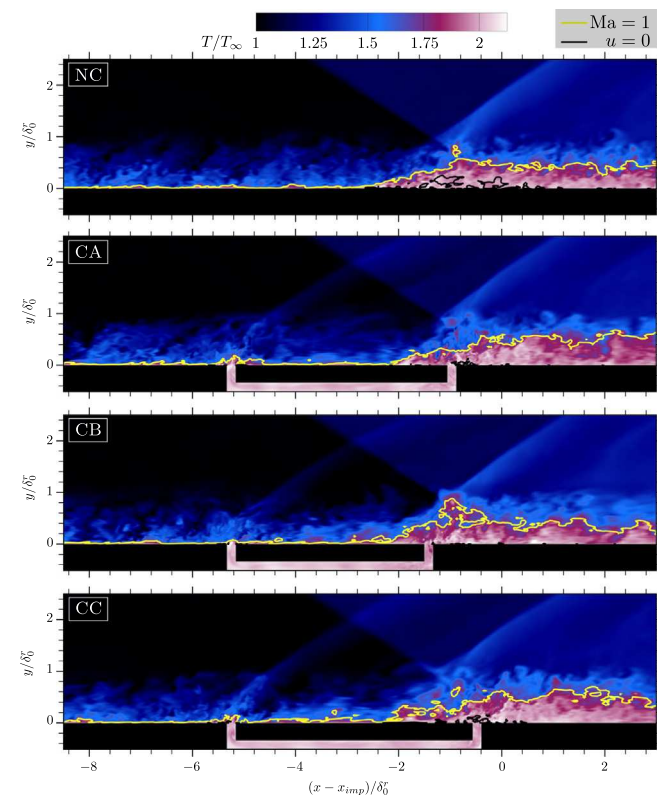
mid-plane are compared, respectively. The sonic line is shown in yellow and zero streamwise velocity is shown in black. The main features identifiable for the controlled cases are the suction effect, which eliminates a great portion of the recirculation zone (black line) and the perturbation of the incoming TBL due to the vertical injection, promoting the formation of additional weak shock-expansion systems similar to the case of AJVG (Souverein and Debiève, 2010).

A comparison of mean flow properties is given in Fig. 13. The lower incoming skin friction level illustrated in Fig. 13(a) highlights the aforementioned perturbation of the upstream TBL for all control cases. Local suction accelerates the near-wall flow, which subsequently leads to an increase in skin friction directly upstream of the individual suction slot. Downstream of the suction slot, the skin friction level drops to greater negative values due to the higher reversed flow amplitude. All control configurations lead to a downstream shift of the mean separation location. The largest effect is observed for control case CB. For this case the skin friction evolution downstream of the suction channel exhibits an upstream shift of the mean reattachment position and an overall higher skin friction level in the relaxation zone. The mean wall pressure distribution in Fig. 13(b) clearly shows a reduction of the upstream influence length for control case CB. The interaction lengths L_{int}/δ_0^r are 3.24, 3.26, 2.75 and 3.09 for the cases NC, CA, CB and CC, respectively. The ability of the control mechanism to reduce the amount of mean recirculating flow is evaluated by analysing the bubble mass per unit span enclosed within the zero streamwise velocity iso-line, see Fig. 13(c). Suction applied within the rear part of the separation bubble (CC) reduces the bubble mass by about 63%, possibly being a direct consequence of the higher mass-flow ratio $\dot{m}_{ch}/\dot{m}_{bl}$ for this case (see Table 3 for details).

The influence of each control configuration on turbulence intensity is studied in the following. Fig. 15 shows contours of the
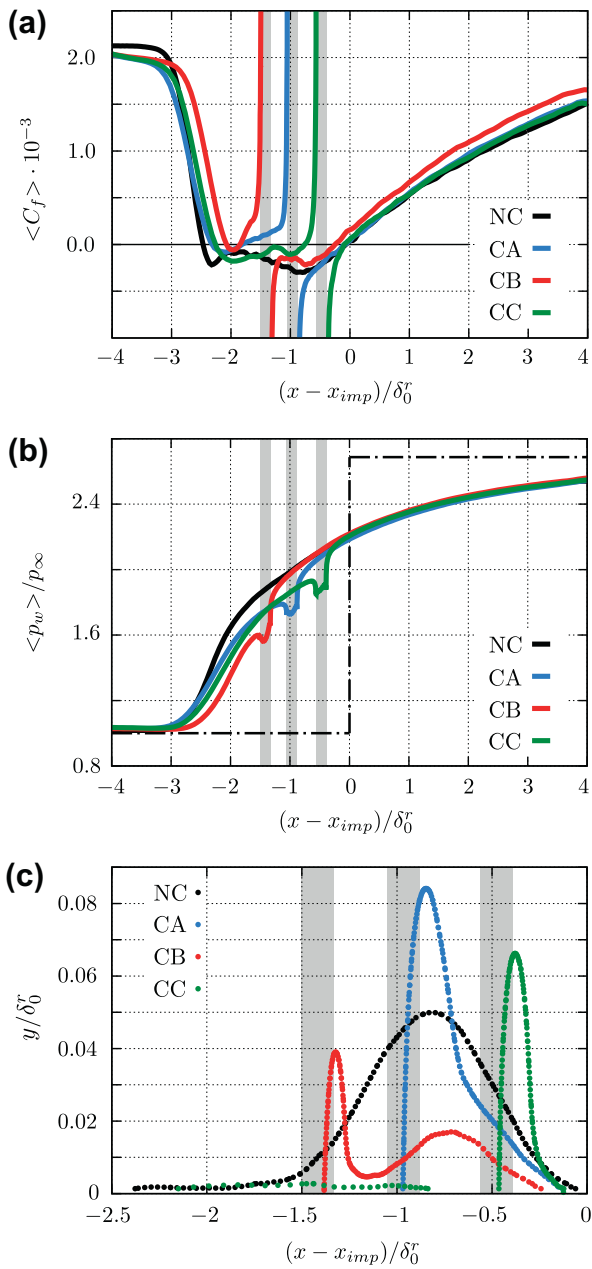

Fig. 11. Instantaneous temperature distribution T/T_∞ in $x - y$ mid-plane with $Ma = 1$ isoline in yellow and $u = 0$ isoline in black for all configurations studied. (For interpretation of the references to color in this figure legend, the reader is referred to the web version of this article.)

Fig. 13. Mean flow properties in the vicinity of the interaction region. (a) Skin friction $\langle C_f \rangle$ (b) and wall-pressure $\langle p_w \rangle / p_\infty$ evolution in the streamwise direction. (c) Bubble topology represented through zero streamwise velocity isoline $\langle u \rangle = 0$. Grey shaded areas indicate individual suction locations.

Table 3
Mean-flow quantities of all cases studied.

Case		NC	CA	CB	CC
Interaction length[a]	L_{int}/δ_0^r	3.24	3.26	2.75	3.09
Max. bubble height[b]	h_{max}/δ_0^r	0.050	0.084	0.038	0.066
Massflow ratio [c]	$\dot{m}_{ch}/\dot{m}_{bl}$ (%)	–	2.66	2.05	3.15
Bubble mass [d]	$m/(\rho_\infty \delta_0^{r\,2})$	0.036	0.030	0.014	0.013

[a] Distance between the mean reflected shock foot position and theoretical inviscid impingement point.
[b] Measured through $\langle u \rangle = 0$ iso-line.
[c] Massflow ratio between the channel flow $\dot{m}_{ch}$ and the undisturbed TBL $\dot{m}_{bl}$.
[d] Bubble mass per unit span.

resolved Reynolds shear stress, the boundary-layer thickness evolution (white) and the sonic line (black) for all cases. White dotted lines indicate suction and injection locations, respectively. For the

baseline configuration a high level of Reynolds shear stress is found along the detached shear layer within the interaction region $-3 < (x - x_{imp})/\delta_0^r < 1$. Its maximum is located approximately one boundary-layer thickness downstream of the mean reattachment location $((x - x_{imp})/\delta_0^r \approx 1)$, confirming the findings by Pirozzoli and Grasso (2006). A high Reynolds shear stress level $\langle u'v' \rangle$ is found along the reflected shock, which is consistent with experimental measurements by Piponniau (2009) and directly associated with the shock motion. Reynolds shear stress changes sign at the tip of the incident shock as a consequence of its flapping motion (Shahab, 2006). For all control cases additional unsteady shocks can be identified in the vicinity of the injection slots (white dotted lines). At the same location, the formation of shear layers due to small recirculation zones directly upstream and downstream of the injection position leads to an increased level of turbulence in this region, which is then convected downstream and interacts with the original reflected shock. The adverse pressure gradient induced by the reflected shock bulges the incoming shear layer, resulting in a spot of increased Reynolds shear stress within the interaction zone. This phenomenon is more pronounced for control cases CA and CC. It is interesting to note that the flapping motion of the incident shock tip and the reflected shock dynamics are significantly reduced for configuration CC, whereas for control case CA the shock-excursion length is increased and for CB comparable to the baseline configuration. Considering the overall boundary-layer thickness evolution (white line in Fig. 15), one can conclude that the present control mechanism has not much effect on the downstream boundary-layer. Amplification factors for Reynolds shear stress and turbulent kinetic energy are reported in Table 4, which represent the ratio of the maximum value of a particular Reynolds stress component after or within the interaction

Table 4
Turbulence amplification factors.

Amplification[a]	NC	CA	CB	CC	DNS[b]
$\langle u'v' \rangle$	3.11	3.11	3.17	2.91	3.2
$0.5\langle u_i'u_i' \rangle$	2.64	2.82	3.19	2.29	2.7

[a] Compared to the undisturbed boundary-layer.
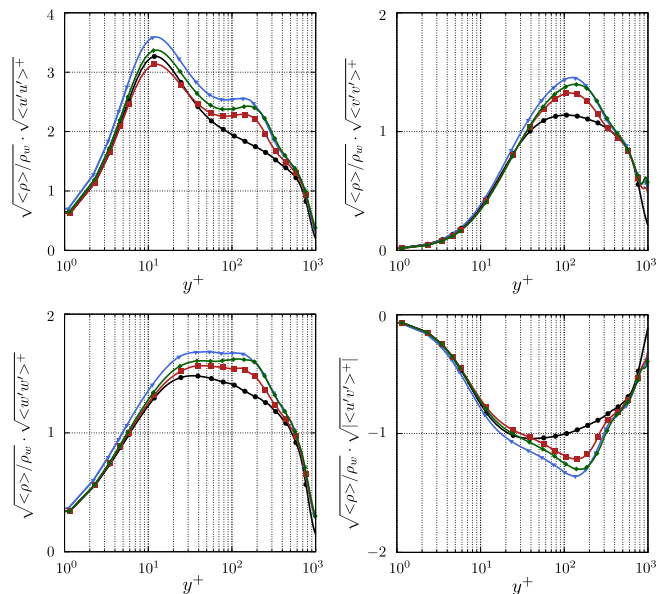[b] Pirozzoli and Grasso (2006), $Ma = 2.25, \Theta = 8°$.

Fig. 14. RMS Reynolds stress profiles with density scaling evaluated at $x^\star = (x - x_{imp})/\delta_0^r = -3$ for all cases studied: (–•–) NC; (—▼—) CA; (—■—) CB; (—♦—) CC.
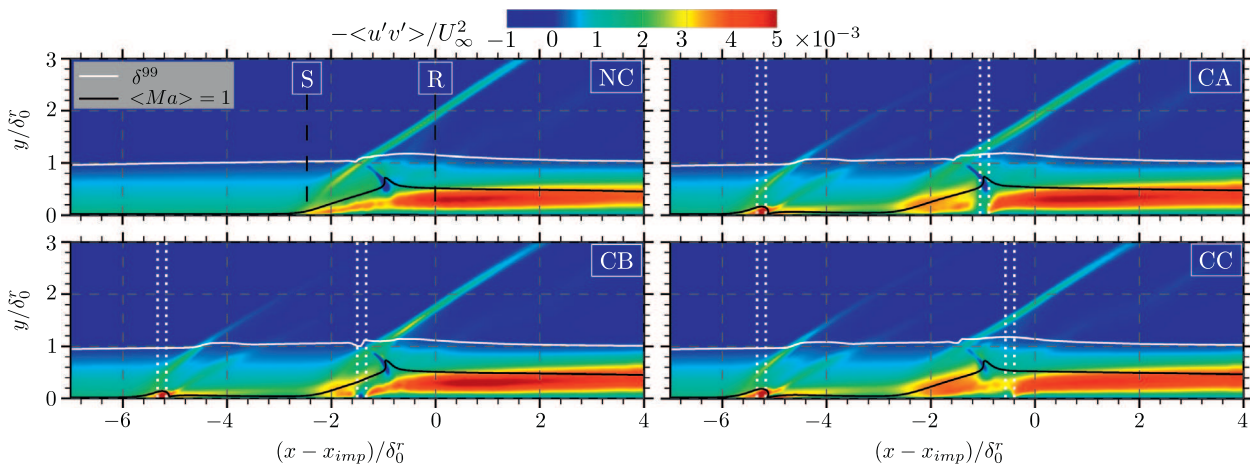
Fig. 15. Mean resolved Reynolds shear stress together with boundary-layer thickness in white and sonic line in black. Vertical dotted lines represent suction and injection locations, respectively. Mean separation and reattachment positions are indicated for the baseline case.
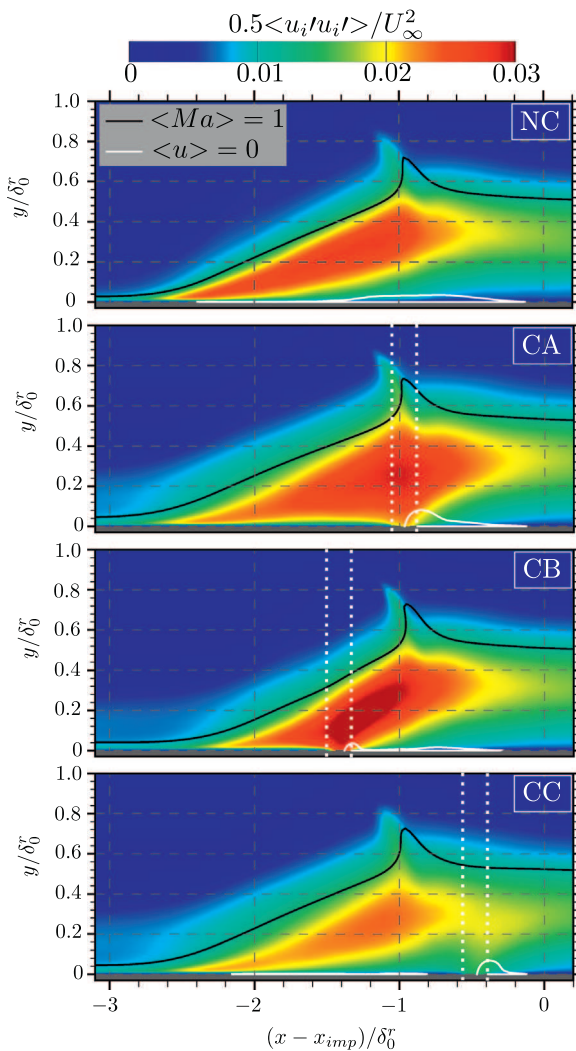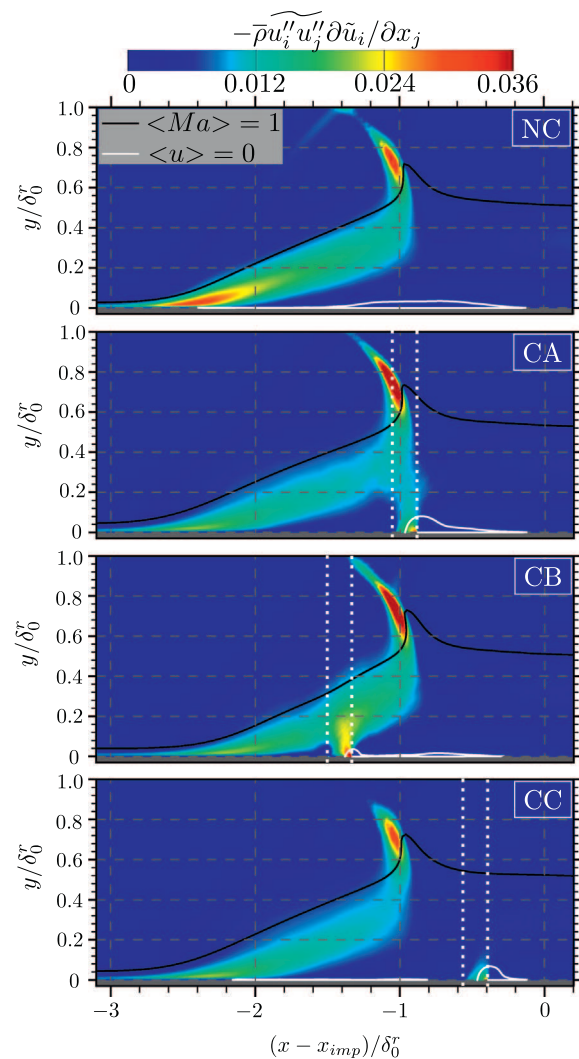

Fig. 16. Resolved turbulent kinetic energy together with zero streamwise velocity iso-line in white and sonic line in black in the vicinity of the interaction zone. Vertical dotted lines represent suction locations.

Fig. 17. Resolved turbulence kinetic energy production together with zero streamwise velocity iso-line in white and sonic line in black in the vicinity of the interaction zone. Vertical dotted lines represent suction locations.

region to the peak value of the same stress component in the undisturbed incoming turbulent boundary layer. The baseline case is overall in good agreement with the DNS data of Pirozzoli and Grasso (2006). Reduced amplification for both Reynolds normal and shear stresses is observed if suction is applied in the rear part of the interaction zone, with lowest values for control case CC.

The influence of the cross-jet on turbulence is further addressed in Fig. 14, where we present Reynolds stresses in Morkovin scaling at the streamwise pre-interaction position $(x - x_{imp})/\delta_0^r = -3$. For all control cases the equilibrium turbulence state is not recovered before the reflected shock foot position is reached. While the near-wall turbulence is very similar to the uncontrolled case, increased Reynolds stresses are observed in the logarithmic region around $y^+ \approx 100$ for all control configurations. The higher turbulence level within the range $y^+ \approx 70, \ldots, 200$ ($y/\delta_0^r \approx 0.09, \ldots, 0.26$) is directly associated with the shear layers that are generated at each discrete suction slot and subsequently convected downstream, see Fig. 15. This implies that it is impossible to differentiate between effects of suction and injection on separation reduction.

A close-up of the interaction zone is shown in Fig. 16, where we present contours of resolved mean TKE, the zero streamwise velocity iso-line in white and the sonic line in black. Without flow control, turbulence is generated when approaching the shock system with TKE maxima being located in the region around the mean separation and along the detached shear layer that originates from it. For all control configurations, the incoming subsonic layer is thicker than for the baseline case. This is a direct consequence of the vertical injection upstream of the SWBLI. However, the zero streamwise velocity iso-line shows that control cases CA and CB significantly reduce the spatial extent of the recirculation zone upstream of the suction slots. Considering the TKE contours, suction applied within the inclined detached shear layer region $(-2.6 < (x - x_{imp})/\delta_0^r < -0.8)$ leads to a strong increase of turbulence, whereas suction applied in the rear part of the bubble (CC) damps turbulent fluctuations. For all three control configurations an increased incoming turbulence level can be observed up to wall distances $y/\delta_0^r \approx 0.3$, which results from additional shear layers directly downstream of the injection slot, see Fig. 15. By investigating contours of turbulence production P, Fig. 17, we find that the deflection of the shear layer towards the suction location strongly enhances turbulence production. This in turn explains the higher TKE level for control cases CA and CB in this region. Considering suction configuration CC, the inclined shear layer remains essentially unaffected and the near-wall flow acceleration contributes to an overall lower turbulence level. As will be seen below, the reflected shock dynamics is significantly weakened for case CC,

which explains the overall lower turbulence level for this configuration.

The influence of the suction location on unsteady reflected shock dynamics is investigated in the following. Fig. 18 illustrates the wall-pressure spectrum for all cases studied. The spectra $f \cdot PSD(f)$ are plotted in a linear scale against $\log(f)$, resulting in an energetic scaling. The area under the resulting curve is proportional to the energy $E_{f_a-f_b}^2$ of the signal between f_a and f_b (Gatski and Bonnet, 2009):

$$E_{f_a-f_b}^2 = \int_{f_a}^{f_b} [f \cdot PSD(f)] d(\log f) = \frac{\langle p'p' \rangle}{(\rho_\infty U_\infty^2)^2}, \tag{12}$$

This scaling guarantees that different configurations and streamwise positions are directly comparable with respect to the frequency and energy content of the wall-pressure signal. From Eq. (12) it is obvious that the resulting contour plot can be interpreted as wall-pressure load. In all spectra we highlight characteristic Strouhal numbers found for the baseline case NC by white horizontal lines. Moreover, black bullets represent the most dominant low-frequencies for each individual configuration. For control cases, suction and injection positions are again illustrated through vertical dashed lines. As already observed in Fig. 15, all control configurations exhibit additional low-frequency content near the injection and suction position. The broadband peak centered around $St \approx 1$ after the suction location indicates that none of the investigated control techniques alters the large-scale turbulence dynamics upstream of the interaction zone significantly. The low-frequency associated to the reflected shock dynamics is still apparent for all three control cases but shifted to higher Strouhal numbers with the greatest effect for configuration CC, see Table 5 for details.

Table 5
Reflected shock characteristic Strouhal numbers.

Case	NC	CA	CB	CC
$St^a = f\delta_0^r/U_\infty$	0.005/0.014	0.01/0.026	0.014/0.033	0.017
$\Delta St/St$ (%)	–/–	100/85	180/135	240/21
n_{LFC}^b	5.6/15.6	9.4/24.6	13.0/30.6	17.1

[a] Characteristic Strouhal numbers associated to the black bullets (●) in Fig. 18.
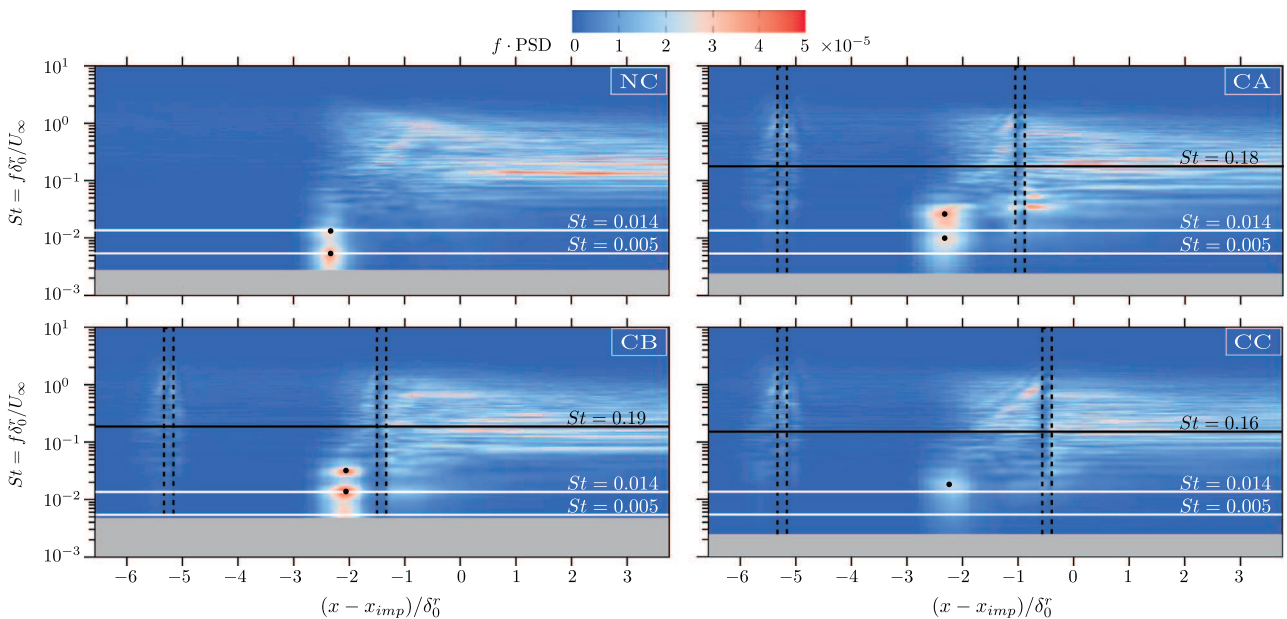[b] Number of low-frequency cycles captured within the available integration time.

Fig. 18. Weighted power spectral density (PSD) of spanwise-averaged wall-pressure probes for all cases studied. Contour: $f \cdot PSD(f)$.
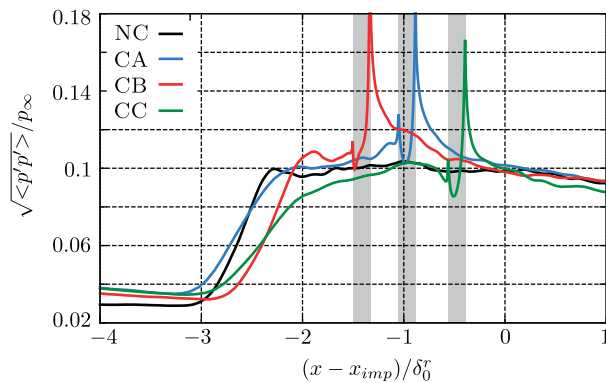
Fig. 19. Root-mean-square profiles of wall-pressure fluctuations in streamwise direction.

One could argue that this is a direct consequence of the lower bubble mass (Souverein and Debiève, 2010), provided that the pulsation of the recirculation zone is responsible for the low-frequency unsteadiness observed Pirozzoli et al. (2010), Grilli et al. (2012). The acoustic coupling provided by the passive-channel concept explains that the same level of low-frequency content is present in the direct vicinity of the suction and injection positions. However, an acoustic feedback mechanism through the channel, which locks the reflected shock dynamics, can be excluded since the characteristic Strouhal number associated with an acoustic disturbance that travels through the channel (see horizontal black lines in Fig. 18) is approximately one order of magnitude larger than the one observed for the reflected shock. As characteristic velocity for the feedback Strouhal number we use the superposition of the average convective velocity and the average speed of sound within each individual channel. The contour in Fig. 18 further reveals an overall lower energy level for control case CC in the low-frequency regime.

Integrating the wall-pressure spectra at each streamwise location results in the RMS of wall-pressure fluctuations $\sqrt{\langle p'p'\rangle}/p_\infty$ shown in Fig. 19. Large amplifications of pressure fluctuations are found around the reflected shock foot, while secondary peaks can be observed at the discrete suction locations. Besides the change in interaction length L_{int} as already discussed in conjunction with the wall-pressure evolution, Fig. 13, one can further observe a significantly lower amplification level for control configuration CC near the reflected shock foot and after the SWBLI, consistent with previous discussions related to Figs. 15 and 17 .

5. Conclusions

We have studied a passive flow-control mechanism for the interaction of an oblique shock with a turbulent flat-plate boundary-layer using well resolved large-eddy simulation. The shock is generated by a $8.8°$ wedge at a freestream Mach numer of $Ma_\infty = 2.3$. The Reynolds number based on the incoming boundary-layer thickness is $Re_{\delta_0} = 60.5 \times 10^3$.

We found that suction applied within the separation zone significantly alters turbulence evolution in this region. Suction acting within the region of the inclined detached shear layer (CA and CB) strongly increases the turbulence level through a deflection towards the discrete suction slot, whereas suction applied in the rear part of the separation bubble (CC) lowers the overall turbulence level. Of course not only the shear layer contributes to turbulence production, but also the unsteady motion of the reflected shock. By investigating contours of resolved Reynolds shear stress we found that control configuration CC significantly reduces the reflected shock dynamics and the flapping motion associated with

the incident shock tip. Both findings support the observation of reduced turbulence levels for this case compared to the baseline configuration without control (NC).

The influence of the control method on the low-frequency unsteadiness has been addressed through a Fourier analysis of wall-pressure probes. All configurations shift the high-energy content associated with the reflected shock to higher frequencies, possibly as a direct consequence of the reduction in bubble mass. Configurations CB and CC are most efficient and at the same time show the largest reduction in bubble mass. Weighted power spectral densities in energetic scaling reveal a remarkably reduced low-frequency energy level for case CC. The streamwise evolution of wall pressure fluctuations shows a significant reduction of wall pressure loads for control case CC around the mean reflected shock foot, which is a direct consequence of the mitigated reflected shock dynamics.

For weak interactions, such as the investigated configurations, the control efficiency strongly depends on the suction position. For stronger shocks with larger deflection angles and otherwise identical flow conditions, the wall-pressure distribution within the recirculation region exhibits a significant pressure plateau due to the presence of a larger separated zone. Consequently, the control method becomes less sensitive with respect to suction position. Moreover, control acts on a higher pressure jump so that one may expect an increased effectiveness for strong interactions.

Acknowledgements

References

Adams, N.A., 2000. Direct simulation of the turbulent boundary layer along a compression ramp at M = 3andRe$_\theta$ = 1685. J. Fluid Mech. 420, 47–83. http://dx.doi.org/10.1017/S0022112000001257.

Beresh, S.J., Clemens, N.T., Dolling, D.S., 2002. Relationship between upstream turbulent boundary-layer velocity fluctuations and separation shock unsteadiness. AIAA J. 40, 2412–2422. http://dx.doi.org/10.2514/2.1609.

Bisek, N., Rizzetta, D., Poggie, J., 2012. Exploration of plasma control for supersonic turbulent flow over a compression ramp. In: 42nd AIAA Fluid Dynamics Conference and Exhibit, American Institute of Aeronautics and Astronautics, New Orleans, Louisiana, doi: 10.2514/6.2012-2700.

Blinde, P.L., 2008. Effects of Micro-Ramps on a Shock Wave/Turbulent Boundary Layer Interaction. Master thesis. Delft University of Technology.

Délery, J., 1985. Shock wave/turbulent boundary layer interaction and its control. Progr. Aerosp. Sci. 22, 209–280. http://dx.doi.org/10.1016/0376-0421(85)90001-6.

Délery, J., Dussauge, J.P., 2009. Some physical aspects of shock wave/boundary layer interactions. Shock Waves 19, 453–468. http://dx.doi.org/10.1007/s00193-009-0220-z.

Doerffer, P., Hirsch, C., Dussauge, J.P., Babinsky, H., Barakos, G.N., 2011. In: Unsteady Effects of Shock Wave Induced Separation. Notes on Numerical Fluid Mechanics and Multidisciplinary Design, vol. 114. Springer, Berlin, Heidelberg. http://dx.doi.org/10.1007/978-3-642-03004-8.

Dolling, D.S., 2001. Fifty years of shock-wave/boundary-layer interaction research: what next? AIAA J. 39, 1517–1531. http://dx.doi.org/10.2514/2.1476.

Dolling, D., Bogdonoff, S., 1981. An experimental investigation of the unsteady behavior of blunt fin-induced shock wave turbulent boundary layer interaction. In: 14th Fluid and Plasma Dynamics Conference, American Institute of Aeronautics and Astronautics, Palo Alto, California, doi: 10.2514/6.1981-1287.

Dupont, P., Haddad, C., Debiève, J.F., 2006. Space and time organization in a shock-induced separated boundary layer. J. Fluid Mech. 559, 255. http://dx.doi.org/10.1017/S0022112006000267.

Dussauge, J.P., Dupont, P., Debiève, J.F., 2006. Unsteadiness in shock wave boundary layer interactions with separation. Aerosp. Sci. Technol. 10, 85–91. http://dx.doi.org/10.1016/j.ast.2005.09.006.

Fulker, J., 1999. The Euroshock programme (A European programme on active and passive control of shock waves), in: 17th Applied Aerodynamics Conference, American Institute of Aeronautics and Astronautics, Norfolk, Virginia, doi: 10.2514/6.1999-3174.

Ganapathisubramani, B., Clemens, N.T., Dolling, D.S., 2007. Effects of upstream boundary layer on the unsteadiness of shock-induced separation. J. Fluid Mech. 585, 369–394. http://dx.doi.org/10.1017/S0022112007006799.

Gatski, T.B., Bonnet, J.P., 2009. Compressibility. Turbulence and High Speed Flow. Elsevier, Oxford.

Ghosh, S., 2010. An Immersed Boundary Method for Simulating the Effects of Control Devices used in Mitigating Shock/Boundary-Layer Interactions. Ph.D. thesis. North Carolina State University.

Grilli, M., Schmid, P.J., Hickel, S., Adams, N.A., 2012. Analysis of unsteady behaviour in shockwave turbulent boundary layer interaction. J. Fluid Mech. 700, 16–28. http://dx.doi.org/10.1017/jfm.2012.37.

Grilli, M., Hickel, S., Adams, N.A., 2013. Large-eddy simulation of a supersonic turbulent boundary layer over a compression-expansion ramp. Int. J. Heat Fluid Flow 42, 79–93. http://dx.doi.org/10.1016/j.ijheatfluidflow.2012.12.006.

Guarini, S.E., Moser, R.D., Shariff, K., Wray, A., 2000. Direct numerical simulation of a supersonic turbulent boundary layer at Mach 2.5. J. Fluid Mech. 414, 1–33. http://dx.doi.org/10.1017/S0022112000008466.

Hickel, S., Larsson, J., 2009. On implicit turbulence modeling for LES of compressible flows. In: Eckhardt, B. (Ed.), Advances in Turbulence XII. Springer, Berlin Heidelberg, pp. 873–875. http://dx.doi.org/10.1007/978-3-642-03085-7_209.

Hickel, S., Adams, N.A., Domaradzki, J.A., 2006. An adaptive local deconvolution method for implicit LES. J. Comput. Phys. 213, 413–436. http://dx.doi.org/10.1016/j.jcp.2005.08.017.

Hopkins, E.J., Inouye, M., 1971. An evaluation of theories for predicting turbulent skin friction and heat transfer on flat plates at supersonic and hypersonic Mach numbers. AIAA J. 9, 993–1003.

Komminaho, J., Skote, M., 2002. Reynolds stress budgets in Couette and boundary layer flows. Flow Turbul. Combust. 68, 167–192. http://dx.doi.org/10.1023/A:1020404706293.

Lee, S., 2009. Large Eddy Simulation Of Shock Boundary Layer Interaction Control Using Micro-Vortex Generators. Ph.D. thesis. University of Illinois.

Loginov, M.S., Adams, N.A., Zheltovodov, A.A., 2006. Large-Eddy Simulation of Shock-Wave/Turbulent-Boundary-Layer Interaction. Ph.D. thesis. Technische Universität München, doi: 10.1017/S0022112006000930.

Lumley, J.L., 1978. Computational modeling of turbulent flows. Adv. Appl. Mech. 18, 123–176.

Maeder, T., Adams, N.A., Kleiser, L., 2001. Direct simulation of turbulent supersonic boundary layers by an extended temporal approach. J. Fluid Mech. 429, 187–216. http://dx.doi.org/10.1017/S0022112000002718.

McCormick, D.C., 1993. Shock/boundary-layer interaction control with vortex generators and passive cavity. AIAA J. 31, 91–96. http://dx.doi.org/10.2514/3.11323.

Piponniau, S., 2009. Instationnarités dans les décollements compressibles: cas des couches limites soumises à ondes de choc. Ph.D. thesis. Université de Provence Aix-Marseille I.

Pirozzoli, S., Bernardini, M., 2011. Turbulence in supersonic boundary layers at moderate Reynolds number. J. Fluid Mech. 688, 120–168. http://dx.doi.org/10.1017/jfm.2011.368.

Pirozzoli, S., Grasso, F., 2004. Direct numerical simulations of isotropic compressible turbulence: influence of compressibility on dynamics and structures. Phys. Fluids 16, 4386–4407. http://dx.doi.org/10.1063/1.1804553.

Pirozzoli, S., Grasso, F., 2006. Direct numerical simulation of impinging shock wave/turbulent boundary layer interaction at M = 2.25. Phys. Fluids 18, 065113. http://dx.doi.org/10.1063/1.2216989.

Pirozzoli, S., Larsson, J., Nichols, J.W., Morgan, B.E., Lele, S.K., 2010. Analysis of unsteady effects in shock/boundary layer interactions. In: Proceedings of the Summer Program 2010, Center of Turbulence Research, Stanford.

Pope, S., 2000. Turbulent Flows. Cambridge University Press, Cambridge.

Priebe, S., Martín, M.P., 2012. Low-frequency unsteadiness in shock wave-turbulent boundary layer interaction. J. Fluid Mech. 699, 1–49. http://dx.doi.org/10.1017/jfm.2011.560.

Schlatter, P., Örlü, R., 2010. Assessment of direct numerical simulation data of turbulent boundary layers. J. Fluid Mech. 659, 116–126. http://dx.doi.org/10.1017/S0022112010003113.

Shahab, M.F., 2006. Numerical Investigation of the Influence of an Impinging Shock Wave And Heat Transfer on a Developing Turbulent Boundary Layer. Ph.D. thesis. École Nationale Supérieure de Mécanique et dAérotechnique.

Shahab, M.F., Lehnasch, G., Gatski, T.B., Comte, P., 2011. Statistical characteristics of an isothermal, supersonic developing boundary layer flow from DNS data. Flow Turbul. Combust. 86, 369–397. http://dx.doi.org/10.1007/s10494-011-9329-0.

Simens, M.P., Jiménez, J., Hoyas, S., Mizuno, Y., 2009. A high-resolution code for turbulent boundary layers. J. Comput. Phys. 228, 4218–4231. http://dx.doi.org/10.1016/j.jcp.2009.02.031.

Smits, A.J., Matheson, N., Joubert, P.N., 1983. Low-Reynolds-number turbulent boundary layers in zero and favorable pressure gradients. J. Ship Res. 27, 147–157.

Souverein, L.J., Debiève, J.F., 2010. Effect of air jet vortex generators on a shock wave boundary layer interaction. Exp. Fluids 49, 1053–1064. http://dx.doi.org/10.1007/s00348-010-0854-8.

Touber, E., Sandham, N.D., 2009a. Comparison of three large-eddy simulations of shock-induced turbulent separation bubbles. Shock Waves 19, 469–478. http://dx.doi.org/10.1007/s00193-009-0222-x.

Touber, E., Sandham, N.D., 2009b. Large-eddy simulation of low-frequency unsteadiness in a turbulent shock-induced separation bubble. Theor. Comput. Fluid Dyn. 23, 79–107. http://dx.doi.org/10.1007/s00162-009-0103-z.

Touber, E., Sandham, N.D., 2011. Low-order stochastic modelling of low-frequency motions in reflected shock-wave/boundary-layer interactions. J. Fluid Mech. 671, 417–465. http://dx.doi.org/10.1017/S0022112010005811.

van Driest, E.R., 1956. The problem of aerodynamic heating. Aeronaut. Eng. Rev. 15, 26–41.

Viswanath, P.R., 1988. Shock-wave-turbulent-boundary-layer interaction and its control: a survey of recent developments. Sadhana 12, 45–104. http://dx.doi.org/10.1007/BF02745660.

Wu, M., Martín, M.P., 2007. Analysis of shock motion in shockwave and turbulent boundary layer interaction using direct numerical simulation data. J. Fluid Mech. 594, 71–83. http://dx.doi.org/10.1017/S0022112007009044.

B.2. A cut-cell finite volume − finite element coupling approach for fluid-structure interaction in compressible flow

Garching bei München, Germany 85748
Attn: Vito Pasquariello

Total   0.00 EUR

Terms and Conditions

INTRODUCTION

1. The publisher for this copyrighted material is Elsevier. By clicking "accept" in connection with completing this licensing transaction, you agree that the following terms and conditions apply to this transaction (along with the Billing and Payment terms and conditions established by Copyright Clearance Center, Inc. ("CCC"), at the time that you opened your Rightslink account and that are available at any time at http://myaccount.copyright.com).

GENERAL TERMS

2. Elsevier hereby grants you permission to reproduce the aforementioned material subject to the terms and conditions indicated.

3. Acknowledgement: If any part of the material to be used (for example, figures) has appeared in our publication with credit or acknowledgement to another source, permission must also be sought from that source. If such permission is not obtained then that material may not be included in your publication/copies. Suitable acknowledgement to the source must be made, either as a footnote or in a reference list at the end of your publication, as follows:

"Reprinted from Publication title, Vol /edition number, Author(s), Title of article / title of chapter, Pages No., Copyright (Year), with permission from Elsevier [OR APPLICABLE SOCIETY COPYRIGHT OWNER]." Also Lancet special credit - "Reprinted from The Lancet, Vol. number, Author(s), Title of article, Pages No., Copyright (Year), with permission from Elsevier."

4. Reproduction of this material is confined to the purpose and/or media for which permission is hereby given.

5. Altering/Modifying Material: Not Permitted. However figures and illustrations may be altered/adapted minimally to serve your work. Any other abbreviations, additions, deletions and/or any other alterations shall be made only with prior written authorization of Elsevier Ltd. (Please contact Elsevier at permissions@elsevier.com). No modifications can be made to any Lancet figures/tables and they must be reproduced in full.

6. If the permission fee for the requested use of our material is waived in this instance, please be advised that your future requests for Elsevier materials may attract a fee.

7. Reservation of Rights: Publisher reserves all rights not specifically granted in the combination of (i) the license details provided by you and accepted in the course of this licensing transaction, (ii) these terms and conditions and (iii) CCC's Billing and Payment terms and conditions.

8. License Contingent Upon Payment: While you may exercise the rights licensed immediately upon issuance of the license at the end of the licensing process for the transaction, provided that you have disclosed complete and accurate details of your proposed use, no license is finally effective unless and until full payment is received from you (either by publisher or by CCC) as provided in CCC's Billing and Payment terms and conditions. If full payment is not received on a timely basis, then any license preliminarily granted shall be deemed automatically revoked and shall be void as if never granted. Further, in the event that you breach any of these terms and conditions or any of CCC's Billing and Payment terms and conditions, the license is automatically revoked and shall be void as if never granted. Use of materials as described in a revoked license, as well as any use of the materials beyond the scope of an unrevoked license, may constitute copyright infringement and publisher reserves the right to take any and all action to protect its copyright in the materials.

9. Warranties: Publisher makes no representations or warranties with respect to the licensed material.

10. Indemnity: You hereby indemnify and agree to hold harmless publisher and CCC, and their respective officers, directors, employees and agents, from and against any and all claims arising out of your use of the licensed material other than as specifically authorized pursuant to this license.

60

11. No Transfer of License: This license is personal to you and may not be sublicensed, assigned, or transferred by you to any other person without publisher's written permission.
12. No Amendment Except in Writing: This license may not be amended except in a writing signed by both parties (or, in the case of publisher, by CCC on publisher's behalf).
13. Objection to Contrary Terms: Publisher hereby objects to any terms contained in any purchase order, acknowledgment, check endorsement or other writing prepared by you, which terms are inconsistent with these terms and conditions or CCC's Billing and Payment terms and conditions. These terms and conditions, together with CCC's Billing and Payment terms and conditions (which are incorporated herein), comprise the entire agreement between you and publisher (and CCC) concerning this licensing transaction. In the event of any conflict between your obligations established by these terms and conditions and those established by CCC's Billing and Payment terms and conditions, these terms and conditions shall control.
14. Revocation: Elsevier or Copyright Clearance Center may deny the permissions described in this License at their sole discretion, for any reason or no reason, with a full refund payable to you. Notice of such denial will be made using the contact information provided by you. Failure to receive such notice will not alter or invalidate the denial. In no event will Elsevier or Copyright Clearance Center be responsible or liable for any costs, expenses or damage incurred by you as a result of a denial of your permission request, other than a refund of the amount(s) paid by you to Elsevier and/or Copyright Clearance Center for denied permissions.

LIMITED LICENSE

The following terms and conditions apply only to specific license types:

15. **Translation**: This permission is granted for non-exclusive world **English** rights only unless your license was granted for translation rights. If you licensed translation rights you may only translate this content into the languages you requested. A professional translator must perform all translations and reproduce the content word for word preserving the integrity of the article.

16. **Posting licensed content on any Website**: The following terms and conditions apply as follows: Licensing material from an Elsevier journal: All content posted to the web site must maintain the copyright information line on the bottom of each image; A hyper-text must be included to the Homepage of the journal from which you are licensing at http://www.sciencedirect.com/science/journal/xxxxx or the Elsevier homepage for books at http://www.elsevier.com; Central Storage: This license does not include permission for a scanned version of the material to be stored in a central repository such as that provided by Heron/XanEdu.

Licensing material from an Elsevier book: A hyper-text link must be included to the Elsevier homepage at http://www.elsevier.com . All content posted to the web site must maintain the copyright information line on the bottom of each image.

Posting licensed content on Electronic reserve: In addition to the above the following clauses are applicable: The web site must be password-protected and made available only to bona fide students registered on a relevant course. This permission is granted for 1 year only. You may obtain a new license for future website posting.

17. **For journal authors:** the following clauses are applicable in addition to the above:
Preprints:
A preprint is an author's own write-up of research results and analysis, it has not been peer-reviewed, nor has it had any other value added to it by a publisher (such as formatting, copyright, technical enhancement etc.).

Authors can share their preprints anywhere at any time. Preprints should not be added to or enhanced in any way in order to appear more like, or to substitute for, the final versions of articles however authors can update their preprints on arXiv or RePEc with their Accepted Author Manuscript (see below).

If accepted for publication, we encourage authors to link from the preprint to their formal publication via its DOI. Millions of researchers have access to the formal publications on ScienceDirect, and so links will help users to find, access, cite and use the best available version. Please note that Cell Press, The Lancet and some society-owned have different preprint policies. Information on these policies is available on the journal homepage.

Accepted Author Manuscripts: An accepted author manuscript is the manuscript of an article that has been accepted for publication and which typically includes author-incorporated changes suggested during submission, peer review and editor-author communications.

Authors can share their accepted author manuscript:

- immediately
  - via their non-commercial person homepage or blog
  - by updating a preprint in arXiv or RePEc with the accepted manuscript
  - via their research institute or institutional repository for internal institutional uses or as part of an invitation-only research collaboration work-group
  - directly by providing copies to their students or to research collaborators for their personal use
  - for private scholarly sharing as part of an invitation-only work group on commercial sites with which Elsevier has an agreement
- After the embargo period
  - via non-commercial hosting platforms such as their institutional repository
  - via commercial sites with which Elsevier has an agreement

In all cases accepted manuscripts should:

- link to the formal publication via its DOI
- bear a CC-BY-NC-ND license - this is easy to do
- if aggregated with other manuscripts, for example in a repository or other site, be shared in alignment with our hosting policy not be added to or enhanced in any way to appear more like, or to substitute for, the published journal article.

Published journal article (JPA): A published journal article (PJA) is the definitive final record of published research that appears or will appear in the journal and embodies all value-adding publishing activities including peer review co-ordination, copy-editing, formatting, (if relevant) pagination and online enrichment.

Policies for sharing publishing journal articles differ for subscription and gold open access articles:

Subscription Articles: If you are an author, please share a link to your article rather than the full-text. Millions of researchers have access to the formal publications on ScienceDirect, and so links will help your users to find, access, cite, and use the best available version.

Theses and dissertations which contain embedded PJAs as part of the formal submission can be posted publicly by the awarding institution with DOI links back to the formal publications on ScienceDirect.

If you are affiliated with a library that subscribes to ScienceDirect you have additional private sharing rights for others' research accessed under that agreement. This includes use for classroom teaching and internal training at the institution (including use in course packs and courseware programs), and inclusion of the article for grant funding purposes.

Gold Open Access Articles: May be shared according to the author-selected end-user license and should contain a CrossMark logo, the end user license, and a DOI link to the formal publication on ScienceDirect.

Please refer to Elsevier's posting policy for further information.

18. **For book authors** the following clauses are applicable in addition to the above: Authors are permitted to place a brief summary of their work online only. You are not allowed to download and post the published electronic version of your chapter, nor may you scan the printed edition to create an electronic version. **Posting to a repository:** Authors are permitted to post a summary of their chapter only in their institution's repository.

19. **Thesis/Dissertation**: If your license is for use in a thesis/dissertation your thesis may be submitted to your institution in either print or electronic form. Should your thesis be published commercially, please reapply for permission. These requirements include permission for the Library and Archives of Canada to supply single copies, on demand, of the complete thesis and include permission for Proquest/UMI to supply single copies, on demand, of the complete thesis. Should your thesis be published commercially, please

reapply for permission. Theses and dissertations which contain embedded PJAs as part of the formal submission can be posted publicly by the awarding institution with DOI links back to the formal publications on ScienceDirect.

Elsevier Open Access Terms and Conditions
You can publish open access with Elsevier in hundreds of open access journals or in nearly 2000 established subscription journals that support open access publishing. Permitted third party re-use of these open access articles is defined by the author's choice of Creative Commons user license. See our open access license policy for more information.
Terms & Conditions applicable to all Open Access articles published with Elsevier:
Any reuse of the article must not represent the author as endorsing the adaptation of the article nor should the article be modified in such a way as to damage the author's honour or reputation. If any changes have been made, such changes must be clearly indicated.
The author(s) must be appropriately credited and we ask that you include the end user license and a DOI link to the formal publication on ScienceDirect.
If any part of the material to be used (for example, figures) has appeared in our publication with credit or acknowledgement to another source it is the responsibility of the user to ensure their reuse complies with the terms and conditions determined by the rights holder.
Additional Terms & Conditions applicable to each Creative Commons user license:
CC BY: The CC-BY license allows users to copy, to create extracts, abstracts and new works from the Article, to alter and revise the Article and to make commercial use of the Article (including reuse and/or resale of the Article by commercial entities), provided the user gives appropriate credit (with a link to the formal publication through the relevant DOI), provides a link to the license, indicates if changes were made and the licensor is not represented as endorsing the use made of the work. The full details of the license are available at http://creativecommons.org/licenses/by/4.0.
CC BY NC SA: The CC BY-NC-SA license allows users to copy, to create extracts, abstracts and new works from the Article, to alter and revise the Article, provided this is not done for commercial purposes, and that the user gives appropriate credit (with a link to the formal publication through the relevant DOI), provides a link to the license, indicates if changes were made and the licensor is not represented as endorsing the use made of the work. Further, any new works must be made available on the same conditions. The full details of the license are available at http://creativecommons.org/licenses/by-nc-sa/4.0.
CC BY NC ND: The CC BY-NC-ND license allows users to copy and distribute the Article, provided this is not done for commercial purposes and further does not permit distribution of the Article if it is changed or edited in any way, and provided the user gives appropriate credit (with a link to the formal publication through the relevant DOI), provides a link to the license, and that the licensor is not represented as endorsing the use made of the work. The full details of the license are available at http://creativecommons.org/licenses/by-nc-nd/4.0.
Any commercial reuse of Open Access articles published with a CC BY NC SA or CC BY NC ND license requires permission from Elsevier and will be subject to a fee.
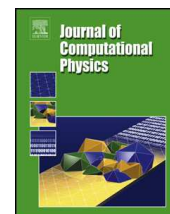Commercial reuse includes:

- Associating advertising with the full text of the Article
- Charging fees for document delivery or access
- Article aggregation
- Systematic distribution via e-mail lists or share buttons

Posting or linking by commercial companies for use by customers of those companies.

20. **Other Conditions**:

v1.9

A cut-cell finite volume – finite element coupling approach for fluid–structure interaction in compressible flow

Vito Pasquariello [a,*], Georg Hammerl [b], Felix Örley [a], Stefan Hickel [a,c], Caroline Danowski [b], Alexander Popp [b], Wolfgang A. Wall [b], Nikolaus A. Adams [a]

[a] *Institute of Aerodynamics and Fluid Mechanics, Technische Universität München, Boltzmannstr. 15, 85748 Garching bei München, Germany*
[b] *Institute for Computational Mechanics, Technische Universität München, Boltzmannstr. 15, 85748 Garching bei München, Germany*
[c] *Aerodynamics Group, Faculty of Aerospace Engineering, Technische Universiteit Delft, Kluyverweg 1, 2629 HS Delft, The Netherlands*

ARTICLE INFO

ABSTRACT

We present a loosely coupled approach for the solution of fluid–structure interaction problems between a compressible flow and a deformable structure. The method is based on staggered Dirichlet–Neumann partitioning. The interface motion in the Eulerian frame is accounted for by a conservative cut-cell Immersed Boundary method. The present approach enables sub-cell resolution by considering individual cut-elements within a single fluid cell, which guarantees an accurate representation of the time-varying solid interface. The cut-cell procedure inevitably leads to non-matching interfaces, demanding for a special treatment. A Mortar method is chosen in order to obtain a conservative and consistent load transfer. We validate our method by investigating two-dimensional test cases comprising a shock-loaded rigid cylinder and a deformable panel. Moreover, the aeroelastic instability of a thin plate structure is studied with a focus on the prediction of flutter onset. Finally, we propose a three-dimensional fluid–structure interaction test case of a flexible inflated thin shell interacting with a shock wave involving large and complex structural deformations.

1. Introduction

Compressible fluid–structure interaction (FSI) occurs in a broad range of technical applications involving, e.g., nonlinear aeroelasticity [16,42] and shock-induced deformations of rocket nozzles [23,55]. The numerical modeling and simulation of compressible FSI can be challenging, in particular if an accurate representation of the structural interface within the fluid solver and a consistent coupling of both subdomains is required.

FSI algorithms are generally classified as monolithic or partitioned. One main advantage often attributed to monolithic approaches is their numerical robustness due to solving a single system which includes the full information of the coupled nonlinear FSI problem. On the other hand, partitioned algorithms for FSI are often used because they facilitate the coupling of different specialized single-field solvers. A further distinction can be made between loosely and strongly coupled algorithms, depending on whether the coupling conditions are satisfied exactly at each time step, or not. While partitioned algorithms can be made strong by introducing equilibrium iterations [34], loosely coupled approaches are more frequently used in the field of aeroelasticity and compressible flows in general [6,16]. A disadvantage of loosely coupled partitioned algorithms is the artificial added mass effect [5,21], which may lead to numerical instability in incompressible flows and for

high fluid–solid density ratios. Recently, so-called Added-Mass Partitioned algorithms have been developed for compressible fluids interacting with rigid and elastic solids [1,3] as well as for incompressible fluids [2]. These methods allow to overcome the added mass instability by formulating appropriate fluid–structure interface conditions.

FSI problems involve a load and motion transfer at the conjoined interface. In the simple case of matching fluid and solid discretization, this results in a trivial task. However, different resolution requirements within the fluid and solid fields lead to non-matching discrete interfaces. An overview of existing coupling methods for non-matching meshes can be found in [9]. Simple methods such as nearest-neighbor interpolation and projection methods are frequently used [17,31]. The mentioned methods do not conserve angular momentum across the interface. Consistency can be achieved with more sophisticated approaches, such as weighted residual methods, which introduce Lagrange multipliers as additional interface variables. In this context, Mortar methods have first been proposed for non-overlapping domain decomposition in [4], enhanced with dual shape functions for the Lagrange multipliers in [53] and applied to FSI problems and mesh tying in fluid flow, e.g. in [13,33]. While Mortar methods introduce Lagrange multipliers only on one side of the interface, Localized Lagrange Multipliers consider them on both sides of the interface [47].

Another classification of FSI methods is based on the representation of the time-varying solid interface within the fluid domain. Two main approaches can be distinguished in this context, which are Arbitrary Lagrangian Eulerian (ALE) methods [10,18], and Immersed Boundary Methods (IBM) [38,41]. ALE approaches employ body-fitted grids, hence requiring a mesh evolution algorithm. This task may be complex in case of large solid displacements. On the other hand, IBM often operate on fixed Cartesian fluid grids, making this type of approach very appealing for the simulation of flows past complex geometries and for the solution of FSI problems with large deformations. IBM, such as continuous forcing and ghost-cell approaches, may suffer from spurious loss or production of mass, momentum and energy at the interface [38]. Such non-conservativity poses a particular problem for large-eddy simulations, which employ coarse grids and rely on an accurate flow prediction in near-wall regions over large time scales. Moreover, the accurate capturing of shocks is based on conservation properties. Conservativity is recovered with Cartesian cut-cell methods, which were first introduced by Clarke et al. [7] and Gaffney and Hassan [22] for inviscid flows and later extended to viscous flows by Udaykumar et al. [52] and Ye et al. [54]. In this method, the finite volume cells at the boundaries are reshaped to fit locally the boundary surface with a sharp interface, which in turn assures strict conservation of mass, momentum and energy. A drawback of cut-cell methods is that the fluid volume fraction of cut-cells may become very small and therefore can lead to numerical instability with explicit time integration schemes. A stabilization of the underlying time integration scheme can be achieved by so-called cell-merging [54], cell-linking [32] or flux redistribution techniques [8,30].

In this paper we develop a loosely coupled approach for the solution of FSI problems between a compressible fluid and a deformable structure. We employ the Finite Volume Method (FVM) for solving the Euler equations on Cartesian grids and the Finite Element Method (FEM) for solving the structural problem. The interface motion is accounted for by a conservative cut-cell IBM. Previous proposed methods reconstruct the interface geometry based on a level-set function [26, 27,36]. Örley et al. [40] developed a conservative cut-element method that allows for representing the fluid–solid interface with sub-cell resolution for rigid body motion. We extend this method to arbitrary interface deformations. The combination of a cut-element IBM with a Mortar method for coupling of the solid and fluid subdomains in a consistent and efficient way is the essential new contribution of this paper.

This paper is structured as follows: First, the governing equations for fluid and solid and the fluid–structure interface conditions are introduced in Section 2. Section 3 gives a detailed overview on the numerical treatment of moving boundaries together with the discretization methods used for the fluid. The FEM used to solve the structural problem is presented in Section 4. In Section 5, the staggered coupling algorithm is presented together with the new coupling approach for non-matching interfaces. In Section 6, the method is validated with well-established two-dimensional test cases and a convergence study is presented. In Section 7, we propose a new test case for the interaction between a flexible inflated thin shell and a shock wave, demonstrating in particular the capability of our FSI approach to handle large three-dimensional deformations. Concluding remarks are given in Section 8.

2. Mathematical and physical model

As depicted in Fig. 1, the computational domain is divided into a fluid and solid domain, Ω_F and Ω_S, respectively. The conjoined interface is denoted as $\Gamma = \Omega_F \cap \Omega_S$ and its normal vector $\boldsymbol{n}^\Gamma$ in spatial configuration points from the solid into the fluid domain.

2.1. Governing equations for the fluid

We consider the three-dimensional, fully compressible Euler equations in conservative form

$$\frac{\partial \boldsymbol{w}}{\partial t} + \nabla \cdot \boldsymbol{K}(\boldsymbol{w}) = 0 \text{ in } \Omega_F. \tag{1}$$

The state vector $\boldsymbol{w} = [\rho_F, \rho_F u_1, \rho_F u_2, \rho_F u_3, E_t]$ contains the conserved variables density ρ_F, momentum $\rho_F \boldsymbol{u}$ and total energy E_t. The subscript F denotes fluid quantities and is used whenever a distinction between both subdomains is necessary. The individual contributions of the flux tensor $\boldsymbol{K} = (\boldsymbol{f}, \boldsymbol{g}, \boldsymbol{h})$ are given as
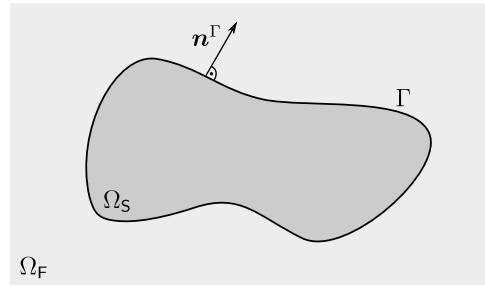
Fig. 1. Schematic of FSI domain.

$$\boldsymbol{f}(\boldsymbol{w}) = \begin{pmatrix} \rho_F u_1 \\ \rho_F u_1{}^2 + p \\ \rho_F u_1 u_2 \\ \rho_F u_1 u_3 \\ u_1(E_t + p) \end{pmatrix}, \; \boldsymbol{g}(\boldsymbol{w}) = \begin{pmatrix} \rho_F u_2 \\ \rho_F u_2 u_1 \\ \rho_F u_2{}^2 + p \\ \rho_F u_2 u_3 \\ u_2(E_t + p) \end{pmatrix}, \; \boldsymbol{h}(\boldsymbol{w}) = \begin{pmatrix} \rho_F u_3 \\ \rho_F u_3 u_1 \\ \rho_F u_3 u_2 \\ \rho_F u_3{}^2 + p \\ u_3(E_t + p) \end{pmatrix}, \tag{2}$$

where p is the static pressure. We consider a perfect gas with a specific heat ratio of $\gamma = 1.4$ and specific gas constant of $R = 287.058 \frac{J}{kg \cdot K}$. The total energy is given by

$$E_t = \frac{1}{\gamma - 1} p + \frac{1}{2} \rho_F u_i u_i, \tag{3}$$

assuming an ideal gas equation of state $p = \rho_F R T$, where T is the static temperature. If not stated otherwise, we use the Einstein summation convention.

2.2. Governing equations for the solid

The structural field is governed by the local form of the balance of linear momentum

$$\rho_{S;0} \ddot{\boldsymbol{d}} = \nabla_0 \cdot (\boldsymbol{F} \cdot \boldsymbol{S}) + \hat{\boldsymbol{b}}_0 \text{ in } \Omega_S, \tag{4}$$

describing equilibrium of the forces of inertia, internal and external forces in the undeformed structural domain Ω_S. Herein $\nabla_0 \cdot (\bullet)$ is the material divergence operator and the index S represents the domain of the structural problem. The structural material density is denoted by $\rho_{S;0}$. Furthermore, $\boldsymbol{d}$ and $\ddot{\boldsymbol{d}}$ are the unknown displacements and accelerations, respectively. The vector field $\hat{\boldsymbol{b}}_0$ is the given material body force. The internal forces are expressed in terms of the second Piola–Kirchhoff stress tensor $\boldsymbol{S}$ and the deformation gradient $\boldsymbol{F}$.

To determine the stresses, various constitutive laws can be used. For the sake of simplicity, in this work a hyperelastic Saint Venant–Kirchhoff material model with strain energy density function Ψ per unit reference volume is chosen as

$$\Psi(\boldsymbol{E}) = \mu_S \boldsymbol{E} : \boldsymbol{E} + \frac{1}{2} \lambda_S (\boldsymbol{E} : \boldsymbol{I})^2, \tag{5}$$

with the Lamé constants λ_S and μ_S and the second-order identity tensor $\boldsymbol{I}$. The Green–Lagrange strain tensor is defined as

$$\boldsymbol{E} = \frac{1}{2}(\boldsymbol{F}^\top \cdot \boldsymbol{F} - \boldsymbol{I}). \tag{6}$$

The second Piola–Kirchhoff stress

$$\boldsymbol{S} = \frac{\partial \Psi}{\partial \boldsymbol{E}} \tag{7}$$

is derived using (5). Alternatively, the first Piola–Kirchhoff stress tensor

$$\boldsymbol{P} = \boldsymbol{F} \cdot \boldsymbol{S} \tag{8}$$

may be used.

The boundary of the structural field $\partial \Omega_S$ is divided into pairwise disjoint boundary segments

$$\partial \Omega_S = \Gamma_{S;D} \cup \Gamma_{S;N} \cup \Gamma. \tag{9}$$

On the Dirichlet boundary $\Gamma_{S;D}$, the displacements are prescribed, whereas on the Neumann boundary $\Gamma_{S;N}$, the traction vector $\hat{\boldsymbol{t}}_0$ is prescribed using the unit normal vector $\boldsymbol{n}_0$ in material configuration. Thus, the boundary conditions

$$\boldsymbol{d} = \hat{\boldsymbol{d}} \quad \text{on } \Gamma_{S;D}, \tag{10}$$

$$\boldsymbol{P} \cdot \boldsymbol{n}_0 = \hat{\boldsymbol{t}}_0 \quad \text{on } \Gamma_{S;N} \tag{11}$$
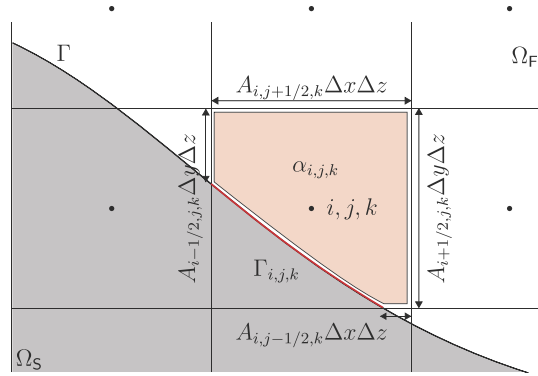
need to be satisfied.

Fig. 2. Two-dimensional sketch of a cut-cell (i, j, k) [40].

For the balance equation (4) initial conditions for displacements $\boldsymbol{d}$ and velocities $\dot{\boldsymbol{d}}$ need to be specified at time $t = 0$,

$$\boldsymbol{d}_0 = \boldsymbol{d}(\boldsymbol{X}, t = 0) = \hat{\boldsymbol{d}}_0 \quad \text{on } \Omega_S, \tag{12}$$

$$\dot{\boldsymbol{d}}_0 = \dot{\boldsymbol{d}}(\boldsymbol{X}, t = 0) = \hat{\dot{\boldsymbol{d}}}_0 \quad \text{on } \Omega_S, \tag{13}$$

where $\boldsymbol{X}$ defines the initial position.

2.3. Fluid–structure interface conditions

Dynamic and kinematic coupling conditions at the conjoined interface Γ ensure the integrity between the subdomains in this partitioned coupling algorithm. Assuming no mass transport across the interface, normal velocities have to match, i.e.

$$\boldsymbol{u}^{\Gamma} \cdot \boldsymbol{n}^{\Gamma} = \frac{\partial \boldsymbol{d}^{\Gamma}}{\partial t} \cdot \boldsymbol{n}^{\Gamma} \quad \text{on } \Gamma, \tag{14}$$

where $\boldsymbol{n}^{\Gamma}$ denotes the interface unit normal vector. The dynamic condition requires the tractions to be equal,

$$\boldsymbol{\sigma}_F^{\Gamma} \cdot \boldsymbol{n}^{\Gamma} = \boldsymbol{\sigma}_S^{\Gamma} \cdot \boldsymbol{n}^{\Gamma} \quad \text{on } \Gamma, \tag{15}$$

where $\boldsymbol{\sigma}_F = -p\boldsymbol{I}$ denotes the fluid stress tensor comprising only contributions due to the pressure in the inviscid case considered here. The Cauchy stress tensor $\boldsymbol{\sigma}_S$ is defined as

$$\boldsymbol{\sigma}_S = \frac{1}{J} \boldsymbol{P} \cdot \boldsymbol{F}^{\mathsf{T}} \tag{16}$$

in which J is the Jacobian.

3. Numerical approach: fluid

We employ the FVM for solving the Euler equations on Cartesian grids. The time-dependent fluid–solid interface conditions on Γ are imposed by a cut-element based IBM.

3.1. Mathematical model

A sketch of a two-dimensional cut-cell is shown in Fig. 2. In the following, Γ denotes the fluid–structure interface of the continuous problem, and $\Gamma_{F/S}$ the flow and structure side of the interface of the discrete problem. We solve the integral form of (1),

$$\int_{t^n}^{t^{n+1}} \int_{\Omega_{i,j,k} \cap \Omega_F} \left(\frac{\partial \boldsymbol{w}}{\partial t} + \nabla \cdot \boldsymbol{K}(\boldsymbol{w}) \right) \mathrm{d}x \mathrm{d}y \mathrm{d}z \, \mathrm{d}t = 0, \tag{17}$$

where the integral is taken over the volume $\Omega_{i,j,k} \cap \Omega_F$ of a computational cell (i, j, k) and time step $\Delta t = t^{n+1} - t^n$. Applying the Gauss theorem results in

$$\int_{t^n}^{t^{n+1}} \int_{\Omega_{i,j,k} \cap \Omega_F} \frac{\partial \boldsymbol{w}}{\partial t} \, \mathrm{d}V \, \mathrm{d}t + \int_{t^n}^{t^{n+1}} \int_{\partial(\Omega_{i,j,k} \cap \Omega_F)} \boldsymbol{K}(\boldsymbol{w}) \cdot \boldsymbol{n} \, \mathrm{d}S \, \mathrm{d}t = 0, \tag{18}$$
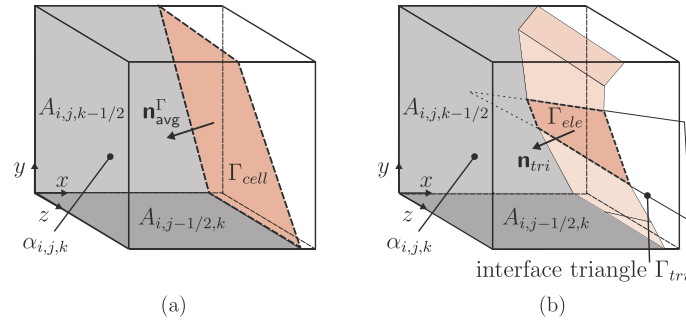
Fig. 3. Computation of cut-cell properties based on a level-set field Φ (a) and on intersection with a provided surface triangulation (b). For a detailed description of the cut algorithm please refer to [40].

where $\partial(\Omega_{i,j,k} \cap \Omega_F)$ denotes the wetted surface of a computational cell (i, j, k), and dV, dS the infinitesimal volume and surface element, respectively. Applying a volume average of the conserved variables

$$\mathbf{w}_{i,j,k} = \frac{1}{\alpha_{i,j,k} V_{i,j,k}} \int\limits_{\Omega_{i,j,k} \cap \Omega_F} \mathbf{w}\, dx dy dz, \tag{19}$$

leads to

$$\begin{aligned}
\alpha_{i,j,k}^{n+1} & \mathbf{w}_{i,j,k}^{n+1} \\
&= \alpha_{i,j,k}^n \mathbf{w}_{i,j,k}^n \\
&+ \frac{\Delta t}{\Delta x_i} \left[A_{i-1/2,j,k}^n \mathbf{f}_{i-1/2,j,k} - A_{i+1/2,j,k}^n \mathbf{f}_{i+1/2,j,k} \right] \\
&+ \frac{\Delta t}{\Delta y_j} \left[A_{i,j-1/2,k}^n \mathbf{g}_{i,j-1/2,k} - A_{i,j+1/2,k}^n \mathbf{g}_{i,j+1/2,k} \right] \\
&+ \frac{\Delta t}{\Delta z_k} \left[A_{i,j,k-1/2}^n \mathbf{h}_{i,j,k-1/2} - A_{i,j,k+1/2}^n \mathbf{h}_{i,j,k+1/2} \right] \\
&+ \frac{\Delta t}{V_{i,j,k}} \boldsymbol{\chi}_{i,j,k}.
\end{aligned} \tag{20}$$

$V_{i,j,k} = \Delta x_i \Delta y_j \Delta z_k$ corresponds to the total volume of cell $\Omega_{i,j,k}$, $\alpha_{i,j,k}$ corresponds to the fluid volume fraction, $\mathbf{w}_{i,j,k}$ is the vector of volume-averaged conserved quantities in the cut-cell, and A is the effective fluid wetted cell face aperture. The face averaged numerical fluxes across the cell faces are denoted as $\mathbf{f}$, $\mathbf{g}$ and $\mathbf{h}$. The flux $\boldsymbol{\chi}_{i,j,k}$ across the interface $\Gamma_{i,j,k} = \Gamma \cap \Omega_{i,j,k}$ is discussed in detail below.

Time integration of the state vector is shown here for a forward Euler time integration scheme with a time step Δt, which corresponds to one sub-step of an explicit Runge–Kutta method. Appropriate initial and boundary conditions are prescribed on the domain Ω_F and the surface $\partial\Omega_F$. For all simulations presented in this paper we employ a spatial flux discretization on local characteristics by an 5th-order WENO scheme [35] together with a Lax–Friedrichs flux function. A 3rd-order strongly stable Runge–Kutta scheme [25] is used for time integration.

3.2. Conservative immersed boundary method

3.2.1. Geometry computation

Moving boundaries with sharp corners and complex geometries may cause numerical artifacts in terms of spurious pressure oscillations. Following Örley et al. [40], these artifacts are mainly caused by a discontinuous evolution of fluid volume fractions when utilizing a level-set based representation of the interface. A solution to overcome these problems is to use an accurate representation of the geometry based on the computational fluid mesh and the provided structural interface. While the level-set method results in a planar approximation of the interface segment Γ_{cell} in a cell, see Fig. 3(a), the cut-element method recovers sub-cell interface resolution by a set of cut-elements Γ_{ele} in a single fluid cell, see Fig. 3(b). The computation of the fluid volume fraction $\alpha_{i,j,k}$ is done by a sub-tetrahedralization of the fluid volume, while face apertures such as $A_{i,j-1/2,k}$ are calculated using a sub-triangulation of the cell faces [40].

A linear approximation of the possibly nonlinear structural interface is used for the cut algorithm as an input. The element surface $\Gamma_S^{(e)}$ of an eight-node linear brick element, which contributes to the fluid–structure interface, is highlighted in gray, see Fig. 4. This surface is split into four interface triangles Γ_{tri} using an additional node at $\mathbf{x}|_{\xi=\eta=0}$ for improved approximation of its bilinear shape.
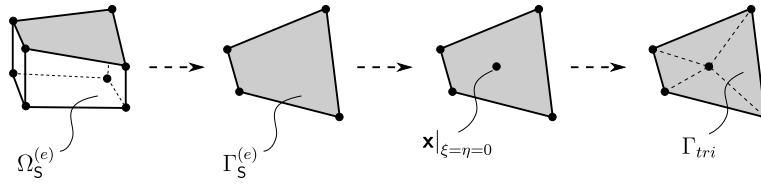
Fig. 4. Triangulation of an eight-node hexahedral element face (gray) contributing to the fluid–structure interface Γ.

3.2.2. Interface exchange term

Interaction of the fluid with a solid interface is modeled by an interface exchange term $\chi_{i,j,k}$, as introduced in Eq. (20). Following the approach introduced above, we can write the interface exchange term as a sum of all individual contributions of all cut-elements contained within this computational cell,

$$\chi_{i,j,k} = \sum_{ele} \chi_{ele}. \tag{21}$$

For inviscid flows, the cut-element based interface exchange term χ_{ele} accounts for the pressure and pressure work at the element interface

$$\chi_{ele} = \begin{bmatrix} 0 \\ p_{ele}^{\Gamma} \Delta\Gamma_{ele}\, n_1^{\Gamma;ele} \\ p_{ele}^{\Gamma} \Delta\Gamma_{ele}\, n_2^{\Gamma;ele} \\ p_{ele}^{\Gamma} \Delta\Gamma_{ele}\, n_3^{\Gamma;ele} \\ p_{ele}^{\Gamma} \Delta\Gamma_{ele} \left(\mathbf{n}^{\Gamma;ele} \cdot \mathbf{u}^{\Gamma;ele} \right) \end{bmatrix}, \tag{22}$$

where $\Delta\Gamma_{ele}$ is the element interface area, $\mathbf{n}^{\Gamma;ele} = [n_1^{\Gamma;ele}, n_2^{\Gamma;ele}, n_3^{\Gamma;ele}]$ is the element unit normal vector obtained directly from the structural interface triangle Γ_{tri}, and $\mathbf{u}^{\Gamma;ele}$ is the interface velocity evaluated at the cut-element face centroid. The element interface pressure p_{ele}^{Γ} is obtained by solving a symmetric face-normal Riemann problem

$$\mathcal{R}\left(\mathbf{w}_{i,j,k}, \mathbf{u}^{\Gamma;ele} \right) = 0 \tag{23}$$

for each cut-element within the cut-cell (i, j, k). The exact solution of the reflective boundary Riemann problem (23) consists of either two shock waves ($\mathbf{u}_{i,j,k} \cdot \mathbf{n}^{\Gamma;ele} < \mathbf{u}^{\Gamma;ele} \cdot \mathbf{n}^{\Gamma;ele}$) or two rarefaction waves ($\mathbf{u}_{i,j,k} \cdot \mathbf{n}^{\Gamma;ele} \geq \mathbf{u}^{\Gamma;ele} \cdot \mathbf{n}^{\Gamma;ele}$), which are symmetric about the path of the moving interface coinciding with the contact wave [51]. The exact solution for the interface pressure p_{ele}^{Γ} is the root of

$$\left(p_{ele}^{\Gamma} - p_{i,j,k} \right) \cdot \sqrt{ \frac{\frac{2}{(\gamma+1)\rho_{i,j,k}}}{p_{ele}^{\Gamma} + \frac{\gamma-1}{\gamma+1} p_{i,j,k}} } + \left(\mathbf{u}_{i,j,k} \cdot \mathbf{n}^{\Gamma;ele} - \mathbf{u}^{\Gamma;ele} \cdot \mathbf{n}^{\Gamma;ele} \right) = 0 \tag{24}$$

for the two-shocks configuration, and

$$p_{ele}^{\Gamma} = p_{i,j,k} \cdot \left[1 + \left(\mathbf{u}^{\Gamma;ele} \cdot \mathbf{n}^{\Gamma;ele} - \mathbf{u}_{i,j,k} \cdot \mathbf{n}^{\Gamma;ele} \right) \cdot \frac{\gamma-1}{2\sqrt{\gamma p_{i,j,k}/\rho_{i,j,k}}} \right]^{\frac{2\gamma}{\gamma-1}} \tag{25}$$

for the two-rarefactions configuration.

3.2.3. Boundary conditions for solid walls

Non-cut cells in the solid part of the computational domain in the vicinity of the interface contain ghost fluid states for imposing boundary conditions at the interface without requiring a modification of interpolation stencils in the finite volume reconstruction scheme. For this purpose, we apply the ghost-cell methodology as proposed by Mittal et al. [37], extended to stationary and moving boundary cut-cell methods. Finding the ghost-cells and extending the fluid solution across the interface does not require the fully detailed cut-cell geometry. We perform this procedure based on the average face centroid and normal vector of the cut-cell, which is an average of all contained cut-elements weighted by their area. In a first step, ghost-cells $\mathbf{x}_{GP}$ that contribute to the interpolation stencil of the baseline discretization are identified, see Fig. 5. Next, for each ghost-cell the boundary intercept point $\mathbf{x}_{BI}$ is computed such that the line segment $\overline{\mathbf{x}_{GP}\mathbf{x}_{BI}}$ intersects the immersed boundary in $\mathbf{x}_{BI}$ normal to the interface segment. The line segment is extended into the fluid region to find the image point

$$\mathbf{x}_{IP} = \mathbf{x}_{BI} + \mathbf{n}_{avg}^{\Gamma} \cdot \Delta l, \tag{26}$$
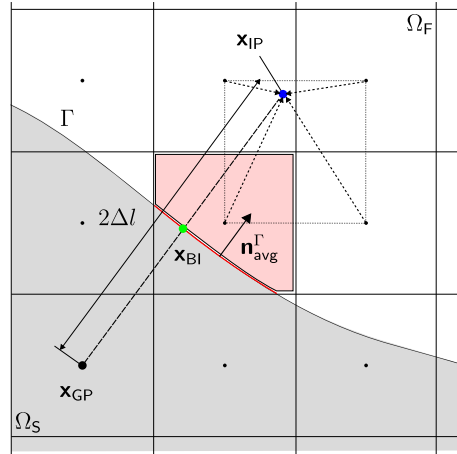
69

Fig. 5. Construction of the ghost-cell extending procedure for a cut-cell (i, j, k).

where $\Delta l = \|\mathbf{x}_{\mathrm{BI}} - \mathbf{x}_{\mathrm{GP}}\|$ denotes the distance between the ghost-cell and the boundary intercept. Once the image point has been identified, a bilinear (in 2-D) or trilinear (in 3-D) interpolation is used for calculating the value of a quantity φ_{IP} at the image point $\mathbf{x}_{\mathrm{IP}}$:

$$3\mathrm{D}: \quad \varphi(x^\star, y^\star, z^\star) = c_1 + c_2 x^\star + c_3 y^\star + c_4 z^\star + c_5 x^\star y^\star + c_6 x^\star z^\star + c_7 y^\star z^\star + c_8 x^\star y^\star z^\star$$

$$2\mathrm{D}: \quad \quad \varphi(x^\star, y^\star) = c_1 + c_2 x^\star + c_3 y^\star + c_4 x^\star y^\star, \tag{27}$$

where $\pmb{x}^\star = \pmb{x} - \mathbf{x}_{\mathrm{IP}}$ is the relative distance vector and $\pmb{c} = \{c_i\}$ are the unknown coefficients. As shown in Fig. 5, the four (eight in 3-D) coefficients can be determined from the variable values of the four (eight in 3-D) surrounding neighboring points,

$$\pmb{c} = \pmb{V}^{-1} \pmb{\varphi}, \tag{28}$$

where $\pmb{\varphi}$ denotes the solution at regular fluid data points and $\pmb{V}^{-1}$ the inverse Vandermonde matrix, which is calculated by LU decomposition. After solving for (28), the value at the image point is given by

$$\varphi_{\mathrm{IP}} = c_1 + \mathcal{O}(\Delta^2). \tag{29}$$

Ghost-cell values are obtained using a linear approximation along the line $\overline{\mathbf{x}_{\mathrm{GP}}\mathbf{x}_{\mathrm{BI}}}$ that satisfies the boundary conditions at the boundary intercept location $\mathbf{x}_{\mathrm{BI}}$. For Dirichlet boundary conditions, ghost-cell data are obtained as

$$\varphi_{\mathrm{GP}} = 2 \cdot \varphi_{\mathrm{BI}} - \varphi_{\mathrm{IP}} + \mathcal{O}(\Delta l^2), \tag{30}$$

whereas Neumann boundary conditions are imposed as

$$\varphi_{\mathrm{GP}} = \varphi_{\mathrm{IP}} - 2 \cdot \Delta l \left(\nabla \varphi \cdot \mathbf{n}_{\mathrm{avg}}^\Gamma \right) \big|_{\mathbf{x}_{\mathrm{BI}}} + \mathcal{O}(\Delta l^2). \tag{31}$$

The 5th-order WENO scheme used in this paper requires at least three layers of ghost-cells to be filled. This, in turn, poses a limitation of the current framework to structures with a size larger than several fluid cells in order to fill the ghost-cell values properly. An adaptive mesh refinement procedure for the flow solver or the decoupling of the ghost-cell method from the underlying Cartesian grid could resolve this limitation.

3.2.4. Treatment of small cut-cells

The time step Δt is adjusted dynamically according to the CFL condition based on full cells of the underlying Cartesian grid. A drawback of cut-cell methods is that the fluid volume fraction of cut-cells may become very small and therefore can lead to numerical instability or require excessively small time steps with explicit time integration schemes and poor convergence with implicit methods. A stabilization of the underlying scheme is therefore required. We employ a so-called mixing procedure as proposed in [30,40].

4. Numerical approach: solid

The FEM is applied to solve the structural problem. Hence, we start with the weak form of the structural field equation, which is obtained by building weighted residuals of the balance equation (4) and Neumann boundary conditions (11) with virtual displacements $\delta \pmb{d}$. Subsequently, the divergence theorem is applied, yielding

$$\int_{\Omega_{\mathrm{S}}} \rho_{\mathrm{S};0} \ddot{\pmb{d}} \cdot \delta \pmb{d} \, \mathrm{d}V_0 + \int_{\Omega_{\mathrm{S}}} \pmb{S} : \delta \pmb{E} \, \mathrm{d}V_0 - \int_{\Omega_{\mathrm{S}}} \hat{\pmb{b}}_0 \cdot \delta \pmb{d} \, \mathrm{d}V_0 - \int_{\Gamma_{\mathrm{N};\mathrm{S}}} \hat{\pmb{t}}_0 \cdot \delta \pmb{d} \, \mathrm{d}A_0 - \delta \mathcal{W}_{\mathrm{S}}^\Gamma = \pmb{0} \tag{32}$$

with infinitesimal volume and surface elements, dV_0 and dA_0, respectively. Herein, $\delta \boldsymbol{E}$ is obtained as result of the variation of the Green–Lagrange strain (6), i.e.

$$\delta \boldsymbol{E} = \frac{1}{2} \left((\nabla_0 \, \delta \boldsymbol{d})^\mathsf{T} \cdot \boldsymbol{F} + \boldsymbol{F}^\mathsf{T} \cdot \nabla_0 \, \delta \boldsymbol{d} \right) \tag{33}$$

with $\nabla_0 \, (\bullet)$ representing the material gradient operator. The influence of the interface on the structure is introduced via the additional virtual work term $\delta \mathcal{W}_S^\Gamma$.

The weak form of equation (32) is discretized in space with the FEM. The solid domain Ω_S is split into n^e elements $\Omega_S^{(e)}$ (subdomains). The semi-discrete weak form of the balance of linear momentum is obtained by assembling the contributions of all elements, leading to

$$\mathbf{M} \ddot{\mathbf{d}} + \mathbf{f}_{S;int}(\mathbf{d}) - \mathbf{f}_{S;ext}(\mathbf{d}) - \mathbf{f}_S^\Gamma = \mathbf{0}, \tag{34}$$

where we have assumed the discrete virtual displacement vector $\delta \mathbf{d}$ to be arbitrary. The vectors $\ddot{\mathbf{d}}$ and $\mathbf{d}$ describe the discrete acceleration and displacement vectors, respectively, $\mathbf{M}$ denotes the mass matrix, $\mathbf{f}_{S;int}$ and $\mathbf{f}_{S;ext}$ the internal and external force vectors. The interface traction of the fluid on the structure is described by $\mathbf{f}_S^\Gamma$. Element technology such as the method of enhanced assumed strains (EAS), as introduced in [49], is used in order to avoid locking phenomena. For time integration, the generalized trapezoidal rule (or one-step-θ scheme) is employed for the structure solver in this work. Thus, applying this scheme to the semi-discrete equation (34), the final fully discrete structural equation at the new time step $n + 1$ is obtained.

The fully discrete structural equation describes a system of nonlinear algebraic equations which is solved iteratively by a Newton–Raphson method. The linearized system reads

$$\mathbf{K}_{SS}(\mathbf{d}_i^{n+1}) \, \Delta \mathbf{d}_{i+1}^{n+1} = -\mathbf{r}_S(\mathbf{d}_i^{n+1}) \tag{35}$$

with iteration step i, the dynamic effective structural stiffness matrix $\mathbf{K}_{SS}$, and the residual vector $\mathbf{r}_S$. Thus, a new solution of the displacement increment $\Delta \mathbf{d}_{i+1}^{n+1}$ for current iteration step $i + 1$ is determined, and the final displacement solution of time step $n + 1$ is obtained via updating

$$\mathbf{d}_{i+1}^{n+1} = \mathbf{d}_i^{n+1} + \Delta \mathbf{d}_{i+1}^{n+1} . \tag{36}$$

The Newton–Raphson iteration is considered as converged if $|\mathbf{r}_S|_2 \le \epsilon$ is satisfied using a sufficiently small tolerance ϵ.

5. Coupling procedure

5.1. Treatment of non-matching interfaces

The reconstruction of the interface on the fluid side based on the structural position leads to a change in the number of cut-elements in each coupling step and to a change in connectivity, which inevitably results in a non-matching interface. A Mortar method has been chosen in this work as it preserves linear and angular momentum. The Mortar method requires the choice of a so-called slave and master side of the interface Γ^{sl} and Γ^{ma}, respectively. Primary coupling variables, such as velocities in our case, are transferred from the master to the slave side, and secondary variables, such as tractions, are transferred vice versa. The Dirichlet–Neumann partitioning chosen here determines the fluid to be the slave side ($\Gamma^{sl} \equiv \Gamma_F$) and the solid to be the master side ($\Gamma^{ma} \equiv \Gamma_S$) with respect to Mortar coupling. The aim is to obtain discrete projection operators for consistent data transferring.

In the following derivation, a no-slip condition between fluid and solid is assumed instead of the slip condition in (14) for simplicity, which will later be released again. The starting point is the weak form of the continuity constraint

$$\delta W_\lambda = \int_{\Gamma^{sl}} \delta \boldsymbol{\lambda}^\mathsf{T} \left(\boldsymbol{u}^\Gamma - \dot{\boldsymbol{d}}^\Gamma \right) d\Gamma = 0 \tag{37}$$

together with weak form of the equilibrium of tractions at the interface

$$\delta W_\Gamma = \int_{\Gamma^{sl}} \boldsymbol{\lambda}^\mathsf{T} \left(\delta \boldsymbol{u}^\Gamma - \delta \dot{\boldsymbol{d}}^\Gamma \right) d\Gamma \tag{38}$$

in which a Lagrange multiplier field $\boldsymbol{\lambda} = \boldsymbol{\sigma}_F^\Gamma \cdot \boldsymbol{n}^\Gamma$ and the corresponding test functions $\delta \boldsymbol{\lambda}$ are introduced. The virtual work term (38) is the conjugate term of (37) and it contains virtual work contributions of interface tractions on the fluid side and on the solid side, $\delta \mathcal{W}_F^\Gamma$ and $\delta \mathcal{W}_S^\Gamma$, respectively. Additionally, $\delta \mathcal{W}_S^\Gamma$ needs to be adapted to the chosen time integration scheme for the solid due to the occurrence of the time derivative of the displacements.

An important question is which ansatz functions should be used for a proper interpolation of the respective fields at the interface. Due to the applied cut procedure in the underlying finite volume discretization it is not possible to obtain the surface ansatz functions for the cut-elements based on a trace space relationship. Without invoking high-order reconstruction,
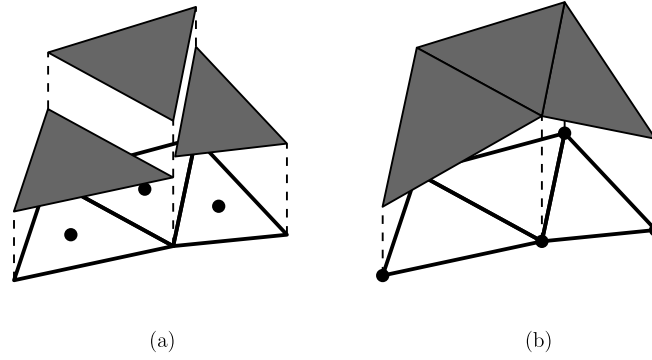
71

(a) (b)

Fig. 6. Interpolation of state variables. (a) FVM: constant value per cell, (b) FEM: linear Lagrange polynomials.

the FVM defines for the state values in the cut-cells a piecewise constant field as it is depicted in Fig. 6(a). For the solid, it is possible to obtain the ansatz functions from the trace space of the underlying volume element leading to an interpolation with standard Lagrange polynomials as it is shown in Fig. 6(b). Hence, a Lagrange multiplier

$$\boldsymbol{\lambda} = \sum_{j=1}^{n^{\mathrm{sl}}} \Phi_j \lambda_j \tag{39}$$

using constant ansatz functions Φ_j on each cut-element can be utilized, which is defined only on the slave side of the interface. The discrete Lagrange multipliers are denoted as λ_j. Due to the constant value in a single cut-element also the velocities can be represented using constant ansatz functions N_k^{sl}. This approach then reads

$$\mathbf{u} = \sum_{k=1}^{n^{\mathrm{sl}}} N_k^{\mathrm{sl}} \mathbf{u}_k. \tag{40}$$

In (39) and (40), the total number of cut-elements is denoted with n^{sl}, which is equal to the number of discrete fluid velocities $\mathbf{u}_k$ due to the piecewise constant field on each cut-element. In contrast, standard shape functions N_l^{ma} based on Lagrange polynomials are used for the interpolation of the velocities on the solid side of the interface. This leads to

$$\dot{\mathbf{d}} = \sum_{l=1}^{n^{\mathrm{ma}}} N_l^{\mathrm{ma}} \dot{\mathbf{d}}_l \tag{41}$$

where the total number of discrete solid velocities $\dot{\mathbf{d}}_l$ is denoted as n^{ma}, which is equal to the number of nodes in the solid interface. Inserting (39)–(41) into (37) leads to

$$\delta W_\lambda = \sum_{j=1}^{n^{\mathrm{sl}}} \sum_{k=1}^{n^{\mathrm{sl}}} \delta \boldsymbol{\lambda}_j^T \left(\int_{\Gamma^{\mathrm{sl}}} \Phi_j N_k^{\mathrm{sl}} \, \mathrm{d}\Gamma \right) \mathbf{u}_k - \sum_{j=1}^{n^{\mathrm{sl}}} \sum_{l=1}^{n^{\mathrm{ma}}} \delta \boldsymbol{\lambda}_j^T \left(\int_{\Gamma^{\mathrm{sl}}} \Phi_j N_l^{\mathrm{ma}} \, \mathrm{d}\Gamma \right) \dot{\mathbf{d}}_l = 0. \tag{42}$$

Therein, nodal blocks of the two Mortar integral matrices commonly denoted as $\mathbf{D}$ and $\mathbf{M}$ can be identified. This leads to the following definitions:

$$\mathbf{D}[j,k] = D_{jk} \mathbf{I}_3 = \int_{\Gamma^{sl}} \Phi_j N_k^{\mathrm{sl}} \, \mathrm{d}\Gamma \mathbf{I}_3 , \tag{43}$$

$$\mathbf{M}[j,l] = M_{jl} \mathbf{I}_3 = \int_{\Gamma^{sl}} \Phi_j N_l^{\mathrm{ma}} \, \mathrm{d}\Gamma \mathbf{I}_3 \tag{44}$$

with the 3×3 identity tensor $\mathbf{I}_3$, whose size is determined by the number of variables to be coupled for each node. Here, $\mathbf{D}$ is a square $3n^{\mathrm{sl}} \times 3n^{\mathrm{sl}}$ matrix, which has only diagonal entries due to the choice of piecewise constant shape functions, whereas the definition of $\mathbf{M}$ generally gives a rectangular matrix of dimensions $3n^{\mathrm{sl}} \times 3n^{\mathrm{ma}}$. The actual numerical integration of the Mortar integrals can be performed either segment-based or element-based, see [15,19,44,45]. Due to its superior numerical efficiency, element-based integration is used exclusively in this work.

Plugging the previously defined Mortar matrices $\mathbf{D}$ and $\mathbf{M}$ into (37) leads to the discrete continuity constraint

$$\mathbf{D} \cdot \mathbf{u} - \mathbf{M} \cdot \dot{\mathbf{d}} = \mathbf{0}, \tag{45}$$

which will be utilized in Section 5.1.1 for the specific transfer of velocities from the solid to the fluid interface. Similarly, inserting (39)–(41) into (38) and again using (43) and (44) results in
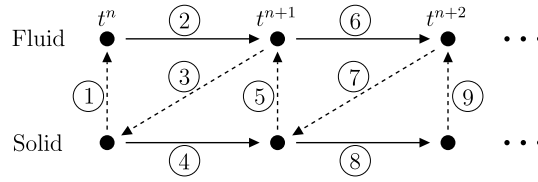
Fig. 7. Schematic of the staggered time integration of the coupled system.

$$\mathbf{f}_F^\Gamma = \mathbf{D}^\mathsf{T}\boldsymbol{\lambda}\,, \tag{46}$$

$$\mathbf{f}_S^\Gamma = \mathbf{M}^\mathsf{T}\boldsymbol{\lambda}\,, \tag{47}$$

which defines the nodal coupling forces $\mathbf{f}_F^\Gamma$ and $\mathbf{f}_S^\Gamma$ of the fluid and the solid, respectively. The transfer of loads is based on (46) and (47) and will be described in Section 5.1.2.

5.1.1. Transfer of solid velocities to fluid interface

The velocity at the cut-element face centroid is needed for both the energy equation and for determining the interface pressure p_{ele}^Γ through a Riemann solver, see (22). Moreover, the kinematic constraint (14) requires matching normal velocities at the interface. In a first step, the full interface velocities are transferred to the fluid by reordering (45) and defining a discrete projection $\mathbf{P}$ operator, viz.

$$\mathbf{u} = \mathbf{D}^{-1} \cdot \mathbf{M}\,\dot{\mathbf{d}} = \mathbf{P}\,\dot{\mathbf{d}}. \tag{48}$$

It shall be noted that the inversion of $\mathbf{D}$ is a trivial task at negligible cost due to its diagonal shape and thus there is no need for solving a possibly large linear system. In a second step, the current normal direction of the cut-element is used to project the velocity to fulfill the slip condition.

5.1.2. Transfer of fluid forces to solid interface

The equilibrium of forces requires the surface tractions of fluid and solid to be equal. As we do not want to solve explicitly for the Lagrange multipliers we reorder (46) and (47), yielding

$$\mathbf{f}_S^\Gamma = \left(\mathbf{D}^{-1} \cdot \mathbf{M}\right)^\mathsf{T} \mathbf{f}_F^\Gamma = \mathbf{P}^\mathsf{T}\mathbf{f}_F^\Gamma\,. \tag{49}$$

One can see that the transfer of loads from the fluid to the solid is based on the transpose of the projection operator for the transfer of solid velocities to the fluid. This is a crucial requirement for the consistent transfer across the interface and a distinctive feature of Mortar methods.

5.2. Loosely coupled partitioned FSI algorithm

In this paper, we use a loosely coupled conventional serial staggered algorithm. In Fig. 7, we illustrate the main steps to advance the coupled system from time level t^n to $t^{n+1} = t^n + \Delta t^n$. This explicit staggering algorithm, which follows the classical Dirichlet–Neumann partitioning, reads as follows:

1. The known structural interface displacements $\mathbf{d}^{\Gamma;n}$ and velocities $\dot{\mathbf{d}}^{\Gamma;n}$ at time t^n are used to update the cut-cells list and geometric properties on the fluid side. For this purpose, the cut-element algorithm is applied on the triangulated structural interface (see Fig. 4).
2. Advance the fluid in time. The evaluation of the interface exchange term (22) and the prescription of ghost-cell values (30) and (31) at time t^{n+1} use given structural interface velocities $\dot{\mathbf{d}}^{\Gamma;n}$. An interpolation procedure is needed to transfer solid velocities to the fluid interface, see Section 5.1.1.
3. Transfer the fluid interface normal tractions $\boldsymbol{\sigma}_F^{\Gamma;n+1} \cdot \mathbf{n}^{\Gamma;n}$ due to pressure loads to the structural solver. The staggering procedure leads to a time shift between the stress tensor and the normal used to compute the tractions. An interpolation procedure is needed to transfer fluid forces to the solid interface, see Section 5.1.2.
4. Advance the structure in time while the fluid interface loads act as additional Neumann boundary condition on the solid.
5. Proceed to the next time step.

Using the structural displacement $\mathbf{d}^{\Gamma;n}$ for the fluid solution at time t^{n+1} results in a first-order in time, $\mathcal{O}(\Delta t)$, coupling scheme [18]. Moreover, the explicit staggering algorithm is only conditionally stable since at time level t^{n+1}, the continuity condition is satisfied only for the dynamic part ($\boldsymbol{\sigma}_F^{\Gamma;n+1} \cdot \mathbf{n}^{\Gamma;n}$ matches $\boldsymbol{\sigma}_S^{\Gamma;n+1} \cdot \mathbf{n}^{\Gamma;n}$). For the kinematic part, the fluid velocities $\mathbf{u}^{\Gamma;n+1}$ at t^{n+1} match the structural velocities $\dot{\mathbf{d}}^{\Gamma;n}$ from the previous time step, but not the current structural velocities $\dot{\mathbf{d}}^{\Gamma;n+1}$. This in turn explains the violation of energy conservation at the interface.
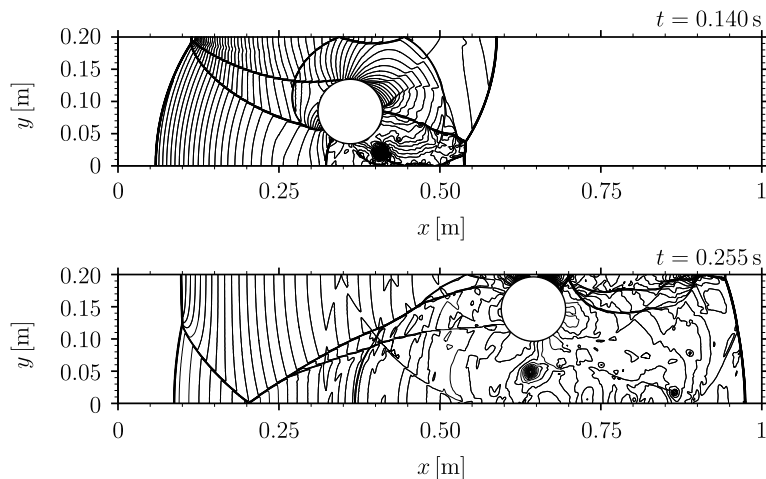
Fig. 8. 60 contours of fluid pressure within 0–28 Pa at two different time instances. Mesh resolution: $\Delta x = \Delta y = 6.25 \times 10^{-4}$ m.

6. Validation of the FSI algorithm

In the following, we present a validation of our method for rigid and deformable structures. The solution of both subdomains (Ω_F, Ω_S) is advanced by the same time step which is based on the CFL condition for the fluid flow. For all examples, coupling is performed at every time step.

6.1. Shock wave impact on rigid cylinder

The following test case for rigid body motion has been originally proposed by Falcovitz et al. [14] and has been widely adopted in the literature, see e.g. [30,39]. The setup consists of a two-dimensional channel filled with air and a rigid light-weight cylinder of density $\rho_{S;0} = 7.6$ kg/m^3 initially resting on the lower wall at a position $(x, y) = (0.15, 0.05)$ m. The cylinder is subsequently driven and lifted upwards by a Ma $= 3$ shock wave entering the domain from the left. The pre-shock conditions $\rho_{F;R} = 1$ kg/m^3, $p_R = 1$ Pa, $u_R = 0$ m/s hold for $x \geq 0.08$ m while for $x < 0.08$ m post-shock conditions $\rho_{F;L} = 3.857$ kg/m^3, $p_L = 10.33$ Pa, $u_L = 2.629$ m/s are initially prescribed. The fluid domain is rectangular with dimensions 1 m $\times$ 0.2 m and is discretized with 1600×320 cells in streamwise and wall-normal direction, respectively. This leads to a grid resolution of $\Delta x = \Delta y = 6.25 \times 10^{-4}$ m. For the lower and upper wall, reflecting slip-wall boundary conditions are used. At the inflow the post-shock values are prescribed while a linear extrapolation of all flow variables is used at the outflow. The cylinder has a radius of $r = 0.05$ m and it is discretized with 240 tri-linearly interpolated hexahedral elements along its circumference, leading to 240 surface elements that are coupled to the fluid. Due to stability reasons the cylinder does not exactly rest on the lower wall initially. We found that a narrow gap equal to 2% of the local cell height leads to stable and accurate results. Rigidity is achieved by imposing a high Young's modulus. The time integration factor $\theta = 0.66$ is chosen for the structural time integration. A CFL number of 0.6 is adopted for all simulations. It should be noted that no analytical solution for the final position of the cylinder exists. We therefore put emphasis on convergence properties of the proposed coupling algorithm.

Instantaneous pressure contours at $t = 0.14$ s and $t = 0.255$ s are shown in Fig. 8. With respect to the cylinder position and the resulting shock patterns our results agree well to Fig. 19 of Hu et al. [30] and Fig. 11 of Monasse et al. [39]. We observe a strong vortex beneath the cylinder, which persists throughout the entire cylinder trajectory, see Fig. 8, supporting the results of [20,39]. By further increasing the mesh resolution up to $\Delta x = \Delta y = 1.5625 \times 10^{-4}$ m the vortex is still apparent, excluding numerical dissipation being responsible for the formation of the vortex. As stated by Monasse et al. [39], a Kelvin–Helmholtz instability of the contact discontinuity present under the cylinder is the likely cause for this vortex.

Fig. 9 shows convergence results on the final horizontal and vertical position of the center of mass of the cylinder together with results from literature [30,39]. The final position is in the same range as the results of [30,39]. Our results show a convergence rate similar to the results obtained by Monasse et al. [39].

Finally, Fig. 10 shows the temporal evolution of resulting fluid forces acting on the rigid cylinder, which has been obtained by summation of all individual cut-element interface exchange terms. The smooth force distribution confirms that our interface treatment is accurate and free of spurious pressure oscillations.

6.2. Shock wave impact on deforming panel

The behavior of a cantilever panel subjected to a shock tube flow is analyzed. This test case has been investigated both experimentally and numerically in [24]. The experimental setup, as shown in Fig. 11, consists of a deformable panel of length $l = [0.04, 0.05]$ m and width $b = 0.001$ m placed within a shock tube. The panel is hit by a Ma $= 1.21$ shock wave, which enters the domain from left. The panel is made of steel ($E_S = 220$ GPa, $\rho_{S;0} = 7600$ kg/m^3, $\nu_S = 0.33$) and is clamped to a
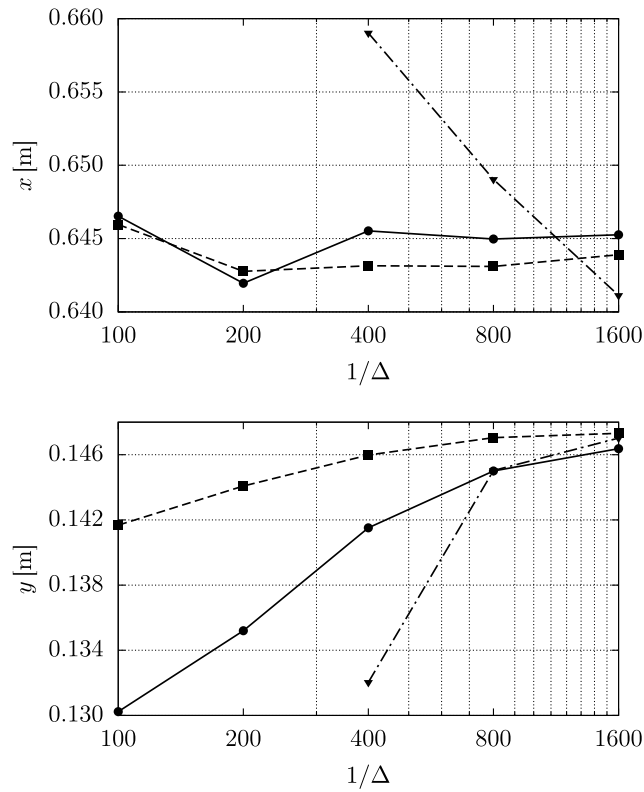
Fig. 9. Convergence study of horizontal (top) and vertical (bottom) cylinder center position for different fluid mesh resolutions. ($-\bullet-$) present results, ($-\cdot-\blacktriangledown-\cdot-$) Hu et al. [30], (- -■- -) Monasse et al. [39]. The *x*-axis is given in logarithmic scale.
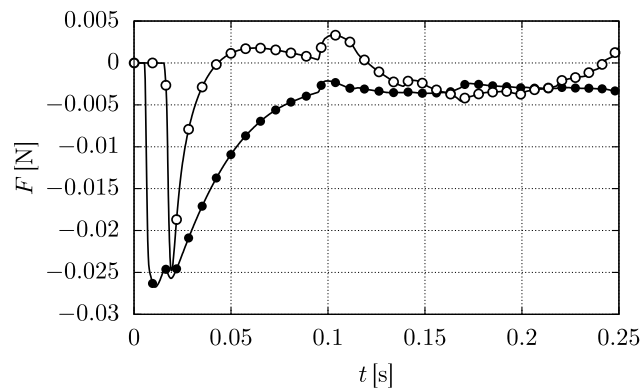

Fig. 10. Temporal evolution of global forces acting on the rigid cylinder. ($-\bullet-$) F_x, ($-\circ-$) F_y. Mesh resolution: $\Delta x = \Delta y = 6.25 \times 10^{-4}$ m.
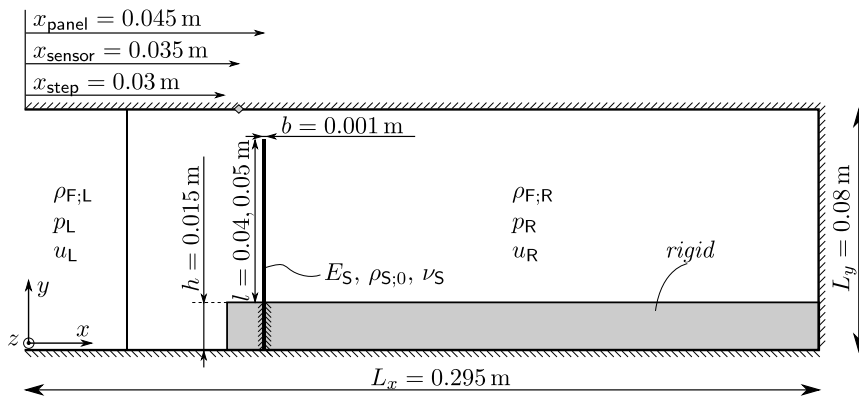

Fig. 11. Setup for shock wave impact on deforming panel including geometric dimensions; see [24] for details.
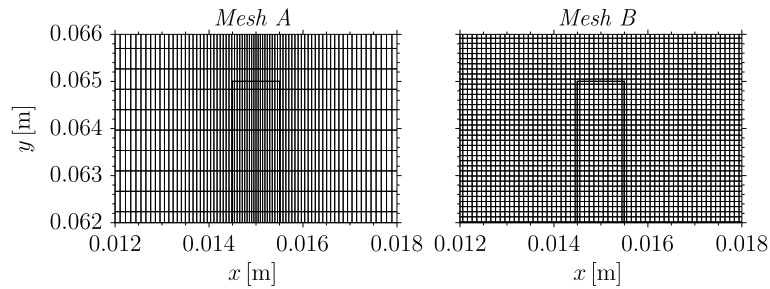
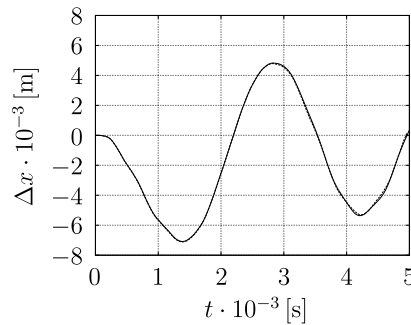**Fig. 12.** Fluid mesh resolutions close to the panel.

Fig. 13. Time evolution of panel tip displacement for 50 mm panel length using different fluid meshes. (—) *Mesh A*, (− − −) *Mesh B*.

rigid forward-facing step at its lower end. The pre-shock conditions resemble air at rest and are set to $\rho_{F;R} = 1.189$ kg/m^3, $p_R = 100$ kPa, $u_R = 0$ m/s, while the post-shock values are $\rho_{F;L} = 1.616$ kg/m^3, $p_L = 154$ kPa, $u_L = 109.68$ m/s. The fluid domain is rectangular with dimensions 0.295 m × 0.08 m in width and height. Since the problem is considered as two-dimensional, we adopt a constant thickness of 0.001 m in spanwise direction. Slip-wall boundary conditions are employed for all boundaries except for the inflow, where we prescribe non-reflective inflow boundary conditions based on Riemann invariants [43]. Two different fluid mesh resolutions are used: *Mesh A* contains 123, 400 cells with grid stretching applied in flow direction close to the panel and *Mesh B* utilizes a homogeneous grid with 1.82 million cells, see Fig. 12. The panel is discretized using 65×2 ($l = 0.05$ m) or 55×2 ($l = 0.04$ m) tri-linearly interpolated hexahedral elements. For both cases the panel is fully clamped at the bottom, and symmetry boundary conditions are applied in spanwise direction. EAS is used in order to avoid shear locking, which may affect the solution in such bending-dominated problems when using first-order displacement-based elements. The time integration factor $\theta = 0.66$ is chosen for the structural time integration. A CFL number of 0.6 is set for all simulations.

Fig. 13 shows the time evolution of the horizontal displacement at the panel tip for the 0.05 m panel length case on *Mesh A* and *Mesh B*. The panel motion is almost identical for both fluid meshes throughout the entire simulation time. Results presented below are obtained on fluid *Mesh B*.

We start with a qualitative analysis of the flow field for the 0.05 m panel. Fig. 14 shows numerical schlieren (left) and experimental shadowgraph visualizations (right) extracted from [24] at a time interval of $\Delta t = 140$ μs for a time period of $T = 840$ μs. At $t = 0$ μs, the incident right-running shock wave has already hit the panel and base plate, leading to the formation of reflected and transmitted shock waves. Downstream of the panel the initially normal shock undergoes transition to a cylindrical shock front due to sudden area increase ($t = 140$ μs). While being reflected at the lower wall ($t = 280$ μs) and traveling downstream, it undergoes a transition from regular to Mach reflection ($t = 280$–420 μs) and is subsequently reflected at the end wall ($t = 700$–840 μs). A main vortex is initially produced at the panel tip due to the roll-up of the slipstream accompanied by a vortex shedding process. All flow characteristics described above match the experimental results without any notable time lag. However, three-dimensional effects due to leaks between the panel and the shock tube side walls are observed in the experiment ($t = 280$ μs). Fig. 15 shows a numerical schlieren image at $t = 4.17$ ms, illustrating the maximum panel deflection together with the interaction of the main vortex and the upstream moving shock wave.

A quantitative analysis is presented in Fig. 16, where the time evolution of the horizontal panel tip displacement is plotted. Fig. 16(a) refers to the 0.05 m panel length case and Fig. 16(b) to the 0.04 m case, respectively. In addition to experimental values [24] represented through error bars, we include recent inviscid numerical results of Sanches and Coda [48], who employed a finite element based partitioned FSI approach utilizing the ALE description to account for moving boundaries and coupling with Lagrangian shell elements. Moreover, numerical results by Giordano et al. [24] are added, who assumed a two-dimensional but viscous flow in the laminar regime. For the 0.05 m panel case, see Fig. 16(a), it is observed that all numerical simulations predict a very similar oscillation of the panel with respect to the maximum amplitude and frequency of the first period. In comparison to the experimental values, both frequency and amplitude of the panel oscillation differ from numerical findings. According to Giordano et al. [24] this difference may be attributed to
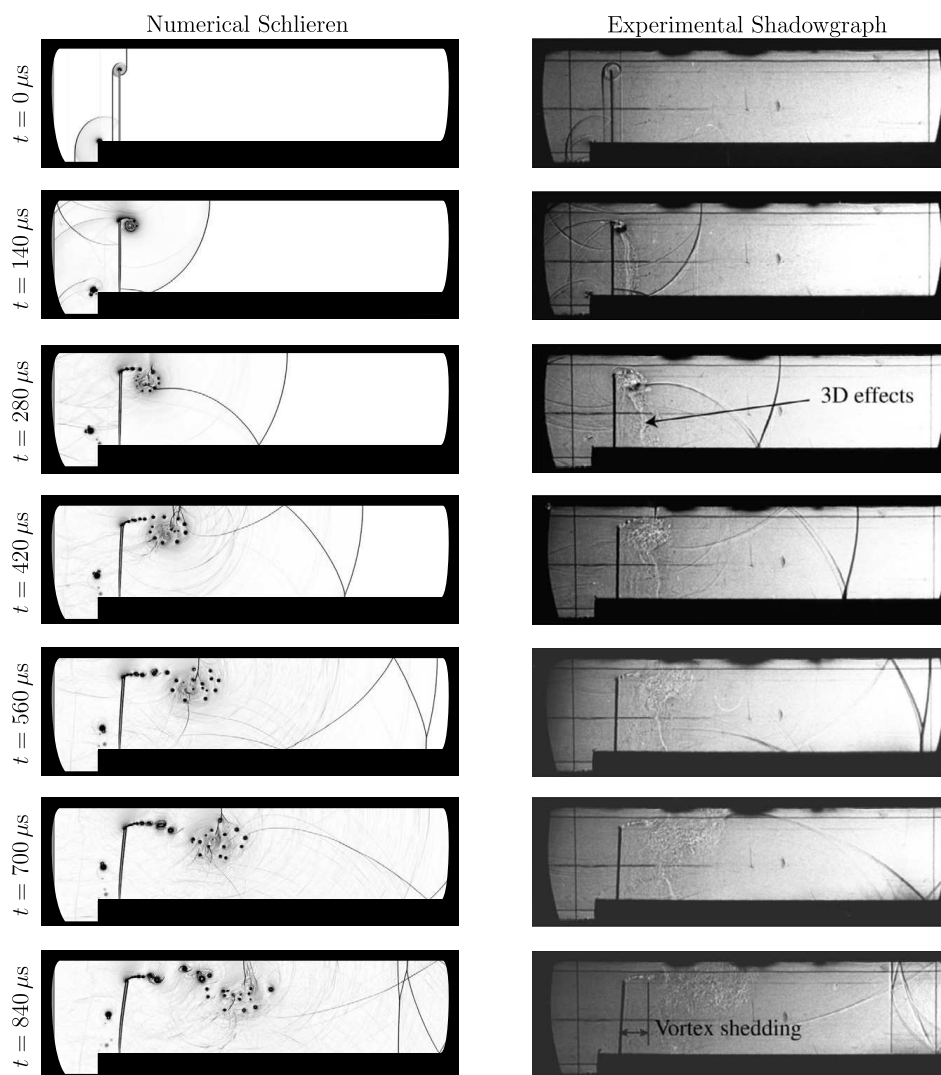
Fig. 14. Qualitative comparison between simulation (left) and experiment [24] (right) for 50 mm panel length by means of schlieren images for selected time instances.
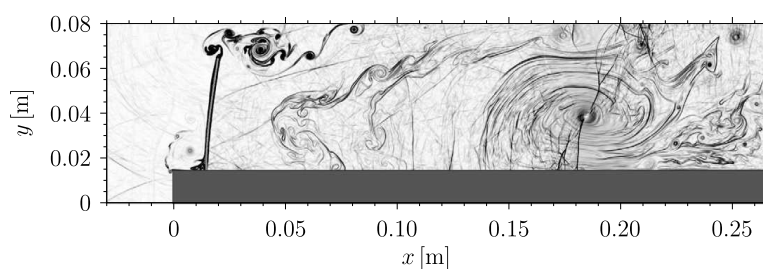

Fig. 15. Contour of density gradient magnitude at $t = 4.17$ ms.

the lack of damping in the structural model, which, however, should be negligible at least for the first period. Another explanation given by the authors relates to small deformations of the base in the direct vicinity of the fixing point, which would slightly alter both frequency and amplitude of the panel motion. The panel oscillation period obtained with our method is 2.85 ms, which is very close to the analytical period of 2.87 ms when considering the first eigenmode of a clamped plate submitted to an impulse load [24]. The experimental period is given as 3.8 ms.

Due to these uncertainties, a second case with 0.04 m panel length has been studied experimentally and numerically in [24]. With the shorter panel, the stresses on the base part are reduced, which also diminishes the influence of the base on the panel motion. We observe excellent agreement with experimental data and numerical references, see Fig. 16(b).

Finally, the pressure signals recorded at $(x, y) = (0.035, 0.08)$ m for both panel lengths are compared to the same numerical and experimental database in Fig. 17. Again, all numerical results are similar with respect to the time of arrival of pressure waves at the sensor and the pressure difference across the waves. While larger deviations are observed between
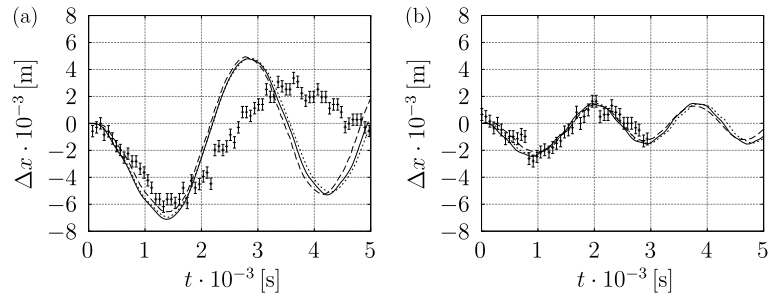
Fig. 16. Time evolution of panel tip displacement for (a) 0.05 m and (b) 0.04 m panel length. (—) present results, (— — —) Giordano et al. [24], (· · ·) Sanches and Coda [48]. Error bars denote experimental data [24].
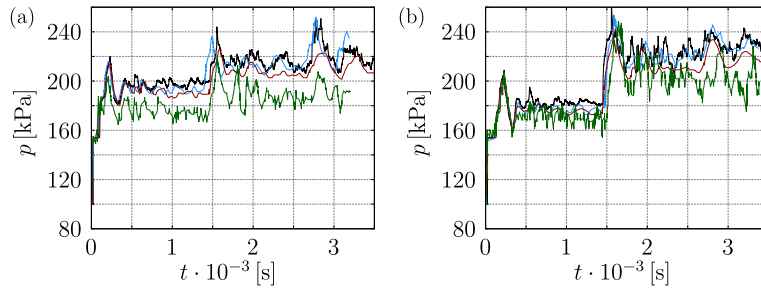

Fig. 17. Pressure signal recorded at sensor position (see Fig. 11 for exact location of pressure probe) for (a) 0.05 m and (b) 0.04 m panel length. (—) present results, (—) Giordano et al. [24], (—) Sanches and Coda [48], (—) experimental values [24]. (For interpretation of the references to color in this figure legend, the reader is referred to the web version of this article.)
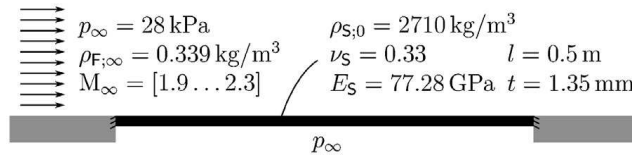

Fig. 18. Schematic and main parameters of the flutter problem.

numerical and experimental data for the 50 mm panel case, almost identical time evolution up to $t = 2$ ms is observed for the 0.04 m panel case. After that time, the pressure obtained experimentally drops continuously due to the arrival of reflected expansion waves inside the shock tube, which are not taken into account in the numerical simulations.

6.3. Flutter of a flat plate

Panel flutter is a self-excited, dynamic aeroelastic instability of thin plate structures, which frequently occurs in supersonic flow and is caused by an interaction between aerodynamic, inertial and elastic forces of the system [11]. For the setup considered here, see Fig. 18, linear instability theory predicts a critical Mach number of $\widetilde{\mathrm{Ma}}_{\mathrm{crit}} = 2.0$ above which a continuous growth of oscillations amplitudes is expected [12]. To trigger the instability, the pressure acting on the bottom of the panel initially is decreased by 0.1% and is kept at this condition for 4 ms. After this time period, the pressure is set back to the free-stream pressure. Since the limit Mach number of $\widetilde{\mathrm{Ma}}_{\mathrm{crit}} = 2.0$ describes a perfect oscillation without damping or amplification [42], this test case assesses effects of numerical damping present in our algorithm.

We consider a supersonic inviscid flow over a flat plate that is clamped at both ends, see Fig. 18. The plate has a length of $l = 0.5$ m, a thickness of $t = 0.00135$ m, a Young's modulus of $E_S = 77.28$ GPa, a Poisson's ratio of $\nu_S = 0.33$, and a density of $\rho_{S;0} = 2710$ kg/m^3. The structure is discretized using 200×8 tri-linearly interpolated hexahedral elements in streamwise and wall-normal direction, respectively. To avoid shear locking phenomena, the EAS method is used. Results obtained with tri-quadratically interpolated hexahedral elements and the same mesh resolution showed only negligible differences. If not stated otherwise, a geometric linear analysis of the structure is performed for comparison with references from the literature. The time integration factor $\theta = 0.5$ is chosen in order to reduce numerical damping. The fluid free-stream properties are: $\rho_{F;\infty} = 0.339$ kg/m^3, $p_\infty = 28$ kPa and Ma $= [1.9 \ldots 2.3]$. The computational domain and the fluid mesh resolution is shown in Fig. 19. For the results presented here, a grid-converged solution with respect to the fluid domain has been obtained with a total number of 16,500 cells. The grid is uniform in the region around the panel (0.25 m $\leq x \leq 0.75$ m) with a cell size of $\Delta x = 4.25 \times 10^{-3}$ m and $\Delta y = 4.8 \times 10^{-4}$ m. A cavity of height $h = 2.2 \times 10^{-2}$ m is added below the panel ($y \leq 0$ m) to account for the panel motion in this region. Since the problem is two-dimensional, we adopted a constant thickness of $\Delta z = 5 \times 10^{-3}$ m in spanwise direction. Slip-wall boundary conditions are imposed at all boundary patches
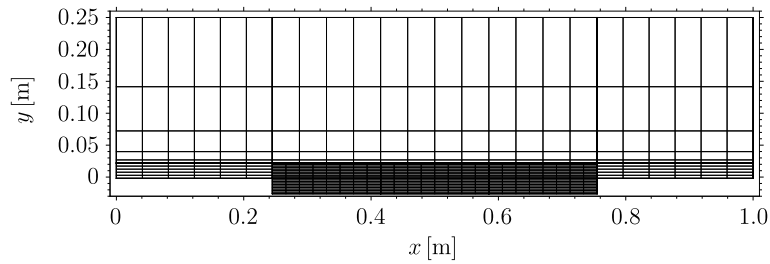
Fig. 19. General view of the computational domain and mesh resolution. Every 5th grid line is shown in the *x*- and *y*-direction, respectively.
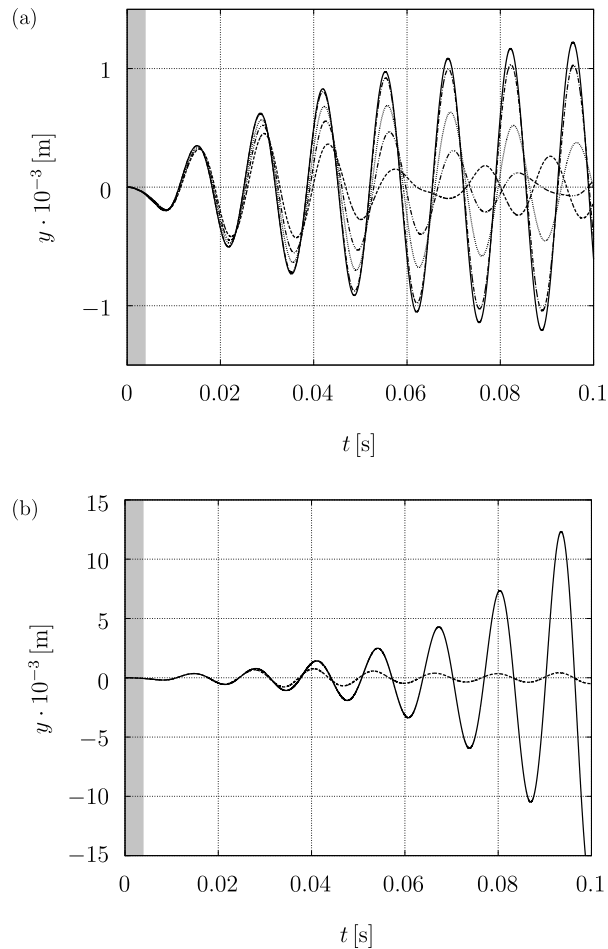

Fig. 20. (a) Vertical deflection of the plate at $x = 0.6$ m for Ma $\in [1.9, 2.0, 2.05, 2.09, 2.1]$. (- - -) Ma $= 1.9$, ($-\cdot\cdot-$) Ma $= 2.0$, ($\cdots$) Ma $= 2.05$, ($-\cdot-$) Ma $= 2.09$, ($-$) Ma $= 2.1$. (b) Geometrically linear and nonlinear plate deflections at $x = 0.6$ m for Ma $= 2.3$. ($-$) linear, (- - -) nonlinear. The gray shaded area indicates the initial perturbation time.

except for the inflow and outflow patch. At the inflow we prescribe all flow quantities which leads to a fully reflective boundary condition. At the outflow we perform linear extrapolation. The CFL number is 0.6 for all simulations.

The time evolution of the vertical displacement of the panel at the streamwise position $x = 0.6$ m for Mach numbers Ma $= [1.9, 2.0, 2.05, 2.09, 2.1]$ is shown in Fig. 20(a). The gray shaded area indicates the initial perturbation time. While the panel oscillations for Mach numbers below Ma $= 2.09$ are damped, amplification of panel deflection can be observed for Ma $= 2.1$. We found the limit Mach number to be Ma$_{crit} = 2.09$, which is close to the analytical solution ($\widetilde{Ma}_{crit} = 2.0$) with an error of 4.5% and to numerical results reported by Teixeira and Awruch [50] and Sanches and Coda [48] (Ma$_{crit} = 2.05$). Fig. 20(b) shows a comparison between geometrically linear and nonlinear panel solutions for a Mach number of Ma $= 2.3$. Exponential growth of the initial disturbance is observed for linear theory, which confirms analytical and numerical results [12,42,48,50]. In the geometrically nonlinear case, limited displacement amplitudes are observed. According to Dowell [11], the behavior of the panel after flutter onset is mainly dominated by structural nonlinearities. Nonlinear structural coupling between bending and stretching of the plate may in fact increase its effective stiffness, thereby modifying the dynamic response of the system.
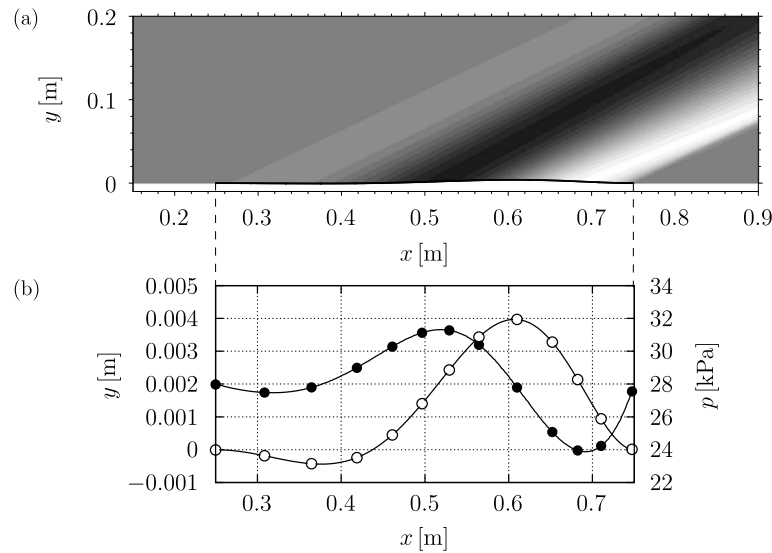
Fig. 21. (a) Pressure distribution for Ma = 2.3 at $t = 0.068$ s. Color scale from white to black using 20 equally spaced contour levels for $p \in [24$–$32]$ kPa. (b) Interface pressure and associated flutter mode. $(- \bullet -)\, p^\Gamma$, $(- \circ -)\, \Delta y$.

Finally, the pressure distribution in the fluid domain together with the associated flutter mode and wall-pressure distribution at time instant $t = 0.068$ s is shown in Fig. 21. The deflection of the panel leads to the formation of compression and expansion waves in the fluid. Compression waves are observed for a positive interface slope, whereas expansion waves occur for negative interface slopes, which is consistent with Ackeret's linear theory. The maximum displacement for the flutter mode is found at 70% of the panel length, confirming analytical [12,29] and numerical [42,48,50] findings. Local minima and maxima in the wall-pressure distribution in Fig. 21(b) coincide with interface inflection points. The smooth wall-pressure distribution confirms once again the accurate interface treatment.

6.4. Grid convergence study

The accuracy of the computed solution is verified through a grid convergence study. The simulation setup is similar to the case presented in Section 6.1. The formerly rigid cylinder is now replaced by an elastic structure and the wind-tunnel walls are removed. For the cylinder, which is initially located at $(x, y) = (0.15, 0.0)$ m, a Young's modulus of $E_S = 800$ Pa, a Poisson's ratio of $\nu_S = 0.3$, and a density of $\rho_{S;0} = 15$ kg/m^3 have been adopted. The remaining parameters are identical to the setup described in Section 6.1.

Since no analytical solution for this complex interaction exists, we have performed a well resolved reference simulation. The reference grid, in the following denoted as $\mathcal{G}^{ref}$, has a resolution of 1280×2560 cells in the fluid domain and spatial dimensions of 0.2 m $\times$ 0.4 m. The cylinder is discretized with 2048 tri-linearly interpolated hexahedral elements along its circumference. For the remaining grids $\mathcal{G}^k|_{k=1...5}$, where $\mathcal{G}^5$ denotes the finest grid, the fluid resolution is successively halved and the unstructured mesh resolution of the solid is halved in radial and circumferential direction. A uniform time step of $\Delta t = 5.1 \times 10^{-6}$ s is used for all simulations, which corresponds to the maximum allowable time step size for the reference simulation at a CFL number of 0.6.

Fig. 22 shows a numerical schlieren visualization of the resulting flow field together with the Cauchy stress field within the solid at times $t = 10, 20, 30$ and 40 ms computed on $\mathcal{G}^{ref}$. As expected, both fields are symmetric with respect to the x axis, even though no symmetry is presumed for the algorithm. At time $t = 10$ ms, the incident shock has already hit the cylinder and is subsequently reflected. The impact on the cylinder generates a shock wave which propagates through the solid. As the shock travels further around the cylinder, it undergoes transition from regular to Mach reflection ($t = 20$ ms). At the same time, the windward side of the cylinder is compressed, while the leeward side moves slightly downstream and generates a shock wave in the fluid. At the triple point, which connects the incident shock, the reflected shock and the Mach stem, a contact discontinuity develops. By the time the cylinder is accelerated ($t = 30$ ms), the reflected shock has propagated further upstream and a roll-up of the contact discontinuity is observed, which is enhanced by the interaction with the leeward shock wave. At the final time $t = 40$ ms, several shock waves emerging from the fluid–structure interface can be observed and an overall complex flow field has developed.

As a qualitative measure of the accuracy of our method, Fig. 23 shows numerical schlieren visualizations together with Cauchy stresses at the final time $t = 40$ ms for all mesh resolutions $\mathcal{G}^k$. While the overall results with respect to the final cylinder position and the incident and reflected shock wave within the fluid domain agree well between all mesh resolutions, the finer grids ($\mathcal{G}^3, \mathcal{G}^4, \mathcal{G}^5$) provide fine scale features such as contact discontinuities and weak shock waves emerging from the cylinder surface which are partially missing or not well resolved on the coarse grids ($\mathcal{G}^1, \mathcal{G}^2$).

A quantitative measure of accuracy within the fluid domain is given by the discrete L_p norm of the error for a solution variable $\mathcal{S}^k$ on grid $\mathcal{G}^k$, which we define as
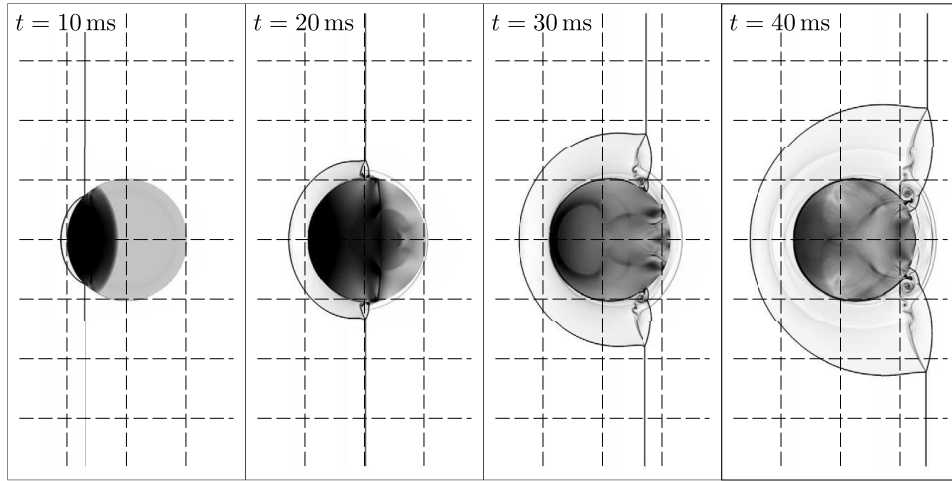
Fig. 22. Contours of density gradient magnitude in the fluid domain and magnitude of the Cauchy stress tensor in the solid domain at four different simulation times for the reference grid $\mathcal{G}^{ref}$.

$$\mathcal{E}_p^k = \left[\frac{1}{N} \sum_{i=1}^{N} \left(\mathcal{S}_i^k - \mathcal{S}_i^{ref} \right)^p \right]^{\frac{1}{p}} . \tag{50}$$

Here, N denotes the total number of fluid cells considered on grid $\mathcal{G}^k$. In order to evaluate the convergence of the coupling problem, interface quantities are used. The error of the magnitude of the interface displacement of the structure is measured by integrating the error over the coupling surface. Thus, the sum in (50) is replaced by an integration and division by the number of grid points is replaced by division by the area of the coupling surface. A second interface quantity of interest is the coupling force in x-direction. The corresponding error is computed as

$$\mathcal{E}^k = \left| \int_{\Gamma_F^k} \boldsymbol{\sigma}_F^{\Gamma,k} \cdot \mathbf{n}_F^{\Gamma,k} \mathrm{d}\Gamma - \int_{\Gamma_F^{ref}} \boldsymbol{\sigma}_F^{\Gamma,ref} \cdot \mathbf{n}_F^{\Gamma,ref} \mathrm{d}\Gamma \right| . \tag{51}$$

Table 1 summarizes estimated errors in the fluid density, pressure and velocity magnitude. Table 2 contains estimated errors in the structural interface displacement magnitude and in the coupling force in x-direction. Both tables include associated convergence rates at time $t = 40$ ms which are estimated from a least squares fit to the logarithm of the errors with the target function $\mathcal{F} = C \cdot \Delta^m$, where Δ denotes either the discrete fluid or structural mesh resolution and C denotes a positive constant independent of the grid. We observe convergence rates with respect to the L_1 norm of approximately 1.3 for all fluid variables, while the L_2 convergence rates are overall lower. Similar results have been observed by Henshaw and Schwendeman [28] for a pure fluid simulation of shock diffraction by a sphere. As expected from the flow field at time $t = 40$ ms, which is dominated by shock waves and contact discontinuities, the convergence order with respect to all fluid variables is first order. Fig. 24 shows the associated variation of the L_1 and L_2 error norms in the fluid variables plotted against the fluid mesh resolution $\Delta x = \Delta y = \Delta_F$. The error of the magnitude of the interface displacement is of order 1.58 and 1.56 in L_1 and L_2 norm, respectively. The convergence rate with respect to coupling force in x-direction computed at the interface from the fluid is 1.75. Due to the fluid–structure coupling and the use of tri-linear finite elements, the overall expected order of convergence is at most second order. Fig. 25 contains the error norms for the magnitude of the interface displacements as well as for the coupling force in x-direction plotted against the structural mesh resolution Δ_S in circumferential direction.

This convergence study still has its limitations. First of all the almost standard limitation in such cases is not to appropriately take into account the coupling of spatial and temporal error but then comparing spatial errors at a certain point in time. An additional limitation in this case is that the specific FSI example does not include real structural dynamics in terms of large deformations, but rather shows a combination of rigid body dynamics combined with wave propagation in the solid, which has obviously different features. Given the lack of an established benchmark example we intended to stay close to a widely accepted example, namely the shock wave impact on a rigid cylinder as given before. Besides all the limitations, however, the provided convergence study should give some insight into the performance of the coupling approach.

7. Numerical example – buckling of a three-dimensional inflated thin shell

We present a numerical example to show the ability of our method to handle large and complex structural deformations in FSI problems. The presented example studies the interaction between a flexible inflated thin shell and a Ma = 1.21 shock
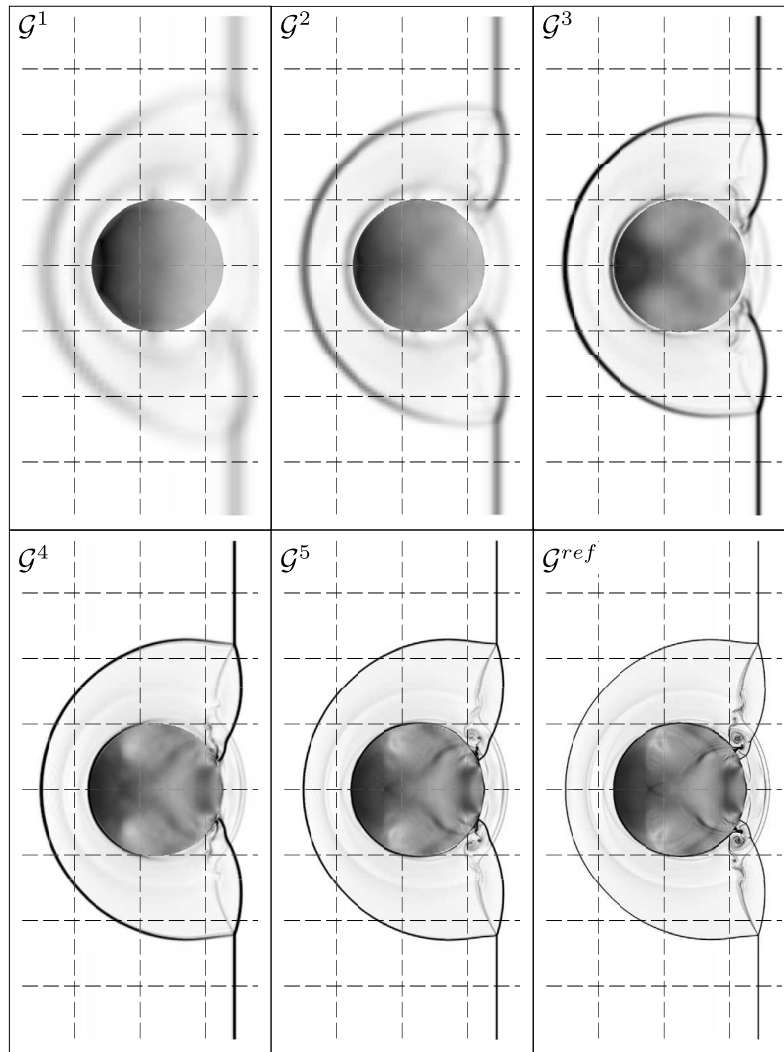
Fig. 23. Contours of density gradient magnitude in the fluid and magnitude of the Cauchy stress tensor in the solid domain at time $t = 40$ ms for all considered mesh resolutions.

Table 1
Computed L_1 and L_2 fluid error norms $\mathcal{E}_1^k$ and $\mathcal{E}_2^k$ on all grids $\mathcal{G}^k$ with respect to density, pressure and velocity magnitude at time $t = 40$ ms. Estimated convergence rates m are based on a least squares fit.

$\mathcal{G}^k$	Δ_F[a]	Δ_S[b]	$\mathcal{E}_{1,\rho}^k$	$\mathcal{E}_{2,\rho}^k$	$\mathcal{E}_{1,p}^k$	$\mathcal{E}_{2,p}^k$	$\mathcal{E}_{1,|\mathbf{u}|}^k$	$\mathcal{E}_{2,|\mathbf{u}|}^k$
$\mathcal{G}^1$	$5 \cdot 10^{-3}$	$4.91 \cdot 10^{-3}$	$2.1 \cdot 10^{-1}$	$4.3 \cdot 10^{-1}$	$7.8 \cdot 10^{-1}$	$1.8 \cdot 10^{0}$	$1.2 \cdot 10^{-1}$	$3.0 \cdot 10^{-1}$
$\mathcal{G}^2$	$2.5 \cdot 10^{-3}$	$2.45 \cdot 10^{-3}$	$8.5 \cdot 10^{-2}$	$2.2 \cdot 10^{-1}$	$3.2 \cdot 10^{-1}$	$8.8 \cdot 10^{-1}$	$4.6 \cdot 10^{-2}$	$1.7 \cdot 10^{-1}$
$\mathcal{G}^3$	$1.25 \cdot 10^{-3}$	$1.23 \cdot 10^{-3}$	$2.7 \cdot 10^{-2}$	$8.9 \cdot 10^{-2}$	$9.7 \cdot 10^{-2}$	$3.3 \cdot 10^{-1}$	$1.9 \cdot 10^{-2}$	$9.5 \cdot 10^{-2}$
$\mathcal{G}^4$	$6.25 \cdot 10^{-4}$	$6.14 \cdot 10^{-4}$	$1.3 \cdot 10^{-2}$	$5.9 \cdot 10^{-2}$	$4.3 \cdot 10^{-2}$	$2.1 \cdot 10^{-1}$	$8.4 \cdot 10^{-3}$	$6.0 \cdot 10^{-2}$
$\mathcal{G}^5$	$3.125 \cdot 10^{-4}$	$3.07 \cdot 10^{-4}$	$5.2 \cdot 10^{-3}$	$3.0 \cdot 10^{-2}$	$1.6 \cdot 10^{-2}$	$1.0 \cdot 10^{-1}$	$3.5 \cdot 10^{-3}$	$3.0 \cdot 10^{-2}$
	Rate m		1.36	1.03	1.37	1.12	1.34	0.80

[a] Fluid cell size in [m]. A uniform grid is used.
[b] Structural element length along the cylinder circumference in [m].

wave. Pre- and post-shock fluid states are equal to the conditions introduced in Section 6.2, with the initial shock position being located at $x = -0.05$ m. Details of the setup are shown in Fig. 26. The spherical membrane has a thickness of $d = 0.001$ m and an inner radius $r_i = 0.029$ m with its center M located at $(x, y, z) = (0, -0.005, 0)$ m. Material properties are $E_S = 0.07$ GPa, $\rho_{S;0} = 1000$ kg/m^3 and $\nu_S = 0.35$ for the Young's modulus, the density and the Poisson ratio, respectively. The thin shell is discretized with tri-linearly interpolated hexahedral elements with EAS, comprising two elements in thickness direction and 768 elements over the surface. The internal pressure keeping the membrane inflated is set equal to the pre-shock state p_R. Zero displacements in all three directions are prescribed for structural nodes located at the bottom of the shell at $y = 0$ m. The time integration factor $\theta = 0.5$ is chosen.

Fig. 27 depicts the computational domain and the fluid mesh in xy- and xz-plane. In addition, we show the triangulated structural coupling interface, which is used for the cut process in the fluid solver. Slip-wall boundary conditions are applied

Table 2
Computed L_1 and L_2 structural error norms $\mathcal{E}_1^k$ and $\mathcal{E}_2^k$ with respect to the interface displacement magnitude and $\mathcal{E}^k$ with respect to the interface force in x-direction on all grids $\mathcal{G}^k$ at time $t = 40$ ms. Estimated convergence rates m are based on a least squares fit.

$\mathcal{G}^k$	Δ_{F}[a]	Δ_{S}[b]	$\mathcal{E}_{1,|\mathbf{d}^\Gamma|}^k$	$\mathcal{E}_{2,|\mathbf{d}^\Gamma|}^k$	$\mathcal{E}_{|\boldsymbol{\sigma}_{\mathrm{F}}^\Gamma \cdot \mathbf{n}_{\mathrm{F}}^\Gamma|}^k$
$\mathcal{G}^1$	$5 \cdot 10^{-3}$	$4.91 \cdot 10^{-3}$	$8.9 \cdot 10^{-4}$	$7.7 \cdot 10^{-4}$	$5.6 \cdot 10^{-3}$
$\mathcal{G}^2$	$2.5 \cdot 10^{-3}$	$2.45 \cdot 10^{-3}$	$6.1 \cdot 10^{-4}$	$5.4 \cdot 10^{-4}$	$2.0 \cdot 10^{-3}$
$\mathcal{G}^3$	$1.25 \cdot 10^{-3}$	$1.23 \cdot 10^{-3}$	$1.5 \cdot 10^{-4}$	$1.3 \cdot 10^{-4}$	$5.8 \cdot 10^{-4}$
$\mathcal{G}^4$	$6.25 \cdot 10^{-4}$	$6.14 \cdot 10^{-4}$	$2.6 \cdot 10^{-5}$	$2.4 \cdot 10^{-5}$	$2.2 \cdot 10^{-4}$
$\mathcal{G}^5$	$3.125 \cdot 10^{-4}$	$3.07 \cdot 10^{-4}$	$1.8 \cdot 10^{-5}$	$1.6 \cdot 10^{-5}$	$4.0 \cdot 10^{-5}$
		RATE m	1.58	1.56	1.75

[a] Fluid cell size in [m]. A uniform grid is used.
[b] Structural element length along the cylinder circumference in [m].
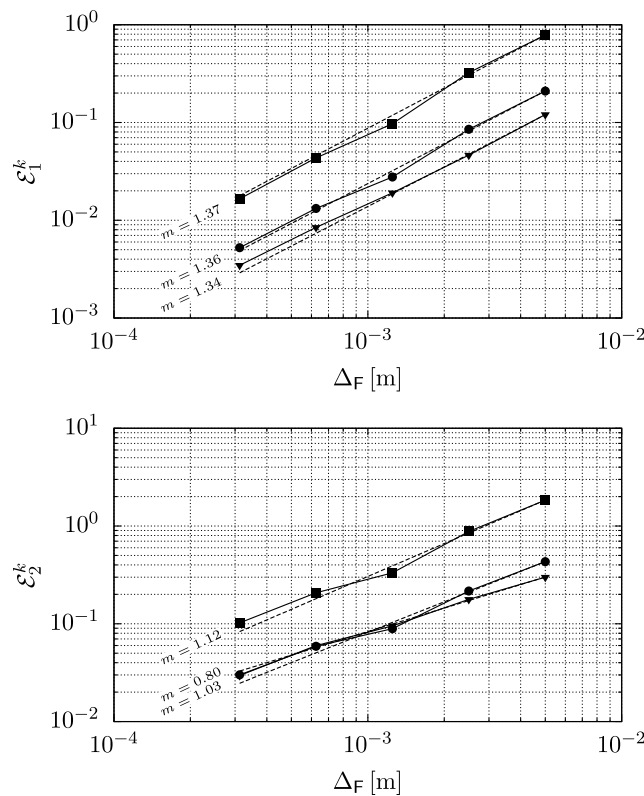

Fig. 24. Computed L_1 (top) and L_2 (bottom) fluid error norms $\mathcal{E}_1^k$ and $\mathcal{E}_2^k$ on all grids $\mathcal{G}^k$ at time $t = 40$ ms. $(- \bullet -) \mathcal{E}_\rho^k$, $(-\blacksquare-) \mathcal{E}_p^k$, $(- \blacktriangledown -) \mathcal{E}_{|\mathbf{u}|}^k$. Dashed lines represent least squares fits. Estimated convergence rates m are highlighted.

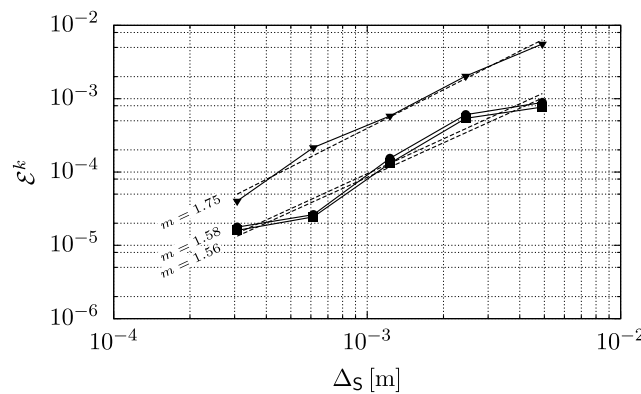**Fig. 25.** Computed interface norms on all grids $\mathcal{G}^k$ at time $t = 40$ ms. $(- \bullet -) \mathcal{E}_{1,|\mathbf{d}^\Gamma|}^k$, $(-\blacksquare-) \mathcal{E}_{2,|\mathbf{d}^\Gamma|}^k$, $(- \blacktriangledown -) \mathcal{E}_{|\boldsymbol{\sigma}_{\mathrm{F}}^\Gamma \cdot \mathbf{n}_{\mathrm{F}}^\Gamma|}^k$. Dashed lines represent least squares fits. Estimated convergence rates m are highlighted.
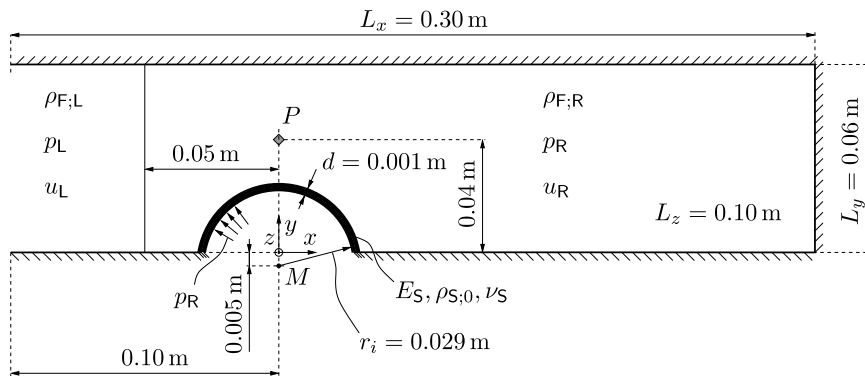
Fig. 26. Setup at xy-midplane for shock wave impact on a thin-walled shell including geometric dimensions.
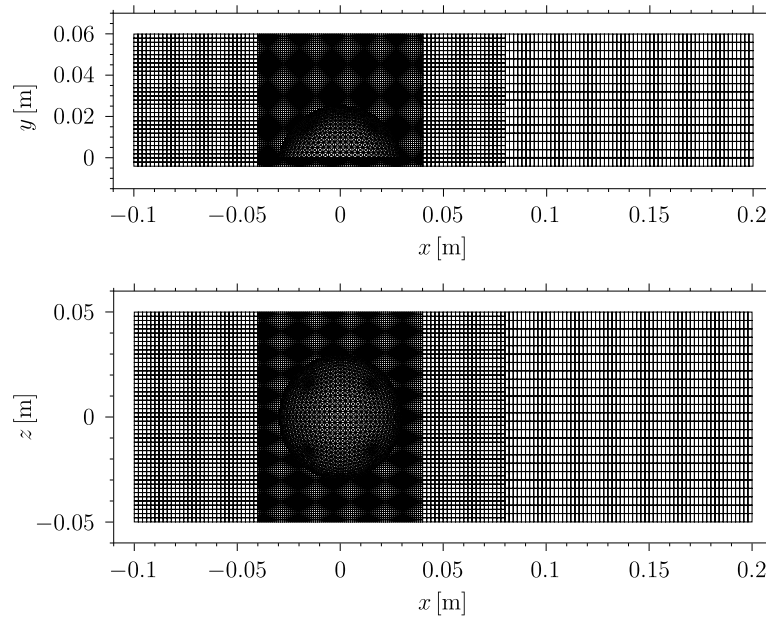

Fig. 27. General view of the computational domain and mesh resolution. The triangulated solid interface is additionally illustrated.
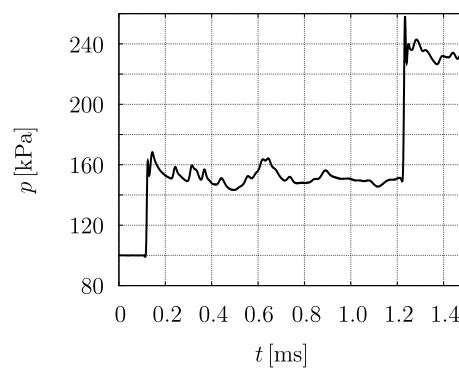
Fig. 28. Pressure signal recorded at sensor position $(x, y, z) = (0, 0.04, 0)$ m.

to all boundaries except for the inflow, where all flow quantities are prescribed leading to a fully reflective boundary condition. In the region around the shell, a uniform grid is used with cell sizes $\Delta x = \Delta y = \Delta z = 0.001$ m. In total, the fluid domain is discretized in space with 616,000 cells. The time step size is chosen to match a CFL number of 0.6.

In Fig. 28, the time evolution of the pressure signal recorded at the sensor position P with $(x, y, z) = (0, 0.04, 0)$ m is shown. The jumps at approximately $t = 0.1167$ ms and at $t = 1.2196$ ms mark the times when the shock wave passes the sensor. Pressure distributions and velocity vectors at the xy-midplane are shown in Fig. 29 for different time instances. The corresponding strain distribution in the thin-walled shell is presented in Fig. 30. The norm of the Euler–Almansi strain tensor $|\boldsymbol{e}|_2 = \sqrt{\boldsymbol{e} : \boldsymbol{e}}$ evaluated at each element center of the top layer is chosen to illustrate the large deformations occurring

(a) $t = 0$ ms, $p \in [100 - 170]$ kPa

(b) $t = 0.285$ ms, $p \in [100 - 170]$ kPa

(c) $t = 0.7704$ ms, $p \in [100 - 170]$ kPa

(d) $t = 1.22$ ms, $p \in [107 - 260]$ kPa

(e) $t = 1.4$ ms, $p \in [107 - 260]$ kPa

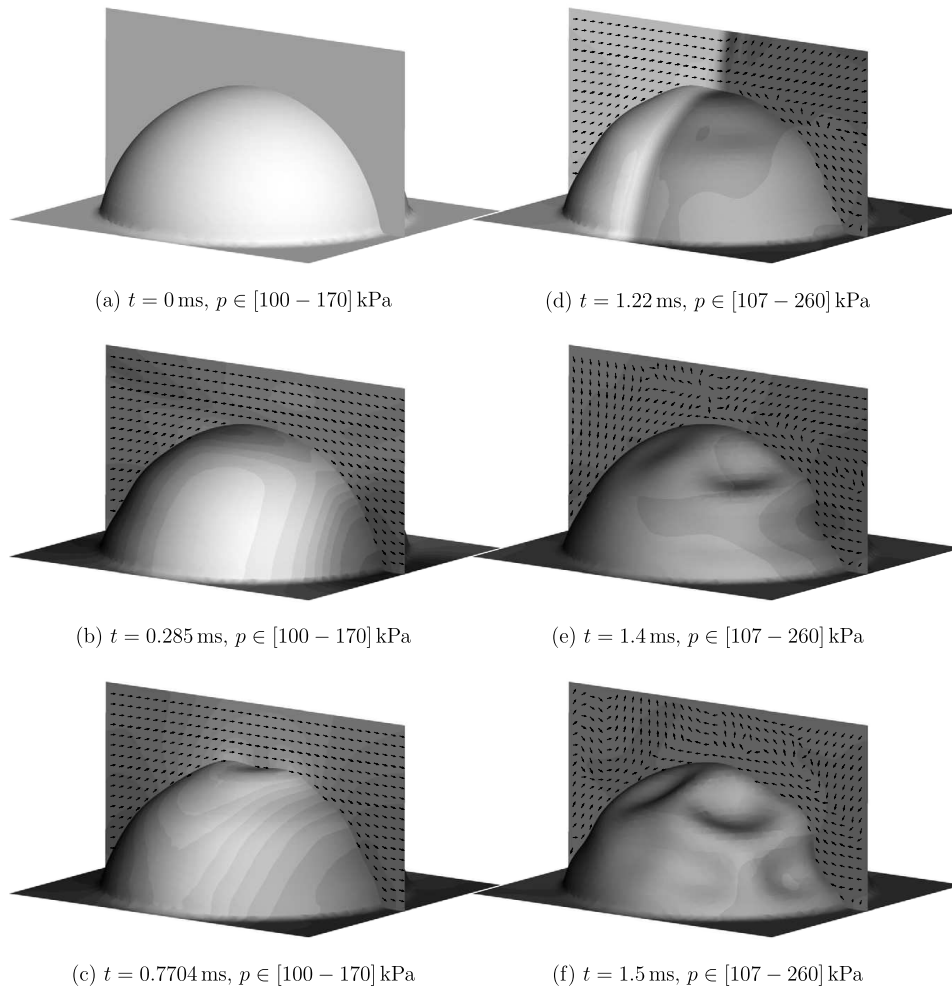(f) $t = 1.5$ ms, $p \in [107 - 260]$ kPa

Fig. 29. Pressure distribution together with uniform-length velocity vectors at different time instances. Every second vector is shown on the *xy*-midplane. Color scale ranges from white to black using 20 equally spaced contour levels within the indicated pressure range.

during the buckling process. Initially, the structure is undeformed and stress-free and the fluid is at rest, see Fig. 29(a) and Fig. 30(a). Due to the overpressure induced by the shock, Fig. 29(b), the windward side of the membrane is compressed, see Fig. 30(b), and is subsequently bouncing back due to its elastic behavior. At time $t = 0.7704$ ms, buckling of the thin-walled shell occurs at its tip, deflecting the flow as depicted in Fig. 29(c). The displacement of the tip node at initial position $(x, y, z) = (0, 0.025, 0)$ m (monitoring point A) is given in Fig. 31(a): the *y*-deflection is approximately 1.5×10^{-3} m during this first shock induced dimpling process. As the shock hits the membrane after reflection at the end wall, see Fig. 29(d)–(f), the pressure increases again. The membrane cannot sustain the additional load, and we observe the formation of buckling dimples, which are symmetrically distributed with respect to the *xy*-midplane as shown in Fig. 29(d)–(f) and Fig. 30(d)–(f). At $t = 1.5$ ms, the norm of the Euler–Almansi strain in the most distorted regions rises up to 0.127, see Fig. 30(f). Considering the monitoring point B, which is initially located at $(x, y, z) = (0.011912, 0.020912, 0.009308)$ m in one of the dimples, a total deflection of 5.23×10^{-3} m is found, see Fig. 31(b).

We refined the grids for both subdomains simultaneously and separately (not shown here for brevity) in order to reveal sensitivities with respect to the dynamic response of the thin-walled membrane. While the displacement of the membrane does not change significantly when varying the fluid resolution and keeping the structural discretization the same (maximum relative error of 2% compared to a fluid grid with $\Delta x = \Delta y = \Delta z = 0.00025$ m), we found that the dynamic response of the membrane and especially the occurring buckling mode can depend on the structural resolution. This observation confirms that buckling is highly sensitive with respect to imperfections of all kinds, including geometric imperfections [46]. Reliable prediction of buckling modes require realistic imperfection models, derived from the particular manufacturing process, to be included in the numerical model, which is beyond the scope of this paper. A well-defined quantity for such a configuration is the integral displacement magnitude shown in Fig. 32. A maximum relative error of 3% is found when comparing the present results to those of a four times finer mesh for both subdomains. A grid converged solution with respect to the integral displacement is obtained for a twice finer mesh. Fig. 32 shows that the membrane starts to collapse at around $t = 1.2$ ms, which coincides with the time when the shock wave, after reflection at the end wall, passes the pressure sensor P.
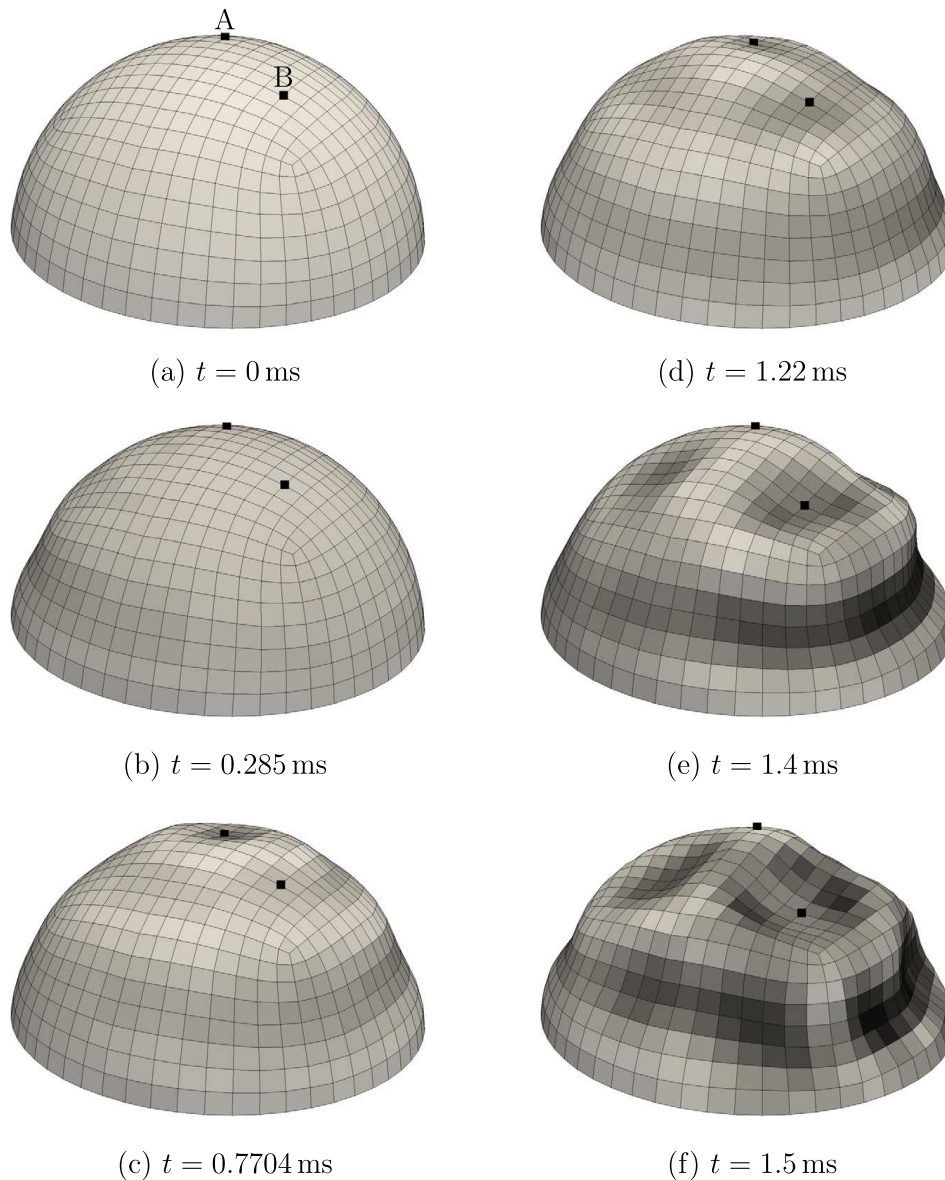
(a) $t = 0\,\mathrm{ms}$

(b) $t = 0.285\,\mathrm{ms}$

(c) $t = 0.7704\,\mathrm{ms}$

(d) $t = 1.22\,\mathrm{ms}$

(e) $t = 1.4\,\mathrm{ms}$

(f) $t = 1.5\,\mathrm{ms}$

Fig. 30. Norm of the Euler–Almansi strain tensor evaluated at each element center over time. Color scale ranges from white to black using 26 equally spaced contour levels for $|\boldsymbol{e}|_2 \in [0\text{–}0.13]$. Monitoring points A and B are marked with squares.

8. Summary and conclusions

The proposed finite volume – finite element coupling approach for the interaction between a compressible fluid and a deformable structure is able to handle large and complex three-dimensional deformations. We make use of a classical Dirichlet–Neumann partitioning in conjunction with a conventional serial staggered procedure for coupling of the two domains.

A representation of the interface within the fluid domain is achieved by means of a cut-element based IBM, which has been successfully extended to deformable structures for the first time. The presented framework leads to a non-matching discretization of the interface between both subdomains. A consistent data transfer has been established using a Mortar method, which preserves linear and angular momentum. Piecewise constant ansatz functions are used for interpolating the fluid state as well as for the Lagrange multipliers on each single cut-element, allowing for a simple inversion of a diagonal matrix at negligible cost for the evaluation of the discrete projection operator. To the authors knowledge, this is the first time a cut-element method has been combined with a Mortar method for coupling the two subdomains in a consistent and efficient way.

The proposed coupling method has been validated through two-dimensional model problems involving rigid and deformable structures with large deformations. Our method correctly predicts the transient behavior of shock-loaded rigid and deformable structures. Moreover, good accuracy was achieved with respect to the correct prediction of flutter onset. The ability of our method to handle three-dimensional FSI problems involving large and complex structural deformations has
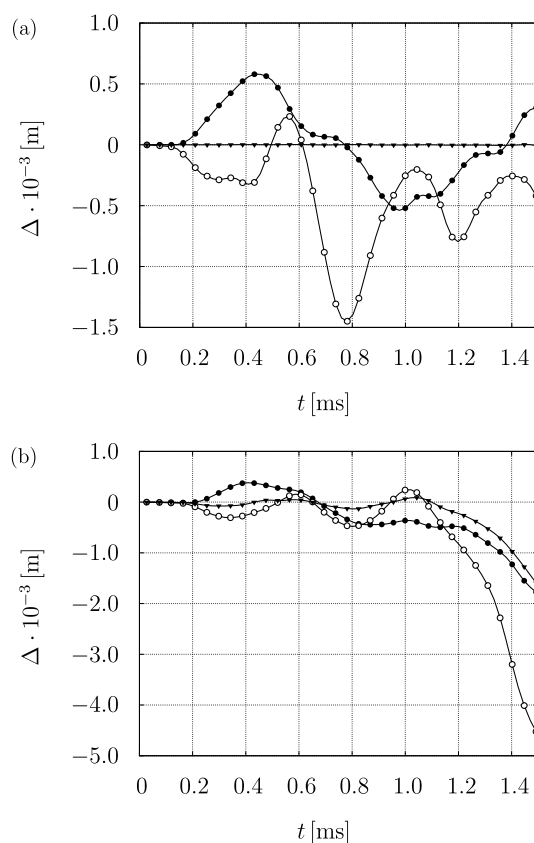
Fig. 31. Time evolution of displacements at two different monitoring points (see Fig. 30): (a) tip of membrane: monitoring point A, (b) monitoring point B. $(- \bullet -) \Delta x$, $(- \circ -) \Delta y$, $(- \blacktriangledown -) \Delta z$.
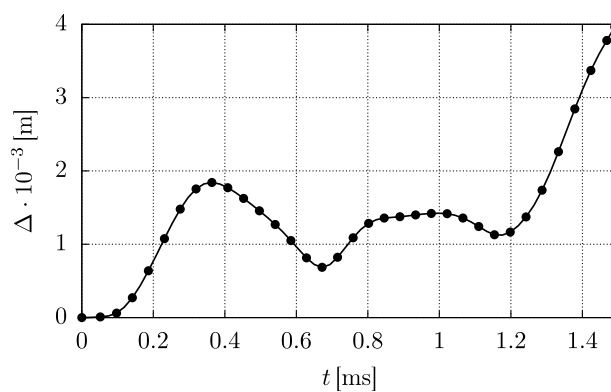
Fig. 32. Time evolution of integral displacement magnitude.

been demonstrated through a newly proposed test case consisting of a flexible inflated thin shell interacting with a shock wave.

The current framework is limited to structures with a size larger than several fluid cells in order to fill the ghost-cell values properly. A remedy could be either an adaptive mesh refinement procedure for the flow solver or the decoupling of the ghost-cell method from the underlying Cartesian grid, which leads to additional degrees of freedom that need to be handled. In order to resolve the possibly different time-scales of both subdomains and increase the overall efficiency, subcycling should be considered for future work.

Acknowledgements

Appendix A. Computational performance

The performance of the proposed coupling algorithm is summarized in Table 3, where we show the percentage of time spent for the fluid solver T_F, the structural solver T_S, and for the communication T_C between both codes for all considered test cases. $N_{F,S}^{ele}$ represents the total number of elements used for the fluid and structural problem, respectively. $N_{F,S}^{ele}/N_{F,S}^{CPU}$ is the associated number of elements per CPU for each subdomain. The majority of the computational time is spent on advancing the solid domain, which, however, also includes load transfer with the Mortar method. Increasing the fluid resolution proportionally increases the number of cut-elements and thus the workload for the structural solver at the interface. Moreover, the implicit time integration leads to an iterative solution procedure with at least two Newton iterations per coupling step to obtain the solid state. The communication between both codes via Message Passing Interface typically requires less than 1% of the runtime. The current implementation of the staggered algorithm can be further optimized in terms of parallel efficiency. Furthermore, subcycling can significantly reduce computational cost of the structural solver and will be considered in future work.

Table 3
Computational performance of the coupling framework for selected simulations.

Case (# Run)	N_F^{ele}	N_S^{ele}	$\frac{N_F^{ele}}{N_F^{CPU}}$	$\frac{N_S^{ele}}{N_S^{CPU}}$	T_F (%)	T_S (%)	T_C (%)
Cylinder[a]							
#1	$2 \cdot 10^3$	$3.6 \cdot 10^3$	$2 \cdot 10^3$	$0.9 \cdot 10^3$	1.7%	98.1%	0.2%
#2	$8 \cdot 10^3$	$3.6 \cdot 10^3$	$8 \cdot 10^3$	$0.9 \cdot 10^3$	4.4%	95.4%	0.2%
#3	$3.2 \cdot 10^4$	$3.6 \cdot 10^3$	$8 \cdot 10^3$	$0.9 \cdot 10^3$	5.0%	94.8%	0.2%
#4	$1.28 \cdot 10^5$	$3.6 \cdot 10^3$	$1.6 \cdot 10^4$	$0.9 \cdot 10^3$	9.4%	90.4%	0.2%
#5	$5.12 \cdot 10^5$	$3.6 \cdot 10^3$	$6.4 \cdot 10^4$	$0.9 \cdot 10^3$	28.5%	71.3%	0.2%
Panel[b]							
#1	$1.234 \cdot 10^5$	$1.3 \cdot 10^2$	$1.12 \cdot 10^4$	$4.3 \cdot 10^1$	56.0%	43.4%	0.6%
#2	$1.82 \cdot 10^6$	$1.3 \cdot 10^2$	$6.07 \cdot 10^4$	$6.5 \cdot 10^1$	45.9%	53.9%	0.2%
Flutter[c]							
#1	$1.65 \cdot 10^4$	$1.6 \cdot 10^3$	$4.125 \cdot 10^3$	$1.3 \cdot 10^2$	13.9%	85.5%	0.6%
Membrane							
#1	$6.16 \cdot 10^5$	$1.536 \cdot 10^3$	$3.08 \cdot 10^4$	$1.28 \cdot 10^2$	45.2%	54.2%	0.6%

[a] Only the rigid cylinder case is considered.
[b] Only the 50 mm panel length case is considered.
[c] Only the Ma = 2.3 case is considered.

References

[1] J. Banks, W. Henshaw, D. Schwendeman, Deforming composite grids for solving fluid structure problems, J. Comput. Phys. 231 (9) (2012) 3518–3547.
[2] J. Banks, W. Henshaw, D. Schwendeman, An analysis of a new stable partitioned algorithm for FSI problems. Part I: Incompressible flow and elastic solids, J. Comput. Phys. 269 (2014) 108–137.
[3] J. Banks, W. Henshaw, B. Sjögreen, A stable FSI algorithm for light rigid bodies in compressible flow, J. Comput. Phys. 245 (2013) 399–430.
[4] C. Bernardi, Y. Maday, A.T. Patera, A new nonconforming approach to domain decomposition: the Mortar element method, in: H. Brezis, J. Lions (Eds.), Nonlinear Partial Differential Equations and Their Applications, Pitman/Wiley, London/New York, 1994, pp. 13–51.
[5] P. Causin, J.-F. Gerbeau, F. Nobile, Added-mass effect in the design of partitioned algorithms for fluid–structure problems, Comput. Methods Appl. Mech. Eng. 194 (2005) 4506–4527.
[6] F. Cirak, R. Deiterding, S.P. Mauch, Large-scale fluid–structure interaction simulation of viscoplastic and fracturing thin-shells subjected to shocks and detonations, Comput. Struct. 85 (2007) 1–33.
[7] D.K. Clarke, H.A. Hassan, M.D. Salas, Euler calculations for multielement airfoils using Cartesian grids, AIAA J. 24 (1986) 353–358.
[8] P. Colella, D.T. Graves, B.J. Keen, D. Modiano, A Cartesian grid embedded boundary method for hyperbolic conservation laws, J. Comput. Phys. 211 (2006) 347–366.
[9] A. de Boer, A.H. van Zuijlen, H. Bijl, Review of coupling methods for non-matching meshes, Comput. Methods Appl. Mech. Eng. 196 (2007) 1515–1525.
[10] J. Donea, S. Giuliani, J. Halleux, An arbitrary Lagrangian–Eulerian finite element method for transient dynamic fluid–structure interactions, Comput. Methods Appl. Mech. Eng. 33 (1982) 689–723.
[11] E.H. Dowell, NASA Space Vehicle Design Criteria, Monograph NASA SP-8005, 1972.
[12] E.H. Dowell, Aeroelasticity of Plates and Shells, Springer, Leyden, 1974.
[13] A. Ehrl, A. Popp, V. Gravemeier, W.A. Wall, A dual Mortar approach for mesh tying within a variational multiscale method for incompressible flow, Int. J. Numer. Methods Fluids 76 (2014) 1–27.
[14] J. Falcovitz, G. Alfandary, G. Hanoch, A two-dimensional conservation laws scheme for compressible flows with moving boundaries, J. Comput. Phys. 138 (1997) 83–102.
[15] P. Farah, A. Popp, W.A. Wall, Segment-based vs. element-based integration for Mortar methods in computational contact mechanics, Comput. Mech. 55 (2015) 209–228.
[16] C. Farhat, M. Lesoinne, Two efficient staggered algorithms for the serial and parallel solution of three-dimensional nonlinear transient aeroelastic problems, Comput. Methods Appl. Mech. Eng. 182 (2000) 499–515.

[17] C. Farhat, M. Lesoinne, P. Le Tallec, Load and motion transfer algorithms for fluid/structure interaction problems with non-matching discrete interfaces: momentum and energy conservation, optimal discretization and application to aeroelasticity, Comput. Methods Appl. Mech. Eng. 157 (1998) 95–114.

[18] C. Farhat, M. Lesoinne, N. Maman, Mixed explicit/implicit time integration of coupled aeroelastic problems: three-field formulation, geometric conservation and distributed solution, Int. J. Numer. Methods Fluids 21 (1995) 807–835.

[19] K.A. Fischer, P. Wriggers, Mortar based frictional contact formulation for higher order interpolations using the moving friction cone, Comput. Methods Appl. Mech. Eng. 195 (2006) 5020–5036.

[20] H. Forrer, M. Berger, Flow simulations on Cartesian grids involving complex moving geometries, in: Hyperbolic Problems: Theory, Numerics, Applications, vol. 129, 1999, pp. 315–324.

[21] C. Förster, W.A. Wall, E. Ramm, Artificial added mass instabilities in sequential staggered coupling of nonlinear structures and incompressible viscous flows, Comput. Methods Appl. Mech. Eng. 196 (2007) 1278–1293.

[22] R.L. Gaffney, H.A. Hassan, Euler calculations for wings using Cartesian grids, in: 25th AIAA Aerospace Sciences Meeting, American Institute of Aeronautics and Astronautics, Reston, Virginia, 1987.

[23] L. Garelli, R.R. Paz, M.A. Storti, Fluid–structure interaction study of the start-up of a rocket engine nozzle, Comput. Fluids 39 (2010) 1208–1218.

[24] J. Giordano, G. Jourdan, Y. Burtschell, M. Medale, D.E. Zeitoun, L. Houas, Shock wave impacts on deforming panel, an application of fluid–structure interaction, Shock Waves 14 (2005) 103–110.

[25] S. Gottlieb, C.-W. Shu, Total variation diminishing Runge–Kutta schemes, Math. Comput. 67 (1998) 73–85.

[26] M. Grilli, S. Hickel, X.Y. Hu, N.A. Adams, Conservative Immersed Interface Method for compressible viscous flows with heat transfer, in: Proceedings of the Academy Colloquium Immersed Boundary Methods: Current Status and Future Research Directions, KNAW, Amsterdam, The Netherlands, 2009.

[27] C. Günther, M. Meinke, W. Schröder, A flexible level-set approach for tracking multiple interacting interfaces in embedded boundary methods, Comput. Fluids 102 (2014) 182–202.

[28] W.D. Henshaw, D.W. Schwendeman, Parallel computation of three-dimensional flows using overlapping grids with adaptive mesh refinement, J. Comput. Phys. 227 (2008) 7469–7502.

[29] J.C. Houbolt, A study of several aerothermoelastic problems of aircraft structures in high-speed flight, Ph.D. thesis, ETH Zürich, 1958.

[30] X.Y. Hu, B.C. Khoo, N.A. Adams, F.L. Huang, A conservative interface method for compressible flows, J. Comput. Phys. 219 (2006) 553–578.

[31] W. Joppich, M. Kürschner, MpCCI – a tool for the simulation of coupled applications, Concurr. Comput. 18 (2006) 183–192.

[32] M.P. Kirkpatrick, S.W. Armfield, J.H. Kent, A representation of curved boundaries for the solution of the Navier–Stokes equations on a staggered three-dimensional Cartesian grid, J. Comput. Phys. 184 (2003) 1–36.

[33] T. Klöppel, A. Popp, U. Küttler, W.A. Wall, Fluid–structure interaction for non-conforming interfaces based on a dual Mortar formulation, Comput. Methods Appl. Mech. Eng. 200 (2011) 3111–3126.

[34] U. Küttler, W.A. Wall, Fixed-point fluid–structure interaction solvers with dynamic relaxation, Comput. Mech. 43 (2008) 61–72.

[35] X.D. Liu, S. Osher, T. Chan, Weighted essentially non-oscillatory schemes, J. Comput. Phys. 115 (1994) 200–212.

[36] M. Meyer, A. Devesa, S. Hickel, X.Y. Hu, N.A. Adams, A conservative immersed interface method for Large-Eddy Simulation of incompressible flows, J. Comput. Phys. 229 (2010) 6300–6317.

[37] R. Mittal, H. Dong, M. Bozkurttas, F.M. Najjar, A. Vargas, A. von Loebbecke, A versatile sharp interface immersed boundary method for incompressible flows with complex boundaries, J. Comput. Phys. 227 (2008) 4825–4852.

[38] R. Mittal, G. Iaccarino, Immersed boundary methods, Annu. Rev. Fluid Mech. 37 (2005) 239–261.

[39] L. Monasse, V. Daru, C. Mariotti, S. Piperno, C. Tenaud, A conservative coupling algorithm between a compressible flow and a rigid body using an Embedded Boundary method, J. Comput. Phys. 231 (2012) 2977–2994.

[40] F. Örley, V. Pasquariello, S. Hickel, N.A. Adams, Cut-element based immersed boundary method for moving geometries in compressible liquid flows with cavitation, J. Comput. Phys. 283, 1–22.

[41] C.S. Peskin, Flow patterns around heart valves: a numerical method, J. Comput. Phys. 10 (1972) 252–271.

[42] S. Piperno, Explicit/implicit fluid/structure staggered procedures with a structural predictor and fluid subcycling for 2D inviscid aeroelastic simulations, Int. J. Numer. Methods Fluids 25 (1997) 1207–1226.

[43] T. Poinsot, S.K. Lele, Boundary conditions for direct simulations compressible viscous flows, J. Comput. Phys. 101 (1992) 104–129.

[44] A. Popp, M. Gitterle, M.W. Gee, W.A. Wall, A dual Mortar approach for 3D finite deformation contact with consistent linearization, Int. J. Numer. Methods Eng. 83 (2010) 1428–1465.

[45] M.A. Puso, A 3D Mortar method for solid mechanics, Int. J. Numer. Methods Eng. 59 (2004) 315–336.

[46] E. Ramm, W.A. Wall, Shell structures – a sensitive interrelation between physics and numerics, Int. J. Numer. Methods Eng. 60 (1) (2004).

[47] M.R. Ross, C.A. Felippa, K.C. Park, M.A. Sprague, Treatment of acoustic fluid–structure interaction by localized Lagrange multipliers: formulation, Comput. Methods Appl. Mech. Eng. 197 (2008) 3057–3079.

[48] R.A.K. Sanches, H.B. Coda, On fluid–shell coupling using an arbitrary Lagrangian–Eulerian fluid solver coupled to a positional Lagrangian shell solver, Appl. Math. Model. 55 (2014) 1–18.

[49] J.C. Simo, F. Armero, Geometrically non-linear enhanced strain mixed methods and the method of incompatible modes, Int. J. Numer. Methods Eng. 33 (1992) 1413–1449.

[50] P.R.F. Teixeira, A.M. Awruch, Numerical simulation of fluid–structure interaction using the finite element method, Comput. Fluids 34 (2005) 249–273.

[51] E.F. Toro, Riemann Solvers and Numerical Methods for Fluid Dynamics, Springer, Berlin, Heidelberg, 2009.

[52] H.S. Udaykumar, W. Shyy, M.M. Rao, Elafint: a mixed Eulerian–Lagrangian method for fluid flows with complex and moving boundaries, Int. J. Numer. Methods Fluids 22 (1996) 691–712.

[53] B.I. Wohlmuth, A Mortar finite element method using dual spaces for the Lagrange multiplier, SIAM J. Numer. Anal. 38 (2000) 989–1012.

[54] T. Ye, R. Mittal, H.S. Udaykumar, W. Shyy, An accurate Cartesian grid method for viscous incompressible flows with complex immersed boundaries, J. Comput. Phys. 156 (1999) 209–240.

[55] X. Zhao, S. Bayyuk, S. Zhang, Aeroelastic response of rocket nozzles to asymmetric thrust loading, Comput. Fluids 76 (2013) 128–148.

B.3. Unsteady effects of strong shock-wave/boundary-layer interaction at high Reynolds number

This Agreement between Vito Pasquariello ("You") and Cambridge University Press ("Cambridge University Press") consists of your license details and the terms and conditions provided by Cambridge University Press and Copyright Clearance Center.

License Number	4301890725313
License date	Mar 04, 2018
Licensed Content Publisher	Cambridge University Press
Licensed Content Publication	The Journal of Fluid Mechanics
Licensed Content Title	Unsteady effects of strong shock-wave/boundary-layer interaction at high Reynolds number
Licensed Content Author	Vito Pasquariello, Stefan Hickel, Nikolaus A. Adams
Licensed Content Date	Jun 22, 2017
Licensed Content Volume	823
Licensed Content Issue	undefined
Start page	617
End page	657
Type of Use	Dissertation/Thesis
Requestor type	Author
Portion	Full article
Author of this Cambridge University Press article	Yes
Author / editor of the new work	Yes
Order reference number	
Territory for reuse	World
Title of your thesis / dissertation	Analysis and Control of Shock-Wave/Turbulent Boundary-Layer Interactions on Rigid and Flexible Walls
Expected completion date	Mar 2018
Estimated size(pages)	170
Requestor Location	Vito Pasquariello Boltzmannstrasse 15 Technische Universität München Garching bei München, 85748 Germany Attn: Vito Pasquariello
Publisher Tax ID	GB823847609
Billing Type	Invoice
Billing Address	Vito Pasquariello Boltzmannstrasse 15 Technische Universität München Garching bei München, Germany 85748 Attn: Vito Pasquariello
Total	0.00 EUR
Terms and Conditions	

TERMS & CONDITIONS

Cambridge University Press grants the Licensee permission on a non-exclusive non-transferable basis to reproduce, make available or otherwise use the Licensed content 'Content' in the named territory 'Territory' for the purpose listed 'the Use' on Page 1 of this Agreement subject to the following terms and conditions.

1. The License is limited to the permission granted and the Content detailed herein and does not extend to any other permission or content.
2. Cambridge gives no warranty or indemnity in respect of any third-party copyright material included in the Content, for which the Licensee should seek separate permission clearance.
3. The integrity of the Content must be ensured.
4. The License does extend to any edition published specifically for the use of handicapped or reading-impaired individuals.
5. The Licensee shall provide a prominent acknowledgement in the following format: author/s, title of article, name of journal, volume number, issue number, page references, , reproduced with permission.

Other terms and conditions:
v1.0

Questions? customercare@copyright.com or +1-855-239-3415 (toll free in the US) or +1-978-646-2777.

Unsteady effects of strong shock-wave/boundary-layer interaction at high Reynolds number

Vito Pasquariello[1,†], **Stefan Hickel**[2] **and Nikolaus A. Adams**[1]

[1]Technical University of Munich, Department of Mechanical Engineering,
Chair of Aerodynamics and Fluid Mechanics, Boltzmannstr. 15,
D-85748 Garching bei München, Germany

[2]Technische Universiteit Delft, Faculty of Aerospace Engineering, P.O. Box 5058,
2600 GB Delft, The Netherlands

We analyse the low-frequency dynamics of a high Reynolds number impinging shock-wave/turbulent boundary-layer interaction (SWBLI) with strong mean-flow separation. The flow configuration for our grid-converged large-eddy simulations (LES) reproduces recent experiments for the interaction of a Mach 3 turbulent boundary layer with an impinging shock that nominally deflects the incoming flow by 19.6°. The Reynolds number based on the incoming boundary-layer thickness of $Re_{\delta_0} \approx 203 \times 10^3$ is considerably higher than in previous LES studies. The very long integration time of $3805\delta_0/U_0$ allows for an accurate analysis of low-frequency unsteady effects. Experimental wall-pressure measurements are in good agreement with the LES data. Both datasets exhibit the distinct plateau within the separated-flow region of a strong SWBLI. The filtered three-dimensional flow field shows clear evidence of counter-rotating streamwise vortices originating in the proximity of the bubble apex. Contrary to previous numerical results on compression ramp configurations, these Görtler-like vortices are not fixed at a specific spanwise position, but rather undergo a slow motion coupled to the separation-bubble dynamics. Consistent with experimental data, power spectral densities (PSD) of wall-pressure probes exhibit a broadband and very energetic low-frequency component associated with the separation-shock unsteadiness. Sparsity-promoting dynamic mode decompositions (SPDMD) for both spanwise-averaged data and wall-plane snapshots yield a classical and well-known low-frequency breathing mode of the separation bubble, as well as a medium-frequency shedding mode responsible for reflected and reattachment shock corrugation. SPDMD of the two-dimensional skin-friction coefficient further identifies streamwise streaks at low frequencies that cause large-scale flapping of the reattachment line. The PSD and SPDMD results of our impinging SWBLI support the theory that an intrinsic mechanism of the interaction zone is responsible for the low-frequency unsteadiness, in which Görtler-like vortices might be seen as a continuous (coherent) forcing for strong SWBLI.

Key words: boundary layer separation, compressible turbulence, shock waves

---

† Email address for correspondence: vito.pasquariello@tum.de

1. Introduction

Shock-wave/turbulent boundary-layer interactions (SWBLI) occur in a wide range of practical flow devices, such as supersonic air intakes, turbomachine cascades, overexpanded nozzles and high-speed aerodynamic applications in general, and are often critical for the system performance. Although SWBLI have been an active research field for more than 60 years (Dolling 2001), there are still many open questions, in particular regarding unsteady effects of interactions where the adverse pressure gradient imposed by the shock leads to boundary-layer separation. Such interactions form a complex dynamical system with a broad range of temporal and spatial scales. Unsteady pressure and friction forces may couple to resonant frequencies of the structure and may result in failure due to fatigue (Dolling 2001; Délery & Dussauge 2009). Of particular interest is the low-frequency unsteadiness of the reflected shock observed in SWBLI with mean boundary-layer separation. This phenomenon occurs at frequencies typically one to two orders of magnitude lower than the characteristic frequency of the integral scales within the incoming turbulent boundary layer U_0/δ_0, where U_0 is the free stream velocity and δ_0 the upstream 99 % velocity-based boundary-layer thickness. While experiments and numerical investigations for canonical SWBLI (e.g. compression ramp, impinging oblique shock, blunt fin, forward-facing step) unanimously confirm the existence of broadband low-frequency shock motions, the precise mechanism that explains the separation in time scales remains unknown. Since the first high-frequency measurements by Kistler (1964), the mechanism responsible for low-frequency large-scale shock oscillations has been the main research focus with the outcome of theories typically categorised as upstream or downstream mechanisms (see also the recent review paper by Clemens & Narayanaswamy (2014) for a summary).

Upstream mechanisms link the source of unsteadiness to flow phenomena or events in the upstream turbulent boundary layer (TBL). Experimentally, Andreopoulos & Muck (1987) were among the first to find a direct correlation between bursting events of the incoming TBL and shock motions for their Mach 3 compression ramp flow. Similarly, Erengil & Dolling (1993) observed a direct response of the reflected shock to upstream pressure fluctuations, which however results in a high-frequency smaller-scale jitter motion that could not explain the large-scale low-frequency oscillations. Adams (2000) performed a direct numerical simulation (DNS) of a Mach 3 compression ramp flow and found the bursting frequency being very close to the shock-crossing frequency, supporting the earlier experimental findings of Andreopoulos & Muck (1987). Ünalmis & Dolling (1994) proposed that a low-frequency thickening/thinning of the upstream TBL causes an upstream/downstream motion of the shock. Later, Beresh, Clemens & Dolling (2002) and Hou, Clemens & Dolling (2003) used particle image velocimetry (PIV) and verified that the upstream conditionally averaged velocity profiles were fuller when the shock foot was downstream (and *vice versa*). Using time-resolved PIV on a streamwise–spanwise plane and applying Taylor's hypothesis, Ganapathisubramani, Clemens & Dolling (2009) found low-velocity fluid upstream of their compression ramp flow that remained coherent for approximately 50 boundary-layer thicknesses. The authors found a strong correlation between these so-called superstructures and an instantaneous separation line surrogate. Based on the length of such a structure $\lambda = 50\delta_0$ and U_0, the authors propose that the superstructure-induced low frequency scales like $U_0/2\lambda$. Since this value is of the order of $O(0.01 U_0/\delta_0)$ which is typically found for the shock motion, they conclude that the passage of these superstructures is responsible for the low-frequency unsteadiness in their interaction. Contrary to this, Wu & Martín (2008)

did not find any significant low-frequency correlation between the true separation point (defined through the zero skin-friction coefficient) and upstream turbulent structures for their DNS of a Mach 2.9 compression ramp configuration. Only when using a similar instantaneous separation surrogate as that of Ganapathisubramani *et al.* (2009) were the authors able to detect significant correlations, demonstrating the uncertainty of such methods when applied to experimental measurements. At the same time the authors found a high-frequency/small-amplitude spanwise wrinkling of the shock which correlated with the mass flux in the incoming TBL. Applying tomographic PIV to a Mach 2.1 impinging SWBLI, Humble *et al.* (2009) further observed that the passage of upstream coherent structures results in a spanwise wrinkling of the shock foot.

Theories of the second category relate the separation-shock motion to mechanisms originating downstream of it, thus basically connecting the dynamics of the separation bubble to unsteady shock movements. This idea traces back to early experimental findings of Dolling & Erengil (1991) and Thomas, Putnam & Chu (1994) for compression ramp configurations, and more recent investigations by Dupont, Haddad & Debiève (2006) for impinging SWBLI. These studies showed that wall-pressure fluctuations measured close to the shock foot and near reattachment are correlated at frequencies connected to the separation-shock motion. The measured phase shift indicates that the separation bubble expands and contracts periodically. Similarly, based on conditionally averaged PIV velocity fields for small and large bubbles, Piponniau *et al.* (2009) found that the position of the reflected shock is located more downstream and upstream, respectively. They proposed a self-sustaining mechanism to explain the low-frequency shock motions based on fluid entrainment by the shear layer generated downstream of the reflected shock above the closed separation bubble. A similar entrainment/recharge mechanism consisting of a feedback loop between the separation bubble, the detached shear layer and the shock system is proposed by Wu & Martín (2008). Pirozzoli & Grasso (2006) conducted a short-duration DNS of a Mach 2.25 impinging SWBLI and proposed an acoustic feedback mechanism as a possible driver of low-frequency unsteadiness. They assume that shear-layer vortices interacting with the incident-shock tip generate acoustic disturbances that propagate upstream through the subsonic layer while subsequently inducing an oscillatory motion of the separation point, similar to Rossiter modes in cavity flows. Touber & Sandham (2009) performed large-eddy simulations (LES) of the impinging SWBLI experiment by Dupont *et al.* (2006) for a weak deflection angle of 8°. Their linear-stability analysis of the mean flow revealed a two-dimensional, zero-frequency, globally unstable mode which could be linked to the low-frequency unsteadiness. Further, the authors detected upstream-travelling acoustic waves within the separation bubble, confirming the possibility of the acoustic feedback mechanism proposed by Pirozzoli & Grasso (2006). Starting from the Navier–Stokes equations and incorporating LES results, Touber & Sandham (2011) derived a stochastic ordinary differential equation for the shock foot low-frequency motions, whose final form was found to be mathematically equivalent to the one postulated by Plotkin (1975). They further argued that the low-frequency unsteadiness is an intrinsic low-pass filter due to the interaction and not necessarily an imposed property due to upstream or downstream forcing. However, some coherent or incoherent (white noise) forcing must be present at low frequency for the system to manifest low-frequency shock oscillations.

Based on conflicting observations in many studies with respect to the source of low-frequency shock motions, Clemens & Narayanaswamy (2009) and Souverein *et al.* (2010) argued that both mechanisms (upstream and downstream) are probably

always present, with a weighting function depending on the state of the SWBLI. For interactions with a separation length smaller or equal to $2\delta_0$, the shock unsteadiness is highly correlated with upstream TBL fluctuations, while stronger interactions are most probably dominated by downstream mechanisms inherent to the shock/bubble system itself (Clemens & Narayanaswamy 2014).

Numerical investigations (DNS, LES) for impinging SWBLI that reached sufficiently long integration times, suitable for addressing the low-frequency unsteadiness, are rare in the literature. DNS results by Pirozzoli & Grasso (2006) covered an integration time of only $25\delta_0/U_0$. Priebe, Wu & Martín (2009) studied the case of a Mach 2.9 impinging SWBLI at a Reynolds number of $Re_{\delta_0} \approx 38 \times 10^3$ and deflection angle of $12°$ by means of DNS, matching experimental flow conditions of Bookey *et al.* (2005). Their simulation covers approximately $800\delta_0/U_0$ and addressed low-frequency aspects of the interaction. However, a direct comparison with experimental unsteady measurements is missing. Touber & Sandham (2009) were probably among the first to publish a successful comparison between their long-time $(10^4\delta_0/U_0)$ narrow-domain LES results and experimental data with respect to the unsteady shock motion. Further LES studies for impinging SWBLI with a focus on low-frequency aspects of the interaction have been published thereafter (Pirozzoli *et al.* 2010; Agostini *et al.* 2012; Hadjadj 2012; Aubard, Gloerfelt & Robinet 2013; Morgan *et al.* 2013; Pasquariello *et al.* 2014; Nichols *et al.* 2016). All of these studies, however, predominantly focused on weak interactions (with respect to the absence of a distinct pressure plateau within the separated flow) and/or low Reynolds numbers being typically below $Re_{\delta_0} \approx 60 \times 10^3$. High Reynolds number compression corner experiments (Dolling & Murphy 1983; Dolling & Or 1985) have shown that the wall-pressure signal near the separation-shock foot is highly intermittent and basically reflects the inviscid pressure jump across the oscillating shock. For low Reynolds number studies, the reflected shock foot does not penetrate as deeply into the TBL as it does in the high Reynolds number case. Increased viscous effects diffuse the separation-shock foot into a compression fan, which in turn results in a broader range of frequencies with attenuated shock intermittency (Ringuette *et al.* 2009). This behaviour is well documented for compression corner flows, but has not been addressed so far in numerical studies for impinging SWBLI.

The purpose of the current study is to extend the available numerical database for high Reynolds number impinging SWBLI by a case with strong flow separation from wall-resolved long-time integrated LES. We adopt the experimental flow configuration of Daub, Willems & Gülhan (2015), where the incoming TBL ($Ma = 3$, $Re_{\delta_0} \approx 200 \times 10^3$) interacts with an oblique shock that is strong enough to cause a very large separation bubble with a length of $15.5\delta_0$. The long integration time of $3805\delta_0/U_0$ allows us to analyse low-frequency aspects of the interaction in detail. A spectral analysis of wall-pressure probes serves as a starting point and provides the dominant frequencies involved in the interaction. Further, a modal decomposition of the flow by dynamic mode decomposition (DMD) (Rowley *et al.* 2009; Schmid 2010) is used to relate global flow phenomena to frequencies identified by the (local) wall-pressure spectra. Similar DMD studies can be found in the literature based on spanwise-averaged snapshots (Pirozzoli *et al.* 2010; Grilli *et al.* 2012; Nichols *et al.* 2016). We adopt this methodology in a first step, and discuss similarities/differences. Subsequently we investigate three-dimensional effects based on snapshots of the two-dimensional skin-friction coefficient. The article is organised as follows: in §2 we provide details of the numerical approach, describe the experimental flow configuration and discuss numerical details for the LES. The main results of this study

are summarised in § 3. A grid- and spanwise-domain-sensitivity study is presented in § 3.1, together with a validation of the incoming TBL. The mean-flow field and a first comparison with experimental wall-pressure measurements are presented in § 3.2. Three-dimensional modulations of the nominally two-dimensional interaction will be highlighted in the same section. A spectral analysis of wall-pressure probes is presented in § 3.3 and compared with unsteady experimental measurements by Daub *et al.* (2015). Furthermore, high Reynolds number effects with respect to the intermittent character of the interaction are analysed. A detailed DMD analysis is provided in § 3.4, giving access to the flow organisation of dominant low- and medium-frequency modes. Finally, we summarise our results and discuss the physical origin of the low-frequency unsteadiness in § 4.

2. Numerical approach and flow configuration

2.1. *Governing equations and numerical approach*

We solve the three-dimensional compressible Navier–Stokes equations in conservative form on Cartesian grids

$$\partial_t \boldsymbol{U} + \nabla \cdot \boldsymbol{F}(\boldsymbol{U}) - \nabla \cdot \boldsymbol{D}(\boldsymbol{U}) = 0, \tag{2.1}$$

with the state vector $\boldsymbol{U} = [\rho, \rho u_1, \rho u_2, \rho u_3, E]$ consisting of density ρ, momentum ρu_i and total energy E. In the above equation the total flux is split into an inviscid part $\boldsymbol{F} = [\boldsymbol{f}_1, \boldsymbol{f}_2, \boldsymbol{f}_3]^{\mathrm{T}}$ following

$$\boldsymbol{f}_i(\boldsymbol{U}) = [u_i \rho, u_i \rho u_1 + \delta_{i1} p, u_i \rho u_2 + \delta_{i2} p, u_i \rho u_3 + \delta_{i3} p, u_i(E + p)]^{\mathrm{T}}, \tag{2.2}$$

and a viscous contribution $\boldsymbol{D} = [\boldsymbol{d}_1, \boldsymbol{d}_2, \boldsymbol{d}_3]^{\mathrm{T}}$ following

$$\boldsymbol{d}_i(\boldsymbol{U}) = [0, \tau_{i1}, \tau_{i2}, \tau_{i3}, u_k \tau_{ik} - q_i]^{\mathrm{T}}, \tag{2.3}$$

where u_i is the velocity vector and τ_{ij} the viscous stress tensor, which according to the Stokes hypothesis for a Newtonian fluid is

$$\tau_{ij} = \mu(\partial_j u_i + \partial_i u_j - 2/3 \delta_{ij} \partial_k u_k). \tag{2.4}$$

The heat flux q_i due to conduction follows from the Fourier law

$$q_i = -\kappa \, \partial_i T. \tag{2.5}$$

We model air as a perfect gas with a specific heat ratio of $\gamma = 1.4$ and a specific gas constant of $\mathcal{R} = 287.05$ J (kg K)$^{-1}$. Pressure p and temperature T are determined by the ideal-gas equation of state

$$p = \rho \mathcal{R} T, \tag{2.6}$$

and the definition of total energy E

$$E = \frac{p}{\gamma - 1} + \frac{1}{2} \rho u_i u_i. \tag{2.7}$$

Temperature dependences of dynamic viscosity μ and thermal conductivity κ are modelled through Sutherland's law and constant Prandtl number,

$$\mu = \mu_{ref} \frac{T_{ref} + C}{T + C} \left(\frac{T}{T_{ref}} \right)^{1.5}, \tag{2.8}$$
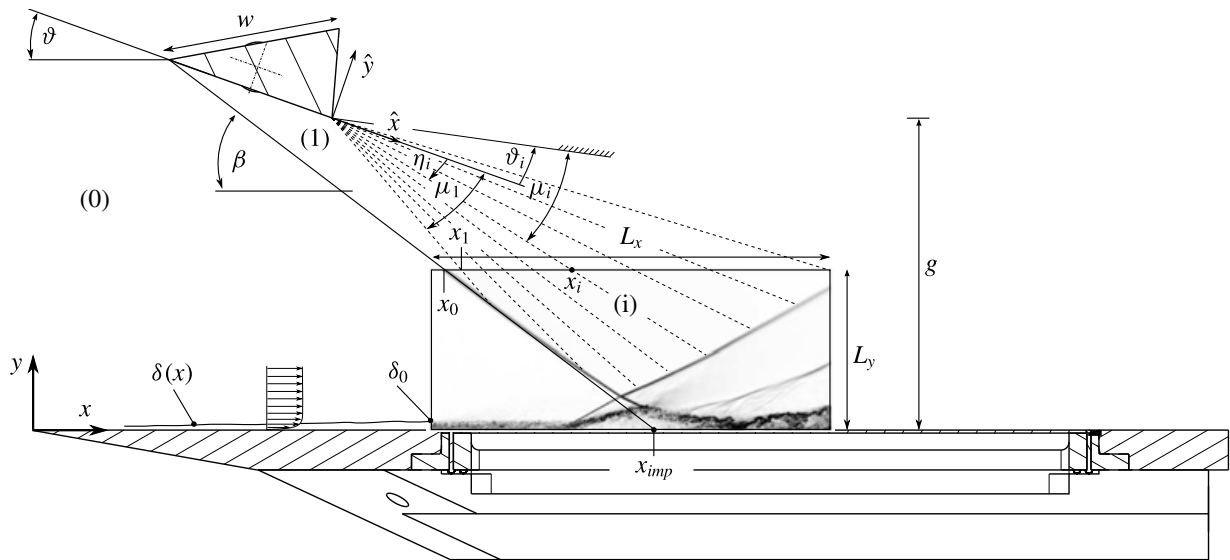
97

FIGURE 1. Schematic of the experimental and numerical set-up. An instantaneous numerical schlieren image is included.

$$\kappa = \frac{\gamma \mathcal{R}}{(\gamma - 1)Pr}\mu, \qquad (2.9)$$

with $Pr = 0.72$, $T_{ref} = 293.15$ K, $C = 122$ K and $\mu_{ref} = 18.21 \times 10^{-6}$ Pa s.

The compressible Navier–Stokes equations are solved using the adaptive local deconvolution method (ALDM) for the discretisation of the convective fluxes (Hickel, Adams & Domaradzki 2006; Hickel, Egerer & Larsson 2014). ALDM is a nonlinear finite volume method that provides a physically consistent subgrid-scale (SGS) turbulence model for implicit LES. Employing a shock sensor based on the sensor functional of Ducros *et al.* (1999) to detect discontinuities and switch on the shock dissipation mechanism, ALDM can capture shock waves, while smooth waves and turbulence are propagated accurately without excessive numerical dissipation (Hickel *et al.* 2014). Although the physically consistent implicit turbulence model (based on the eddy damped quasi-normal Markovian (EDQNM) theory (Lesieur, Métais & Comte 2005)) implies a second-order truncation error, ALDM provides a similar spectral resolution of linear waves (modified wavenumber) as sixth-order central difference schemes. The interested reader is referred to Hickel *et al.* (2014) for a detailed validation based on canonical shock–turbulence cases and a modified wavenumber analysis. The viscous flux is discretised using a second-order central difference scheme, and the third-order Runge–Kutta scheme of Gottlieb & Shu (1998) is used for time integration. This numerical method has been successfully applied to a wide range of LES involving shock–turbulence interaction, ranging from canonical test cases (Hickel *et al.* 2014) to SWBLI at a compression–expansion ramp (Grilli *et al.* 2012; Grilli, Hickel & Adams 2013), flow control of SWBLI on a flat plate (Pasquariello *et al.* 2014), shock train in a divergent nozzle (Quaatz *et al.* 2014) and transition analysis between regular and irregular shock patterns of SWBLI (Matheis & Hickel 2015).

2.2. *Experimental and numerical set-up*

The flow configuration for the present study has been adopted from recent experiments conducted by Daub *et al.* (2015), a schematic of which is shown in figure 1. The test

Ma	T_0	p_0	U_0	ϑ	δ_0	θ_0	Re_{δ_0}	Re_{θ_0}
3.0	273.7 K	582 kPa	594 m s^{-1}	19.6°	4.0 mm	0.28 mm	203×10^3	14×10^3

TABLE 1. Main flow parameters.

facility is a blowdown wind tunnel with a continuously adjustable nozzle, enabling a Mach number range of $Ma = [0.5, 4.5]$, and a closed test section of 0.6×0.6 m. A wedge is mounted on a shaft and deflects the incoming flow by $\vartheta = 19.6°$, resulting in a steady incident shock that interacts with a spatially developing flat plate TBL. For fluid–structure interaction (FSI) experiments, the baseplate can be optionally equipped with an elastic panel and the shock generator may be pitched, inducing a time-varying load on the panel (Daub, Willems & Gülhan 2016). The shock generator as well as the baseplate span the wind tunnel width. The wide test section together with the full-span model (shock generator and baseplate) lead to a nearly two-dimensional SWBLI, which is demonstrated in Daub *et al.* (2015). They show that the streamwise wall-pressure evolution measured at the centreline and 90 mm off centre coincide (see figure 5 in the respective publication). The TBL is tripped close to the leading edge of the baseplate by a 5 mm wide strip of F150-macrogrits with mean diameter of 60 μm. Figure 1 includes an instantaneous numerical schlieren image obtained from the LES. The adverse pressure gradient imposed by the incident shock is sufficient to cause strong flow separation. Note that the incident shock is curved due to the interaction with the characteristics emanating from the centred Prandtl–Meyer expansion (PME). This interaction results from the short wedge length w, which was a deliberate experimental design to facilitate actuation in FSI experiments employing the wedge as fast-pitching shock generator (Daub *et al.* 2016). The theoretical incident-shock path is also shown to reflect the degree of shock curvature and to further indicate the nominal inviscid impingement location $x_{imp} = 0.311$ m.

Main flow parameters for the LES are summarised in table 1 and are set in accordance with the reference experiment. The flat plate TBL is characterised by a free stream Mach number of $Ma = 3$, a stagnation temperature of $T_0 = 273.7$ K and a stagnation pressure of $p_0 = 582$ kPa. Note that the stagnation conditions differ slightly from the ones reported in Daub *et al.* (2015) since the values summarised in table 1 refer to the specific SWBLI experimental realisation with wedge angle $\vartheta = 19.6°$ and resulting shock angle $\beta = 37.3°$, while in the referred publication an ensemble average over multiple runs is reported. The TBL thickness, based on 99 % of the free stream velocity U_0, is estimated to be $\delta_0 = 4$ mm at the LES-domain inlet. The compressible momentum thickness is $\theta_0 = 0.28$ mm. The Reynolds number based on the incoming boundary-layer thickness is $Re_{\delta_0} = U_0\delta_0/\nu_0 = 203 \times 10^3$, where ν_0 is the free stream kinematic viscosity. Based on the compressible momentum thickness the Reynolds number is $Re_{\theta_0} = U_0\theta_0/\nu_0 = 14 \times 10^3$. The wedge width is $w = 21.75\delta_0$ and the channel height to wedge width ratio equals $g^+ = g/w = 1.8$, see also figure 1. For a given shock-generator position the non-dimensional quantity g^+ implicitly determines the relative impingement position of the first PME characteristic on the baseplate with respect to x_{imp}, a quantity often referred to when dealing with transition studies between regular and irregular SWBLI (Naidoo & Skews 2011; Matheis & Hickel 2015).

The experimental database includes mean and unsteady wall-pressure measurements within the interaction region. The former are realised through 48 Pressure Systems,

Inc. (PSI) pressure ports placed at the *xy*-centreplane and 90 mm off centre, while fluctuating wall-pressure measurements are collected through 10 high-speed Kulite Semiconductor, Inc. (Model XCQ-062) pressure transducers placed at the *xy*-centreplane. The natural frequency of the sensors is 240 kHz. Data acquisition is performed with a National Instruments 24-bit bridge module PXIe 4331 at a sampling rate of 100 kHz, thus limiting the frequency response of the unsteady measurements to about 50 kHz. Please refer to Daub *et al.* (2015) for a more detailed discussion on applied measurement techniques.

2.3. *Boundary conditions, grid distribution and numerical parameters*

The LES domain in the *xy*-plane is shown in figure 1 and covers a rectangular box with dimensions $L_x = 50\delta_0$ in the streamwise and $L_y = 20\delta_0$ in the wall-normal direction. The spanwise width is varied in conjunction with a domain-sensitivity study (see table 3 and § 3.1) and covers $L_z = [2.25, 4.5, 9]\delta_0$. At the domain inlet a digital filter based boundary condition is used (Klein, Sadiki & Janicka 2003), for which first and second-order statistical moments have been prescribed through a precursor zero pressure gradient temporal boundary-layer simulation with target TBL thickness of δ_0 and otherwise same flow conditions as the SWBLI simulations. The digital filter technique is particularly suitable for the present studies as it does not generate spurious correlations of the inflow data, a drawback exhibited by recycling–rescaling techniques (Stolz & Adams 2003). The only delicate requirement when using synthetic turbulence generators is to specify realistic integral length scales for all three velocity components and coordinate directions to avoid laminarisation issues (Touber & Sandham 2009). The digital filter technique induces a spatial transient downstream of the inflow which depends on the chosen integral length scales and additionally constraints the streamwise domain extent. By inspecting mean and root-mean-square (r.m.s.) profiles we found that a transient distance of approximately $10\delta_0$ is sufficient. Similar values can be found in the literature for supersonic TBL, e.g. Grilli *et al.* (2013) report a transient length of $8\delta_0$ for their LES of a compression–expansion ramp configuration and Wang *et al.* (2015) find a transient length of $12\delta_0$ for their three-dimensional SWBLI studies including side walls.

Linear extrapolation of all flow variables is used at the outlet and the flat plate is modelled as an adiabatic no-slip wall. Spanwise periodicity is enforced, which is a legitimate assumption for the present flow configuration as discussed in § 2.2. Confinement effects as extensively studied by Bermejo-Moreno *et al.* (2014) are not expected to be relevant for the SWBLI under investigation. As shown in figure 1 the LES domain does not include the shock generator. We rather chose the domain height in such a way that the first characteristic from the PME does not intersect the incident shock, thus requiring $x_0 < x_1$. We neglect the boundary layer on the wedge surface and analytically prescribe the aerodynamic and thermodynamic states upstream of the incident shock (0), downstream of the incident shock and upstream of the PME (1) and within the PME (i) in terms of Riemann invariants. The incident shock is introduced by imposing a jump of the flow variables at x_0 that satisfies the Rankine–Hugoniot relations for the shock angle $\beta = 37.3°$. The locations x_0 and x_1 with respect to the *xy* coordinate system can be calculated from

$$\left.\begin{aligned} x_0 &= x_{exp} - \cos\vartheta \cdot w + \frac{y_{exp} - L_y + \sin\vartheta \cdot w}{\tan\beta} \\ x_1 &= x_{exp} + \frac{y_{exp} - L_y}{\tan(\mu_1 + \vartheta)}, \end{aligned}\right\} \tag{2.10}$$

where $(x_{exp}, y_{exp}) = (0.149, 0.157)$ m denotes the location of the PME, and μ_1 is the Mach angle in flow region (1). For the present configuration we obtain $x_0 = 0.206$ m and $x_1 = 0.215$ m, thus resulting in a gap of $2.25\delta_0$ between the incident shock and the first characteristic of the PME on the top boundary patch.

In order to derive the flow states for an individual grid point x_i within the PME region, it is useful to introduce an additional coordinate system $\hat{x}\hat{y}$ which is aligned with the wedge surface and has its origin at (x_{exp}, y_{exp}). Each grid point on the top boundary patch can be associated with an individual Mach line inside the PME, which itself is characterised by the angle η_i. One can find the solution on the Mach line (i) by considering an imaginary wall at an angle ϑ_i for which the Mach line (i) defines the trailing edge characteristic of this auxiliary PME. The Mach number on ray (i) can be explicitly calculated from

$$Ma_i = \sqrt{1 + \frac{\gamma + 1}{\gamma - 1} \cdot \tan^2 z_i}, \qquad (2.11)$$

where z_i replaces η_i by means of

$$z_i = \left(\frac{\gamma - 1}{\gamma + 1}\right)^{0.5} \cdot (\nu_{(1)} + \pi/2 - \eta_i), \quad 0 \leqslant z_i \leqslant \pi/2. \qquad (2.12)$$

Herein $\nu_{(1)}$ denotes the Prandtl–Meyer function for the known flow state (1) which in its general form is given by

$$\nu_{(\bullet)} = \sqrt{\frac{\gamma + 1}{\gamma - 1}} \cdot \tan^{-1} \sqrt{\frac{\gamma - 1}{\gamma + 1}(Ma_{(\bullet)}^2 - 1)} - \tan^{-1} \sqrt{Ma_{(\bullet)}^2 - 1}. \qquad (2.13)$$

Once the Mach number Ma_i has been calculated, the state vector U at x_i is obtained by considering the flow state (1), the local flow angle with respect to the xy coordinate system $(\vartheta - \mu_i - \eta_i)$ and isentropic relations. An auxiliary two-dimensional Reynolds-averaged Navier–Stokes (RANS) simulation including the shock generator has been used to verify the boundary condition as well as the assumption of neglecting the boundary-layer growth on the wedge surface. By comparing the streamwise evolution of flow variables at a specific wall-normal distance we found that the boundary-layer growth and its influence on the trailing edge PME can be neglected.

Table 2 summarises simulation parameters for the computations that have been performed for a grid-sensitivity study. In total four different grid resolutions were considered. For all configurations the streamwise and spanwise directions are uniformly discretised, whereas a hyperbolic grid stretching is applied in the wall-normal direction following

$$y_j = L_y \cdot \tanh\left(\frac{\beta_y(j - 1)}{N_y - 1}\right) \bigg/ \tanh(\beta_y). \qquad (2.14)$$

Herein, j is the grid point index and β_y is a stretching factor which is the same for all configurations studied (see table 2). The number of cells in wall-normal direction N_y is the same for all cases and chosen in such a way that in combination with a given β_y at least 10 cells reside within the streamwise Reynolds normal stress peak of the incoming TBL and at the same time guarantees a grid resolution in wall units of $\Delta y_{min}^+ < 1$ for the first wall cell.

Grid	$\mathcal{G}^1$	$\mathcal{G}_z^1$	$\mathcal{G}^2$	$\mathcal{G}_x^2$
Domain size				
$L_x \times L_y \times L_z$ in δ_0	$50 \times 20 \times 4.5$	$50 \times 20 \times 4.5$	$50 \times 20 \times 4.5$	$50 \times 20 \times 4.5$
Grid parameters				
$N_x \times N_y \times N_z$	$880 \times 328 \times 315$	$880 \times 328 \times 630$	$1760 \times 328 \times 630$	$3520 \times 328 \times 630$
$\Delta x^+ \times \Delta y_{min}^+ \times \Delta z^+$	$78 \times 0.9 \times 19.6$	$78 \times 0.9 \times 9.8$	$39 \times 0.9 \times 9.8$	$19.5 \times 0.9 \times 9.8$
β_y	3.56	3.56	3.56	3.56
Runtime & statistics				
TU_0/δ_0 (FTT)	$446(9)$	$446(9)$	$446(9)/3805(76)$	$446(9)$
$\Delta t U_0/\delta_0 \cdot 10^3$	0.84	0.83	0.83	0.82
Sampling rate	Every $20\Delta t$	Every $20\Delta t$	Every $20\Delta t$	Every $20\Delta t$

TABLE 2. Numerical parameters for the grid-sensitivity study.

Domain	$\mathcal{D}^1$	$\mathcal{D}^2$	$\mathcal{D}^3$
Domain size			
$L_x \times L_y \times L_z$ in δ_0	$50 \times 20 \times 2.25$	$50 \times 20 \times 4.5$	$50 \times 20 \times 9$
Grid parameters			
$N_x \times N_y \times N_z$	$1760 \times 328 \times 315$	$1760 \times 328 \times 630$	$1760 \times 328 \times 1260$
$\Delta x^+ \times \Delta y_{min}^+ \times \Delta z^+$	$39 \times 0.9 \times 9.8$	$39 \times 0.9 \times 9.8$	$39 \times 0.9 \times 9.8$
β_y	3.56	3.56	3.56
Runtime & statistics			
TU_0/δ_0 (FTT)	$446(9)$	$446(9)/3805(76)$	$446(9)$
$\Delta t U_0/\delta_0 \cdot 10^3$	0.84	0.83	0.82
Sampling rate	Every $20\Delta t$	Every $20\Delta t$	Every $20\Delta t$

TABLE 3. Numerical parameters for the domain-sensitivity study.

The incoming TBL thickness δ_0 is discretised with 162 cells. Non-dimensionalisation is performed with respect to the inner length scale $l^+ = \nu_w/u_\tau$ measured at a reference plane $12.5\delta_0$ downstream of the LES inflow, where $u_\tau = \sqrt{\tau_w/\rho_w}$ is the friction velocity and $\tau_w = \mu_w (\partial u/\partial y)|_w$ is the wall shear stress. The coarsest grid configuration $\mathcal{G}^1$ results in streamwise and spanwise resolutions of $\Delta x^+ = 78$ and $\Delta z^+ = 19.6$, respectively. For $\mathcal{G}_z^1$ the number of cells in the spanwise direction N_z is doubled, resulting in $\Delta z^+ = 9.8$. For grid level $\mathcal{G}^2$, both the x and z resolutions are halved simultaneously when compared to $\mathcal{G}^1$, thus leading to $\Delta x^+ = 39$ and $\Delta z^+ = 9.8$. Finally, the number of cells in streamwise direction N_x is doubled for $\mathcal{G}_x^2$ which leads to $\Delta x^+ = 19.5$. A total amount of 90.9, 181.8, 363.6 and 727.3 million cells is used for $\mathcal{G}^1$, $\mathcal{G}_z^1$, $\mathcal{G}^2$ and $\mathcal{G}_x^2$, respectively. Statistics were gathered by averaging instantaneous three-dimensional snapshots of the flow every 20 steps (both in time and spanwise direction if not stated otherwise), excluding an initial transient of approximately $594\delta_0/U_0$ (or 11 flow-through times, FTT). After this transient we collect samples for a time period of $446\delta_0/U_0$ for the grid-sensitivity study. It will be shown in §3.1 that grid configuration $\mathcal{G}^2$ is sufficient to capture accurately the interaction zone. For corroborations of the low-frequency analysis this case has been additionally run for a much longer time period of $3805\delta_0/U_0$ (or 76 FTT). Besides investigating the sensitivity of statistical results with respect to the grid resolution, we
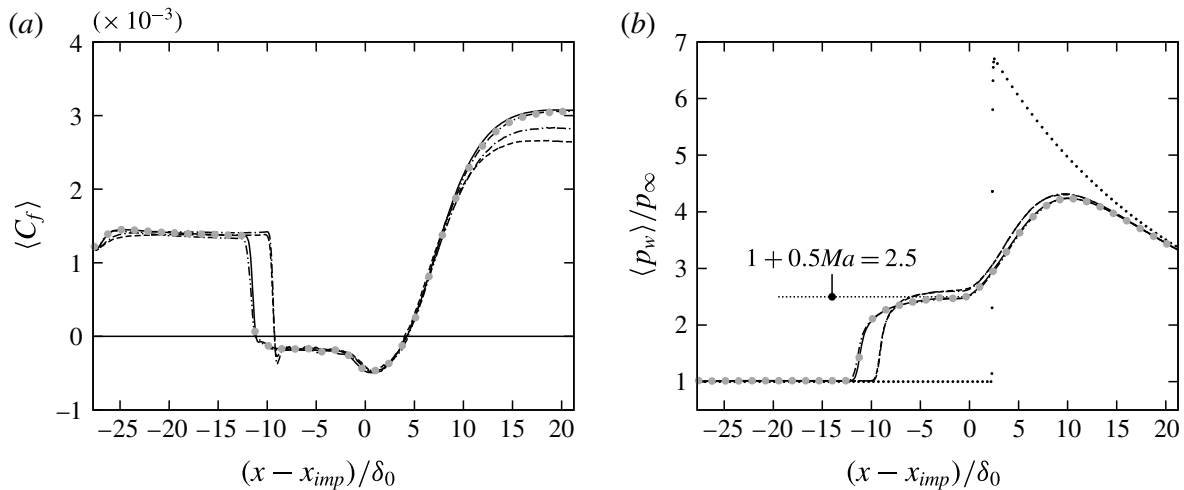
FIGURE 2. Grid-sensitivity study with respect to (*a*) skin-friction coefficient and (*b*) wall-pressure evolution. Reported quantities are time and spanwise averaged. (- - - -) $\mathcal{G}^1$, (—·—·—) $\mathcal{G}^1_z$, (———) $\mathcal{G}^2$, (—··—··) $\mathcal{G}^2_x$, (● (grey)) $\mathcal{G}^2$ averaged over $446\delta_0/U_0$, (······) inviscid interaction. The plateau pressure prediction according to Zukoski (1967) is also shown. See table 2 for reference.

perform a domain-sensitivity study in the spanwise direction based on $\mathcal{G}^2$, see table 3. The reference span of $L_z = 4.5\delta_0$ ($\mathcal{D}^2$) is halved ($\mathcal{D}^1$) and doubled ($\mathcal{D}^3$), resulting in three domain configurations $\mathcal{D}^i$.

3. Results

3.1. *Grid- and domain-sensitivity study*

A sensitivity study with respect to the chosen grid resolution as well as the spanwise domain extent is provided in the following. We start with the grid-sensitivity study for which table 2 summarises the main parameters. Figure 2(*a*,*b*) gives a comparison of time- and spanwise-averaged skin-friction coefficient $\langle C_f \rangle$ and wall-pressure evolution $\langle p_w \rangle / p_\infty$. Comparing the coarsest grid resolution $\mathcal{G}^1$ ($\Delta x^+ = 78$, $\Delta y^+_{min} = 0.9$, $\Delta z^+ = 19.6$) with the next level $\mathcal{G}^1_z$ (refinement in spanwise direction) one can state that the overall wall-pressure evolution coincides, while larger deviations can be observed in the post-interaction region for the skin-friction coefficient. Mean separation and reattachment locations (defined through $\langle C_f \rangle = 0$) and thus the resulting separation length L_{sep} remain unaltered. Note that the pressure strongly decreases in the relaxation zone due to the influence of the PME, resulting in a significantly higher skin-friction level than for the incoming TBL. The inviscid wall-pressure evolution (dotted line in figure 2*a*) clearly deviates from the stepwise pressure signal characteristic of a canonical inviscid shock reflection without PME. Characteristics emanating from the centred expansion in the current SWBLI already influence the incident shock (see shock curvature in figure 1), shifting the nominal inviscid shock impingement location downstream to $(x - x_{imp})/\delta_0 = 2.35$. Note that the wall pressure in the post-interaction zone for $(x - x_{imp})/\delta_0 > 20$ asymptotically reaches the inviscid solution. The next grid level $\mathcal{G}^2$ differs from the previous one $\mathcal{G}^1_z$ in the number of cells in streamwise direction, resulting in a grid resolution of $\Delta x^+ = 39$, $\Delta y^+_{min} = 0.9$ and $\Delta z^+ = 9.8$ in streamwise, wall-normal and spanwise directions, respectively. A strong effect is found for the skin friction and wall pressure, which is related to a significant change in separation length (relative increase of 14.8 % compared to $\mathcal{G}^1_z$) and probably caused

by the slightly different development of synthetic turbulence in the upstream TBL (see also the discussion related to Reynolds stresses in figure 4*b*). Note that the location of reattachment remains the same, while the mean separation point moves upstream.

Having identified an influence on the results by the streamwise resolution, we doubled the number of cells in this direction, which results in grid configuration $\mathcal{G}_x^2$ ($\Delta x^+ = 9.8$) with a total number of 727.3 million cells. Both the mean wall pressure and skin friction now do not show significant changes any more. Note that we also include results on $\mathcal{G}^2$ for the same integration time of $446\delta_0/U_0$ as for the remaining grid resolutions (see grey bullets (●) in figure 2*a,b*). The results suggest that the number of samples used in this study are sufficient to consider the results to be statistically converged with respect to the skin friction and wall pressure. Touber & Sandham (2009) also investigated the sensitivity of their results to the grid resolution by refining the grid in each coordinate direction separately. They did not find significant dependencies of the size of the separation bubble with respect to the chosen grid resolution. While our results may imply a different conclusion it must be noted that their reference grid has a similar resolution expressed in wall units ($\Delta x^+ = 40.6$, $\Delta y_{min}^+ = 1.6$, $\Delta z^+ = 13.5$) as our configuration $\mathcal{G}^2$, for which we have identified that a further refinement does not change the overall results.

To further address the effect of grid resolution, we analyse the prediction of the plateau pressure by applying the free interaction concept. Carrière, Sirieix & Solignae (1969) report a generalised correlation function $\widetilde{\mathcal{F}}$ independent of Mach and Reynolds number. It accounts for non-uniformities in the incoming outer flow as well as for wall curvature effects and is especially suited for SWBLI featuring strong streamline curvature in the free interaction zone (Matheis & Hickel 2015). While the pressure plateau value is around $\widetilde{\mathcal{F}}_p = 6.4$ on $\mathcal{G}^1$ and $\mathcal{G}_z^1$, we find a value of $\widetilde{\mathcal{F}}_p = 6.0$ for the grid configurations $\mathcal{G}^2$ and $\mathcal{G}_x^2$. The latter value is in perfect agreement with Erdos & Pallone (1963) who proposed a value of 6.0 for the pressure plateau in turbulent flow. Figure 2(*b*) includes the plateau pressure prediction by Zukoski (1967). The prediction again matches the numerical results on grid levels $\mathcal{G}^2$ and $\mathcal{G}_x^2$, suggesting that the Reynolds number in our studies ($Re_{\delta_0} \approx 2 \times 10^5$) is high enough such that the plateau pressure ratio essentially depends on the upstream Mach number.

Finally, we investigate the sensitivity of statistical results to the domain width. In total three configurations based on the grid resolution $\mathcal{G}^2$ have been considered. The reference span of $L_z = 4.5\delta_0$ ($\mathcal{D}^2$) is halved for $\mathcal{D}^1$ ($L_z = 2.25\delta_0$) and doubled for $\mathcal{D}^3$ ($L_z = 9\delta_0$), see table 3 for simulation parameters and figure 3 for corresponding results. While the small span LES ($\mathcal{D}^1$) reveals a slightly smaller separation bubble (downstream and upstream shift of the separation and reattachment location, respectively) and a different skin-friction recovery, the results for the reference span ($\mathcal{D}^2$) and the large span ($\mathcal{D}^3$) are nearly undistinguishable.

In figure 4, we report the van Driest transformed mean velocity profile as well as the r.m.s. of Reynolds stresses in Morkovin scaling for all grid resolutions and evaluated at the streamwise location $(x - x_{imp})/\delta_0 = -15.25$, which corresponds to a friction Reynolds number of $Re_\tau = \rho_w u_\tau \delta / \mu_w = 1523$. The figure also includes incompressible DNS data of Schlatter & Örlü (2010) at their highest available friction Reynolds number of $Re_\tau = 1271$. The inner layer and log-law region are in good agreement with the logarithmic law of the wall (with $\kappa = 0.41$ and $C = 5.2$) and the DNS data, with small differences recognisable in the wake region. The strength of the wake component increases with increasing momentum thickness Reynolds number and remains nearly constant above a value of approximately 6000 (Coles 1962; Smits & Dussauge 2006; Gatski & Bonnet 2009). For the incompressible DNS data a
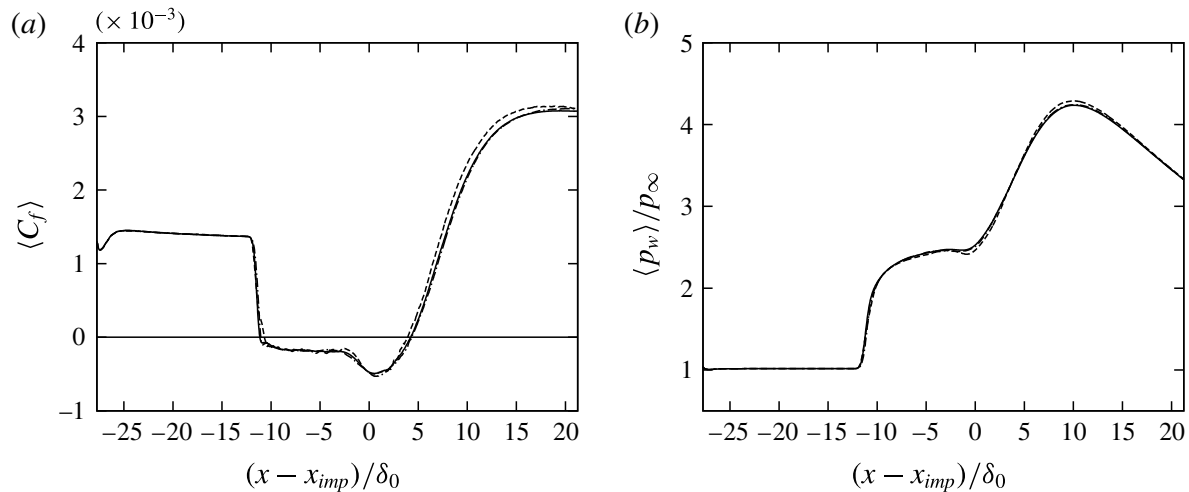
FIGURE 3. Domain-sensitivity study with respect to (*a*) skin-friction coefficient and (*b*) wall-pressure evolution. Reported quantities are time and spanwise averaged. (- - - -) $\mathcal{D}^1$, (——) $\mathcal{D}^2$, (– · – · –) $\mathcal{D}^3$. See table 3 for reference.
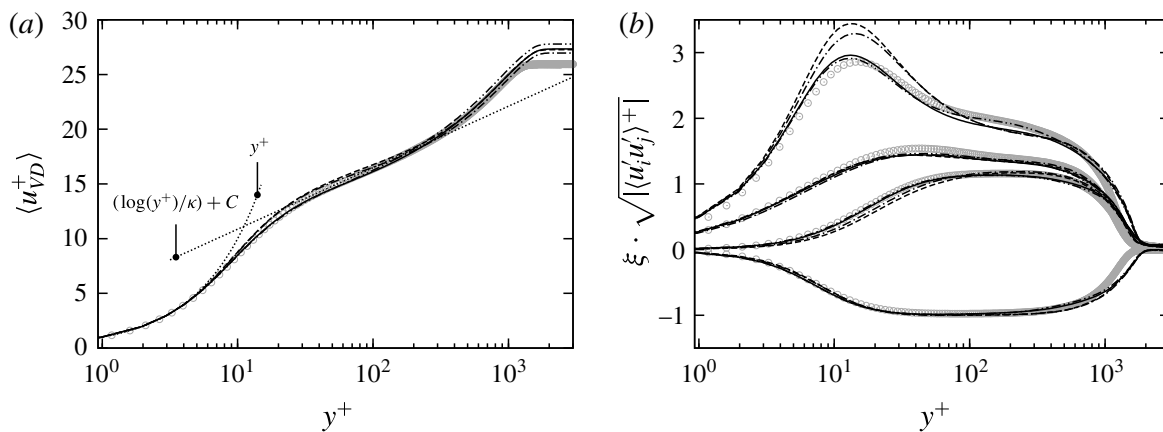

FIGURE 4. (*a*) van Driest transformed mean velocity profile and (*b*) r.m.s. of Reynolds stresses with density scaling $\xi = \sqrt{\langle\rho\rangle/\langle\rho_w\rangle}$ for all grid resolutions at $Re_\tau = 1523$ and $(x - x_{imp})/\delta_0 = -15.25$: (- - - -) $\mathcal{G}^1$, (– · – · –) $\mathcal{G}^1_z$, (——) $\mathcal{G}^2$, (– ·· – ··) $\mathcal{G}^2_x$. See table 2 for reference. (⊙ (grey)) Incompressible DNS data adopted from Schlatter & Örlü (2010) at $Re_\tau = 1271$.

momentum thickness Reynolds number of 4061 is reported. In order to compare with incompressible data we compute $Re_{\theta_i} = (\mu_0/\mu_w)Re_\theta = \rho_\infty\theta U_0/\mu_w = 6500$, explaining the higher wake velocity observed in figure 4(*a*) for the present LES. The streamwise Reynolds stress on grid levels $\mathcal{G}^1$ and $\mathcal{G}^1_z$, see figure 4(*b*), shows a significant overestimation of the peak value situated around $y^+ \approx 10.5$ when compared to the DNS data. On grid level $\mathcal{G}^2$ the agreement with the reference data is very good, both in the inner and log layer. Further improvement within the log layer is obtained with $\mathcal{G}^2_x$ for the streamwise Reynolds stress. Note that the friction Reynolds number Re_τ for the reference DNS is slightly lower, resulting in an earlier drop of the r.m.s. profiles at the wake region.

Finally we compare the skin-friction evolution obtained by the LES on grid level $\mathcal{G}^2$ with well-established correlations for incompressible flows, reference data from DNS and experimental data at different Mach numbers. A direct comparison with
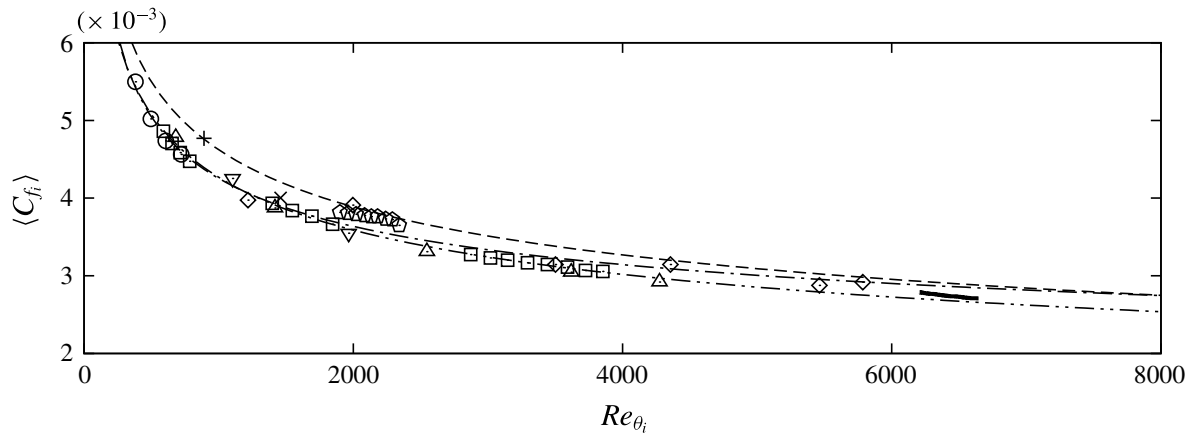
FIGURE 5. Incompressible skin-friction distribution. (——) Present LES ($\mathcal{G}^2$), (----) Blasius, (–·–·–) Kármán–Schoenherr (both adopted from Hopkins & Inouye (1971)), (–··–··) Smits, Matheson & Joubert (1983), (⊡) Pirozzoli & Bernardini (2011), (⊙) Komminaho & Skote (2002), (△) Schlatter & Örlü (2010), (▽) Simens *et al.* (2009), (⌂) Pirozzoli, Grasso & Gatski (2004), (×) Maeder, Adams & Kleiser (2001), (+) Guarini *et al.* (2000), (◇) Coles (1953) (CAT5301, from Fernholz & Finley (1977)).

incompressible data is possible after applying the van Driest II transformation to the compressible results (van Driest 1956). Figure 5 shows the incompressible skin-friction coefficient $\langle C_{f_i} \rangle$ as a function of Re_{θ_i}. Our present LES results agree well with the incompressible relations of Smits *et al.* (1983), Blasius and Kármán–Schoenherr (both adopted from Hopkins & Inouye (1971)), and available high Reynolds number data of Fernholz & Finley (1977).

The above grid- and domain-sensitivity studies have shown that the grid resolution $\mathcal{G}^2$ with a reference span of $L_z = 4.5\delta_0$ properly resolves the incoming TBL and accurately predicts the interaction region. Small improvements of the streamwise Reynolds stress prediction within the log layer are possible by further increasing the streamwise grid resolution ($\mathcal{G}_x^2$). However, the interaction region is unaffected by further refinement and thus we are confident that the grid resolution $\mathcal{G}^2$ is sufficiently fine. The analyses in the following are based on $\mathcal{G}^2$.

3.2. *Instantaneous and mean-flow organisation*

A first impression of the flow field is provided in figure 6, where we show both instantaneous and mean contours of temperature. Isolines in figure 6(*a*) indicate the instantaneous and mean reversed flow (defined through $u/u_\infty = 0$ and $\langle u \rangle/u_\infty = 0$, respectively). Additional isolines in figure 6(*b*) represent the shock system, the sonic line and the boundary-layer edge, where the latter is defined through an isovalue of mean spanwise vorticity $\langle \omega_z \rangle$ that gives the same boundary-layer thickness as the velocity-valued definition upstream of the interaction. Clearly, the adverse pressure gradient imposed by the incident shock is strong enough to cause a large flow separation and a separation shock originating well ahead of the inviscid impingement location. Note that x_{imp} is related to the theoretical location at which a straight incident shock would impinge on the flat plate in the absence of a centred PME, thus neglecting shock curvature effects. The separation shock intersects the incident shock well outside the TBL, indicating the strong character of the interaction. Délery & Marvin (1986) further characterised a strong interaction through the presence of three inflection points in the wall-pressure evolution, which are associated with the
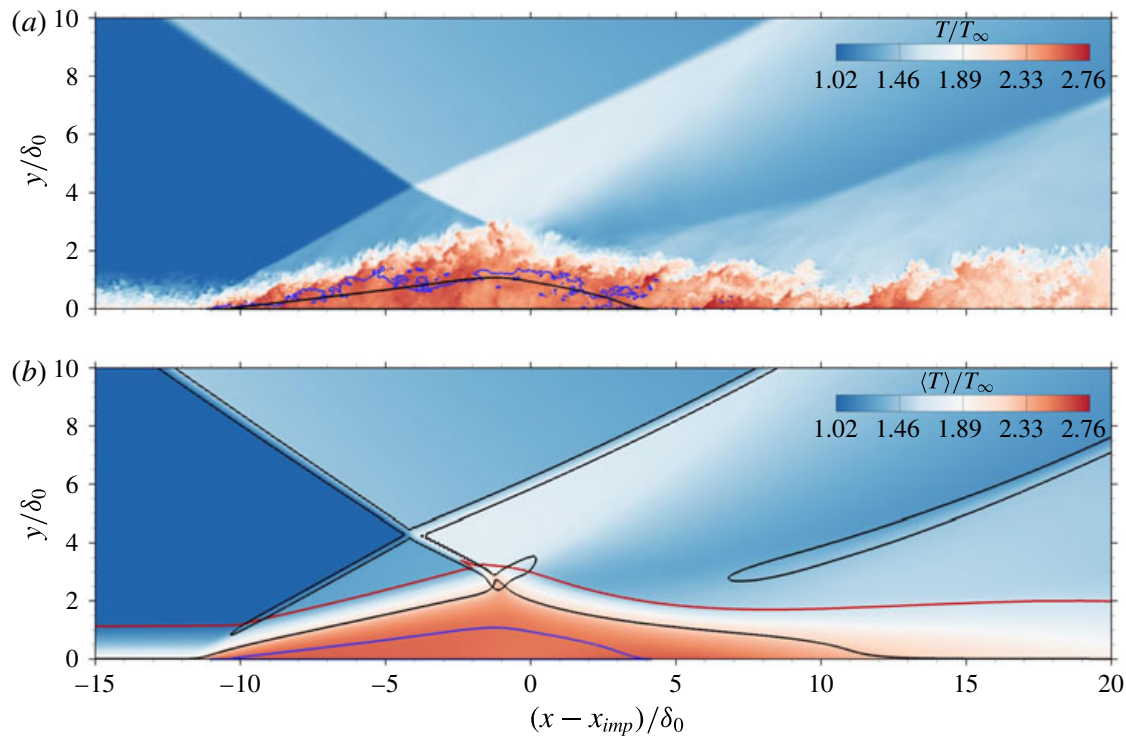
FIGURE 6. (Colour online) (*a*) Instantaneous contours of temperature in the *xy* midplane together with isolines indicating mean (——— (black)) and instantaneous (——— (blue)) reversed flow. (*b*) Time- and spanwise-averaged contours of temperature. The shock system is visualised by isolines of pressure gradient magnitude $|\nabla p|\delta_0/p_\infty = \{1.08, 3.28\}$. (——— (red)) $\langle\delta\rangle$, (——— (black)) $\langle Ma\rangle = 1$, (——— (blue)) $\langle u\rangle = 0$.

separation, the onset of reattachment and the reattachment compression. For even stronger interactions with an extended separated flow, a noticeable pressure plateau develops, as is the case for the present study (see figure 2*b*,*c*). The separation-shock foot penetrates deeply into the incoming TBL, a phenomenon associated with the high Reynolds number of the flow (Loginov, Adams & Zheltovodov 2006; Ringuette *et al.* 2009). As will be discussed later in § 3.3, this feature causes a stronger footprint on the fluctuating wall-pressure signal as compared to SWBLI at lower Reynolds number and same Mach number (Adams 2000; Pasquariello *et al.* 2014; Nichols *et al.* 2016). In the same figure the formation of a detached turbulent shear layer originating from the separation shock is visible and contains the separated-flow area. Compression waves are formed along with the reattachment process, which finally coalesce into the reattachment shock. The instantaneous separation bubble is strongly perturbed near the initial part of the interaction zone, probably being related to fluid entrainment through the shear-layer vortices in this region (Piponniau *et al.* 2009). The TBL grows significantly across the interaction, reaching a maximum of approximately $3\delta_0$ in the vicinity of the separation-bubble apex, see figure 6(*b*). The subsequent PME reduces the TBL thickness, which settles down to a value of $2\delta_0$ downstream of the interaction.

The mean separation length is determined from the skin-friction distribution shown in figure 7(*a*) and results in $L_{sep} = 15.5\delta_0$. Mean separation x_s and reattachment x_r locations are indicated by vertical dashed lines and are located at $(x - x_{imp})/\delta_0 = -11.25\delta_0$ and $4.25\delta_0$, respectively. Priebe & Martín (2012) found in their compression corner results that the separation is not uniformly strong in the sense that the
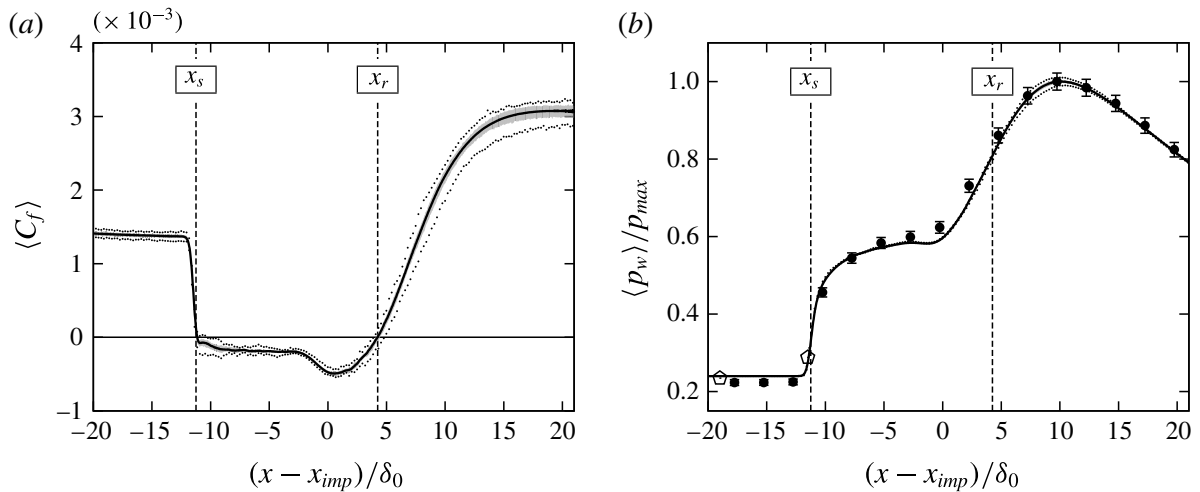
FIGURE 7. (*a*) Skin-friction and (*b*) wall-pressure evolution: (——) present LES (averaged in time and spanwise direction; spanwise minimum and maximum values of the time-averaged data are indicated by the grey shaded area for the long integration time of $3805\delta_0/U_0$ and by dots for the short integration time of $446\delta_0/U_0$), (●) experimental static pressure measurements and (◇) mean experimental unsteady pressure measurements from Daub *et al.* (2015). Error bar indications are only approximate experimental estimates due to Willems (2016).

skin-friction coefficient varies within the separated-flow region. More precisely, their skin-friction distribution (see figure 4(*a*) in their publication) reveals a less strong separated flow approximately $1/3L_{sep}$ downstream of the mean separation location, resulting in a local $\langle C_f \rangle$ maximum. They related this behaviour to collapse events of the separation bubble during the low-frequency unsteadiness and found a positive skin-friction coefficient in this region for conditional averages of collapsing bubbles. Our results, however, show a rather uniformly strong separation over a streamwise length of approximately $2/3L_{sep}$, which is probably related to the intensity of the present SWBLI. The pressure distribution reported in Priebe & Martín (2012) does not exhibit a pressure plateau and the overall separation length of $3\delta_0$ is considerably smaller compared to our results. Furthermore, Clemens & Narayanaswamy (2014) have shown by a simple scaling analysis that the upstream momentum fluctuations may be large enough to provoke a bubble collapse in case of weakly separated flows but not for strong separations.

The grey shaded area in figure 7(*a*) indicates three-dimensional structures in the nominally two-dimensional interaction by considering spanwise minimum and maximum values of the time-averaged data ($3805\delta_0/U_0$). In the incoming TBL, a very low spanwise variation of $\langle C_f \rangle$ is found, indicating statistical convergence. Two regions can be identified where evidence of stationary or slowly evolving three-dimensional flow structures exists: in the proximity of the mean separation location at $-11.25 < (x - x_{imp})/\delta_0 < -7.5$ and downstream of the inviscid impingement location at $(x - x_{imp})/\delta_0 > 0$. Note that we also include results of the short duration LES (the dotted lines correspond to an integration time of $446\delta_0/U_0$). Our results imply that a significant spanwise modulation of the flow is present close to the separation and reattachment location. The underlying flow structures provoking this variation are unsteady in nature, as the time-averaged spanwise minimum and maximum values reduce with longer integration times. Time scales associated with such flow phenomena are considerably longer than the characteristic time scale of the

incoming TBL (δ_0/U_0), since spanwise variations are still visible for the long-duration LES close to the separation and reattachment locations but vanish upstream of the interaction. We will provide support for this assumption in the course of this section and later in § 3.4.

A similar analysis has been conducted by Loginov *et al.* (2006) for their LES of a compression corner flow. Their results cover an integration time of $703\delta_0/U_0$, possibly explaining the strong spanwise variation of $\pm2.4 \times 10^{-4}$ found in their incoming TBL. Note that our short time LES shows a significantly lower variation of $\pm5.0 \times 10^{-5}$. They found two pairs of possibly steady counter-rotating streamwise vortices originating in the proximity of the compression corner and termed them Görtler-like vortices, bearing similarities with the instability mechanism found experimentally for laminar boundary layers developing on sufficiently concave surfaces (Görtler 1941; Floryan 1991). We will resume this discussion later in this section and show that a similar mechanism exists for the current SWBLI. Figure 7(*b*) shows the wall-pressure distribution for both LES and experiment. Similar to the findings of Loginov *et al.* (2006), a less strong spanwise variation is observed for the wall pressure. Experimental uncertainties have been estimated taking into account the accuracy of the sensors, uncertainties in wind tunnel flow conditions (total pressure, Mach number) and geometric uncertainties (alignment of the shock generator and the baseplate), see Willems (2016). Both datasets are in good agreement, with a relative error with respect to the maximum pressure of $\langle p_{max,LES}\rangle/\langle p_{max,exp}\rangle - 1 = -0.029$. For demonstration, the mean wall pressure obtained through unsteady pressure measurements is shown for an upstream position and close to the separation location.

The effect of the SWBLI on the normal Reynolds stress components is analysed in figure 8. In each figure, we again indicate the shock system, boundary-layer thickness, sonic line and reverse flow region by individual isolines. Additionally, the grey isoline indicates the dividing streamline defined by the set of points $y_{ds}(x)$ for which $\int_0^{y_{ds}}\langle\rho u\rangle\,\mathrm{d}y = 0$. The region of highest Reynolds stress is indicated by a star and eight contour levels are superimposed by dashed lines. A high level of streamwise Reynolds stress $\langle u'u'\rangle$ is found along the detached shear layer with its maximum located at the separation-shock foot, see figure 8(*a*). The strong convex streamline curvature near the bubble apex considerably damps the Reynolds stresses (see Smits & Dussauge 2006, e.g.). A similar observation was made by Sandham (2016). A second branch of increased $\langle u'u'\rangle$ is found in the proximity of the reattachment location but located farther away from the wall. Shear-layer vortices in this region are convected downstream with the flow and interact with the reattachment compression, possibly explaining this local maximum of streamwise Reynolds stress. For the wall-normal Reynolds stress component $\langle v'v'\rangle$, see figure 8(*b*), increased levels are found along the separation and reattachment shocks and are directly associated with their unsteady motion. The spanwise Reynolds stress component $\langle w'w'\rangle$ shares some similarities with the streamwise component, but one remarkable difference is observed: in the proximity of reattachment, where the dividing streamline shows a high level of concave curvature, another area of increased Reynolds stress is observed with its maximum located approximately $3\delta_0$ downstream and attached to the wall. This region of increased spanwise Reynolds stress covers $3.5 < (x - x_{imp})/\delta_0 < 12.5$. To the authors' knowledge, no such phenomenon has been previously reported for impinging SWBLI. Similarities with the compression corner results of Loginov *et al.* (2006) discussed previously suggest that a similar centrifugal instability plays a role for the current SWBLI, which would explain the increased spanwise Reynolds stress found in figure 8(*c*). Furthermore, the PME centred at the bubble apex, the dividing
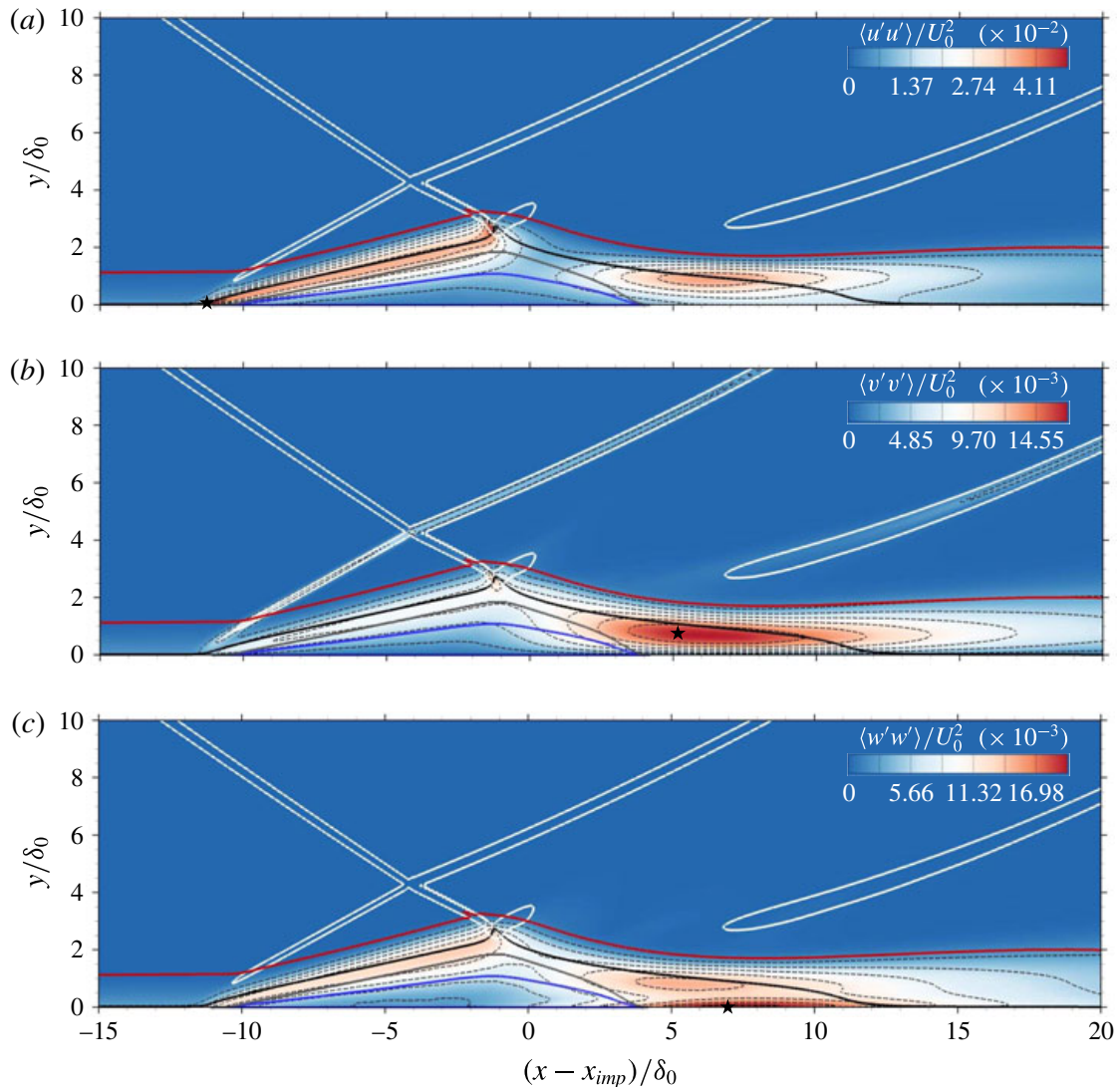
FIGURE 8. (Colour online) Time- and spanwise-averaged Reynolds normal stress components. The shock system is visualised by isolines of pressure gradient magnitude $|\nabla p|\delta_0/p_\infty = \{1.08, 3.28\}$. (—— (red)) $\langle\delta\rangle$, (—— (black)) $\langle Ma\rangle = 1$, (—— (blue)) $\langle u\rangle = 0$, (—— (grey)) dividing streamline y_{ds}. A star ($\star$) indicates the location of maximum contour level. Eight discrete contour levels are shown by dashed lines.

streamline and the downstream recompression correspond to a two-dimensional supersonic backward-facing step flow, for which streamwise vortices have been found experimentally in laminar, transitional and turbulent flows over a large range of Mach numbers (Ginoux 1971).

In figure 9, we show the instantaneous structure of the flow at two uncorrelated time instants. The blue isosurface indicates the reverse flow region ($u = 0$), while the white and black isosurfaces correspond to a positive and negative value of streamwise vorticity ($\omega_x = \pm 0.4 U_0/\delta_0$). As other authors have already pointed out (Loginov *et al.* 2006; Grilli *et al.* 2013), the circulation of the Görtler-like vortices found in compression corner studies is rather small, which makes it difficult to extract them from background turbulent structures. For visualisation purposes we apply both a temporal and spatial filter on three-dimensional snapshots of the flow. Temporal filtering is accomplished by a simple moving-average filter. Although the roll-off capabilities and the frequency response for such a filter are very poor, the noise suppression in the time domain is excellent. The LES database consists of $n_s = 7614$
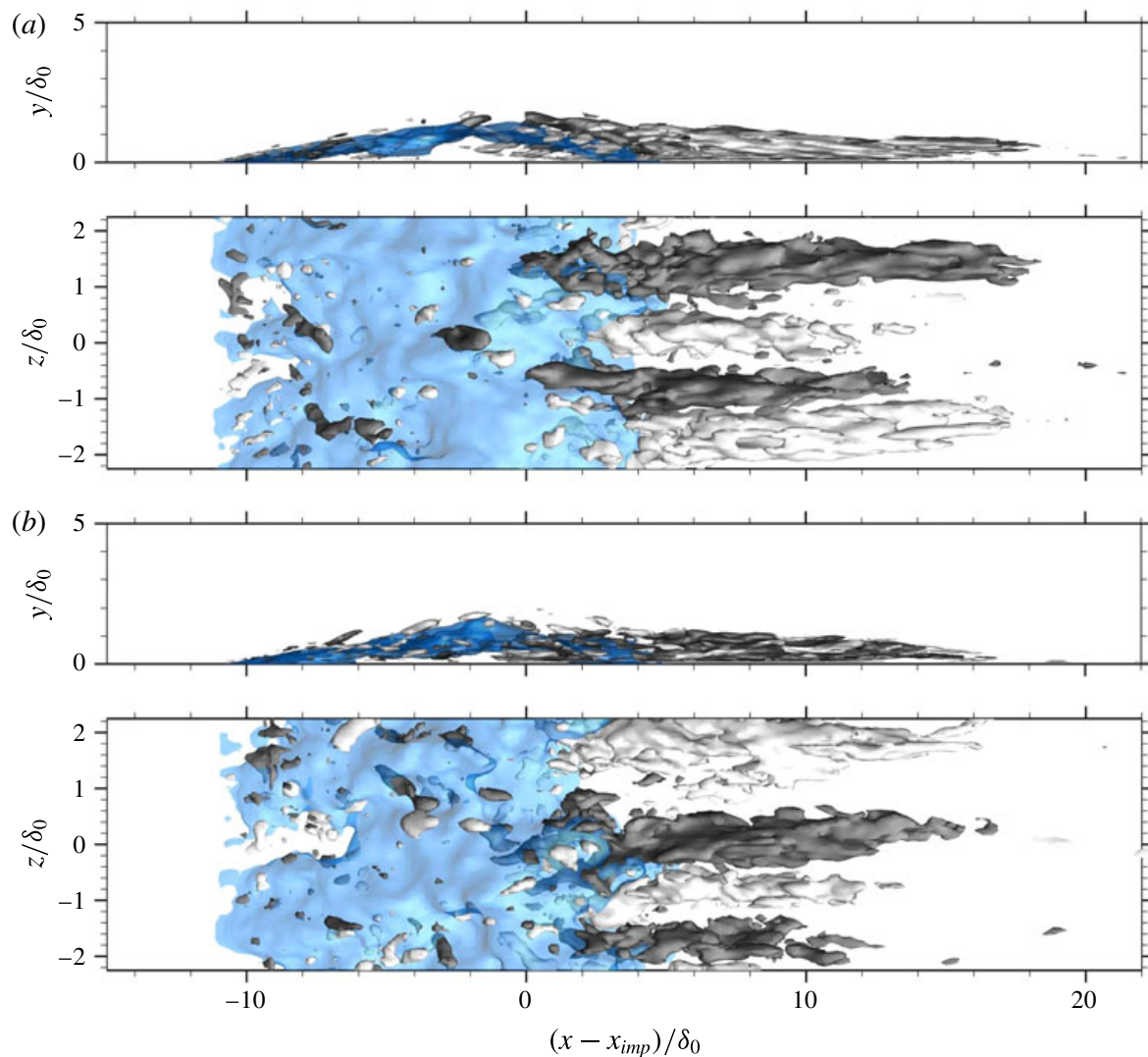
FIGURE 9. (Colour online) Instantaneous visualisation of the reversed flow and the Görtler-like vortices at two uncorrelated times. Translucent isosurface of streamwise velocity $u = 0$ (blue) and isosurfaces of streamwise vorticity $\omega_x = \pm 0.4 U_0/\delta_0$ (white/black) are shown.

three-dimensional snapshots recorded at a sampling interval of $\Delta t_s = 0.5\delta_0/U_0$. We select a filter width of $n_f = 51$ snapshots for the moving-average frame. Subsequently, a top-hat filter is applied to the temporally averaged data with a constant filter width in streamwise and spanwise direction equal to $\Delta x_f = 0.22\delta_0$ and $\Delta z_f = 0.07\delta_0$, while in wall-normal direction the filter width is spanned by four computational cells.

The following qualitative observations can be made from figure 9(*a,b*): two pairs of counter-rotating streamwise vortices develop in the reattachment region. These Görtler-like vortices are not fixed at a specific spanwise position, contrary to the results of Loginov *et al.* (2006). Note that the inflow boundary condition in their LES contained low-amplitude steady structures, which may lock the spanwise position of the streamwise vortices, similar to model imperfections in experimental configurations (Floryan 1991). Another aspect is their short integration time, which might not capture low-frequency modulations of such flow structures. In accordance with experimental observations (Görtler 1941; Floryan 1991; Schülein & Trofimov 2011) as well as numerical findings (Loginov *et al.* 2006; Grilli *et al.* 2013), the spanwise width of each vortex pair is approximately $2\delta_0$. The spanwise width of our
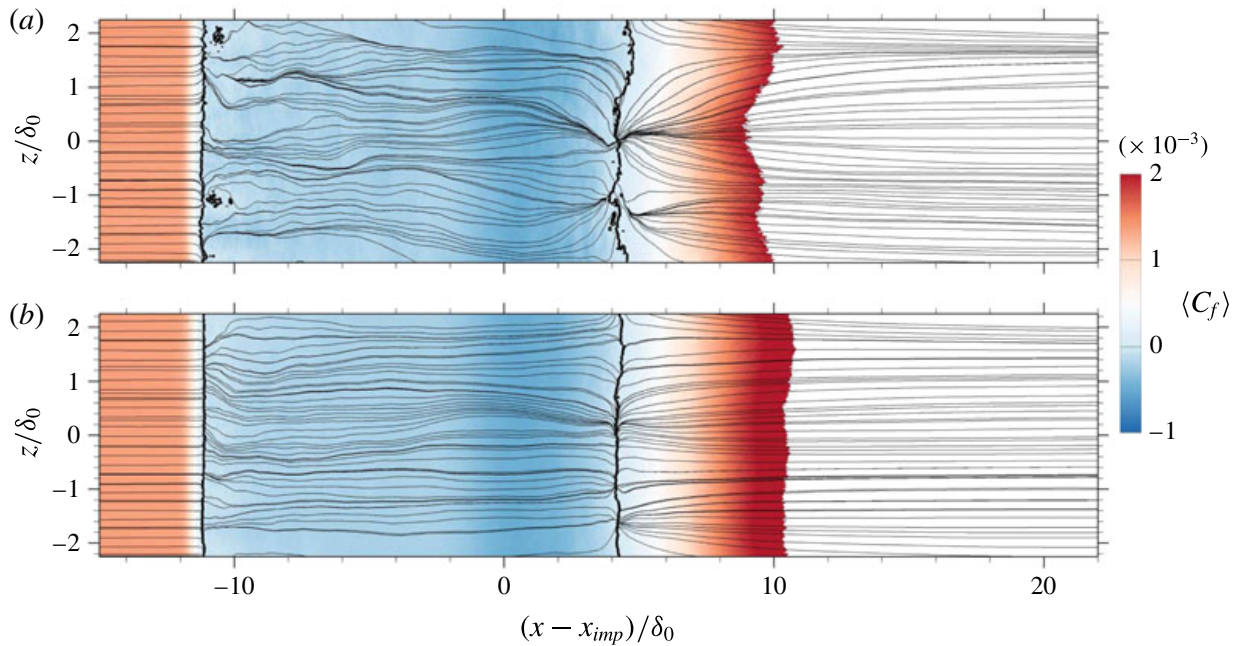
111

FIGURE 10. (Colour online) Numerical oil paint imitation together with mean skin-friction contours. Thick solid lines indicate time-averaged separation and reattachment locations defined by $\langle C_f \rangle = 0$. Contour cutoff level is $\langle C_f \rangle = 2 \times 10^{-3}$. Time integration covers (a) $446\delta_0/U_0$ and (b) $3805\delta_0/U_0$.

computational domain of $L_z = 4.5\delta_0$ in combination with periodic boundary conditions allow flow structures with a spanwise wavelength of at most $4.5\delta_0$ to be captured. We investigated the wavelength on our large-span configuration $\mathcal{D}^3$ with $L_z = 9\delta_0$ and found the same width of about $2\delta_0$ for a vortex pair. The effect of the streamwise vortices on the separated flow is clearly visible in figure 9(b): vortex-induced upwash decreases the shear stress at this specific spanwise location and directly influences the reattachment position by shifting it further downstream. Indeed, at $z/\delta_0 \approx -0.4$ such a flow configuration can be observed. Vortex-induced downwash ($z/\delta_0 \approx 1$) increases the local shear stress and subsequently shifts the reattachment position further upstream. The above findings suggest a direct coupling between the separated-flow dynamics and the streamwise vortices. As pointed out by Floryan (1991), such vortices in turbulent flow have no spanwise preference position and thus meander in time. Steady non-uniformities, e.g. when small vortex generators are placed in the settling chamber of a wind tunnel, might induce a preferred lateral position around which the spanwise motion occurs. In case that the level of unsteady disturbances of the oncoming flow is large compared to that of the steady disturbances, however, no preferred spanwise position can be observed for Görtler-like vortices (Kottke 1988; Floryan 1991). An animation of figure 9 reveals that the streamwise vortices tend to meander in the lateral direction. At the same time the vortices appear and disappear, coalesce and separate in an apparently random manner. Consequently, the effect of the Görtler-like vortices on the mean spanwise flow modulation diminishes with increasing averaging time. This is also evident when looking at figure 10, where we show a numerical oil flow visualisation together with mean skin-friction contours evaluated for the wall plane. While figure 10(a) is obtained for the short-duration LES, figure 10(b) includes a large number of low-frequency oscillations of the separation bubble. Characteristic node and saddle points close to the reattachment location can be observed for the former. Convergence and divergence lines associated with regions
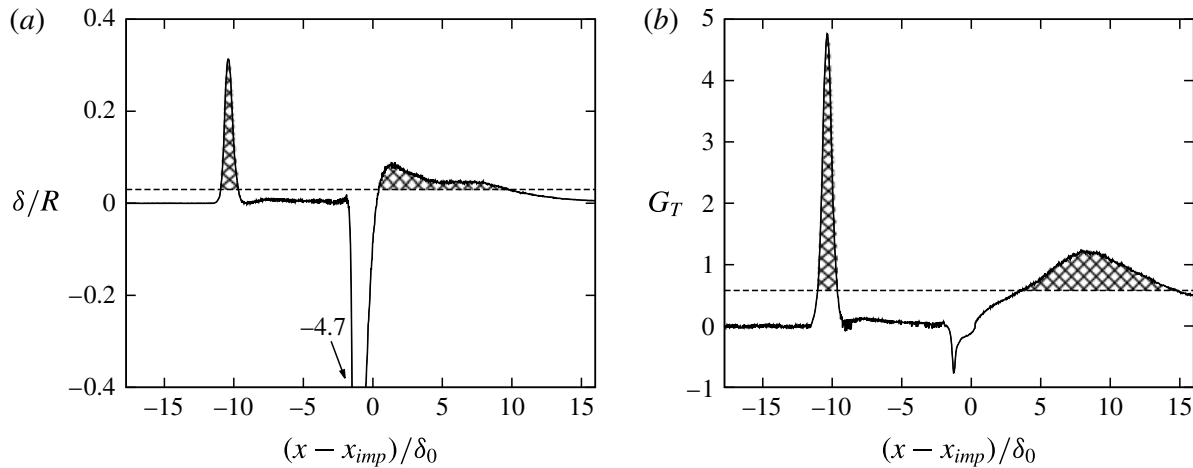
FIGURE 11. (a) Curvature parameter δ/R and (b) Görtler number G_T evaluated along a mean-flow streamline passing through $(x - x_{imp})/\delta_0 = -15$ and $y/\delta_0 = 0.75$. (- - - -) stability limits according to Görtler (1941) and Smits & Dussauge (2006).

of vortex-induced upwash and downwash indicate a strong spanwise modulation of the flow for the time frame considered. While figure 10(a) might suggest a system of steady streamwise vortices to be present, the results for the long-run LES clearly suggest the streamwise vortices to be unsteady. Node and saddle points as well as convergence and divergence lines appear suppressed in figure 10(b), indicating a less strong spanwise modulation of the mean flow with increasing averaging time.

Figure 11 analyses the curvature parameter δ/R and the Görtler number G_T for a mean-flow streamline passing through $(x - x_{imp})/\delta_0 = -15$ and $y/\delta_0 = 0.75$. According to Loginov *et al.* (2006) and Smits & Dussauge (2006), the Görtler number for a compressible turbulent flow may be defined as

$$G_T = \frac{\theta}{0.018\delta_1} \sqrt{\frac{\theta}{|R|}} \cdot \mathrm{sgn}(R). \tag{3.1}$$

Therein δ_1, θ and R denote the displacement thickness, the momentum thickness and the streamline curvature radius of the mean flow, respectively. Note that we have modified the above expression to indicate convex and concave curvature. Smits & Dussauge (2006) report a lower limit for the curvature parameter above which longitudinal vortices are expected to develop, this being $\delta/R \approx 0.03$ for a $Ma = 3$ flow. In laminar flow the critical Görtler number is $G_T = 0.58$ (Görtler 1941). Both limits are significantly exceeded within a short region close to the separation point as well as within a long region at reattachment (see filled patterns in figure 11(a,b). Although it is unclear whether such stability criteria hold also for turbulent flow, the high values within the reattachment region, which last over a significantly long streamwise distance of $11\delta_0$, indicate a centrifugal instability to be a plausible mechanism for the generation of Görtler-like vortices.

3.3. *Spectral analysis*

The unsteadiness of the present SWBLI is studied in this section by means of spectral analysis. For this purpose, 1230 equally spaced wall-pressure probes have been placed in streamwise direction along the midplane of the computational domain. The probes
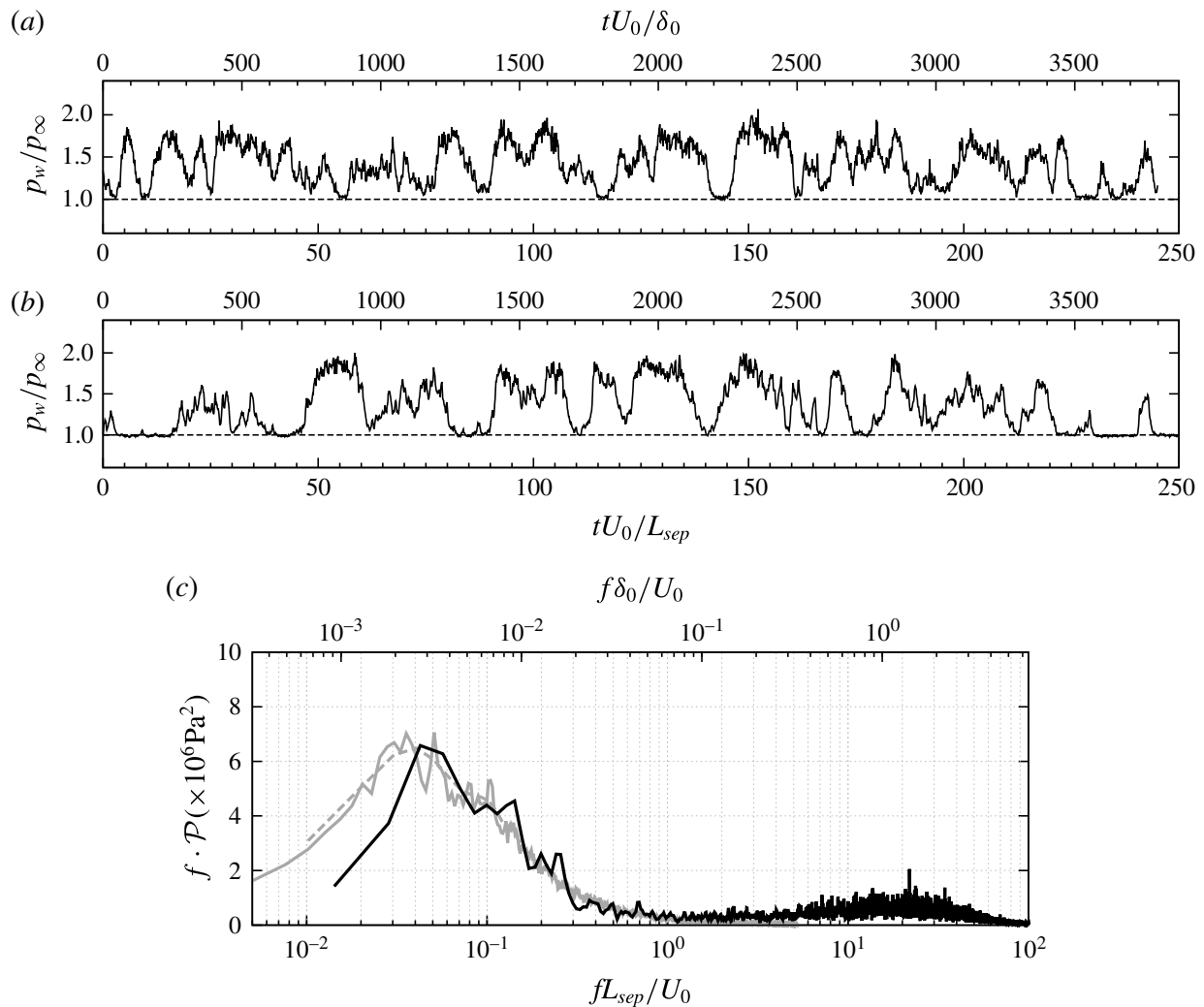
FIGURE 12. (*a*) Numerical and (*b*) experimental wall-pressure signal near the separation-shock foot. The numerical probe is located at mean separation x_s, low-pass filtered with a finite impulse rate filter (cutoff Strouhal number of $St_\delta = 0.33$, filter order of 900) and subsequently projected on the experimental time axis via linear interpolation. Locations of the experimental and numerical pressure probe are indicated in figure 7. (*c*) Weighted power spectral density $f \cdot \mathcal{P}(f)$ for the raw pressure signals without low-pass filtering. Experimental data from Daub *et al.* (2015) with (—— (grey)) $T_{seg} = 374 L_{sep}/U_0$ ($n_{seg} = 130$) and (- - - - (grey)) $T_{seg} = 51 L_{sep}/U_0$ ($n_{seg} = 973$). (——) LES with $T_{seg} = 51 L_{sep}/U_0$ ($n_{seg} = 12$).

span the region $-17.74 < (x - x_{imp})/\delta_0 < 17.18$ and are sampled at a frequency of approximately $f_s = 60 U_0/\delta_0$, which corresponds to 8.9 MHz. Figure 12(*a*,*b*) compares a section of the experimental wall-pressure measurement (Daub *et al.* 2015) with the LES signal. Both signals have been evaluated near the separation-shock foot, i.e. the experimental location is given by the unsteady pressure transducer indicated in figure 7(*b*), whereas the LES signal has been extracted at the mean separation location x_s. As mentioned in § 2.2, the cutoff frequency of the experimental measurements is 50 kHz($0.33 U_0/\delta_0$). Consequently, scales in the incoming TBL, whose characteristic frequency is of the order of U_0/δ_0, are undersampled. In order to mimic the experimental cutoff effect, we low-pass filter the LES signal with a finite impulse rate (FIR) filter of order 900 and a -6 dB cutoff Strouhal number of $St_\delta = 0.33$. Subsequently, the filtered signal is projected on the experimental time axis via linear

interpolation. Qualitative similarities between both datasets can be observed in terms of intermittency, occurring time scales and wall-pressure amplitudes. In contrast to previous low Reynolds numerical studies (Adams 2000; Touber & Sandham 2009; Priebe & Martín 2012; Pasquariello *et al.* 2014), our filtered signal shows the well-known intermittent character typically observed in high Reynolds number experiments, that is, the wall-pressure jumps from the incoming TBL value to that behind the separation shock and back again. This effect is attributed to the high Reynolds number of the flow as shown experimentally by Dolling & Murphy (1983) and Dolling & Or (1985). At lower Reynolds number the separation shock does not penetrate as far into the TBL as it does at high Reynolds number. In fact, the separation shock is diffused by increased viscous effects when approaching the wall. Since its motion is no longer associated with a single, well-defined shock wave, its intermittency is attenuated (Adams 2000; Ringuette *et al.* 2009).

A more quantitative comparison of both signals is given in figure 12(*c*), where we show the weighted power spectral density (PSD) of the two signals. Note that the LES signal is not low-pass filtered for this comparison, thus retaining the high-frequency TBL content. Welch's algorithm with Hamming windows is used to estimate the PSD. For the LES signal (black solid line), a total number of $n_{seg} = 12$ segments is used with 65 % overlap. These parameters lead to a segment length of approximately $783\delta_0/U_0(51L_{sep}/U_0)$. For the available experimental signal two segmentation configurations have been used. The grey solid line reflects a total number of $n_{seg} = 130$ segments with 65 % overlap. This leads to an individual window length of $5797\delta_0/U_0(374L_{sep}/U_0)$ and should resolve all expected low-frequency dynamics properly. The parameters for the grey dashed line are chosen in such a way that the individual segment length is the same as for the LES, leading to a total number of $n_{seg} = 973$ segments. The good qualitative agreement between both signals observed in figure 12(*a,b*) is also confirmed by their spectra. Both spectra indicate the presence of a dominant low-frequency peak around a non-dimensional frequency of $St_{L_{sep}} = fL_{sep}/U_0 \approx 0.04$. This value agrees well with experimental studies for different flow geometries and upstream conditions by Dussauge, Dupont & Debiève (2006), who found that the unsteadiness occurs at frequencies centred about $St_{L_{sep}} = 0.02$–0.05. While the peak amplitude for the shock unsteadiness is captured very well by the LES, we observe a lower energy level for frequencies below the low-frequency peak. We have computed the PSD for a reduced number of segments n_{seg} in order to allow for increased low-frequency resolution. We find that the energy content of the LES signal at frequencies below $St_{L_{sep}} < 0.04$ essentially is unaffected. We believe that the observed discrepancies may be caused by side wall effects in the experiment which mainly show up at low frequencies. The LES data show an additional bump centred around $f\delta_0/U_0 \approx 1$, associated with the most energetic scales of the TBL. The experimental cutoff frequency of $0.33U_0/\delta_0$ excludes this range from the experimental data.

The wall-pressure spectrum for all numerical probes is shown in figure 13. Mean separation and reattachment locations are indicated by vertical dashed lines. Note that no energetically significant low-frequency content is apparent in the upstream TBL, proving the suitability of the digital filter technique. In accordance with previous numerical (Touber & Sandham 2009; Priebe & Martín 2012; Grilli *et al.* 2012) and experimental (Thomas *et al.* 1994; Dupont *et al.* 2006) studies, the broadband peak associated with energetic scales in the incoming TBL shifts towards significantly lower frequencies close to the mean separation location and moves back again to higher frequencies downstream of the interaction. Within the rear part of the separation
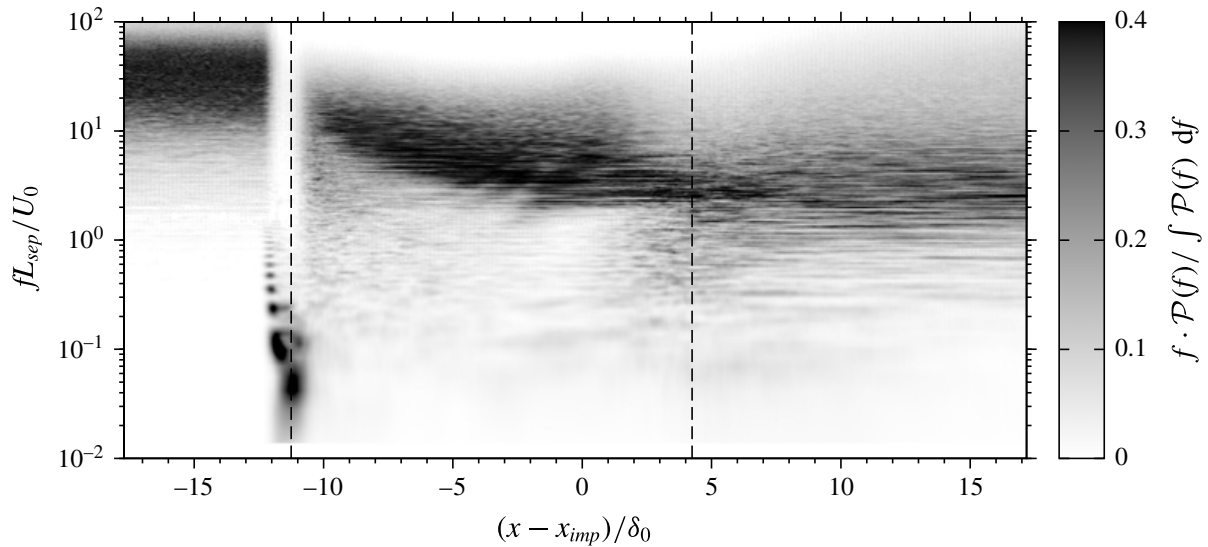
FIGURE 13. Weighted power spectral density map. At each streamwise location the weighted spectra are normalised by $\int \mathcal{P}(f)\,\mathrm{d}f$. Mean separation and reattachment locations are highlighted by vertical dashed lines.

bubble so-called medium frequencies around $St_{L_{sep}} \approx 0.5$ develop, which are probably related to shear-layer vortices convected over the recirculation (Dupont *et al.* 2006). While the low-frequency activity is concentrated around the mean separation location, another significant level of unsteadiness is found slightly upstream and at frequencies around $0.1 U_0/L_{sep}$. Associated time scales of approximately $10 L_{sep}/U_0$ can be found in the wall-pressure signal, see figure 12(*a,b*), and are related to the intermittent character of the separation shock as will be shown in figure 15.

The streamwise variation in r.m.s. wall-pressure fluctuations is shown in figure 14. The distributions are obtained by integrating the power spectra over a given frequency range

$$\langle p'p'\rangle|_{f_1-f_2} = \int_{f_1}^{f_2} \mathcal{P}(f)\,\mathrm{d}f. \tag{3.2}$$

We focus on the low-frequency contributions of pressure fluctuations and thus select $f_2 = 1 U_0/L_{sep}$, see also figure 12(*c*). At the same time this value is sufficiently far away from the experimental cutoff frequency of $5.2 U_0/L_{sep}$, hence avoiding aliasing effects. The lower limit f_1 is chosen to be the smallest resolved frequency, individually selected for experiment (filled bullets) and LES (solid line). The overall agreement within the separated-flow region and after reattachment is satisfactory, while the peak value associated with the separation shock motion is underestimated by the LES. This effect can be attributed to the longer sampling time for the experiment, thus resolving much lower frequencies that contribute to the overall energy level. In fact, when restricting the integration of the experimental data to the same lower value f_1 as for the LES (open symbols in figure 14*a*), the peak r.m.s. value reproduces the numerical result without affecting the other measurement locations.

Similarly to experimental observations (Dolling & Murphy 1983; Dolling & Or 1985; Selig *et al.* 1989), the high Reynolds number of the flow leads to a distinct r.m.s. peak centred around x_s. Directly downstream a plateau region develops, followed by a continuous increase in pressure fluctuations until a second maximum
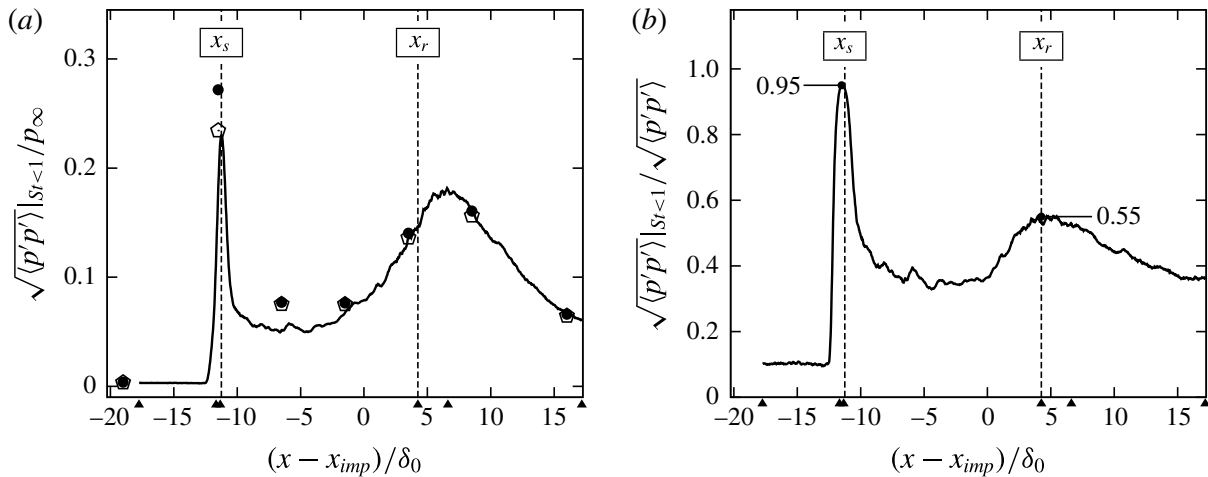
FIGURE 14. (*a*) Band-limited root mean square of wall-pressure fluctuations. (——) LES data obtained by integrating the PSD for $St_{L_{sep}} < 1$, (●) experimental data from Daub *et al.* (2015) obtained by integrating the PSD for $St_{L_{sep}} < 1$ and (○) by integrating the PSD for $0.014 < St_{L_{sep}} < 1$. (*b*) Band-limited ($St_{L_{sep}} < 1$) relative root mean square of wall-pressure fluctuations for the present LES. (▲) indicate locations which will be discussed in conjunction with figure 15.

is reached. Note that the second maximum is located $2.4\delta_0$ downstream of the mean reattachment location. This position apparently coincides with the reattaching shear layer, see figure 6(*a*), for which a characteristic frequency of the reattaching large-scale vortices is usually found around $0.5U_0/L_{sep}$ (Dupont *et al.* 2006). In figure 14(*b*) we further investigate the band-limited low-frequency contribution of pressure fluctuations to the total fluctuation energy for the present LES. In the incoming TBL approximately 10 % of the total r.m.s. of wall-pressure fluctuations reside in the lower-frequency range of $f < 1U_0/L_{sep}$. A similar value has been found experimentally by Thomas *et al.* (1994). When approaching the mean separation point, almost the complete (95 %) pressure-fluctuation intensity is associated with such low frequencies. Thomas *et al.* (1994) investigated experimentally a compression corner flow at a free stream Mach number of 1.5 and a Reynolds number of $Re_\delta \approx 178 \times 10^3$. They found that the fraction of fluctuation intensity that is associated with separation-shock oscillation increases with increasing ramp angle. For their largest ramp angle of 12° a ratio of 55 % is reported, which is significantly lower than our value and possibly related to the considerably lower Mach number and weaker interaction in their study. Close to reattachment the low-frequency contribution is still responsible for 55 % of the total wall-pressure-fluctuation intensity and composed of a superposition of separation-bubble dynamics and reattaching shear-layer vortices convected downstream.

The intermittent character of the wall pressure is further analysed in figure 15. On the left we show the normalised wall-pressure evolution for six different streamwise locations. On the right the corresponding normalised probability density functions (PDFs) computed from 228 681 samples grouped into 478 bins, together with a standard Gaussian distribution are shown. The individual positions are indicated in the r.m.s. plot of wall-pressure fluctuations, see figure 14. From top to bottom they refer to the undisturbed TBL, the onset of interaction, the location of maximum wall-pressure fluctuation intensity, the mean reattachment position, the reattaching shear layer and the post-interaction location. The incoming TBL signal is effectively Gaussian, which is also reflected by the skewness α_3 and flatness α_4 coefficients.
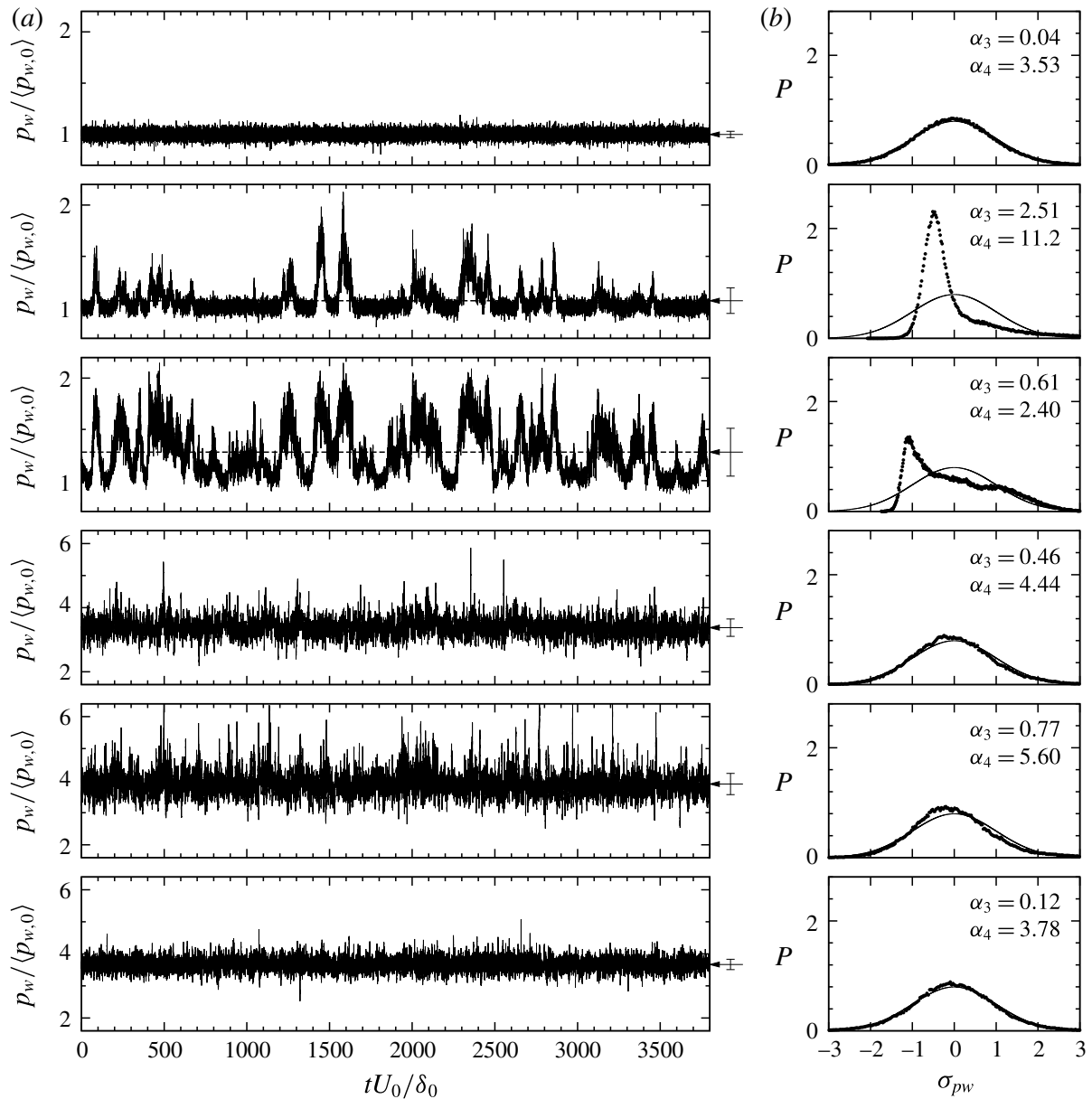
117

FIGURE 15. Wall-pressure signals (*a*) and corresponding normalised probability density distributions (*b*) evaluated at $(x - x_{imp})/\delta_0 = \{-17.74, -11.66, -11.34, 4.25, 6.61, 17.18\}$. Refer to the text and figure 14 for a physical interpretation of the wall-pressure positions. The mean wall pressure is indicated by a horizontal dashed line. Arrows together with vertical bars indicate the mean wall pressure and its standard deviation. Values of skewness α_3 and flatness α_4 coefficients and a Gaussian distribution are included for reference.

The next probe is located $0.41\delta_0$ upstream of the mean separation location at a pressure level of $\langle p_w \rangle / \langle p_{w,0} \rangle = 1.07$. The signal is strongly intermittent. This is also confirmed by the associated PDF which is highly skewed and has a single mode at $-0.5\sigma_{p_w}$, thus reflecting the probability of finding pressures in the range of the incoming TBL. Close to the mean separation location, at a pressure level of $\langle p_w \rangle / \langle p_{w,0} \rangle = 1.27$, the signal is still intermittent. Its PDF is highly left skewed with tendencies to develop a bimodal shape whose centres are located around $\pm 1 \sigma_{p_w}$. These two pressure probes have been evaluated at a very similar pressure ratio as done by Dolling & Murphy (1983). The reported wall-pressure signals and PDF qualitatively agree with experimental observations by Dolling & Murphy (1983) (see
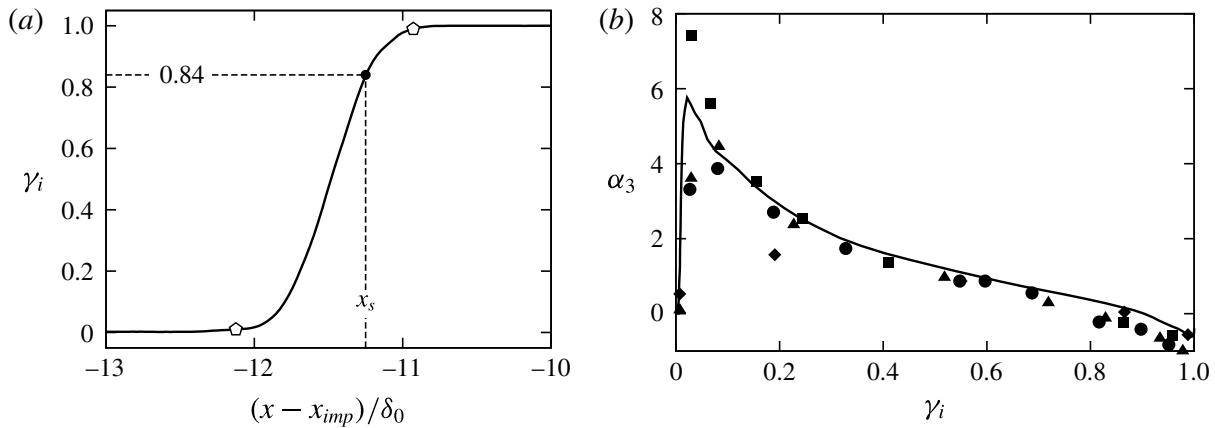
FIGURE 16. (a) Streamwise intermittency distribution $\gamma_i(x)$. The mean separation location x_s is indicated. ($\ocircle$) highlight 1 % and 99 % intermittency boundaries and define the intermittent length scale $L_i = 1.2\delta_0$. (b) Skewness coefficient α_3 as a function of intermittency γ_i. (——) LES. Symbols represent experimental data from Dolling & Or (1985) for a compression ramp flow at a Mach number of $Ma = 2.9$ and a Reynolds number of $Re_{\delta_0} = 1.43 \times 10^6$ with wedge angles ($\blacklozenge$) $\vartheta = 12°$ (attached flow), ($\bullet$) $\vartheta = 16°$ (incipient separation), ($\blacktriangle$) $\vartheta = 20°$ (separated flow) and ($\blacksquare$) $\vartheta = 24°$ (separated flow).

figure 6 in the respective publication) and Dolling & Or (1985) (see figure 3 in their publication), which again confirms the high Reynolds number character of the present SWBLI. The bimodal character is more pronounced in their studies, which is probably because of the even higher Reynolds number of $Re_{\delta_0} = 1.43 \times 10^6$ in their experiment. At the mean reattachment position the signal is slightly left skewed, see also Adams (2000). Wall-pressure fluctuations increase for the next downstream probe, which is located in the proximity of the reattaching shear layer. At the same time the skewness coefficient increases. Further downstream the signal has returned to an almost Gaussian shape with relaxed pressure fluctuations.

In figure 16(a) we show the intermittency factor $\gamma_i(x)$. According to Dolling & Or (1985) it is defined as

$$\gamma_i = \frac{\int_{t_1}^{t_2} \begin{cases} 1, & p_w > \langle p_{w,0} \rangle + 3\sigma_{p_{w,0}} \\ 0, & \text{else} \end{cases} \, \mathrm{d}t}{t_2 - t_1}, \qquad (3.3)$$

which describes the fraction of time that the wall pressure is above the threshold value defined by the undisturbed incoming TBL. A high intermittency level of $\gamma_i(x_s) = 0.84$ is found at the mean separation location. Based on the 1 % and 99 % intermittency boundaries we can derive an intermittent length scale of $L_i = 1.2\delta_0$. For comparison, Loginov *et al.* (2006) reported a value of $\gamma_i(x_s) = 0.88$ and $L_i = 1.3\delta_0$. According to Dolling & Or (1985), higher-order moments such as α_3 are only a function of γ_i and do not depend on the flow geometry. Their compression corner results at $Re_{\delta_0} = 1.43 \times 10^6$ and four different ramp angles are shown in figure 16(b). The overall correlation is satisfactory and our LES results (solid line) support the experimental findings. Dolling & Or (1985) also analysed data for a different flow geometry (blunt fin) and a variety of Reynolds numbers. These results generally support the free interaction concept and suggest a Reynolds number dependency for the peak value of α_3.

3.4. *Dynamic mode decomposition*

The previous section addressed the unsteady character of the interaction by means of local flow diagnostics. The aim of the following modal analysis is to relate global flow phenomena to the frequencies found in § 3.3. We will start with a two-dimensional DMD in terms of spanwise-averaged snapshots. This is motivated by the successful application of the DMD method to similar SWBLI problems by Pirozzoli *et al.* (2010), Grilli *et al.* (2012), Tu (2013) and Nichols *et al.* (2016), the analysis of low-pass filtered and spanwise-averaged flow fields by Priebe & Martín (2012) and the global stability analysis by Touber & Sandham (2009). Three-dimensional effects are however present for the current study as already shown in the previous sections. Therefore we will subsequently apply the DMD to snapshots of the two-dimensional skin-friction data, which will enable us to conclude whether three-dimensional modulations of the separated-flow region are present.

A short overview of the DMD is given in the following. DMD is a Koopman-operator-based spectral analysis technique that decomposes the flow field into coherent spatial structures sharing the same temporal frequency (Rowley *et al.* 2009; Schmid 2010). It operates on a discrete sequence of snapshots and can be used to extract a reduced-order representation of the underlying dynamical system. Starting point is a given sequence of snapshots $V_1^n = \{v_1, v_2, \ldots, v_n\} \in \mathbb{R}^{m \times n}$ sampled at constant time intervals Δt_s, where each v_i is a column vector with m entries (e.g. velocities on the computational grid). A linear, time-invariant operator is assumed to relate two consecutive snapshots, that is $v_{i+1} = A v_i$. The dynamics of the underlying system is determined once the eigenvalues and eigenvectors of this operator $A \in \mathbb{R}^{m \times m}$ are found. Note that in case of a nonlinear system this assumption is equivalent to a linear approximation. The time-invariant mapping allows to formulate a Krylov sequence of the data of the form $V_1^n = \{v_1, A v_1, A^2 v_1, \ldots, A^{n-1} v_1\}$. In general m is so large that we cannot compute eigenvalues of A directly, which is why we seek for a low-order representation. A method that does not require explicit knowledge of A is based on the assumption that we can express v_n as a linear combination of the previous $n - 1$ linearly independent vectors v_i according to

$$v_n = a_1 v_1 + a_2 v_2 + \cdots + a_{n-1} v_{n-1} + r. \tag{3.4}$$

Following the work of Schmid (2010), the above relation can be applied to the snapshot sequence to obtain

$$A V_1^{n-1} = V_2^n = V_1^{n-1} S + r e^{\mathrm{T}}, \tag{3.5}$$

where $e = (0, \ldots, 1) \in \mathbb{R}^{n-1}$. The matrix $S \in \mathbb{R}^{(n-1) \times (n-1)}$ is a companion matrix with the only unknowns a_i. It is a lower-dimensional representation of A and shares a subset of approximate eigenvalues, which are often referred to as Ritz values (Rowley *et al.* 2009). In case of a linear system the residual r vanishes. We will later use (3.4) in our analysis to verify whether enough snapshots have been collected. The companion matrix S can be obtained by solving (3.4) in a least-squares sense. The resulting decomposition in terms of eigenvalues and eigenvectors of S, however, often produces an ill-conditioned and noise-sensitive algorithm, which is why Schmid (2010) proposed a more robust implementation based on a singular value decomposition (SVD) of $V_1^{n-1} = U \Sigma V^{\mathrm{T}}$. The SVD of V_1^{n-1} in combination with (3.5) yields the approximate matrix $\widetilde{S} = U^{\mathrm{T}} V_2^n V \Sigma^{-1} = U^{\mathrm{T}} A U$, which is the same result as when the linear operator A is projected onto the proper orthogonal decomposition (POD) basis

implicitly contained in the matrix U. Finally, the individual DMD modes $\boldsymbol{\phi}_i \in \mathbb{C}^m$ are obtained by

$$\boldsymbol{\phi}_i = U\boldsymbol{y}_i, \tag{3.6}$$

where $\boldsymbol{y}_i \in \mathbb{C}^{n-1}$ denotes the ith eigenvector of $\widetilde{S}$, that is $\widetilde{S}\boldsymbol{y}_i = \mu_i\boldsymbol{y}_i$ with $\mu_i \in \mathbb{C}$ being the associated eigenvalue. With the above decomposition it is possible to approximate experimental or numerical snapshots using a linear combination of the DMD modes

$$\boldsymbol{v}_m \approx \sum_{i=1}^{n-1} \boldsymbol{\phi}_i \mu_i^m \alpha_i, \quad m \in \{1, \ldots, n-1\}, \tag{3.7}$$

where $\alpha_i \in \mathbb{C}$ can be recognised as the amplitude of the individual DMD mode. In matrix form we obtain

$$V_1^{n-1} \approx \underbrace{[\boldsymbol{\phi}_1, \boldsymbol{\phi}_2, \ldots, \boldsymbol{\phi}_{n-1}]}_{\boldsymbol{\phi}} \underbrace{\begin{bmatrix} \alpha_1 & & & \\ & \alpha_2 & & \\ & & \ddots & \\ & & & \alpha_{n-1} \end{bmatrix}}_{D_\alpha} \underbrace{\begin{bmatrix} 1 & \mu_1 & \cdots & \mu_1^{n-1} \\ 1 & \mu_2 & \cdots & \mu_2^{n-1} \\ \vdots & \vdots & \ddots & \vdots \\ 1 & \mu_{n-1} & \cdots & \mu_{n-1}^{n-1} \end{bmatrix}}_{V_{and}}. \tag{3.8}$$

The choice of the DMD amplitudes α_i is not unique. Here we follow the strategy by Jovanović, Schmid & Nichols (2014), who proposed to solve the following optimisation problem for the unknown amplitudes

$$\boldsymbol{\alpha}_{opt} = \arg\min_{\boldsymbol{\alpha}} |V_1^{n-1} - \boldsymbol{\phi}D_\alpha V_{and}|_F^2, \tag{3.9}$$

where $|\cdot|_F$ denotes the Frobenius norm. Resulting amplitudes $\boldsymbol{\alpha}_{opt}$ in combination with (3.7) optimally approximate the entire data sequence. Note that the above optimisation problem reduces to the classical first snapshot scaling (Tu & Rowley 2012) for a full-rank system.

One of the main problems when applying the DMD algorithm is to properly select the dynamically most important and robust modes of the underlying dataset. The amplitude of a mode α_i might be a good indicator for modes having an almost zero growth rate, but could be misleading for transient modes associated with large negative growth rates. We therefore use a more sophisticated and automated mode selection algorithm developed by Jovanović *et al.* (2014). Their sparsity-promoting DMD (SPDMD) algorithm augments the optimisation problem (3.9) by a regularisation term that penalises the ℓ_1-norm of the vector of DMD amplitudes α_i

$$\widetilde{\boldsymbol{\alpha}} = \arg\min_{\boldsymbol{\alpha}} |V_1^{n-1} - \boldsymbol{\phi}D_\alpha V_{and}|_F^2 + \gamma \sum_{i=1}^{n-1} |\alpha_i|, \tag{3.10}$$

where γ is a given positive regularisation parameter that for large values enforces a sparse vector $\widetilde{\boldsymbol{\alpha}}$, while for $\gamma = 0$ the conventional optimisation problem (3.9) is recovered. When for a given γ a desired sparsity structure is achieved, the amplitudes for the non-zero entries of $\widetilde{\boldsymbol{\alpha}}$ are adjusted according to (3.9). For algorithmic details on how to effectively solve this convex optimisation problem please refer to Jovanović

et al. (2014). Besides the mode selection algorithm via SPDMD we will also look at the magnitude of a mode $|\phi_i|$, which has been shown to correlate with the spectral behaviour of the underlying flow field when compared to local measurements (Rowley *et al.* 2009).

Finally, dynamic information of an individual DMD mode in terms of growth rate β_i and angular frequency ω_i are implicitly available through the eigenvalues μ_i after applying a logarithmic mapping

$$\lambda_i = \ln \mu_i / \Delta t_s \quad \rightarrow \quad \begin{array}{l} \beta_i = \mathrm{Re}(\lambda_i) = \ln |\mu_i| / \Delta t_s \\ \omega_i = \mathrm{Im}(\lambda_i) = \arg(\mu_i) / \Delta t_s \end{array}. \tag{3.11}$$

Our database for the spanwise-averaged DMD analysis consists of $n = 7000$ snapshots of pressure and velocity fields $\{p, u, v\}$, equispaced in time with an interval of $\Delta t_s = 0.5 \delta_0 / U_0$. Only a subdomain of the full computational box is used for the modal analysis, which covers the region $-15.25 < (x - x_{imp})/\delta_0 < 19.75$ and $0 < y/\delta_0 < 7.5$. We thus focus on the dynamically interesting interaction region. This leads to a snapshot matrix of $V_1^n \in \mathbb{R}^{m \times n}$ with dimensions $m = 968\,352$ and $n = 7000$. The particular choice of the number of snapshots for the current analysis is motivated by studying the DMD residual introduced in (3.4). The normalised ℓ_2-norm of the residual vector is plotted over the number of snapshots in figure 17(*a*). The DMD residual appears sufficiently saturated after approximately 7000 snapshots. It is thus plausible to assume that enough snapshots have been gathered to accurately predict the dynamics of the system. We show contours of the residual for both the pressure and streamwise velocity in figure 17(*b*) for the chosen snapshot set of $n = 7000$. The above settings lead to a frequency resolution expressed in Strouhal number of $2.86 \times 10^{-4} < St_\delta < 1$ ($4.43 \times 10^{-3} < St_{L_{sep}} < 15.5$). The high sampling rate is motivated by the fact that, besides the low-frequency phenomenon, we want to accurately resolve the medium-frequency unsteadiness typically found around frequencies of $0.5 U_0 / L_{sep}$ (Dupont *et al.* 2006). Moreover, as pointed out by Nichols *et al.* (2016), the signal-to-noise ratio is significantly increased as we partially resolve turbulence, having a favourable effect on convergence properties of the DMD algorithm.

In figure 18(*a*) we show the spectrum of eigenvalues resulting from the standard DMD algorithm. Since real-valued input data are processed the modes arise as complex conjugate pairs, which results in a symmetric spectrum. Nearly all eigenvalues reside on the unit circle $|\mu_i| = 1$. This is expected for statistically stationary systems and further indicates that the snapshot sequence V_1^n lies on or near an attracting set (Rowley *et al.* 2009). The normalised magnitudes of the individual DMD modes $|\phi_i|$ for positive frequencies are shown in figure 18(*b*). To facilitate mode selection, we apply the SPDMD algorithm of Jovanović *et al.* (2014). The filled bullets indicate a subset of $N_{sub} = 13$ modes that have been categorised as dynamically important. Note that the SPDMD method does not simply chose the DMD modes based on their magnitude, but identifies modes having the strongest influence on the complete snapshot sequence (Jovanović *et al.* 2014). The DMD spectrum shares some similarities with the local PSD at the mean separation location shown in figure 12(*c*), that is the low-frequency unsteadiness appears as a broadband bump involving multiple low frequencies. This implies that the unsteadiness is connected to a global flow phenomenon. In agreement with the spectral analysis of wall-pressure probes presented in §3.3, one of the low-frequency modes obtained by the DMD algorithm is located at $St_{L_{sep}} = 0.039$ and is part of the SPDMD subset. The modes selected by the SPDMD algorithm can be categorised into two different types as
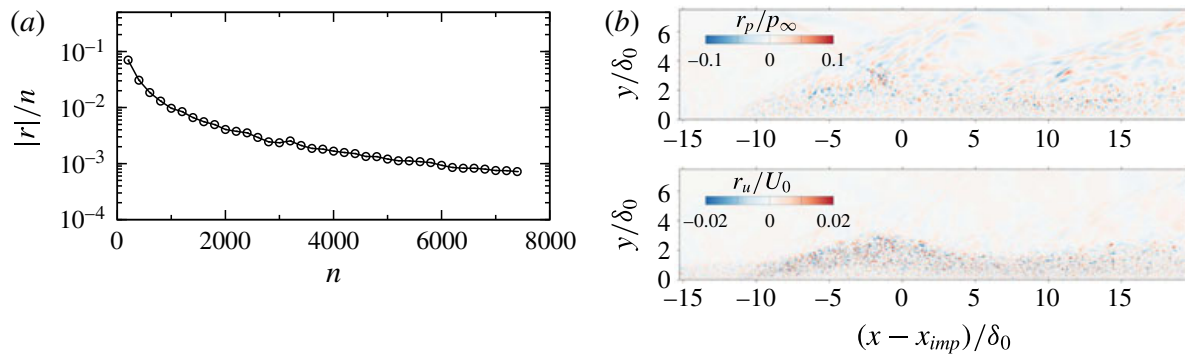
FIGURE 17. (Colour online) (*a*) Normalised DMD residual according to (3.4). (*b*) Contours of DMD residual for pressure (top) and streamwise velocity (bottom) for $n = 7000$.
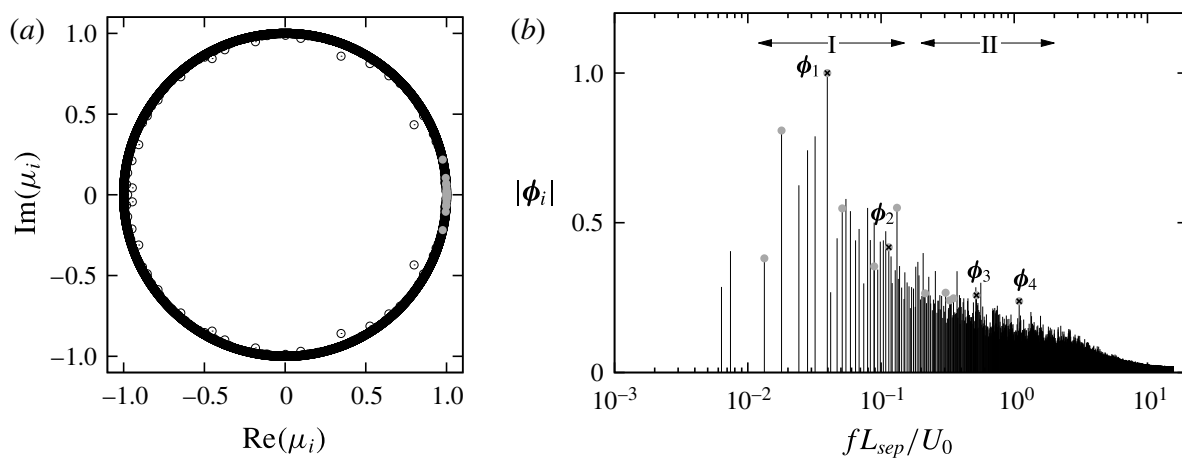

FIGURE 18. (*a*) Spectrum of eigenvalues resulting from the standard DMD algorithm. (*b*) Normalised magnitudes of the DMD modes. (● (grey)) indicate a SPDMD subset of $N_{sub} = 13$ modes.

indicated by the frequency bins I and II in figure 18(*b*). Modes belonging to the first group (I) describe a flow modulation that involves the shock system and separation bubble as an entity, while modes belonging to the second group (II) correspond to shedding motions of the detached shear layer. We post-processed the SPDMD modes within each single bin and found that they share similar flow structures, which is why in the following we only select two representatives out of each region, see the labels ϕ_1, ϕ_2, ϕ_3 and ϕ_4 in figure 18(*b*). The associated frequencies are $f_1 = 0.039 U_0/L_{sep}$, $f_2 = 0.114 U_0/L_{sep}$, $f_3 = 0.52 U_0/L_{sep}$ and $f_4 = 1.087 U_0/L_{sep}$.

Animations of the mean-flow modulation through the individual modes are available as a supplement to the online version at https://doi.org/10.1017/jfm.2017.308 of this article and should be considered in conjunction with the following discussions. For a selected mode ϕ_i we reconstruct an individual real-valued flow variable $\boldsymbol{u}$ according to $\boldsymbol{u}(\boldsymbol{x}, t) = \phi_m + a_f \cdot \mathrm{Re}\{\alpha_{i,opt}\phi_i \mathrm{e}^{\mathrm{i}\omega_i t} + \mathrm{cc}\}$, where ϕ_m denotes the mean mode, cc indicates the contribution of the complex conjugate of ϕ_i and a_f is an optional amplification factor. We only study the oscillatory component of each DMD mode and thus neglect the individual growth rate β_i, since in the limit of infinitely many snapshots the growth rate tends towards zero for a nonlinear statistically stationary system (Pirozzoli *et al.* 2010). In contrast to the results of Grilli *et al.* (2012), where
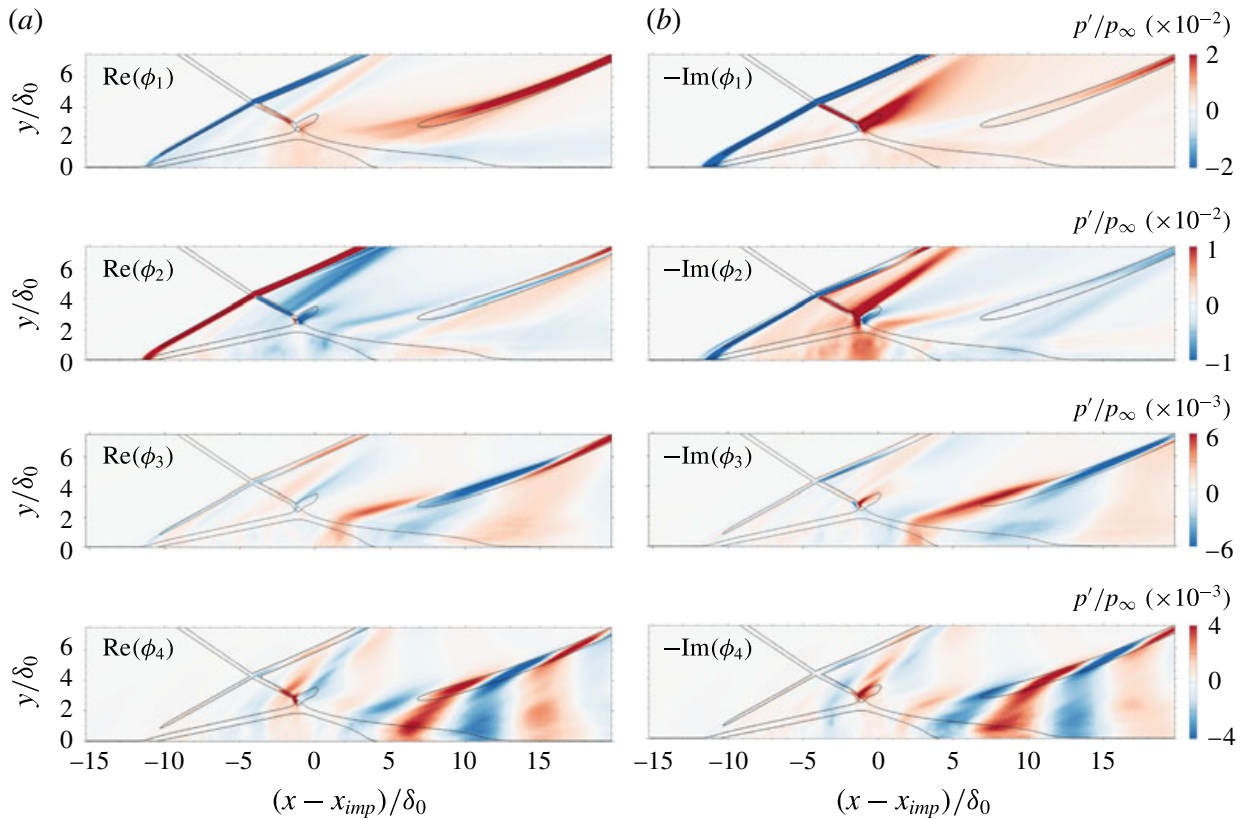
FIGURE 19. (Colour online) Real and imaginary part of DMD modes showing contours of modal pressure fluctuations p'/p_∞. (a) $\text{Re}(\boldsymbol{\phi}_i)$. (b) $-\text{Im}(\boldsymbol{\phi}_i)$. Refer to figure 18 for the mode selection. For clarity, the mean shock system, the mean sonic line and the mean dividing streamline are superimposed by black solid lines.

the low-frequency unsteadiness is restricted to a few discrete phase-locked modes, the DMD spectrum in figure 18(a) shows a large number of contributing modes. Indeed, increasing the number N_{sub} for the SPDMD algorithm results in selecting nearly all modes within the low-frequency bin. Consequently, the contribution of a single mode to the mean-flow field is hardly seen, which is why we chose a suitable magnification factor a_f for $\boldsymbol{\phi}_i$ before adding it to the mean mode $\boldsymbol{\phi}_m$. The supplementary animations show contours of the pressure gradient magnitude in the range $|\nabla p|\delta_0/p_\infty = [0, 10]$ at 8 equally spaced phase angles, that is $\omega_i t = j\pi/4, j = 0 \ldots 7$. The mean shock system together with the instantaneous separation bubble are highlighted by black solid lines.

In figures 19 and 20 we show the real and (negative) imaginary part of the selected DMD modes with contours of pressure and velocity fluctuations, respectively. The temporal mode evolution between the two discrete phase angles $\omega_i t = 0$ and $\omega_i t = \pi/2$ is equivalent to the real and negative imaginary part when neglecting the individual growth rate β_i. Note that the contour range has been adjusted for best visibility and thus does not reflect the actual minimum and maximum values.

Considering the pressure modulation with respect to the low-frequency mode $\boldsymbol{\phi}_1$, a high level of p' is found along the separation and reattachment shock. These fluctuations are out of phase and describe an oscillation of the shock system as a whole, i.e. a periodic contraction and expansion of the interaction region. While the separation shock exhibits a nearly translational motion, a flapping motion is observed for the reattachment shock. No fluctuations are found along the incident shock above the shock-intersection location, which remains steady. Similarly to the
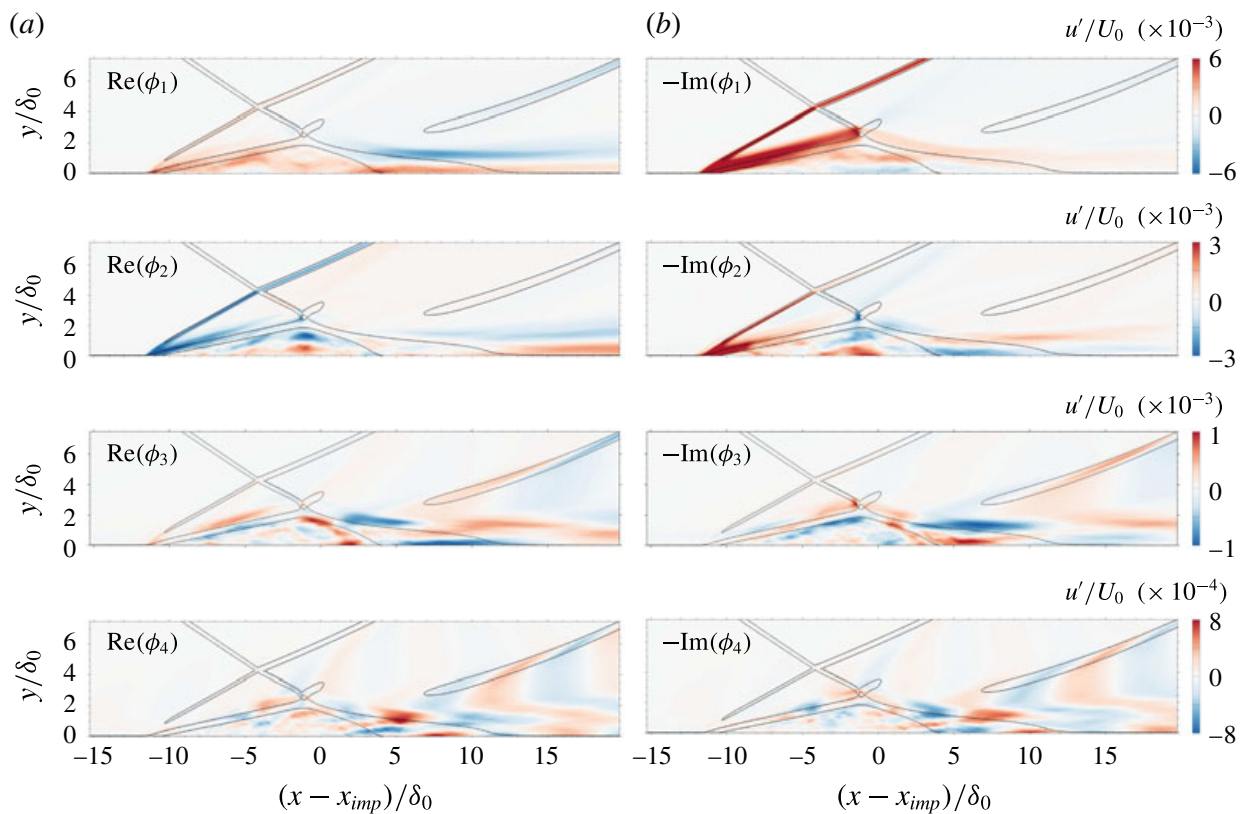
FIGURE 20. (Colour online) Real and imaginary part of DMD modes showing contours of modal velocity fluctuations u'/U_0. (a) $\mathrm{Re}(\boldsymbol{\phi}_i)$. (b) $-\mathrm{Im}(\boldsymbol{\phi}_i)$. Refer to figure 18 for the mode selection. For clarity, the mean shock system, the mean sonic line and the mean dividing streamline are superimposed by black solid lines.

results of Nichols *et al.* (2016), velocity fluctuations (see $\mathrm{Im}(\boldsymbol{\phi}_1)$ in figure 20) are mainly concentrated along the separation shock and the detached shear layer, with minor contributions within the recirculation bubble. Increased levels of pressure and velocity fluctuations are not visible within the incoming TBL for $\boldsymbol{\phi}_1$. Mode $\boldsymbol{\phi}_2$ is associated with a frequency of $f_2 = 0.114 U_0/L_{sep}$ and shares some similarities with the former low-frequency mode: high levels of pressure fluctuations are found along the separation and transmitted incident shock. However, the strength is not uniform along the former, indicating a change of the shock angle with respect to the free stream (see also the animation available online). Pressure fluctuations are increased within the recirculation region close to the bubble apex and probably related to a flapping motion of the incident-shock tip (see $\mathrm{Im}(\boldsymbol{\phi}_2)$ in figure 19), which strongly perturbs the mean separation bubble in this region.

The medium-frequency mode $\boldsymbol{\phi}_3$ and its higher harmonic $\boldsymbol{\phi}_4$ have a strong impact on the reattachment shock in terms of shock wrinkling. This shock wrinkling is clearly seen from an animation of the snapshot sequence and caused by shear-layer vortices interacting with the reattachment compression. The modal shapes provide a proof of this observation, see $\mathrm{Re}(\boldsymbol{\phi}_3)$ and $\mathrm{Re}(\boldsymbol{\phi}_4)$ in figure 19. Their activity is concentrated along the mean sonic line and associated with shear-layer vortices convected downstream while simultaneously inducing eddy Mach waves in the supersonic part of the flow. This finding is consistent with global linear-stability analysis of impinging SWBLI in the laminar regime by Guiho, Alizard & Robinet (2016). Besides the corrugation of the reattachment shock, Mach wave radiation
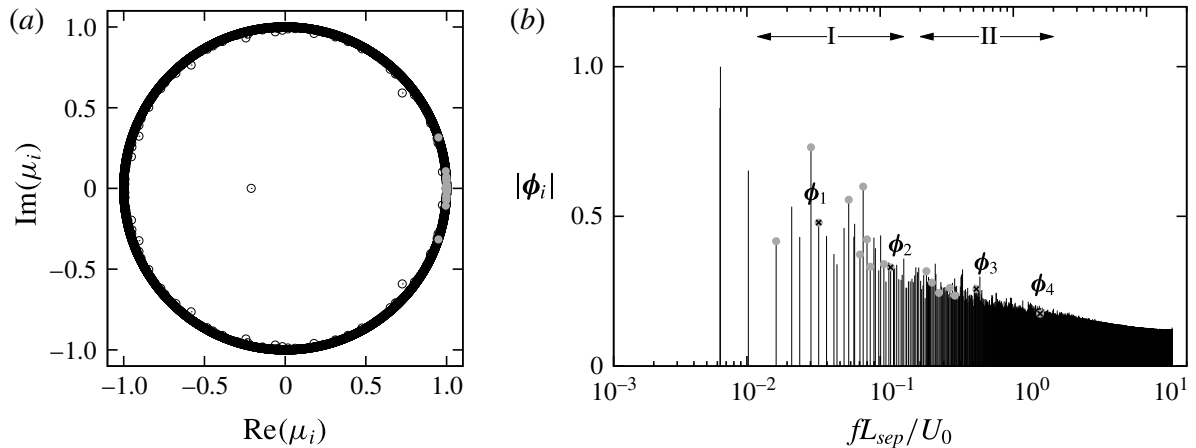
FIGURE 21. (*a*) Spectrum of eigenvalues resulting from the standard DMD algorithm. (*b*) Normalised magnitudes of the DMD modes. (● (grey)) indicate a SPDMD subset of $N_{sub} = 17$ modes.

induces disturbances along the reflected shock above the shock-intersection location. Similar results have been found by Agostini *et al.* (2012) through cross-correlation maps between the pressure field and time series of the streamwise location of the reflected shock for their LES studies of incipient, mildly and fully separated SWBLI at $Ma = 2.3$ and $Re_{\delta_0} \approx 60 \times 10^3$ (see figure 8 in the respective publication). The supplementary online material further highlights that the modes ϕ_3 and ϕ_4 primarily influence the rear part of the separation bubble starting from the bubble apex. While the separation point remains quasi unaltered, the reattachment location is strongly perturbed by the shear-layer vortices reattaching nearby.

We now move on to the DMD analysis of the skin-friction coefficient $\{C_f\}$. The sampling time interval and frequency resolution is the same as for the former analysis. The subdomain chosen for the modal decomposition coincides in streamwise direction with the DMD of spanwise-averaged snapshots, while in spanwise direction we take the full LES domain extent of $-2.25 < z/\delta_0 < 2.25$. As expected, nearly all eigenvalues lie on the unit circle, see figure 21(*a*). The normalised mode magnitudes $|\phi_i|$ are shown in figure 21(*b*). We again employ the SPDMD algorithm to ease the mode selection process and highlight a subset of $N_{sub} = 17$ modes. The spectrum is similar to the one from the spanwise-averaged analysis shown in figure 18(*b*) with respect to the frequencies selected by the SPDMD within each single frequency bin. However, differences can be observed for the high-frequency part starting from $f > 3U_0/L_{sep}$. Since we partially resolve high-frequency related turbulent structures and do not filter them out through spanwise averaging as in the former analysis, the spectrum still shows significant energy content in this region. Note that two modes with the same low frequency of $f = 6 \times 10^{-3} U_0/L_{sep}$ and large modal norm are visible in the spectrum. We do not, however, pay much attention to these modes, as they are very close to the minimum resolvable frequency of the snapshot sequence given by $4.43 \times 10^{-3} U_0/L_{sep}$. Moreover, the SPDMD algorithm does not classify these modes as being dynamically important, even if we increase the subset size.

Figure 22 shows the real and (negative) imaginary part of four dynamically important DMD modes with contours of skin-friction perturbation and isolines of mean separation and reattachment location. The frequencies of the selected modes, $f_1 = 0.035U_0/L_{sep}$, $f_2 = 0.12U_0/L_{sep}$, $f_3 = 0.52U_0/L_{sep}$ and $f_4 = 1.58U_0/L_{sep}$ (see also figure 21(*b*) for reference), are similar to the ones of the spanwise-averaged DMD
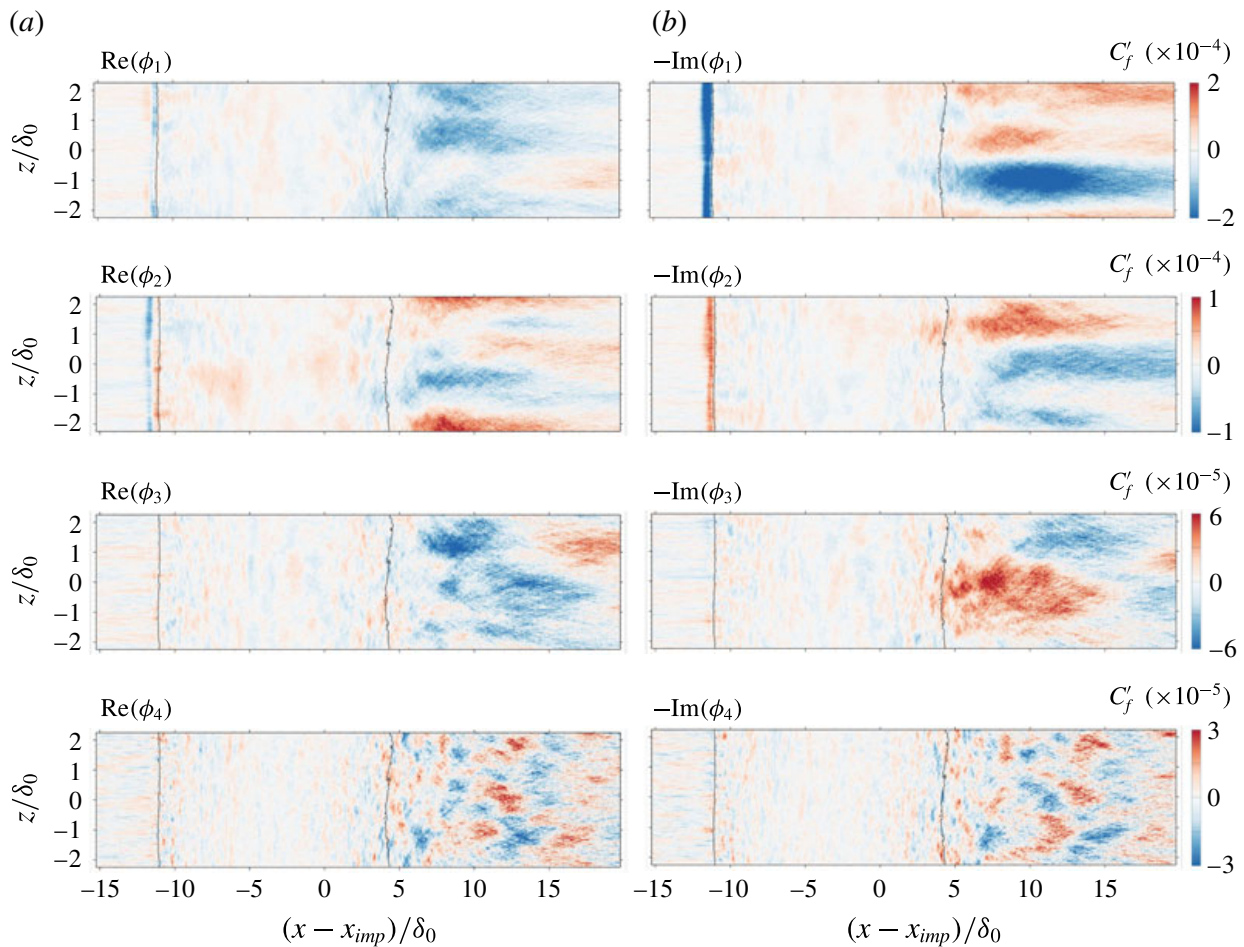
126

FIGURE 22. (Colour online) Real and imaginary part of DMD modes showing contours of modal skin-friction fluctuations C'_f. (a) $\text{Re}(\boldsymbol{\phi}_i)$. (b) $-\text{Im}(\boldsymbol{\phi}_i)$. Refer to figure 21 for the mode selection. For clarity, the mean separation and reattachment locations are superimposed by black solid lines.

analysis. An animation of each mode superimposed on the mean solution is again available as a supplement to the online version of this article and should be considered for the following discussion. There, the instantaneous separation and reattachment locations are highlighted by black solid lines, whereas the mean lines are shown in the print version. The low-frequency mode $\boldsymbol{\phi}_1$ shows a nearly two-dimensional modulation of the separation-shock foot, see $\text{Im}(\boldsymbol{\phi}_1)$ in figure 22, with comparably low activity inside the recirculation zone. Remarkably, streamwise streaks (generated through Görtler-like vortices) starting slightly upstream of the mean reattachment location and extending up to the domain end are clearly visible. A spanwise wavelength of approximately $2\delta_0$ is found (similar to the spanwise width of each vortex pair shown in figure 9), from which we conclude to have identified footprints of Görtler-like vortices. Their impact on the skin friction results in a large-scale flapping of the reattachment line, superimposed on a breathing motion of the separation bubble as a whole (see also the animation available online). In the absence of Görtler-like vortices, the separation bubble would uniformly expand and shrink across the span. The shape of the second dynamically important mode $\boldsymbol{\phi}_2$ is similar to the former. Streamwise streaks of same wavelength are dominant at this frequency and the separation line moves essentially back and forth. The animation reveals a spanwise

127

motion of the streaks, which provokes a spanwise wrinkling of the reattachment line without significant influence on its streamwise position.

The medium-frequency mode $\boldsymbol{\phi}_3$ ($f_3 = 0.52U_0/L_{sep}$) is connected to large-scale vortices reattaching downstream of the mean reattachment line, which are subsequently convected towards the domain outlet. Similarly to the results from the spanwise-averaged DMD analysis, modes $\boldsymbol{\phi}_3$ and $\boldsymbol{\phi}_4$ do not considerably affect the separation line but leave a strong footprint on the reattachment dynamics (see also the animation available online).

4. Summary and discussion

The present work was motivated by the lack of an analysis of strong impinging shock-wave/turbulent boundary-layer interactions (SWBLI) with very large mean-flow separation at high Reynolds number based on well-resolved numerical simulation data. We have performed wall-resolved large-eddy simulations for the flow configuration of a recent experiment (Daub *et al.* 2015), consisting of a flat plate turbulent boundary layer at Mach number $Ma = 3$ and Reynolds number $Re_{\delta_0} = 203 \times 10^3$. The incoming TBL interacts with a wedge-induced shock wave that deflects the incoming flow by $\vartheta = 19.6°$ and leads to a strongly separated mean-flow region with a length of $L_{sep} = 15.5\delta_0$.

The mean wall-pressure evolution agrees with experimental measurements and exhibits a distinct pressure plateau representative of a strong SWBLI. Similarly to LES results of Loginov *et al.* (2006) for their compression corner flow, Görtler-like vortices exist in our configuration. These counter-rotating streamwise vortices develop slightly downstream of the bubble apex and induce a strong spanwise flow modulation in this region. In our case, however, these vortices are not locked at a specific spanwise position, but rather undergo a meandering motion that is coupled to the separation-bubble dynamics.

Our well-resolved and long-time integrated LES data enable an accurate analysis of the low-frequency SWBLI dynamics. Spectral analyses of numerical and experimental wall-pressure signals near the separation point demonstrate a broadband low-frequency unsteadiness with a peak amplitude near $St_{L_{sep}} = 0.04$, consistent with experimental values found by Dussauge *et al.* (2006) for different flow geometries and upstream conditions. High Reynolds number effects lead to a distinct peak (global maximum) in the r.m.s. wall-pressure fluctuations centred around the mean separation location with 95 % fluctuation intensity associated with frequencies below $1U_0/L_{sep}$. Furthermore, the wall-pressure signal is strongly intermittent at this location.

Sparsity-promoting dynamic mode decomposition (Jovanović *et al.* 2014) has proven effective in identifying robust and dynamically important modes of our SWBLI when applied to spanwise-averaged snapshots as well as snapshots of the two-dimensional skin-friction coefficient. Essentially, two types of modes have been found: low-frequency modes ($St_{L_{sep}} \approx 0.04$) primarily involve the shock system, the separated shear layer and the separation bubble as an entity, leading to the classical breathing motion of the recirculating flow together with a forward/backward motion of the shock system. Medium-frequency modes ($St_{L_{sep}} \approx 0.5$) involve shear-layer vortices convected downstream while simultaneously inducing eddy Mach waves in the supersonic part of the flow. Shock corrugation, both for the reattachment and reflected shock, is found to be connected to these frequencies. Low-frequency skin-friction modes include streamwise streaks downstream of the nominal impingement location, which we have identified as footprints of Görtler-like vortices. These vortices cause a

large-scale flapping of the reattachment line superimposed on a breathing motion of the separation bubble.

In contrast to experimental observations by Ganapathisubramani *et al.* (2009) for a compression corner flow, our modal analysis does not identify any coherent structure of sufficient length (superstructure) upstream of the interaction that could possibly provoke the SWBLI unsteadiness. Our turbulent inflow conditions and domain size limit such structures to a minimum frequency one order of magnitude larger than the observed characteristic frequencies. The scaling analysis of Clemens & Narayanaswamy (2014) further shows that an upstream mechanism related to momentum fluctuations in the incoming TBL is unlikely responsible for the large-scale separation-shock motion in the present study. Collapse events of the separation bubble as observed by Priebe & Martín (2012) for their weak compression corner flow have not been found for our strong SWBLI. Increasing the shock strength and keeping the upstream TBL conditions the same decreases the natural frequency of the SWBLI system and hence reduces its receptive frequency band. Upstream mechanisms cannot explain the observed frequencies for our particular interaction and the quasi-constant Strouhal number found both experimentally and numerically for a wide range of interaction parameters. Our analyses support a mechanism proposed by Touber & Sandham (2011) and Grilli *et al.* (2012), where the low-frequency unsteadiness is an intrinsic property of the interaction. It may not be self-sustaining and thus may require a coherent or incoherent forcing (Touber & Sandham 2011) originating from upstream or within the interaction zone (Sansica, Sandham & Hu 2014). For our strong high Reynolds number SWBLI the separation-bubble dynamics is clearly coupled to unsteady Görtler-like vortices, which might act as a source for continuous (coherent) forcing of the separation-shock-system dynamics. Interestingly, since the discoveries were made independently of one another, this is the same conclusion as the one drawn by Priebe *et al.* (2016). These authors recently have analysed previous DNS results of Priebe & Martín (2012) of a $Ma = 2.9$ compression corner flow using DMD of spanwise-averaged as well as three-dimensional snapshots. Therein, low-frequency modes are characterised by streamwise-elongated regions of low and high momentum that the authors identified as being induced through Görtler-like vortices. Similar to our results, such vortices are unsteady and move in spanwise direction. While Priebe *et al.* (2016) remain in doubt whether the observed dynamics constitutes an unusual event due to a relatively short time duration captured in their DNS ($200\delta_0/U_0$), our results with a much longer time period of $3805\delta_0/U_0$ confirm this assertion. Furthermore, our results show that unsteady large-scale streamwise structures are also present in strong impinging SWBLI.

Acknowledgements

Supplementary movies

Supplementary movies are available at https://doi.org/10.1017/jfm.2017.308.

REFERENCES

ADAMS, N. A. 2000 Direct simulation of the turbulent boundary layer along a compression ramp at $M = 3$ and $Re_\theta = 1685$. *J. Fluid Mech.* **420**, 47–83.

AGOSTINI, L., LARCHEVÊQUE, L., DUPONT, P., DEBIÈVE, J.-F. & DUSSAUGE, J.-P. 2012 Zones of influence and shock motion in a shock/boundary-layer interaction. *AIAA J.* **50** (6), 1377–1387.

ANDREOPOULOS, J. & MUCK, K. C. 1987 Some new aspects of the shock-wave/boundary-layer interaction in compression-ramp flows. *J. Fluid Mech.* **180**, 405–428.

AUBARD, G., GLOERFELT, X. & ROBINET, J.-C. 2013 Large-eddy simulation of broadband unsteadiness in a shock/boundary-layer interaction. *AIAA J.* **51** (10), 2395–2409.

BERESH, S. J., CLEMENS, N. T. & DOLLING, D. S. 2002 Relationship between upstream turbulent boundary-layer velocity fluctuations and separation shock unsteadiness. *AIAA J.* **40**, 2412–2422.

BERMEJO-MORENO, I., CAMPO, L., LARSSON, J., BODART, J., HELMER, D. & EATON, J. K. 2014 Confinement effects in shock wave/turbulent boundary layer interactions through wall-modelled large-eddy simulations. *J. Fluid Mech.* **758**, 5–62.

BOOKEY, P., WYCKHAM, C., SMITS, A. & MARTÍN, M. P. 2005 New experimental data of STBLI at DNS/LES accessible Reynolds numbers. In *43rd AIAA Aerospace Sciences Meeting and Exhibit, Reston, Virigina*, pp. 1–18. American Institute of Aeronautics and Astronautics.

CARRIÈRE, P., SIRIEIX, M. & SOLIGNAE, J.-L. 1969 Similarity properties of the laminar or turbulent separation phenomena in a non-uniform supersonic flow. In *Applied Mechanics – Proceedings of the Twelfth International Congress of Applied Mechanics*, pp. 145–157. Springer.

CLEMENS, N. T. & NARAYANASWAMY, V. 2009 Shock/turbulent boundary layer interactions: review of recent work on sources of unsteadiness (invited). In *39th AIAA Fluid Dynamics Conference, Reston, Virigina*, pp. 1–25. American Institute of Aeronautics and Astronautics.

CLEMENS, N. T. & NARAYANASWAMY, V. 2014 Low-frequency unsteadiness of shock wave/turbulent boundary layer interactions. *Annu. Rev. Fluid Mech.* **46** (1), 469–492.

COLES, D. E. 1962 The turbulent boundary layer in a compressible fluid. *Tech. Rep.* R-403-PR.

COLES, D. L. 1953 Measurements in the boundary layer on a smooth flat plate in supersonic flow. PhD thesis, California Institute of Technology.

DAUB, D., WILLEMS, S. & GÜLHAN, A. 2015 Experimental results on unsteady shock-wave/boundary-layer interaction induced by an impinging shock. *CEAS Space J.* **8** (1), 3–12.

DAUB, D., WILLEMS, S. & GÜLHAN, A. 2016 Experiments on the interaction of a fast-moving shock with an elastic panel. *AIAA J.* **54** (2), 670–678.

DÉLERY, J. & DUSSAUGE, J.-P. 2009 Some physical aspects of shock wave/boundary layer interactions. *Shock Waves* **19** (6), 453–468.

DÉLERY, J. & MARVIN, J. G. 1986 Shock-wave boundary layer interactions. AGARD-AG *Tech. Rep.* 280.

DOLLING, D. S. 2001 Fifty years of shock-wave/boundary-layer interaction research: what next? *AIAA J.* **39** (8), 1517–1531.

DOLLING, D. S. & ERENGIL, M. E. 1991 Unsteady wave structure near separation in a Mach 5 compression ramp interaction. *AIAA J.* **29**, 728–735.

DOLLING, D. S. & MURPHY, M. T. 1983 Unsteadiness of the separation shock wave structure in a supersonic compression ramp flowfield. *AIAA J.* **21** (12), 1628–1634.

DOLLING, D. S. & OR, C. T. 1985 Unsteadiness of the shock wave structure in attached and separated compression ramp flows. *Exp. Fluids* **3** (1), 24–32.

VAN DRIEST, E. R. 1956 The problem of aerodynamic heating. *Aeronaut. Engng Rev.* **15**, 26–41.

DUCROS, F., FERRAND, V., NICOUD, F., WEBER, C., DARRACQ, D., GACHERIEU, C. & POINSOT, T. 1999 Large-eddy simulation of the shock/turbulence interaction. *J. Comput. Phys.* **152** (2), 517–549.

DUPONT, P., HADDAD, C. & DEBIÈVE, J.-F. 2006 Space and time organization in a shock-induced separated boundary layer. *J. Fluid Mech.* **559**, 255–277.

DUSSAUGE, J.-P., DUPONT, P. & DEBIÈVE, J.-F. 2006 Unsteadiness in shock wave boundary layer interactions with separation. *Aerosp. Sci. Technol.* **10** (2), 85–91.

ERDOS, J. & PALLONE, A. 1963 Shock-boundary layer interaction and flow separations. In *Proceedings of the 1962 Heat Transfer and Fluid Mechanics Institute*.

ERENGIL, M. E. & DOLLING, D. S. 1993 Physical causes of separation shock unsteadiness in shock-wave/turbulent boundary layer interactions. *AIAA Paper* 93–3134.

FERNHOLZ, H. H. & FINLEY, P. J. 1977 A critical compilation of compressible turbulent boundary layer data. AGARD-AG *Tech. Rep.* 223.

FLORYAN, J. M. 1991 On the Görtler instability of boundary layers. *Prog. Aerosp. Sci.* **28** (3), 235–271.

GANAPATHISUBRAMANI, B., CLEMENS, N. T. & DOLLING, D. S. 2009 Low-frequency dynamics of shock-induced separation in a compression ramp interaction. *J. Fluid Mech.* **636**, 397–425.

GATSKI, T. B. & BONNET, J.-P. 2009 *Compressibility, Turbulence and High Speed Flow*. Elsevier.

GINOUX, J. J. 1971 Streamwise vortices in reattaching high-speed flows – A suggested approach. *AIAA J.* **9** (4), 759–760.

GÖRTLER, H. 1941 Instabilität laminarer Grenzschichten an konkaven Wänden gegenüber gewissen dreidimensionalen Störungen. *Z. Angew. Math. Mech.* **21** (4), 250–252.

GOTTLIEB, S. & SHU, C.-W. 1998 Total variation diminishing Runge–Kutta schemes. *Math. Comput. Am. Math. Soc.* **67** (221), 73–85.

GRILLI, M., HICKEL, S. & ADAMS, N. A. 2013 Large-eddy simulation of a supersonic turbulent boundary layer over a compression expansion ramp. *Intl J. Heat Fluid Flow* **42**, 79–93.

GRILLI, M., SCHMID, P. J., HICKEL, S. & ADAMS, N. A. 2012 Analysis of unsteady behaviour in shockwave turbulent boundary layer interaction. *J. Fluid Mech.* **700**, 16–28.

GUARINI, S. E., MOSER, R. D., SHARIFF, K. & WRAY, A. 2000 Direct numerical simulation of a supersonic turbulent boundary layer at Mach 2.5. *J. Fluid Mech.* **414**, 1–33.

GUIHO, F., ALIZARD, F. & ROBINET, J.-CH. 2016 Instabilities in oblique shock wave/laminar boundary-layer interactions. *J. Fluid Mech.* **789**, 1–35.

HADJADJ, A. 2012 Large-eddy simulation of shock/boundary-layer interaction. *AIAA J.* **50** (12), 2919–2927.

HICKEL, S., ADAMS, N. A. & DOMARADZKI, J. A. 2006 An adaptive local deconvolution method for implicit LES. *J. Comput. Phys.* **213** (1), 413–436.

HICKEL, S., EGERER, C. P. & LARSSON, J. 2014 Subgrid-scale modeling for implicit large eddy simulation of compressible flows and shock-turbulence interaction. *Phys. Fluids* **26** (10), 106101.

HOPKINS, E. J. & INOUYE, M. 1971 An evaluation of theories for predicting turbulent skin friction and heat transfer on flat plates at supersonic and hypersonic Mach numbers. *AIAA J.* **9** (6), 993–1003.

HOU, Y. X., CLEMENS, N. T. & DOLLING, D. 2003 Wide-field study of shock-induced turbulent boundary layer separation. In *41st Aerospace Sciences Meeting and Exhibit*, *Reno, Nevada*. AIAA.

HUMBLE, R. A., ELSINGA, G. E., SCARANO, F. & VAN OUDHEUSDEN, B. W. 2009 Three-dimensional instantaneous structure of a shock wave/turbulent boundary layer interaction. *J. Fluid Mech.* **622**, 33–62.

JOVANOVIĆ, M. R., SCHMID, P. J. & NICHOLS, J. W. 2014 Sparsity-promoting dynamic mode decomposition. *Phys. Fluids* **26** (2), 024103.

KISTLER, A. L. 1964 Fluctuating wall pressure under a separated supersonic flow. *J. Acoust. Soc. Am.* **36** (3), 543–550.

KLEIN, M., SADIKI, A. & JANICKA, J. 2003 A digital filter based generation of inflow data for spatially developing direct numerical or large Eddy simulations. *J. Comput. Phys.* **186**, 652–665.

KOMMINAHO, J. & SKOTE, M. 2002 Reynolds stress budgets in Couette and boundary layer flows. *Flow Turbul. Combust.* **68** (2), 167–192.

KOTTKE, V. 1988 On the instability of laminar boundary layers along concave walls towards Görtler vortices. In *Propagation in Systems Far from Equilibrium, Springer Series in Synergetics, Berlin, Heidelberg*, vol. 41, pp. 390–398. Springer.

LESIEUR, M., MÉTAIS, O. & COMTE, P. 2005 *Large-Eddy Simulations of Turbulence*. Cambridge University Press.

LOGINOV, M. S., ADAMS, N. A. & ZHELTOVODOV, A. A. 2006 Large-eddy simulation of shock-wave/turbulent-boundary-layer interaction. *J. Fluid Mech.* **565**, 135.

MAEDER, T., ADAMS, N. A. & KLEISER, L. 2001 Direct simulation of turbulent supersonic boundary layers by an extended temporal approach. *J. Fluid Mech.* **429**, 187–216.

MATHEIS, J. & HICKEL, S. 2015 On the transition between regular and irregular shock patterns of shock-wave/boundary-layer interactions. *J. Fluid Mech.* **776**, 200–234.

MORGAN, B., DURAISAMY, K., NGUYEN, N., KAWAI, S. & LELE, S. K. 2013 Flow physics and RANS modelling of oblique shock/turbulent boundary layer interaction. *J. Fluid Mech.* **729**, 231–284.

NAIDOO, K. & SKEWS, B. W. 2011 Dynamic effects on the transition between two-dimensional regular and Mach reflection of shock waves in an ideal, steady supersonic free stream. *J. Fluid Mech.* **676**, 432–460.

NICHOLS, J. W., LARSSON, J., BERNARDINI, M. & PIROZZOLI, S. 2016 Stability and modal analysis of shock/boundary layer interactions. *Theor. Comput. Fluid Dyn.* **31** (1), 33–50.

PASQUARIELLO, V., GRILLI, M., HICKEL, S. & ADAMS, N. A. 2014 Large-eddy simulation of passive shock-wave/boundary-layer interaction control. *Intl J. Heat Fluid Flow* **49**, 116–127.

PIPONNIAU, S., DUSSAUGE, J.-P., DEBIÈVE, J.-F. & DUPONT, P. 2009 A simple model for low-frequency unsteadiness in shock-induced separation. *J. Fluid Mech.* **629**, 87.

PIROZZOLI, S. & BERNARDINI, M. 2011 Turbulence in supersonic boundary layers at moderate Reynolds number. *J. Fluid Mech.* **688**, 120–168.

PIROZZOLI, S. & GRASSO, F. 2006 Direct numerical simulation of impinging shock wave/turbulent boundary layer interaction at $M = 2.25$. *Phys. Fluids* **18** (6), 065113.

PIROZZOLI, S., GRASSO, F. & GATSKI, T. B. 2004 Direct numerical simulation and analysis of a spatially evolving supersonic turbulent boundary layer at $M = 2.25$. *Phys. Fluids* **16** (3), 530–545.

PIROZZOLI, S., LARSSON, J., NICHOLS, J. W., MORGAN, B. E. & LELE, S. K. 2010 Analysis of unsteady effects in shock/boundary layer interactions. In *Proceedings of the 2010 CTR Summer Program*. Center of Turbulence Research.

PLOTKIN, K. J. 1975 Shock wave oscillation driven by turbulent boundary-layer fluctuations. *AIAA J.* **13** (8), 1036–1040.

PRIEBE, S. & MARTÍN, M. P. 2012 Low-frequency unsteadiness in shock wave-turbulent boundary layer interaction. *J. Fluid Mech.* **699**, 1–49.

PRIEBE, S., TU, J. H., ROWLEY, C. W. & MARTÍN, M. P. 2016 Low-frequency dynamics in a shock-induced separated flow. *J. Fluid Mech.* **807**, 441–477.

PRIEBE, S., WU, M. & MARTÍN, M. P. 2009 Direct numerical simulation of a reflected-shock-wave/turbulent-boundary-layer interaction. *AIAA J.* **47** (5), 1173–1185.

QUAATZ, J. F., GIGLMAIER, M., HICKEL, S. & ADAMS, N. A. 2014 Large-eddy simulation of a pseudo-shock system in a Laval nozzle. *Intl J. Heat Fluid Flow* **49**, 108–115.

RINGUETTE, M. J., BOOKEY, P. B., WYCKHAM, C. & SMITS, A. J. 2009 Experimental study of a Mach 3 compression ramp interaction at $Re_\theta = 2400$. *AIAA J.* **47** (2), 373–385.

ROWLEY, C. W., MEZIĆ, I., BAGHERI, S., SCHLATTER, P. & HENNINGSON, D. S. 2009 Spectral analysis of nonlinear flows. *J. Fluid Mech.* **641**, 115–127.

SANDHAM, N. D. 2016 Effects of compressibility and shock-wave interactions on turbulent shear flows. *Flow Turbul. Combust.* **97** (1), 1–25.

SANSICA, A., SANDHAM, N. D. & HU, Z. 2014 Forced response of a laminar shock-induced separation bubble. *Phys. Fluids* **26** (9), 093601.

SCHLATTER, P. & ÖRLÜ, R. 2010 Assessment of direct numerical simulation data of turbulent boundary layers. *J. Fluid Mech.* **659**, 116–126.

SCHMID, P. J. 2010 Dynamic mode decomposition of numerical and experimental data. *J. Fluid Mech.* **656**, 5–28.

SCHÜLEIN, E. & TROFIMOV, V. M. 2011 Steady longitudinal vortices in supersonic turbulent separated flows. *J. Fluid Mech.* **672**, 451–476.

SELIG, M. S., ANDREOPOULOS, J., MUCK, K. C., DUSSAUGE, J. P. & SMITS, A. J. 1989 Turbulence structure in a shock wave/turbulent boundary-layer interaction. *AIAA J.* **27** (7), 862–869.

SIMENS, M. P., JIMÉNEZ, J., HOYAS, S. & MIZUNO, Y. 2009 A high-resolution code for turbulent boundary layers. *J. Comput. Phys.* **228** (11), 4218–4231.

SMITS, A. J. & DUSSAUGE, J.-P. 2006 *Turbulent Shear Layers in Supersonic Flow*. Springer.

SMITS, A. J., MATHESON, N. & JOUBERT, P. N. 1983 Low-Reynolds-number turbulent boundary layers in zero and favorable pressure gradients. *J. Ship Res.* **27**, 147–157.

SOUVEREIN, L. J., DUPONT, P., DEBIÈVE, J.-F., DUSSAUGE, J.-P., VAN OUDHEUSDEN, B. W. & SCARANO, F. 2010 Effect of interaction strength on unsteadiness in turbulent shock-wave-induced separations. *AIAA J.* **48** (7), 1480–1493.

STOLZ, S. & ADAMS, N. A. 2003 Large-eddy simulation of high-Reynolds-number supersonic boundary layers using the approximate deconvolution model and a rescaling and recycling technique. *Phys. Fluids* **15** (8), 2398.

THOMAS, F. O., PUTNAM, C. M. & CHU, H. C. 1994 On the mechanism of unsteady shock oscillation in shock wave/turbulent boundary layer interactions. *Exp. Fluids* **18-18** (1–2), 69–81.

TOUBER, E. & SANDHAM, N. D. 2009 Large-eddy simulation of low-frequency unsteadiness in a turbulent shock-induced separation bubble. *Theor. Comput. Fluid Dyn.* **23** (2), 79–107.

TOUBER, E. & SANDHAM, N. D. 2011 Low-order stochastic modelling of low-frequency motions in reflected shock-wave/boundary-layer interactions. *J. Fluid Mech.* **671**, 417–465.

TU, J. H. 2013 On dynamic mode decomposition: theory and applications. PhD thesis, Princeton University.

TU, J. H. & ROWLEY, C. W. 2012 An improved algorithm for balanced POD through an analytic treatment of impulse response tails. *J. Comput. Phys.* **231** (16), 5317–5333.

ÜNALMIS, O. & DOLLING, D. 1994 Decay of wall pressure field and structure of a Mach 5 adiabatic turbulent boundary layer. In *Fluid Dynamics Conference, Reston, Virigina*. AIAA.

WANG, B., SANDHAM, N. D., HU, Z. & LIU, W. 2015 Numerical study of oblique shock-wave/boundary-layer interaction considering sidewall effects. *J. Fluid Mech.* **767**, 526–561.

WILLEMS, S. 2016 Strömung-Struktur-Wechselwirkung in Überschallströmungen. PhD thesis, German Aerospace Center (DLR).

WU, M. & MARTÍN, M. P. 2008 Analysis of shock motion in shockwave and turbulent boundary layer interaction using direct numerical simulation data. *J. Fluid Mech.* **594**, 71–83.

ZUKOSKI, E. E. 1967 Turbulent boundary-layer separation in front of a forward-facing step. *AIAA J.* **5** (10), 1746–1753.

B.4. Coupled simulation of shock-wave/turbulent boundary-layer interaction over a flexible panel

Coupled simulation of shock-wave/turbulent boundary-layer interaction over a flexible panel

V. Pasquariello[†,1], S. Hickel[1,2] and N. A. Adams[1]

[1]*Institute of Aerodynamics and Fluid Mechanics, Technische Universität München*
Boltzmannstr. 15, D-85748 Garching
[2]*Faculty of Aerospace Engineering*
Technische Universiteit Delft, Kluyverweg 1, NL-2629 HS Delft

G. Hammerl[3] and W. A. Wall[3]
[3]*Institute for Computational Mechanics*
Technische Universität München, Boltzmannstr. 15, D-85748 Garching

D. Daub[4], S. Willems[4] and A. Gülhan[4]
[4] *Institute of Aerodynamics and Flow Technology*
German Aerospace Center (DLR), Linder Höhe, D-51147 Cologne

[†]Corresponding author, E-mail: vito.pasquariello@tum.de

Abstract

We investigate the interaction of an oblique shock generated by a pitching wedge with a turbulent boundary-layer at a free-stream Mach number of $Ma_\infty = 3.0$ and a Reynolds number based on the incoming boundary-layer thickness of $Re_{\delta_{0,I}} = 205 \cdot 10^3$. Large-eddy simulations (LES) are performed for two configurations, that differ in the treatment of the wind-tunnel wall and shock generator movement within the experiment: A fixed panel with a static shock generator that deflects the flow by $\Theta = 20°$, and the transient interaction of a pitching shock generator with an elastic panel. Besides mean and instantaneous flow quantities, we investigate unsteady aspects of the interaction region by means of wall-pressure spectra and provide comparison with experimental data whenever possible.

1. Introduction

Shock-wave/boundary-layer interactions (SWBLI) frequently occur in flows of technological interest, such as supersonic air intakes, turbomachine cascades, helicopter blades, supersonic nozzles and launch vehicles in general. SWBLI can critically affect the vehicle or machine performance in several ways. The adverse pressure gradient acting on the flow strongly retards the boundary-layer, eventually leading to flow separation if the imposed pressure gradient is strong enough [5].

A schematic of the basic interaction type studied in this work is shown in Fig. 1. The adverse pressure gradient imposed by the incident shock C_1 is large enough to cause boundary-layer separation. Separation takes place well ahead of the inviscid impingement x_{imp}. The upstream propagation of the pressure gradient within the subsonic part of the turbulent boundary-layer (TBL) induces compression waves in the supersonic part of the TBL, which coalesce into the reflected shock C_2. The reflected shock intersects the incident shock at point I and the original shocks continue traveling as the transmitted shocks C_3 and C_4, respectively. The shock C_4 penetrates into the separated shear layer, curves due to the local Mach number variation and finally reflects at the sonic line as an expansion fan. The separated shear layer, being primarily responsible for turbulence amplification, follows the inclination of the initial part of the separation bubble, while being deflected towards the wall due to the expansion fan and finally reattaching further downstream. The compression waves associated with reattachment merge to form the reattachment shock C_5. Downstream of the SWBLI the TBL recovers an equilibrium state.

Until the 1950's, SWBLI have been described as a steady process, which nowadays is known to be incorrect when shock-induced boundary-layer separation occurs. As stated by [6], the interaction region is the main source of maximum mean and fluctuating pressure levels as well as thermal loads. Turbulence production is enhanced in
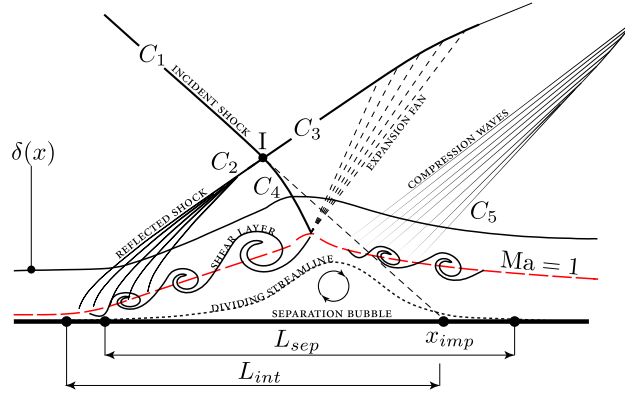
Figure 1: Schematic of the oblique shock-wave/boundary-layer interaction with mean separation [15].

the vicinity of the mean separation location, which in turn increases viscous dissipation in this region [5]. The low-frequency unsteadiness of the reflected shock is a crucial aspect with regard to the choice of materials, since it is a main contribution to failure due to fatigue. [24] have shown that the separation acts as a broadband amplifier, for upstream distburbances.

In the context of launch vehicles, SWBLI are common flow features that may critically affect the rocket nozzle performance. During the start-up of liquid propellant fueled rocket engines, the rocket nozzle operates in an overexpanded condition, which leads to unsteady internal flow separation. The asymmetry of the separation and the inherent shock movement result in a net lateral force, which is often referred to as "side-load". These high-magnitude transient loads can be severe enough to fail interfacing components as well as the complete nozzle in the rocket engine. Experimental tests of full-scale and sub-scale nozzles by [2] revealed a feedback mechanism between the unsteady SWBLI and one specific structural mode for a particular range of nozzle pressure ratios, resulting in a self-excited or aeroelastic vibration phenomenon. A comprehensive work on rocket nozzle flow separation and various side-load mechanisms can be found in [14]. With future rocket technologies focusing on optimal weight systems, fluid-structure interactions (FSI) become significant and must be taken into account in the design process in order to ensure the structural integrity. Multi-disciplinary numerical tools are necessary for a correct prediction of the complex flow physics influenced by structural deformations.

Within the collaborative research program "Transregio 40" (SFB-TRR 40) one objective is to develop high-fidelity numerical tools for an integrated interdisciplinary design process. For our studies we developed a Finite Volume – Finite Element coupling approach for the solution of compressible FSI problems based on a staggered Dirichlet-Neumann partitioning, where the interface motion within the Eulerian flow solver is accounted for by a cut-element based immersed boundary method [16]. Coupling conditions at the non-matching conjoined interface are enforced using a Mortar method.

Previous numerical studies concentrate on SWBLI with respect to a rigid surface [1, 7, 15] or deal with the aeroelastic response of elastic panels exposed to a laminar SWBLI [25]. To the authors knowledge, there is no high-fidelity large-eddy simulation (LES) available in the literature that deals with turbulent SWBLI coupled with a structural solver. In this study, we investigate the interaction of a TBL subjected to an adverse pressure gradient with a rigid and flexible panel. The adverse pressure gradient is generated by a pitching shock generator, inducing a time-varying pressure load on the panel, which subsequently leads to shock-induced flow separation and resembles typical overexpanded nozzle flow conditions. Besides mean and instantaneous flow quantities, we investigate unsteady aspects by means of wall-pressure spectra and the influence of the panel motion on turbulence.

Table 1: Flow parameters for the present studies.

Ma_∞	T_∞	p_∞	$\delta_{0,I}{}^a$	$\delta_{0,II}{}^b$	$Re_{\delta_{0,I}}$	$Re_{\delta_{0,II}}$
3.0	100.7 [K]	15.2 [kPa]	4.5 [mm]	5.2 [mm]	$205 \cdot 10^3$	$237 \cdot 10^3$

a. Evaluated at $x = 0.2$ m *b*. Evaluated at $x = 0.26$ m

2. Experimental setup

Experiments were conducted in the Trisonic Wind Tunnel (TMK) of the Supersonic and Hypersonic Technologies Department at DLR, Cologne. The TMK is a blow-down facility with a closed test section of 0.6×0.6 m. The
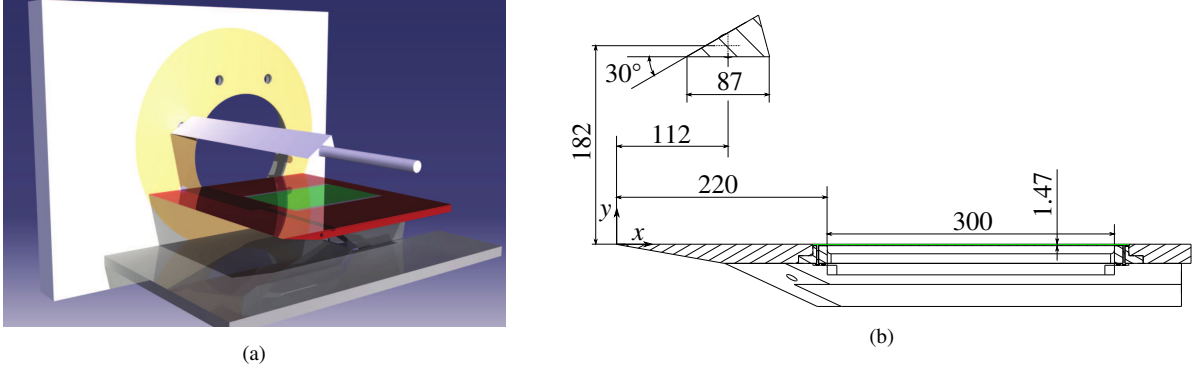
(a)

(b)

Figure 2: (a) Schematic of the experimental model. The baseplate consists of a fixed part (red) and an optional flexible insert (green). The shock generator is mounted on a shaft and spans the complete wind-tunnel width. (b) Two-dimensional sketch with main dimensions in millimeters.

continuously adjustable nozzle enables a Mach number range of $\text{Ma}_\infty = 0.5 \cdots 4.5$. Table 1 summarizes the flow conditions used for this investigation.

Figure 2(a) shows the setup that is used to validate our numerical tools. The interested reader is referred to [3, 4] for a detailed description. The test setup consists of a wedge mounted on a shaft that spans the complete wind-tunnel width, and of a baseplate with an optionally elastic part (green portion of the baseplate in Fig. 2(a)) for FSI experiments. The baseplate has the same width as the wind-tunnel test section. Main dimensions are given in Fig. 2(b). For the FSI configuration, a frame is inserted into the baseplate, which carries an elastic panel made of 1.47 mm thick spring steel (CK 75). It has a length of L = 300 mm and width of W = 200 mm. Two rows of rivets at the front side ($x \in [205, 220]$ mm) as well as at the rear side ($x \in [520, 535]$ mm) of the elastic panel are used to fix the panel with the surrounding frame. In spanwise direction the panel motion is not restricted. A cavity below the panel carries measurement instrumentations. It is sealed through a thick layer of a soft foam rubber, applied between the underside of the elastic panel and the frame. Pressure equalization of the cavity is done at a point upstream of the interaction, resembling undisturbed free-stream conditions. Boundary-layer tripping is applied behind the leading edge to ensure a fully developed TBL.

In order to ensure well-defined initial conditions for both fluid and solid subdomain for the FSI configuration, the initial position of the wedge is chosen in such a way that the generated shock-wave does not impinge on the elastic panel, yielding a sufficiently undeformed and unstressed structure. In case of FSI experiments, the wedge is pitched from $\Theta_{t_0} = 0°$ to $\Theta_{t_1} = 17.5°$ in approximately $T_{rot} = 15$ ms, inducing a time-varying load on the plate with significant boundary-layer separation. For the baseline uncoupled configuration, the static shock generator deflects the flow by $\Theta = 20°$.

3. Numerical approach

The governing equations for the fluid domain are the compressible Navier-Stokes equations. The Adaptive Local Deconvolution Method (ALDM, [9, 10]) is used for the discretization of the convective fluxes and provides a physically consistent subgrid-scale turbulence model for implicit LES. Employing a shock sensor to detect discontinuities and switch on the shock-dissipation mechanism, ALDM can capture shock waves while smooth waves and turbulence are propagated accurately without excessive numerical dissipation [10]. The diffusive fluxes are discretized using a 2nd order central difference scheme, and a 3rd order Runge Kutta scheme is used for the time integration. The flow solver operates on Cartesian grids for a high parallel performance. The elastic wall boundary is represented by a cut-element immersed boundary method [13, 16].

The structural field is governed by the weak form of the linear-momentum balance, describing equilibrium of the forces of inertia, internal and external forces. A hyperelastic Saint Venant-Kirchhoff material model is chosen. The structural field is discretized with the Finite Element method. The fully discrete nonlinear structural system is solved iteratively by a Newton-Raphson method. The method of enhanced assumed strains (EAS) is used in order to avoid locking phenomena. For time integration, the generalized trapezoidal rule (or one-step-θ scheme) is employed.

We make use of a classical Dirichlet-Neumann partitioning in conjunction with a Conventional Serial Staggered procedure for coupling of the two domains. Our framework [16] inevitably leads to a non-matching discretization of the interface between both subdomains. Load transfer is established by a consistent Mortar method, which preserves linear and angular momentum. In order to resolve the different time-scales of both subdomains and increase the overall

efficiency, subcycling within the fluid domain is used. The chosen subcycling time-step is $\Delta t_s = 2 \cdot 10^{-6}$ s, which on the one hand leads to a sampling factor of 2250 with respect to the first structural eigenfrequency found in the experiment ($f_1 = 222$ Hz) and on the other hand guarantees that high-frequency fluctuations associated to the TBL ($f_{\mathrm{TBL}} = \delta_{0,I}/U_\infty = 7.5 \cdot 10^{-6}$ s) are still resolved.

4. Computational setup

The origin of the coordinate system used for our studies is placed at the sharp leading edge of the baseplate, see Fig. 2(b). For the baseline SWBLI, the computational domain is rectangular with dimensions $L_x = 55\,\delta_{0,I}$, $L_y = 11\,\delta_{0,I}$, $L_z = 2\,\delta_{0,I}$ and it is discretized with $1800 \times 460 \times 128$ cells in streamwise, wall-normal and spanwise directions, respectively. This leads to a grid resolution of $\triangle x^+ = 42$, $\triangle y_{min}^+ = 1$, $\triangle z^+ = 21$ evaluated at the origin of the LES domain ($x = 0.2$ m). In the wall-normal direction hyperbolic grid stretching is used with a stretching factor of $\beta_y = 3.0$, where the stretching function reads $y = L_y \left(1 - \tanh\left(\beta_y \left(1 - j/N_y\right)\right)/\tanh(\beta_y)\right)$. Here, j denotes the individual grid point, L_y the domain height and N_y the total number of cells in wall-normal direction. The following boundary conditions have been used for the LES. At the domain inlet a Digital Filter (DF) based boundary condition is used [23], for which first and second order statistical moments have been obtained through a precursor temporal boundary-layer simulation at the same flow conditions. This type of boundary condition omits the introduction of artificially correlated data, which would potentially force low-frequency periodic motion of the reflected shock. At the top boundary, flow conditions are adopted from an inviscid simulation at $\Theta = 20°$ wedge angle and interpolated onto the target grid. This guarantees the correct interaction of the incident shock and the expansion fan originating from the static shock generator. The nominal inviscid impingement point at the wall is $x_{imp} = 0.307$ m, neglecting the influence of the expansion fan on the incident shock. At the supersonic outlet, linear extrapolation of all flow variables is used. The wall is modeled as adiabatic and periodic boundary conditions are used in the spanwise direction. Statistical quantities have been obtained by averaging instantaneous three-dimensional flow fields in time and spanwise direction after an initial transient of $5\,L_x/U_\infty$ and at a mean sampling time of $0.04\,\delta_{0,I}/U_\infty$, resulting in a total of 57200 samples within the available integration time. For the low-frequency analysis presented later, 1008 equally spaced pressure probes have been placed in streamwise direction along the wall ($y = 0$) ranging between $x = 0.24$ m and $x = 0.38$ m.

Considering the FSI setup, the LES domain starts from $x_{min} = 0.17$ m and ranges up to $x_{max} = 0.57$ m in streamwise direction, thus covering the complete elastic panel section (see Fig. 2(b)). This corresponds to a domain length of $L_x = 88\,\delta_{0,I}$. In spanwise direction, the same domain width as for the baseline case of $L_z = 2\,\delta_{0,I}$ is used, which implicitly assumes a two-dimensional FSI. In order to account for the panel motion within the Cartesian flow solver, a cavity of height 5 mm is used within the elastic panel section. Thus, in wall-normal direction the domain covers the section $y_{min} = -0.005$ m up to $y_{max} = 0.1$ m, leading to $L_y = 23\,\delta_{0,I}$. To reduce the overall amount of computational cells, we first performed inviscid FSI simulations to identify the region of panel motion. Subsequently, the cavity is split into several smaller blocks and those which remain uncut within the whole simulation time have been deleted. In total, the computational grid comprises $79.56 \cdot 10^6$ cells, with a final grid resolution expressed in wall-units of $\triangle x^+ = 62$, $\triangle y_{min}^+ = 5$, $\triangle z^+ = 30$. The same grid stretching strategy has been used for the boundary-layer block as for the baseline configuration, whereas a uniform grid spacing is used within the cavity region in order to ensure the same wall resolution throughout the whole simulation time. The boundary conditions for the fluid subdomain are the same as the ones described beforehand, with the only difference that at the top of the domain a transient boundary condition has been implemented, which prescribes pre-shock, post-shock and expansion states at each individual grid position according to the experimental time-dependent wedge angle.

The panel is discretized using $200 \times 2 \times 12$ tri-linearly interpolated hexahedral elements in streamwise, wall-normal and spanwise direction, respectively. To avoid shear locking phenomena, the EAS method is used. The panel has a Young's modulus of $E_S = 206$ GPa, a Poisson's ratio of $\nu_S = 0.33$, and a density of $\rho_{S;0} = 7800\,\mathrm{kg/m}^3$. No perfectly clamped boundary condition is achieved in the experiment. Both, the rivets as well as the frame to which the panel is connected deform, which in turn leads to larger wall-normal deformations of the panel [26]. In order to account for this effect, elastic boundary conditions with linear springs at both ends of the panel are used. A spring constant of $k_{lin} = 4.15 \cdot 10^8$ N/m is used, which has been calibrated using results of experiments during which the panel was exposed to a constant pressure difference (see Fig. 11(b)). At the bottom surface of the panel, a time-dependent cavity pressure extracted from the experiment is imposed. A coupled simulation is started by first assuming a rigid panel. After one flow-through time (FTT) of the TBL, the rigidity constraint is removed and the coupled simulation starts. Before the pitching of the shock generator is enabled, the whole system is integrated for again one FTT to reduce the influence of initial transients on the later panel motion.
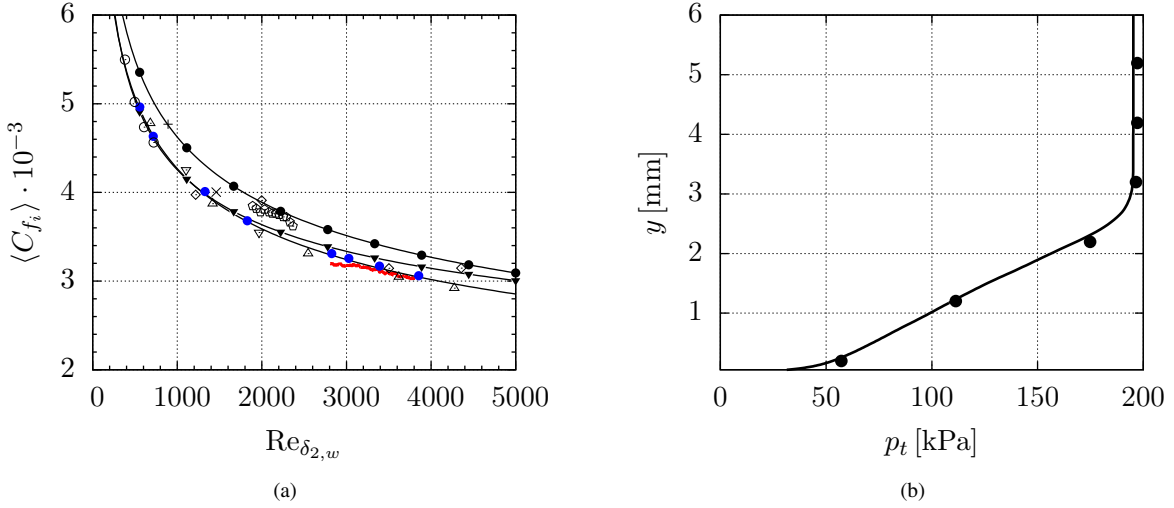
4

(a)

(b)

Figure 3: (a) Incompressible skin friction evolution. (–•–) Blasius; (–▼–) Kàrmàn-Schoenherr; (——) Smits; (——) LES; (◯) [18]; (•) [17]; (⊙) [11], △ [20]; (▽) [22], (◇) CAT5301 AGARD 223, (+) [8], (×) [12]. (b) Wall-normal total pressure distribution at $x = 0.15$ m. The LES pressure distribution has been corrected according to the Rayleigh Pitot tube formula, see Eq. (1). (——) LES, (•) experimental data.

5. Results and discussion

5.1 Incoming turbulent boundary-layer

The spatial extent of the separation bubble is sensitive on the level of turbulence in the incoming TBL. Thus, before the SWBLI simulations are considered, a spatially developing TBL simulation without shock generator has been conducted, which covers the experimental Pitot rake position located at $x = 0.15$ m.

Since no direct measurement of the skin-friction is available for this flow configuration, the incompressible skin friction distribution $\langle C_{f_i} \rangle$ obtained from the van-Driest II transformation is compared to algebraic incompressible relations, various DNS and experimental data for a wide range of Mach numbers; see Fig. 3(a). The computed incompressible skin friction coefficient (——) is in good agreement with the DNS results by [17]. In Fig. 3(b), we provide a comparison between experiment and LES in terms of ram-pressure measured at the streamwise location $x = 0.15$ m. In order to account for the shock-losses generated by the Pitot rake, the LES pressure is corrected according to the Rayleigh Pitot tube formula

$$\frac{p_t}{p} = \left[\frac{(\gamma + 1)^2 \text{Ma}^2}{4\gamma \text{Ma}^2 - 2(\gamma - 1)} \right]^{\gamma/(\gamma-1)} \cdot \frac{1 - \gamma + 2\gamma \text{Ma}^2}{\gamma + 1}, \tag{1}$$

where Ma denotes the local Mach number. The good agreement between experiment and LES confirms the correct boundary-layer thickness evolution within the simulation and justifies the assumption of a fully TBL.

For further validation, the van-Driest transformed mean-velocity profile together with the RMS of Reynolds stresses in Morkovin scaling at the same streamwise position $x = 0.15$ m are presented in Fig. 4(a)/(b) and compared with DNS data of [17] for a similar friction Reynolds number ($Re_{\tau,\text{LES}} = 840$, $Re_{\tau,\text{DNS}} = 900$). Note that the DNS has a different Mach number of $\text{Ma}_\infty = 2.0$ and a lower local Reynolds number of $Re_{\delta,\text{DNS}} = 55170$. The velocity profile is in good agreement with the logarithmic law of the wall and the DNS data. Small differences in the wake region are due to a higher Reynolds number in the LES. The Reynolds stresses are in good agreement with the DNS data in the near-wall region, while larger deviations occur in the logarithmic and wake region.

5.2 Baseline SWBLI at $\Theta = 20°$

The baseline SWBLI considers the experimental configuration with a static shock generator, which deflects the flow by $\Theta = 20°$. Contours of the instantaneous and time-averaged temperature, see Fig. 5, give a first impression of the flow topology. The sonic line is shown in black and zero streamwise velocity is shown in blue. The adverse pressure gradient imposed by the incident shock is strong enough to cause a massive boundary-layer separation. The same flow
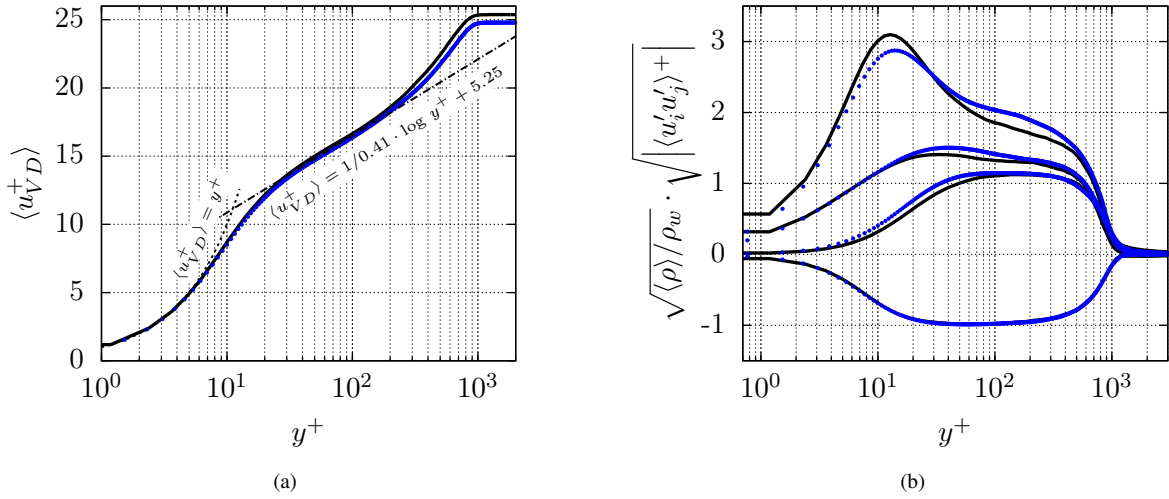
5

(a)

(b)

Figure 4: (a) van-Driest transformed mean-velocity profile at $x = 0.15$ m ($Re_\tau = 840$). (b) RMS of Reynolds stresses with density scaling at $x = 0.15$ m ($Re_\tau = 840$). (—) LES, (•) DNS data at Ma = 2.0 and $Re_\tau = 900$ from [17]
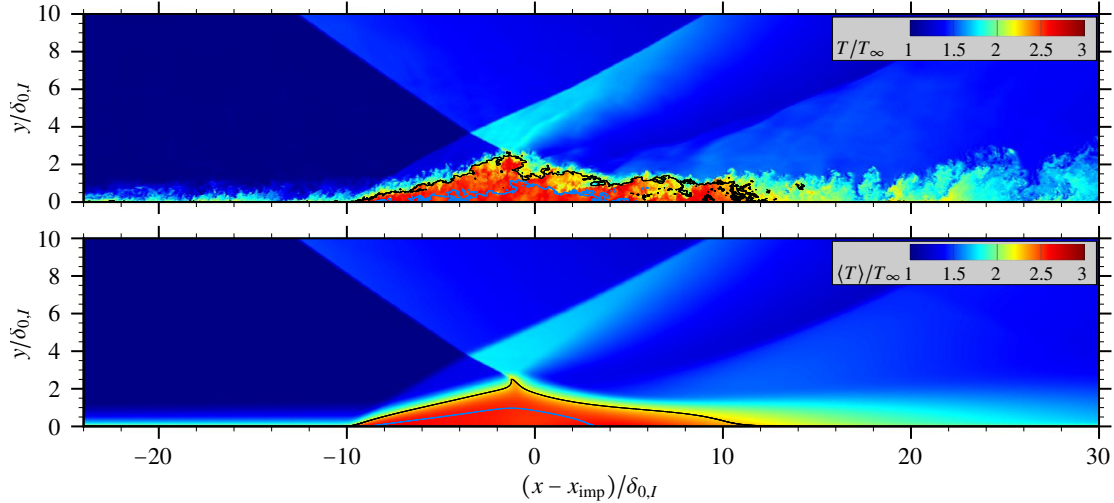

Figure 5: Top: Instantaneous temperature distribution T/T_∞ in $x-y$ mid-plane. Bottom: Time- and spanwise-averaged temperature distribution $\langle T \rangle / T_\infty$. (—) Ma = 1, (—) $u = 0$.

features as described in Fig. 1 can be identified. Moreover, the contour plot clearly highlights a heating process of the fluid within the recirculating region.

A qualitative comparison between experiment and simulation is given in Fig. 6, where we show instantaneous schlieren pictures. The opacity of the fluid solution is decreased from top to bottom. Qualitatively, one can observe a good agreement in terms of the separation shock angle, the extent of separated flow, the thickening of the TBL after the SWBLI and the evolution of the detached shear layer. Note that due to the interaction of the incident shock with the wind-tunnel side-wall TBL, the incident and separation shock within the experiment appear smeared. This is not the case for the LES due to the periodic boundary conditions applied in spanwise direction. However, as will be shown later in conjunction with the wall-pressure evolution (Fig. 7), this effect does not affect the interaction near the $x-y$ mid-plane.

The mean skin friction evolution is shown in Fig. 7(a). The synthetic turbulence generator leads to a spatial transient close to the inflow, wherein the flow recovers modeling errors introduced by the DF procedure. Due to the adverse pressure gradient imposed on the TBL, the flow is decelerated and forms a recirculation zone as indicated by the change of sign in the friction coefficient $\langle C_f \rangle$. The mean separation length for the baseline configuration is $L_{\text{sep}} = 13.11\,\delta_{0,I}$. The effect of the shock generator trailing-edge expansion fan on the interaction is clearly visible. After reattachment, the skin friction level significantly exceeds the value for the incoming TBL. After $(x - x_{\text{imp}}) \approx 16\,\delta_{0,I}$,
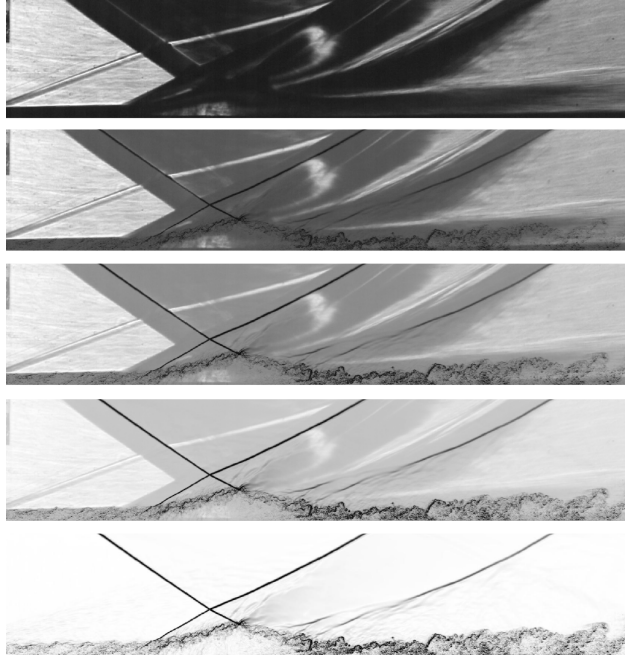
6

Figure 6: Instantaneous schlieren comparison between LES and experiment for the static SWBLI case at $\Theta = 20°$ deflection angle. The opacity of the fluid solutions is decreased from top to bottom. The LES schlieren is evaluated at the $x - y$ mid-plane.

the effect of decreasing skin friction due to a thickening of the TBL dominates and $\langle C_f \rangle$ starts to decrease.

The wall-pressure evolution is shown in Fig. 7(b) for experiment and LES. The experimental data has been evaluated at the mid-plane and is time-averaged, while the LES data has been both time- and spanwise-averaged. Besides experimental data points from static pressure probes ($\bullet$), we also provide the mean pressure extracted from unsteady pressure measurements through eight Kulites ($\triangle$). The pressure increase associated with the impinging shock is felt approximately $10\,\delta_{0,I}$ before the theoretical inviscid impingement location x_{imp}, also known as the upstream influence mechanism [5]. Within the initial part of the separation bubble ($x_s < x < x_{\mathrm{imp}}$), a significant pressure plateau can be observed, indicating the presence of a strong interaction, followed by a monotonically increasing pressure associated to the reattachment process. The trailing-edge Prandtl-Meyer expansion leads to a strong pressure drop after the SWBLI. Numerical and experimental data for the pressure evolution are in excellent agreement, confirming the ability of our LES solver to correctly predict SWBLI at high Reynolds numbers. In particular, the pressure plateau is captured well, indicating that the present experimental setup is sufficiently two-dimensional and accessible through LES with assumed homogeneity in spanwise direction.

The influence of the SWBLI on turbulence evolution is studied in Fig. 8 in terms of mean resolved Reynolds shear stress (top) and turbulence kinetic energy (bottom). The mean sonic line (black) and the separated flow region (red) are highlighted. A high level of Reynolds shear stress is found along the detached shear layer within the interaction region. Its maximum value is found approximately one boundary-layer thickness downstream of the mean reattachment location, consistent with previous findings for different flow conditions [15, 19]. In addition, high levels of $\langle u'v' \rangle$ can be observed along the reflected (C_2, C_3) and reattachment (C_5) shock, being directly associated with unsteady shock motions and coupled to a breathing motion of the separation bubble [7]. At the incident shock tip (C_4), $\langle u'v' \rangle$ changes sign as a consequence of its flapping motion [21]. The mean resolved turbulence kinetic energy contour confirms amplification of turbulence along the shear layer that originates from the separation point.

Unsteady aspects related to reflected shock dynamics are investigated by means of Power Spectral Densities (PSD) of wall-pressure probes. Pressure signals have been recorded at a mean sampling time interval of $8 \cdot 10^{-4}\,\delta_{0,I}/U_\infty$ covering a length of $1900\,\delta_{0,I}/U_\infty$. This leads to a maximum resolvable Strouhal number of $\mathrm{St}_{\max} = f_{\max}\delta_{0,I}/U_\infty = 625$ and a minimum resolvable Strouhal number of $\mathrm{St}_{\min} = f_{\min}\delta_{0,I}/U_\infty = 5 \cdot 10^{-4}$. Consequently, the current LES is well able to capture the expected low-frequency unsteadiness. Fig. 9 provides a two-dimensional map of wall-pressure spectra evaluated at each streamwise pressure-probe location. The spectra have been obtained using the Welch algorithm by splitting the signal in three segments with $50\,\%$ overlap using Hanning windows. Each pre-multiplied PSD contour has been normalized, such that their integral over frequency becomes unity, i.e. $f \cdot \mathrm{PSD}(f)/\int \mathrm{PSD}(f)\,\mathrm{d}f$. This normalization has the favorable effect to highlight frequencies that contribute most at each individual streamwise
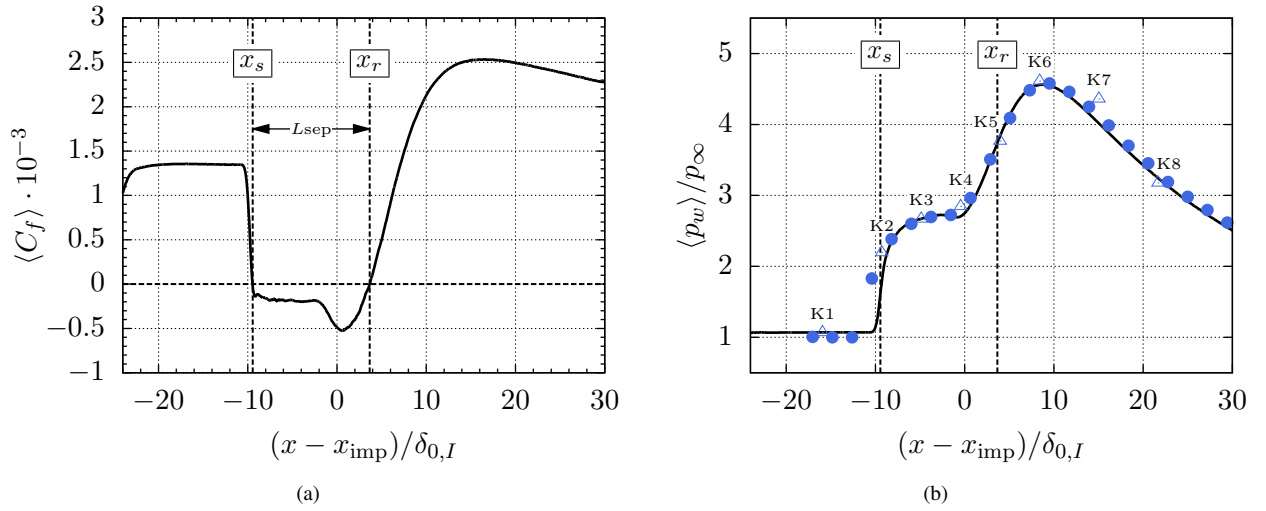
Figure 7: (a) Skin friction $\langle C_f \rangle$ (b) and wall-pressure $\langle p_w \rangle / p_\infty$ evolution in the streamwise direction. (——) LES, (●) experimental static data, (△) experimental Kulite data. Kulite positions $K_i|_{i=1\ldots8}$ are highlighted for later reference.
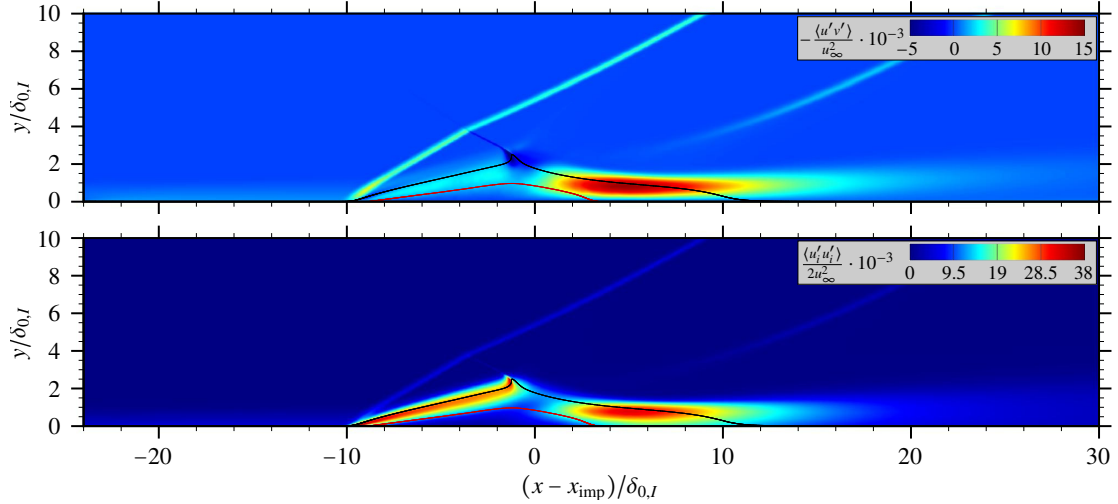

Figure 8: Top: Mean resolved Reynolds shear stress. Bottom: Mean resolved turbulence kinetic energy. (——) Ma = 1, (——) u = 0.

location. The PSD map shows a broadband peak centered around unity Strouhal number before separation takes place ($x < x_s$), being directly associated to the characteristic frequency of energetic scales within the incoming TBL ($U_\infty / \delta_{0,I}$). The energy peak shifts towards significantly lower frequencies in the vicinity of the mean separation location and moves back again to higher frequencies downstream of the interaction zone. Due to a thickening of the TBL after the SWBLI, the broadband peak shifts to overall lower Strouhal numbers. The low-frequency peak close to the mean separation location is related to the back and forth motion of the reflected shock and covers a streamwise shock-excursion length of about one boundary-layer thickness, consistent with previous findings [7, 15]. A characteristic Strouhal number of $\text{St}_{L_{\text{sep}}} = 0.08$ based on the mean separation length L_{sep} is found for the low-frequent shock motion. A total number of 12 low-frequency cycles is captured within the available integration time.

Selected PSDs at the Kulite positions $x_{K2} \ldots x_{K5}$ are compared to experimental data, see Fig. 10. Each Kulite has 550000 data points at a sampling frequency of 100 kHz. For the experimental PSDs, the signal is split in 50 segments with 50 % overlap using Hanning windows, which leads to a smooth spectrum compared to the ones obtained for the LES. The Kulites have a diameter of 1.7 mm and cover several LES wall-pressure probes. Therefore, LES spectra corresponding to the same Kulite position have been averaged. For the first Kulite position, x_{K2}, the LES reveals an energetically dominant low-frequency peak which is not present in the experiment. From Fig. 7 it is evident, that x_{K2} perfectly matches the mean separation location predicted by the LES, thus explaining the low-frequency peak in
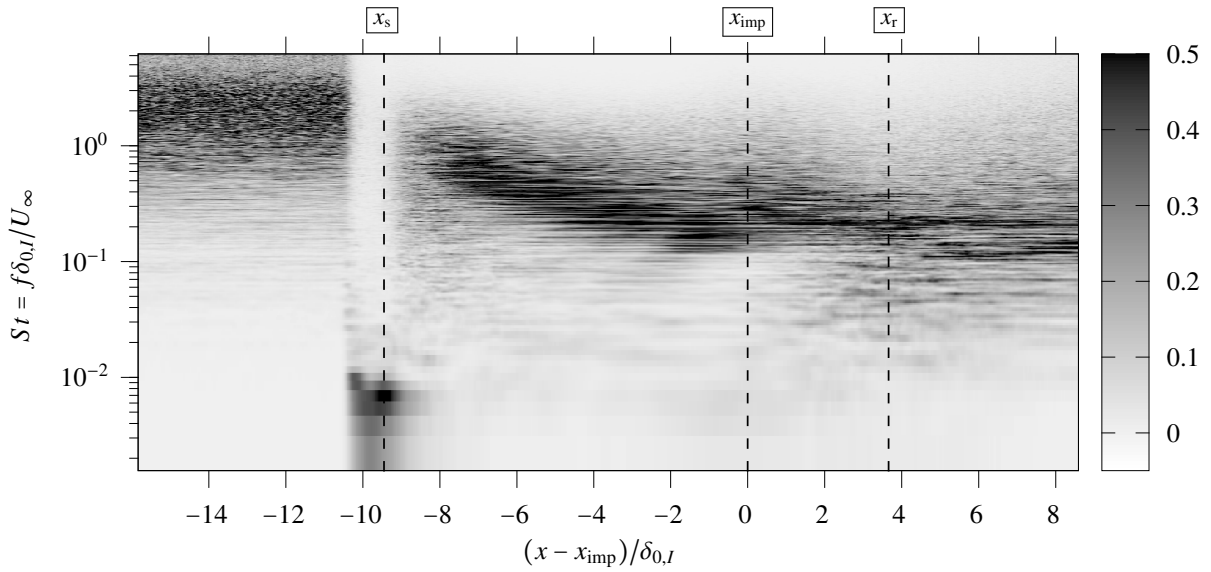
Figure 9: Weighted power spectral density map extracted from all wall-pressure signals for the baseline configuration. Contour: $f \cdot \mathrm{PSD}(f) / \int \mathrm{PSD}(f) \, \mathrm{d}f$.
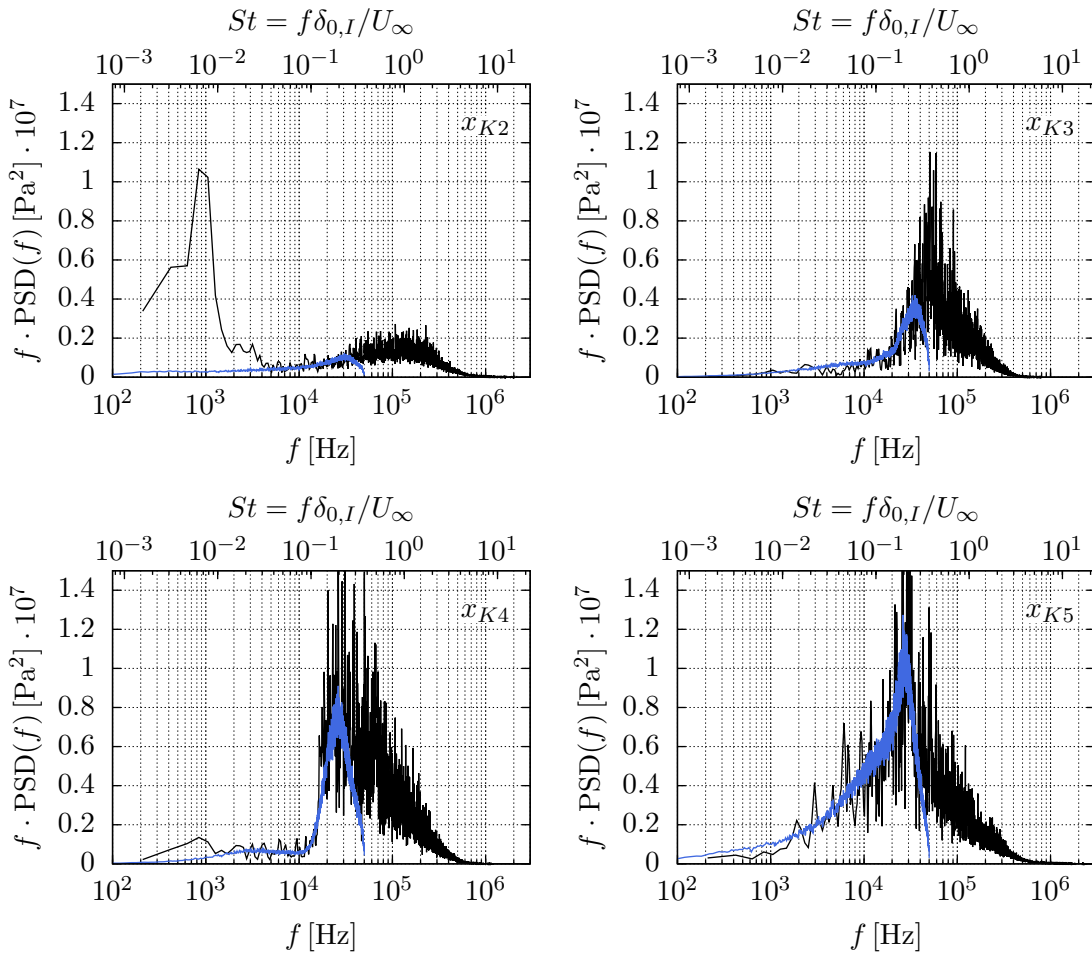

Figure 10: Weighted power spectral density at streamwise locations associated to experimental Kulite positions $x_{K2} \ldots x_{K5}$, see Fig. 7 for reference. (—) LES, (—) experiment.
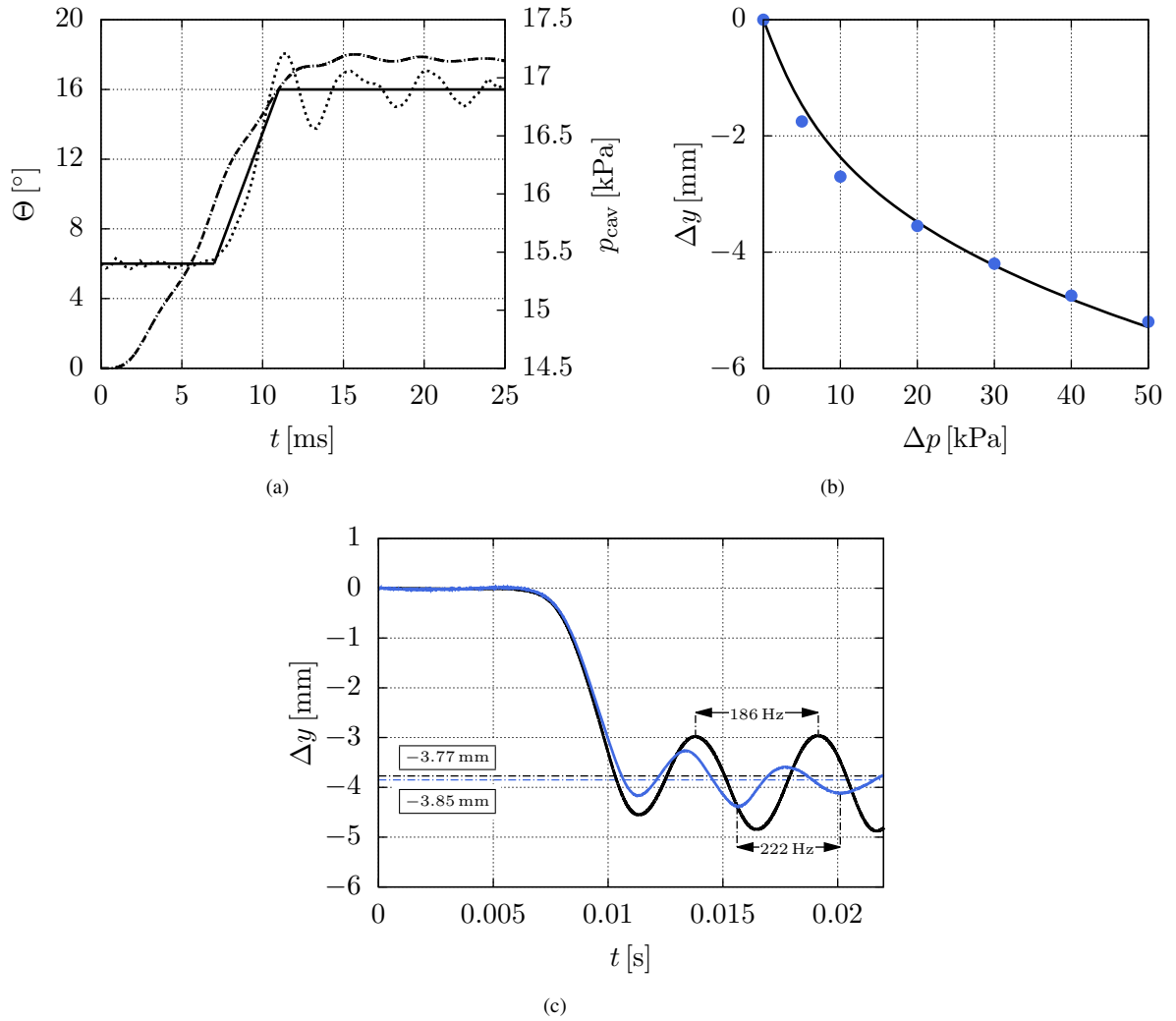
(a)

(b)

(c)

Figure 11: (a) Experimental parameters of the coupled setup: $(- \cdot -)$ deflection angle Θ measured with respect to the horizontal axis, $(\cdots)$ cavity pressure p_{cav}, (—) approximated pressure load for the structural model. (b) Calibration of the linear springs: (—) static deflection with $k_{lin} = 4.15 \cdot 10^8$ N/m, $(\bullet)$ experimental data. (c) Deflection of the panel mid-node over time. Mean static deflection and characteristic frequencies are highlighted. (—) LES, (—) experiment.

the associated PSD. However, the experimental mean separation location is probably located $1.5\,\delta_{0,I}$ upstream of x_{K2}. Since the shock-excursion length is assumed to be around $1\,\delta_{0,I}$, see Fig. 9, Kulite 2 probably misses the low-frequent shock motion. Besides this discrepancy, the high-frequency energy content is very similar between experiment and LES for the remaining Kulite positions. Moreover, the steep gradient found for x_{K4} close to St = 0.1 is captured very well by the LES.

5.3 Coupled SWBLI at $\langle \Theta \rangle = 17.5°$

The coupled SWBLI considers the experimental configuration with a pitching shock generator and a final mean deflection angle of $\langle \Theta \rangle = 17.5°$. Fig. 11(a) summarizes experimental parameters. Within $T = 15$ ms, the wedge is pitched from $\Theta_{t_0} = 0°$ to $\Theta_{t_1} = 17.5°$, inducing a time-varying load on the plate. At $t = 3$ ms, the incident shock hits the end of the panel. The nominal mean inviscid impingement location is $x_{\text{imp}} = 0.328$ m. Note, that low-amplitude oscillations of the shock generator at a frequency of $f_{\text{SG}} \approx 247$ Hz are still visible after the transient pitching. The time-varying wedge angle is used for the LES to prescribe a transient boundary condition at the top of the domain. In the same figure, the experimental cavity pressure p_{cav} is shown. No perfect sealing between the main stream and the cavity below the panel can be achieved in the experiment, thus leading to a pressure increase inside the cavity once the shock hits the panel. In order to account for the increased pressure in the cavity, a simplified pressure curve is assumed, which is imposed

10
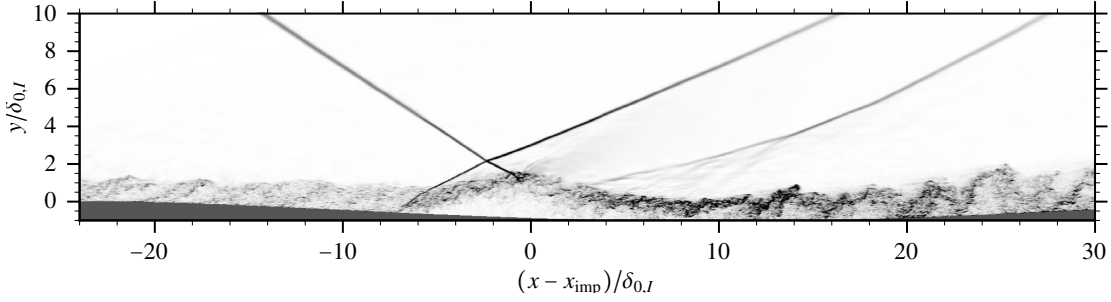
Figure 12: Instantaneous schlieren of the coupled LES evaluated at the mid-plane at $t = 16.46$ ms.
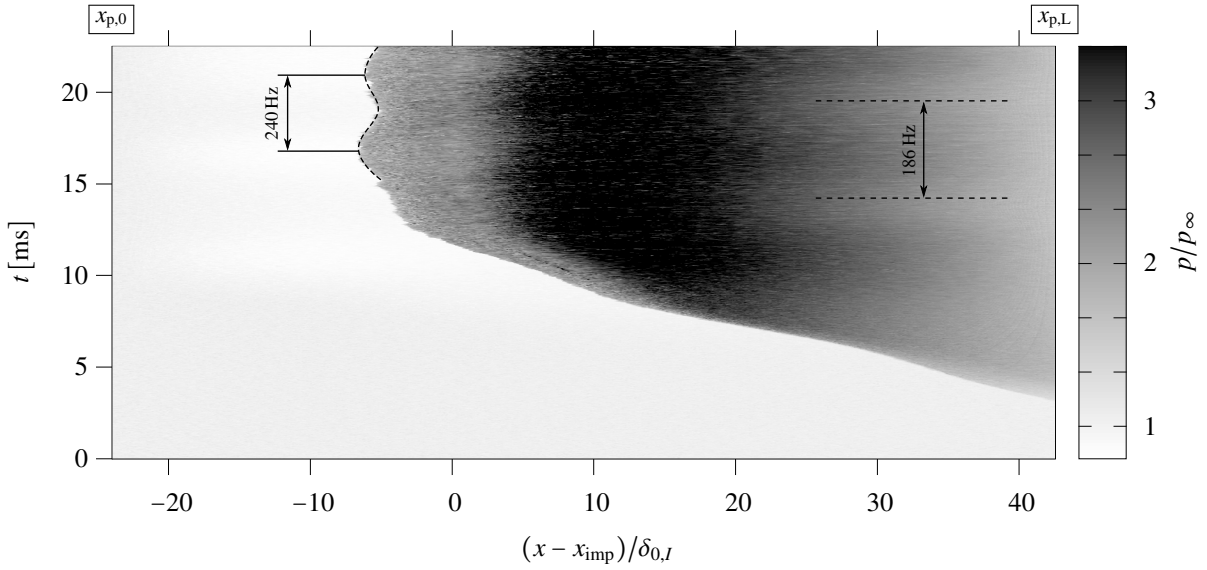
Figure 13: $x - t$ diagram of recorded pressure at $y = 0$ evaluated at the mid-plane. Panel start $x_{p,0}$ and panel end $x_{p,L}$ are indicated.

as a time-dependent Neumann boundary condition, see solid black line in Fig. 11(a). Actually, the pressure is coupled to the panel deflection, which is neglected in the present setup. Fig. 11(b) shows results after calibration of the linear springs with a spring constant of $k_{lin} = 4.15 \cdot 10^8$ N/m, indicating an overall good agreement between experiment and simulation in terms of static deflections. The deflection of the panel mid-node over time for the coupled SWBLI is shown for both experiment and LES in Fig. 11(c). Mean static deflection and characteristic frequency of the panel oscillation are indicated. Within $7 < t < 11$ ms, the panel displacement increases linearly, followed by an oscillatory behavior. A mean static deflection of $\Delta y_{LES} = -3.77$ mm is found for the LES, which is in excellent agreement with the experimental value of $\Delta y_{EXP} = -3.85$ mm. Considering the time-evolution of the panel displacement, an overall good agreement can be observed for the initial pitching region ($t < 11$ ms), whereas larger deviations occur at the onset of panel oscillations. Both, the frequency of the panel oscillation ($f_{LES} = 186$ Hz, $f_{EXP} = 222$ Hz) as well as the displacement amplitudes differ significantly from the experiment. The authors believe, that the compressible air within the cavity constitutes an additional stiffness which is not included in our setup, but could be possibly modeled through an additional set of springs acting on the underside of the elastic panel. This would in turn increase the frequency of the panel oscillation and explain the current mismatch between experiment and simulation. Regarding the oscillation amplitudes, a relatively high damping is observed in the experiment, which is not the case for the LES. The authors believe, that two effects are mainly responsible for this discrepancy: The cavity is sealed through a thick layer of a soft foam rubber, which may increase the overall damping of the system and leads to a damping effect that scales linearly with the panel velocity. The second reason is attributed to the aerodynamic damping imposed by the cavity, which is expected to scale with the square of the panel velocity. As it is not yet clear how to model this damping behavior correctly, more experiments are necessary for modeling purposes. Therefore, damping in the structural model is neglected in the current numerical setup.

An instantaneous schlieren picture of the coupled LES at $t = 16.46$ ms is shown in Fig. 12. Basically, the same
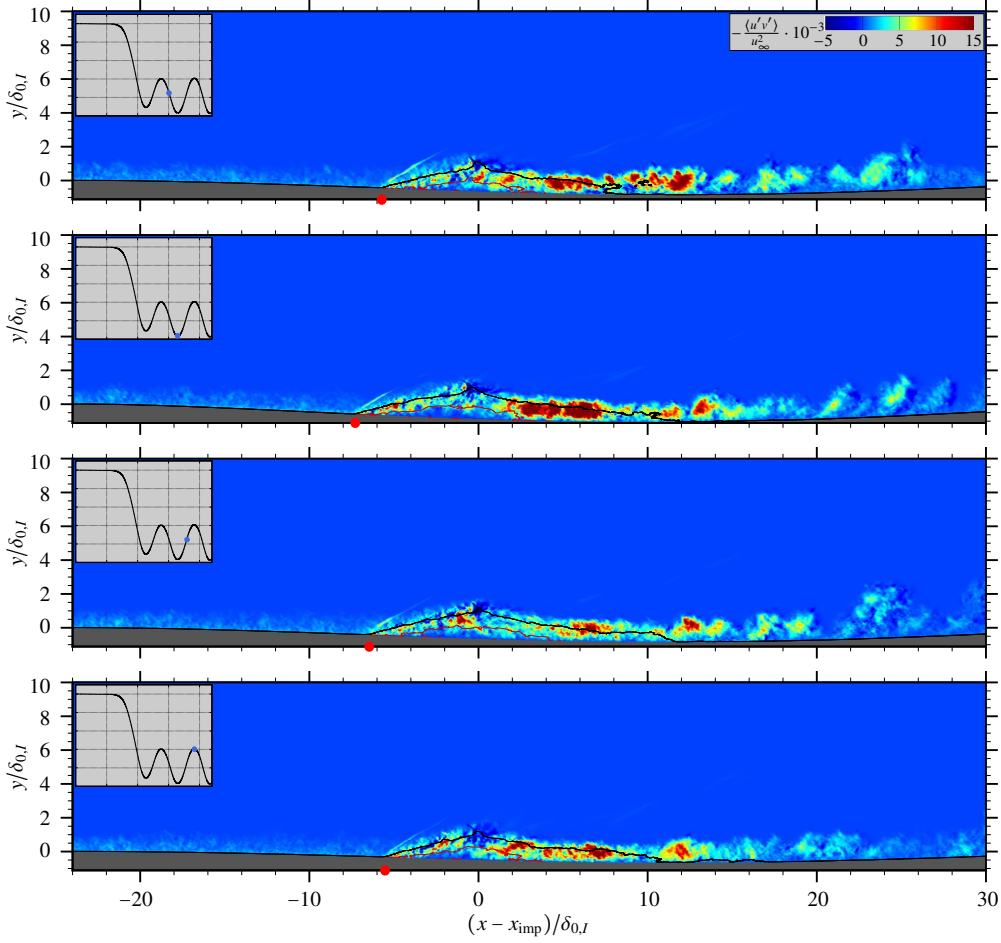
Figure 14: Resolved spanwise-averaged Reynolds shear stress for selected snapshots (——) Ma = 1, (——) u = 0. $(x_{p,0} - x_{imp})/\delta_{0,I} = -23.89$, $(x_{p,L} - x_{imp})/\delta_{0,I} = 42.48$. Red bullets indicate the instantaneous separation shock location.

flow features can be identified when compared to the baseline configuration (Fig. 6), with the only difference being a large mean static deflection of the order of one $\delta_{0,I}$. Equally spaced pressure probes have been placed in streamwise direction along the undeflected panel (y = 0) ranging between x = 0.22 m and x = 0.52 m. The recorded pressure for the coupled SWBLI is shown in Fig. 13 in terms of a $x - t$ diagram. Panel start $x_{p,0}$ and panel end $x_{p,L}$ are indicated. Starting from t = 3 ms, the panel is exposed to an increasing pressure force. Boundary-layer separation can be observed for t > 8 ms with growing spatial extent up to t = 15 ms. For t > 15 ms, a quasi-stationary state of the coupled SWBLI is obtained. Compression and expansion waves emanating from the panel oscillation (f_{LES} = 186 Hz) can be clearly seen in the rear part of the panel. A large-scale separation shock movement can be observed at $x - x_{imp} \approx -6\,\delta_{0,I}$, probably caused by the oscillating incident shock, see Fig. 11(a). We found a frequency of 240 Hz for the large-scale separation shock movement, which is closely related to the shock generator oscillation frequency, being 247 Hz. At the same time, the reattachment shock ($x - x_{imp} \approx 4\,\delta_{0,I}$) exhibits an opposite motion, which constitutes an overall breathing motion of the separation bubble.

Four selected spanwise averaged snapshots with contours of resolved Reynolds shear stress are shown in Fig. 14. The snapshots are taken in the time interval $t \in [15.1, 19.1]$ ms, representing one oscillation period within the quasi-stationary state. Each insert shows the panel deflection evaluated at the mid-node together with a blue bullet, which indicates the associated snapshot time. The sonic line is shown in black and zero streamwise velocity is shown in red. The reflected shock foot is tracked with a red bullet. The large-scale shock motion discussed in conjunction with Fig. 13 is clearly visible and covers a maximum excursion length of approximately $2\,\delta_{0,I}$.

A comparison between the baseline SWBLI and the coupled configuration is given in Fig. 15 in terms of time- and spanwise-averaged resolved Reynolds shear stress. The coupled results have been averaged over one oscillation period ($t \in [15.0, 20.3]$ ms) with a total number of 165 samples, explaining the noisy contours compared to the baseline setup. Compared to the uncoupled case, the separation, reflected and reattachment shock exhibit a low-frequent shock
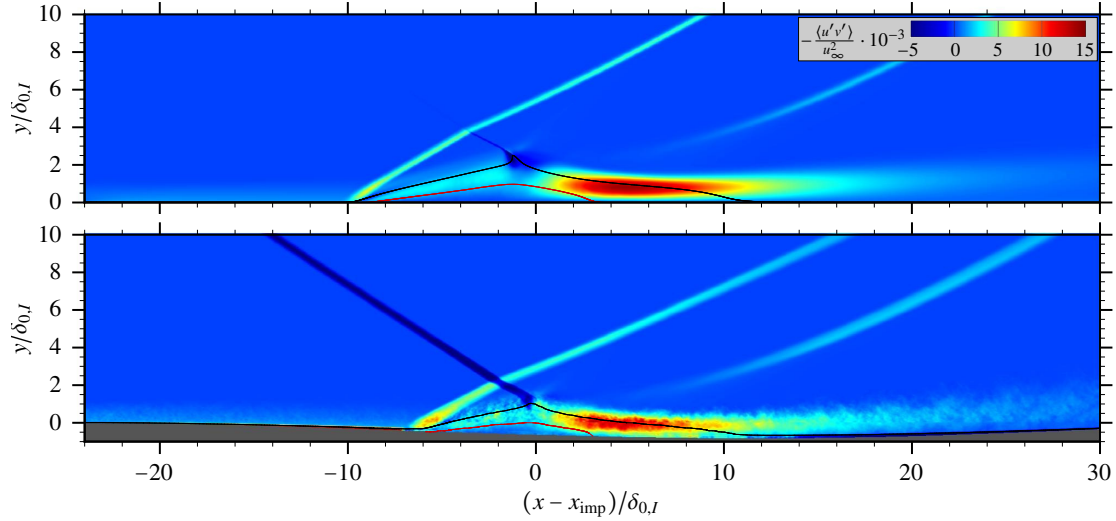
Figure 15: Time- and spanwise-averaged resolved Reynolds shear stress. Top: Baseline SWBLI at $\langle\Theta\rangle = 20°$. Bottom: Coupled SWBLI at $\langle\Theta\rangle = 17.5°$. (—) Ma = 1, (—) $u = 0$. The coupled results have been averaged over one oscillation period.
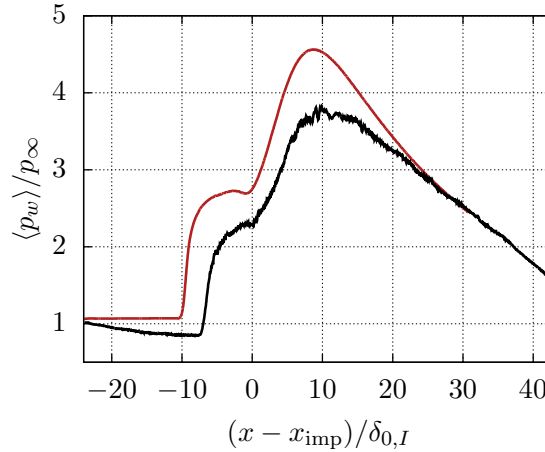

Figure 16: Wall-pressure $\langle p_w\rangle/p_\infty$ evolution in the streamwise direction. (—) coupled SWBLI at $\langle\Theta\rangle = 17.5°$, (—) baseline SWBLI at $\langle\Theta\rangle = 20°$. The coupled results have been averaged over one oscillation period.

motion with greater spatial extent, probably caused by a superposition of the oscillating incident shock and the panel motion. The mean separation length is approximately $2\,\delta_{0,I}$ smaller for the coupled SWBLI. One must keep in mind that a direct comparison between both cases is not possible, since different mean deflection angles are considered. As a consequence, both, the smaller mean deflection angle and a negative static displacement of the panel contribute to an overall weaker interaction.

Finally, Fig. 16 shows the mean wall-pressure evolution for both cases. The mean deflection of the panel leads to an overall lower pressure level before the interaction region ($x - x_{\text{imp}} < -10\,\delta_{0,I}$), indicating the presence of expansion waves which accelerate the near-wall flow. This effect in turn contributes to an overall reduced interaction length. As already explained in conjunction with Fig. 15, a weaker mean SWBLI is present for the coupled SWBLI. Thus, a superposition of both effects leads to a lower pressure plateau and lower maximum pressure increase across the interaction.

6. Conclusions

We have studied the interaction of an oblique shock with a turbulent boundary-layer (TBL) using well-resolved large-eddy simulation (LES) and experimental data. The flow is deflected by a rotatable shock generator at a free-stream Mach number of Ma = 3.0. The Reynolds number upstream of the interaction region is $Re_{\delta_{0,I}} = 205 \cdot 10^3$. Two configurations have been investigated: The first one considers a steady shock generator with a deflection angle of $\Theta = 20°$. The second setup investigates the fluid-structure interaction (FSI) arising from a pitching shock generator, whose incident shock interacts with a flexible panel.

The validity of the incoming TBL has been assessed through a direct comparison between LES results and data from direct numerical simulation found in the literature. An overall good agreement could be found in terms of van-Driest transformed mean velocity, Reynolds stresses and incompressible skin-friction evolution. Experimental stagnation pressure measurements before the interaction region confirmed the validity of the incoming TBL.

The baseline shock-wave/boundary-layer interaction (SWBLI) revealed a strong interaction with massive mean flow separation. Excellent agreement between LES and experiment in terms of mean wall-pressure evolution has been found, confirming the ability of our LES solver to correctly predict SWBLI at high Reynolds numbers. The pressure plateau within the recirculation zone is perfectly reproduced in the simulation, from which we conclude that the present experimental setup is sufficiently two-dimensional and accessible through simulations with assumed homogeneity in spanwise direction. Unsteady wall-pressure measurements revealed a low-frequency unsteadiness associated to the reflected shock foot. Power spectral densities within the separated zone agree very well with experimental findings. However, the unsteady shock motion is not properly captured in the experiment with the available sensors.

For the coupled SWBLI, panel deflections increase linearly during the pitch motion, followed by an oscillatory movement. While the static deflection predicted by the LES agrees very well with experimental findings, significant deviations in terms of oscillation frequency and damping could be found. The authors believe, that the compressible air within the cavity constitutes an additional stiffness which is not included in our setup. Moreover, damping effects probably caused through sealing materials and the cavity itself have been neglected for simplicity. A large-scale separation shock movement could be found, which is probably caused by two effects: Low-amplitude oscillations of the incident shock are still present after pitching is completed. Moreover, the panel oscillations probably contribute to the separation shock motion. Compared to the baseline SWBLI, an overall weaker interaction is found by investigating mean contours of Reynolds shear stress and the mean wall-pressure evolution. Again, two effects are responsible for this finding: The wedge angle for the coupled SWBLI settles at $\langle \Theta \rangle = 17.5°$, leading to a smaller pressure gradient across the incident shock. The static panel displacement leads to a near-wall flow acceleration with a favorable effect on the interaction length.

Acknowledgements

References

[1] N. A. Adams. Direct simulation of the turbulent boundary layer along a compression ramp at M = 3 and Re θ = 1685. *Journal of Fluid Mechanics*, 420:47–83, 2000.

[2] A. M. Brown, J. Ruf, D. Reed, M. D'Agostino, and R. Keanini. Characterization of side load phenomena using measurement of fluid/structure interaction. *AIAA Paper*, (2002-3999), 2002.

[3] D. Daub, S. Willems, and A. Gülhan. Experimental Results on Shock-Wave/Boundary-Layer Interaction Induced by a Movable Wedge. In *8th European Symposium on Aerothermodynamics*, 2015.

[4] D. Daub, S. Willems, A. Gülhan, and B. Esser. Experimental Setup for Excitation of Fluid-Structure Interaction. *Sonderforschungsbereich/Transregio 40 - Annual Report*, 2014.

[5] J. Délery and J.-P. Dussauge. Some physical aspects of shock wave/boundary layer interactions. *Shock Waves*, 19(6):453–468, 2009.

[6] D. S. Dolling. Fifty years of shock-wave/boundary-layer interaction research: what next? *AIAA Journal*, 39(8):1517–1531, 2001.

[7] M. Grilli, P. J. Schmid, S. Hickel, and N. A. Adams. Analysis of unsteady behaviour in shockwave turbulent boundary layer interaction. *Journal of Fluid Mechanics*, 700:16–28, 2012.

[8] S. E. Guarini, R. D. Moser, K. Shariff, and A. Wray. Direct numerical simulation of a supersonic turbulent boundary layer at Mach 2.5. *Journal of Fluid Mechanics*, 414:1–33, 2000.

[9] S. Hickel, N. A. Adams, and J. A. Domaradzki. An adaptive local deconvolution method for implicit LES. *Journal of Computational Physics*, 213:413–436, 2006.

[10] S. Hickel, C. P. Egerer, and J. Larsson. Subgrid-scale modeling for implicit large eddy simulation of compressible flows and shock-turbulence interaction. *Physics of Fluids*, 26:106101, 2014.

[11] J. Komminaho and M. Skote. Reynolds stress budgets in Couette and boundary layer flows. *Flow, Turbulence and Combustion*, 68:167–192, 2002.

[12] T. Maeder, N. A. Adams, and L. Kleiser. Direct simulation of turbulent supersonic boundary layers by an extended temporal approach. *Journal of Fluid Mechanics*, 429:187–216, 2001.

[13] F. Örley, V. Pasquariello, S. Hickel, and N. A. Adams. Cut-element based immersed boundary method for moving geometries in compressible liquid flows with cavitation. *Journal of Computational Physics*, 283:1–22, 2015.

[14] J. Östlund. *Flow processes in rocket engine nozzles with focus on flow separation and side-loads*. PhD thesis, Royal Institute of Technology, 2002.

[15] V. Pasquariello, M. Grilli, S. Hickel, and N. A. Adams. Large-eddy simulation of passive shock-wave/boundary-layer interaction control. *International Journal of Heat and Fluid Flow*, 49:116–127, 2014.

[16] V. Pasquariello, G. Hammerl, F. Örley, S. Hickel, C. Danowski, A. Popp, W. A. Wall, and N. A. Adams. A cut-cell Finite Volume – Finite Element coupling approach for fluid-structure interaction in compressible flow. *Journal of Computational Physics (in review)*, 2015.

[17] S. Pirozzoli and M. Bernardini. Turbulence in supersonic boundary layers at moderate Reynolds number. *Journal of Fluid Mechanics*, 688:120–168, 2011.

[18] S. Pirozzoli and F. Grasso. Direct numerical simulations of isotropic compressible turbulence: Influence of compressibility on dynamics and structures. *Physics of Fluids*, 16:4386–4407, 2004.

[19] S. Pirozzoli and F. Grasso. Direct numerical simulation of impinging shock wave/turbulent boundary layer interaction at M=2.25. *Physics of Fluids*, 18(6), 2006.

[20] P. Schlatter and R. Örlü. Assessment of direct numerical simulation data of turbulent boundary layers. *Journal of Fluid Mechanics*, 659:116–126, 2010.

[21] M. F. Shahab. *Numerical Investigation Of The Influence Of An Impinging Shock Wave And Heat Transfer On A Developing Turbulent Boundary Layer*. PhD thesis, École Nationale Supérieure de Mécanique et d'Aérotechnique, 2006.

[22] M. P. Simens, J. Jiménez, S. Hoyas, and Y. Mizuno. A high-resolution code for turbulent boundary layers. *Journal of Computational Physics*, 228:4218–4231, 2009.

[23] E. Touber and N. D. Sandham. Large-eddy simulation of low-frequency unsteadiness in a turbulent shock-induced separation bubble. *Theoretical and Computational Fluid Dynamics*, 23:79–107, 2009.

[24] E. Touber and N. D. Sandham. Low-order stochastic modelling of low-frequency motions in reflected shock-wave/boundary-layer interactions. *Journal of Fluid Mechanics*, 671:417–465, 2011.

[25] M. R. Visbal. Viscous and inviscid interactions of an oblique shock with a flexible panel. *Journal of Fluids and Structures*, 48, 2014.

[26] S. Willems, A. Gülhan, and B Esser. Shock induced fluid-structure interaction on a flexible wall in supersonic turbulent flow. In *Progress in Flight Physics*, volume 5, pages 285–308, 2013.

C. Bibliography

N. A. Adams. Direct simulation of the turbulent boundary layer along a compression ramp at M = 3 and Re_θ = 1685. *Journal of Fluid Mechanics*, 420:47–83, 2000.

N. A. Adams, S. Hickel, and S. Franz. Implicit subgrid-scale modeling by adaptive deconvolution. *Journal of Computational Physics*, 200:412–431, 2004.

L. Agostini, L. Larchevêque, P. Dupont, J.-F. Debiève, and J.-P. Dussauge. Zones of Influence and Shock Motion in a Shock/Boundary-Layer Interaction. *AIAA Journal*, 50(6):1377–1387, 2012.

J. D. Anderson. *Computational Fluid Dynamics: The Basics With Applications*. McGraw-Hill, 1995.

J. Andreopoulos and K. C. Muck. Some new aspects of the shock-wave/boundary-layer interaction in compression-ramp flows. *Journal of Fluid Mechanics*, 180:405–428, 1987.

G. Aubard, X. Gloerfelt, and J.-C. Robinet. Large-Eddy Simulation of Broadband Unsteadiness in a Shock/Boundary-Layer Interaction. *AIAA Journal*, pages 1–15, 2013.

W. J. Baars and C. E. Tinney. Transient wall pressures in an overexpanded and large area ratio nozzle. *Experiments in Fluids*, 54(2):1468, 2013.

W. J. Baars, J. H. Ruf, and C. E. Tinney. Non-stationary shock motion unsteadiness in an axisymmetric geometry with pressure gradient. *Experiments in Fluids*, 56(5):92, 2015.

H. Babinsky and H. Ogawa. SBLI control for wings and inlets. *Shock Waves*, 18(2):89–96, 2008.

S. J. Beresh, N. T. Clemens, and D. S. Dolling. Relationship Between Upstream Turbulent Boundary-Layer Velocity Fluctuations and Separation Shock Unsteadiness. *AIAA Journal*, 40:2412–2422, 2002.

M. Berger, M. J. Aftosmis, and S. R. Allmaras. Progress Towards a Cartesian Cut-Cell Method for Viscous Compressible Flow. In *50th AIAA Aerospace Sciences Meeting including the New Horizons Forum and Aerospace Exposition*, 2012.

N. J. Bisek, D. P. Rizzetta, and J. Poggie. Plasma Control of a Turbulent Shock Boundary-Layer Interaction. *AIAA Journal*, pages 1–16, 2013.

P. L. Blinde. Effects of Micro-Ramps on a Shock Wave/Turbulent Boundary Layer Interaction. Master's thesis, Delft University of Technology, 2008.

W. Bo, L. Weidong, Z. Yuxin, F. Xiaoqiang, and W. Chao. Experimental investigation of the micro-ramp based shock wave and turbulent boundary layer interaction control. *Physics of Fluids*, 24(5):055110, 2012.

N. Boyer, J. J. McNamara, and D. V. Gaitonde. Study on Shock-Induced Panel Flutter in 2-D Laminar Flow. In *15th Dynamics Specialists Conference*, pages 1–14, Reston, Virginia, 2016. American Institute of Aeronautics and Astronautics.

A. Brown, R. Keanini, J. Ruf, D. Reed, and M. D'Agostino. Characterization of Side Load Phenomena Using Measurement of Fluid/Structure Interaction. In *38th AIAA/ASME/SAE/ASEE Joint Propulsion Conference & Exhibit*. American Institute of Aeronautics and Astronautics, 2002.

P. Causin, J. F. Gerbeau, and F. Nobile. Added-mass effect in the design of partitioned algorithms for fluid–structure problems. *Computer Methods in Applied Mechanics and Engineering*, 194(42-44):4506–4527, 2005.

D. R. Chapman, D. M. Kuehn, and H. K. Larson. Investigation of separated flows in supersonic and subsonic streams with emphasis on the effect of transition. Technical Report NACA 1356, 1958.

F. Cirak, R. Deiterding, and S. P. Mauch. Large-scale fluid–structure interaction simulation of viscoplastic and fracturing thin-shells subjected to shocks and detonations. *Computers & Structures*, 85(11-14):1049–1065, 2007.

D. K. Clarke, M. D. Salast, and H. A. Hassanj. Euler Calculations for Multielement Airfoils Using Cartesian Grids. 24(3), 1986.

N. T. Clemens and V. Narayanaswamy. Shock/Turbulent Boundary Layer Interactions: Review of Recent Work on Sources of Unsteadiness (Invited). In *39th AIAA Fluid Dynamics Conference*, pages 1–25, Reston, Virigina, 2009. American Institute of Aeronautics and Astronautics.

N. T. Clemens and V. Narayanaswamy. Low-Frequency Unsteadiness of Shock Wave/Turbulent Boundary Layer Interactions. *Annual Review of Fluid Mechanics*, 46(1):469–492, 2014.

P. Colella, D. T. Graves, B. J. Keen, and D. Modiano. A Cartesian grid embedded boundary method for hyperbolic conservation laws. *Journal of Computational Physics*, 211(1):347–366, 2006.

D. Daub, S. Willems, A. Gülhan, and B. Esser. Experimental Setup for Excitation of Fluid-Structure Interaction. In *Sonderforschungsbereich/Transregio 40 - Annual Report 2014*, 2014.

D. Daub, S. Willems, and A. Gülhan. Experimental results on unsteady shock-wave/boundary-layer interaction induced by an impinging shock. *CEAS Space Journal*, 8(1):3–12, 2015a.

D. Daub, S. Willems, and A. Gülhan. Experiments on the Interaction of a Fast-Moving Shock with an Elastic Panel. *AIAA Journal*, 54(2):670–678, 2015b.

A. de Boer, A. H. van Zuijlen, and H. Bijl. Review of coupling methods for non-matching meshes. *Computer Methods in Applied Mechanics and Engineering*, 196(8):1515–1525, 2007.

R. Deiterding, F. Cirak, and S. P. Mauch. Efficient Fluid-Structure Interaction Simulation of Viscoplastic and Fracturing Thin-Shells Subjected to Underwater Shock Loading. In *Fluid-Structure Interaction: Theory, Numerics and Applications*, pages 65–79, Herrsching am Ammersee, Germany, 2008.

J. Délery. Shock wave/turbulent boundary layer interaction and its control. *Progress in Aerospace Sciences*, 22(4):209–280, 1985.

J. Délery and J.-P. Dussauge. Some physical aspects of shock wave/boundary layer interactions. *Shock Waves*, 19(6):453–468, 2009. ISSN 0938-1287.

J. Délery and J. G. Marvin. Shock-wave boundary layer interactions. Technical Report AGARD-AG-280, 1986.

G. Dhondt. *The Finite Element Method for Three-dimensional Thermomechanical Applications*. John Wiley & Sons, Ltd, 2004.

G. Dhondt. *CalculiX CrunchiX USER'S MANUAL version 2.11*. Munich, 2016.

D. S. Dolling. Fifty Years of Shock-Wave/Boundary-Layer Interaction Research: What Next? *AIAA Journal*, 39(8):1517–1531, 2001.

D. S. Dolling and M. E. Erengil. Unsteady wave structure near separation in a Mach 5 compression rampinteraction. *AIAA Journal*, 29:728–735, 1991.

D. S. Dolling and M. T. Murphy. Unsteadiness of the Separation Shock Wave Structure in a Supersonic Compression Ramp Flowfield. *AIAA Journal*, 21(12):1628–1634, 1983.

D. S. Dolling and C. T. Or. Unsteadiness of the shock wave structure in attached and separated compression ramp flows. *Experiments in Fluids*, 3(1):24–32, 1985.

J. Donea, S. Giuliani, and J. Halleux. An arbitrary lagrangian-eulerian finite element method for transient dynamic fluid-structure interactions. *Computer Methods in Applied Mechanics and Engineering*, 33(1-3):689–723, 1982.

P. Dupont, C. Haddad, and J.-F. Debiève. Space and time organization in a shock-induced separated boundary layer. *Journal of Fluid Mechanics*, 559:255–277, 2006.

J.-P. Dussauge, P. Dupont, and J.-F. Debiève. Unsteadiness in shock wave boundary layer interactions with separation. *Aerospace Science and Technology*, 10(2):85–91, 2006.

T. G. Eason and S. M. Spottswood. A Structures Perspective on the Challenges Associated with Analyzing a Reusable Hypersonic Platform. In *54th AIAA/ASME/ASCE/AHS/ASC Structures, Structural Dynamics, and Materials Conference*, pages 1–15. American Institute of Aeronautics and Astronautics, 2013.

A. Ehrl, A. Popp, V. Gravemeier, and W. A. Wall. A dual mortar approach for mesh tying within a variational multiscale method for incompressible flow. *International Journal for Numerical Methods in Fluids*, 76:1–27, 2014.

M. E. Erengil and D. S. Dolling. Physical causes of separation shock unsteadiness in shock-wave/turbulent boundary layer interactions. *AIAA Paper 93–3134*, 1993.

C. Farhat and V. K. Lakshminarayan. An ALE formulation of embedded boundary methods for tracking boundary layers in turbulent fluid–structure interaction problems. *Journal of Computational Physics*, 263:53–70, 2014.

C. Farhat and M. Lesoinne. Two efficient staggered algorithms for the serial and parallel solution of three-dimensional nonlinear transient aeroelastic problems. *Computer Methods in Applied Mechanics and Engineering*, 182(3-4):499–515, 2000.

C. Farhat, M. Lesoinne, and N. Maman. Mixed explicit/implicit time integration of coupled aeroelastic problems: Three-field formulation, geometric conservation and distributed solution. *International Journal for Numerical Methods in Fluids*, 21(10):807–835, 1995.

C. Farhat, M. Lesoinne, and P. Le Tallec. Load and motion transfer algorithms for fluid/structure interaction problems with non-matching discrete interfaces: Momentum and energy conservation, optimal discretization and application to aeroelasticity. *Computer Methods in Applied Mechanics and Engineering*, 157(1-2):95–114, 1998.

C. Farhat, K. G. van der Zee, and P. Geuzaine. Provably second-order time-accurate loosely-coupled solution algorithms for transient nonlinear computational aeroelasticity. *Computer Methods in Applied Mechanics and Engineering*, 195(17-18):1973–2001, 2006.

C. A. Felippa, K. C. Park, and C. Farhat. Partitioned analysis of coupled mechanical systems. *Computer Methods in Applied Mechanics and Engineering*, 190(24-25):3247–3270, 2001.

J. H. Ferziger and M. Perić. *Numerische Strömungsmechanik*. Springer-Verlag Berlin Heidelberg, 2008.

M. Frey. *Behandlung von Strömungsproblemen in Raketendüsen bei Überexpansion*. PhD thesis, Universität Stuttgart, 2001.

M. Frey, K. Makowka, and T. Aichner. The TICTOP nozzle: a new nozzle contouring concept. *CEAS Space Journal*, pages 1–7, 2016.

B. Ganapathisubramani, N. T. Clemens, and D. S. Dolling. Low-frequency dynamics of shock-induced separation in a compression ramp interaction. *Journal of Fluid Mechanics*, 636:397–425, 2009.

E. Garnier, P. Sagaut, and N. A. Adams. *Large Eddy Simulation for Compressible Flows*. Springer Netherlands, 2009.

S. Ghosh. *An immersed boundary method for simulating the effects of control devices used in mitigating shock/boundary-layer interactions*. PhD thesis, North Carolina State University, 2010.

R. H. M. Giepman, F. F. J. Schrijer, and B. W. van Oudheusden. Flow control of an oblique shock wave reflection with micro-ramp vortex generators: Effects of location and size. *Physics of Fluids*, 26(6):066101, 2014.

J. Giordano, G. Jourdan, Y. Burtschell, M. Medale, D. E. Zeitoun, and L. Houas. Shock wave impacts on deforming panel, an application of fluid-structure interaction. *Shock Waves*, 14(1-2):103–110, 2005.

A. Gogulapati, R. Deshmukh, A. R. Crowell, J. J. McNamara, V. Vyas, X. Wang, M. P. Mignolet, T. Beberniss, S. M. Spottswood, and T. G. Eason. Response of a Panel to Shock Impingement: Modeling and Comparison with Experiments. In *55th AIAA/ASME/ASCE/AHS/ASC Structures, Structural Dynamics, and Materials Conference*, pages 1–23, 2014.

S. Gottlieb and C.-W. Shu. Total variation diminishing Runge-Kutta schemes. *Mathematics of Computation of the American Mathematical Society*, 67:73–85, 1998.

M. Grilli, S. Hickel, X. Y. Hu, and N. A. Adams. Conservative Immersed Interface Method for compressible viscous flows with heat transfer. In *Academy Colloquium on Immersed boundary methods: current status and future research directions*, Amsterdam, The Netherlands, 2009.

M. Grilli, S. Hickel, and N. A. Adams. Large-eddy simulation of a supersonic turbulent boundary layer over a compression–expansion ramp. *International Journal of Heat and Fluid Flow*, 42:79–93, 2013.

A. Hadjadj. Large-Eddy Simulation of Shock/Boundary-Layer Interaction. *AIAA Journal*, 50(12):2919–2927, 2012.

G. Hagemann, M. Frey, and W. Koschel. Appearance of Restricted Shock Separation in Rocket Nozzles. *Journal of Propulsion and Power*, 18(3):577–584, 2002.

G. Hammerl, A. Seitz, F. Verdugo, W. A. Wall, D. Daub, S. Willems, and Gülhan. FSI of rocket nozzles - On the influence of simplified modeling of structural boundary conditions for an FSI experiment & scalable solvers for strongly coupled problems. In *Sonderforschungsbereich/Transregio 40 - Annual Report 2016*, pages 253–262, 2016.

S. Hickel and N. A. Adams. On implicit subgrid-scale modeling in wall-bounded flows. *Physics of Fluids*, 19:1–14, 2007.

S. Hickel, N. A. Adams, and J. A. Domaradzki. An adaptive local deconvolution method for implicit LES. *Journal of Computational Physics*, 213(1):413–436, 2006.

S. Hickel, C. P. Egerer, and J. Larsson. Subgrid-scale modeling for implicit large eddy simulation of compressible flows and shock-turbulence interaction. *Physics of Fluids*, 26(10):106101, 2014.

H. M. Hilber, T. J. R. Hughes, and R. L. Taylor. Improved numerical dissipation for time integration algorithms in structural dynamics. *Earthquake Engineering & Structural Dynamics*, 5(3):283–292, 1977.

Y. Hou, N. J. Clemens, and D. Dolling. Wide-Field Study of Shock-Induced Turbulent Boundary Layer Separation. In *41st Aerospace Sciences Meeting and Exhibit*, Reno, Nevada, 2003. AIAA.

X. Y. Hu, B. C. Khoo, N. A. Adams, and F. L. Huang. A conservative interface method for compressible flows. *Journal of Computational Physics*, 219(2):553–578, 2006.

R. A. Humble, G. E. Elsinga, F. Scarano, and B. W. van Oudheusden. Three-dimensional instantaneous structure of a shock wave/turbulent boundary layer interaction. *Journal of Fluid Mechanics*, 622:33–62, 2009.

K. Karagiozis, R. Kamakoti, F. Cirak, and C. Pantano. A computational study of supersonic disk-gap-band parachutes using Large-Eddy Simulation coupled to a structural membrane. *Journal of Fluids and Structures*, 27(2):175–192, 2011.

M. P. Kirkpatrick, S. W. Armfield, and J. H. Kent. A representation of curved boundaries for the solution of the Navier–Stokes equations on a staggered three-dimensional Cartesian grid. *Journal of Computational Physics*, 184(1):1–36, 2003.

A. L. Kistler. Fluctuating Wall Pressure under a Separated Supersonic Flow. *The Journal of the Acoustical Society of America*, 36(3):543, 1964.

M. Klein, A. Sadiki, and J. Janicka. A digital filter based generation of inflow data for spatially developing direct numerical or large Eddy simulations. *Journal of Computational Physics*, 186:652–665, 2003.

T. Klöppel, A. Popp, U. Küttler, and W. A. Wall. Fluid-structure interaction for nonconforming interfaces based on a dual mortar formulation. *Computer Methods in Applied Mechanics and Engineering*, 200:3111–3126, 2011.

D. D. Knight and G. Degrez. Shock Wave Boundary Layer Interactions in High Mach Number Flows - A Critical Survey of Current Numerical Prediction Capabilities. *AGARD Advisor Report*, 2(319):1.1–1.35, 1998.

D. D. Knight, H. Yan, A. G. Panaras, and A. Zheltovodov. Advances in CFD Prediction of Shock Wave Turbulent Boundary Layer Interactions. Technical Report RTO-TR-AVT-007-V3, 2002.

H. Kobayashi. The subgrid-scale models based on coherent structures for rotating homogeneous turbulence and turbulent channel flow. *Physics of Fluids*, 17:1–13, 2005.

A. G. Kravchenko and P. Moin. On the Effect of Numerical Errors in Large Eddy Simulations of Turbulent Flows. *Journal of Computational Physics*, 322:310–322, 1997.

S. Lee. *Large Eddy Simulation Of Shock Boundary Layer Interaction Control Using Micro-Vortex Generators*. PhD thesis, University of Illinois, 2009.

A. Leonard. Energy Cascade in Large-Eddy Simulations of Turbulent Fluid Flows. In *Turbulent Diffusion in Environmental Pollution*, pages 237–248, Charlottesville, 1975.

M. Lesieur, O. Métais, and P. Comte. *Large-Eddy Simulations of Turbulence*. Cambridge University Press, 2005.

M. S. Loginov, N. A. Adams, and A. A. Zheltovodov. Large-eddy simulation of shock-wave/turbulent-boundary-layer interaction. *Journal of Fluid Mechanics*, 565:135, 2006.

W. E. Lorensen and H. E. Cline. Marching cubes: A high resolution 3D surface construction algorithm. In *Proceedings of the 14th annual conference on Computer graphics and interactive techniques - SIGGRAPH '87*, volume 21, pages 163–169, 1987.

L. Maestrello and T. L. J. Linden. Measurements of the response of a panel excited by shock boundary-layer interaction. *Journal of Sound and Vibration*, 16(3):385–391, 1971.

D. C. McCormick. Shock/boundary-layer interaction control with vortex generators and passive cavity. *AIAA Journal*, 31(1):91–96, 1993.

M. Meyer, A. Devesa, S. Hickel, X. Y. Hu, and N. A. Adams. A conservative immersed interface method for Large-Eddy Simulation of incompressible flows. *Journal of Computational Physics*, 229(18):6300–6317, 2010.

M. P. Mignolet, A. Przekop, S. A. Rizzi, and S. M. Spottswood. A review of indirect/non-intrusive reduced order modeling of nonlinear geometric structures. *Journal of Sound and Vibration*, 332(10):2437–2460, 2013.

R. Mittal and G. Iaccarino. Immersed Boundary Methods. *Annual Review of Fluid Mechanics*, 37(1):239–261, 2005.

R. Mittal, H. Dong, M. Bozkurttas, F. M. Najjar, A. Vargas, and A. von Loebbecke. A versatile sharp interface immersed boundary method for incompressible flows with complex boundaries. *Journal of computational physics*, 227:4825–4852, 2008.

B. Morgan, K. Duraisamy, N. Nguyen, S. Kawai, and S. K. Lele. Flow physics and RANS modelling of oblique shock/turbulent boundary layer interaction. *Journal of Fluid Mechanics*, 729:231–284, 2013.

L. Nave and G. Coffey. Sea level side loads in high-area-ratio rocket engines. In *9th Propulsion Conference*. American Institute of Aeronautics and Astronautics, 1973.

J. W. Nichols, J. Larsson, M. Bernardini, and S. Pirozzoli. Stability and modal analysis of shock/boundary layer interactions. *Theoretical and Computational Fluid Dynamics*, 2016.

F. Örley, V. Pasquariello, S. Hickel, and N. A. Adams. Cut-element based immersed boundary method for moving geometries in compressible liquid flows with cavitation. *Journal of Computational Physics*, 283:1–22, 2015.

J. Östlund. *Flow processes in rocket engine nozzles with focus on flow separation and side-loads*. PhD thesis, Royal Institute of Technology, 2002.

J. Östlund and B. Muhammad-Klingmann. Supersonic Flow Separation with Application to Rocket Engine Nozzles. *Applied Mechanics Reviews*, 58(3):143, 2005.

V. Pasquariello. Large Eddy Simulation of Shock-Wave/Boundary-Layer Interaction Control. Master's thesis, Technische Universität München, 2012.

V. Pasquariello, S. Hickel, and N. A. Adams. Extension of the Conservative Immersed Interface Method towards high-order interpolation. In *Sonderforschungsbereich/Transregio 40 - Annual Report 2013*, 2013.

V. Pasquariello, M. Grilli, S. Hickel, and N. A. Adams. Large-eddy simulation of passive shock-wave/boundary-layer interaction control. *International Journal of Heat and Fluid Flow*, 49:116–127, 2014.

V. Pasquariello, S. Hickel, N. A. Adams, G. Hammerl, W. A. Wall, D. Daub, S. Willems, and A. Gülhan. Coupled simulation of shock-wave/turbulent boundary-layer interaction over a flexible panel. In *6th European Conference For Aerospace Sciences*, Kraków, Poland, 2015.

V. Pasquariello, G. Hammerl, F. Örley, S. Hickel, C. Danowski, A. Popp, W. A. Wall, and N. A. Adams. A cut-cell finite volume – finite element coupling approach for fluid–structure interaction in compressible flow. *Journal of Computational Physics*, 307:670–695, 2016.

V. Pasquariello, S. Hickel, and N. A. Adams. Unsteady Effects of Strong Shock-Wave/Boundary-Layer Interaction at High Reynolds Number. *Journal of Fluid Mechanics*, 823:617–657, 2017.

C. S. Peskin. Flow patterns around heart valves: A numerical method. *Journal of Computational Physics*, 10(2):252–271, 1972.

S. Piponniau, J. P. Dussauge, J. F. Debiève, and P. Dupont. A simple model for low-frequency unsteadiness in shock-induced separation. *Journal of Fluid Mechanics*, 629: 87, 2009.

S. Pirozzoli and F. Grasso. Direct numerical simulation of impinging shock wave/turbulent boundary layer interaction at M=2.25. *Physics of Fluids*, 18(6):065113, 2006.

S. Pirozzoli, A. Beer, M. Bernardini, and F. Grasso. Computational analysis of impinging shock-wave boundary layer interaction under conditions of incipient separation. *Shock Waves*, 19(6):487–497, 2009.

S. Pirozzoli, J. Larsson, J. W. Nichols, B. E. Morgan, and S. K. Lele. Analysis of unsteady effects in shock/boundary layer interactions. In *Proceedings of the 2010 CTR Summer Program*, Center of Turbulence Research, Stanford, 2010.

K. J. Plotkin. Shock Wave Oscillation Driven by Turbulent Boundary-Layer Fluctuations. *AIAA Journal*, 13(8):1036–1040, 1975.

S. Pope. *Turbulent Flows*. Cambridge University Press, 2000.

S. Priebe, M. Wu, and M. P. Martín. Direct Numerical Simulation of a Reflected-Shock-Wave/Turbulent-Boundary-Layer Interaction. *AIAA Journal*, 47(5):1173–1185, 2009.

M. A. Puscas, L. Monasse, A. Ern, C. Tenaud, and C. Mariotti. A conservative embedded boundary method for an inviscid compressible flow coupled with a fragmenting structure. *International Journal for Numerical Methods in Engineering*, 103(13):970–995, 2015a.

M. A. Puscas, L. Monasse, A. Ern, C. Tenaud, C. Mariotti, and V. Daru. A time semi-implicit scheme for the energy-balanced coupling of a shocked fluid flow with a deformable structure. *Journal of Computational Physics*, 296:241–262, 2015b.

M. J. Ringuette, P. B. Bookey, C. Wyckham, and A. J. Smits. Experimental Study of a Mach 3 Compression Ramp Interaction at $Re_\theta = 2400$. *AIAA Journal*, 47(2):373–385, 2009.

J. Ruf, D. McDaniels, and A. Brown. Nozzle Side Load Testing and Analysis at MSFC. In *45th AIAA/ASME/SAE/ASEE Joint Propulsion Conference & Exhibit*, pages 1–14. American Institute of Aeronautics and Astronautics, 2009.

P. Sagaut. *Large Eddy Simulation for Incompressible Flows*. Springer-Verlag Berlin Heidelberg, 2006. ISBN 3-540-26344-6.

M. F. Shahab. *Numerical Investigation Of The Influence Of An Impinging Shock Wave And Heat Transfer On A Developing Turbulent Boundary Layer*. PhD thesis, École Nationale Supérieure de Mécanique et d'Aérotechnique, 2006.

L. J. Souverein and J.-F. Debiève. Effect of air jet vortex generators on a shock wave boundary layer interaction. *Experiments in Fluids*, 49(5):1053–1064, 2010.

L. J. Souverein, P. Dupont, J.-F. Debiève, J.-P. Dussauge, B. W. van Oudheusden, and F. Scarano. Effect of Interaction Strength on Unsteadiness in Turbulent Shock-Wave-Induced Separations. *AIAA Journal*, 48(7):1480–1493, 2010.

S. M. Spottswood, T. Eason, and T. Beberniss. Influence of shock-boundary layer interactions on the dynamic response of a flexible panel. In *Proceedings of International Conference on Noise and Vibration Engineering (ISMA 2012)*, pages 603–616, Leuven (Belgium), 2012.

S. M. Spottswood, T. Eason, and T. Beberniss. Full-field, dynamic pressure and displacement measurements of a panel excited by shock boundary-layer interaction. In *19th AIAA/CEAS Aeroacoustics Conference*, pages 1–18. American Institute of Aeronautics and Astronautics, 2013.

K. R. Srinivasan, E. Loth, and C. J. Dutton. Aerodynamics of Recirculating Flow Control Devices for Normal Shock/Boundary-Layer Interactions. *AIAA Journal*, 44(4):751–763, 2006.

E. Stanewsky, J. Délery, J. Fulker, and W. Geißler. *EUROSHOCK - Drag Reduction by Passive Shock Control*, volume 56. Vieweg, 1997. ISBN 978-3-322-90713-4.

E. Stanewsky, J. Délery, J. Fulker, and P. Matteis. *Drag Reduction by Shock and Boundary Layer Control*. Springer-Verlag Berlin Heidelberg, 2002. ISBN 978-3-642-07762-3.

A. Thari, V. Pasquariello, N. Aage, and S. Hickel. Adaptive Reduced-Order Modeling for Non-Linear Fluid-Structure Interaction. *ArXiv e-prints*, arXiv:1702.04332, 2017.

F. O. Thomas, C. M. Putnam, and H. C. Chu. On the mechanism of unsteady shock oscillation in shock wave/turbulent boundary layer interactions. *Experiments in Fluids*, 18-18(1-2):69–81, 1994.

E. Touber and N. D. Sandham. Large-eddy simulation of low-frequency unsteadiness in a turbulent shock-induced separation bubble. *Theoretical and Computational Fluid Dynamics*, 23(2):79–107, 2009.

E. Touber and N. D. Sandham. Low-order stochastic modelling of low-frequency motions in reflected shock-wave/boundary-layer interactions. *Journal of Fluid Mechanics*, 671: 417–465, 2011.

O. Ünalmis and D. Dolling. Decay of wall pressure field and structure of a Mach 5 adiabatic turbulent boundary layer. In *Fluid Dynamics Conference*, Reston, Virigina, 1994. AIAA.

S. B. Verma and M. Chidambaranathan. Transition control of Mach to regular reflection induced interaction using an array of micro ramp vane-type vortex generators. *Physics of Fluids*, 27(10):107102, 2015.

S. B. Verma and C. Manisankar. Shockwave/Boundary-Layer Interaction Control on a Compression Ramp Using Steady Micro Jets. *AIAA Journal*, 50(12):2753–2764, 2012.

S. B. Verma, R. Stark, and O. Haidn. Relation between shock unsteadiness and the origin of side-loads inside a thrust optimized parabolic rocket nozzle. *Aerospace Science and Technology*, 10(6):474–483, 2006.

S. B. Verma, C. Manisankar, and C. Raju. Control of shock unsteadiness in shock boundary-layer interaction on a compression corner using mechanical vortex generators. *Shock Waves*, 22(4):327–339, 2012.

M. R. Visbal. On the interaction of an oblique shock with a flexible panel. *Journal of Fluids and Structures*, 30:219–225, 2012.

M. R. Visbal. Viscous and inviscid interactions of an oblique shock with a flexible panel. *Journal of Fluids and Structures*, 48:27–45, 2014.

P. R. Viswanath. Shock-wave-turbulent-boundary-layer interaction and its control: A survey of recent developments. *Sādhanā*, 12(1-2):45–104, 1988.

B. Vreman, B. Geurts, and H. Kuerten. A priori tests of large eddy simulation of the compressible plane mixing layer. *Journal of Engineering Mathematics*, 29:299–327, 1995.

J. L. Wagner, K. B. Yuceil, A. Valdivia, N. T. Clemens, and D. S. Dolling. Experimental Investigation of Unstart in an Inlet/Isolator Model in Mach 5 Flow. *AIAA Journal*, 47 (6):1528–1542, 2009.

K. Wang, J. Grétarsson, A. Main, and C. Farhat. Computational algorithms for tracking dynamic fluid-structure interfaces in embedded boundary methods. *International Journal for Numerical Methods in Fluids*, 70(4):515–535, 2012.

K. G. Wang, A. Rallu, J.-F. Gerbeau, and C. Farhat. Algorithms for interface treatment and load computation in embedded boundary methods for fluid and fluid-structure interaction problems. *International Journal for Numerical Methods in Fluids*, 67(9): 1175–1206, 2011.

K. G. Wang, P. Lea, and C. Farhat. A computational framework for the simulation of high-speed multi-material fluid-structure interaction problems with dynamic fracture. *International Journal for Numerical Methods in Engineering*, 104(7):585–623, 2015.

S. Willems, A. Gülhan, and B. Esser. Shock induced fluid-structure interaction on a flexible wall in supersonic turbulent flow. In *Progress in Flight Physics*, volume 5, pages 285–308, Munich, Germany, 2013.

M. Wu and M. P. Martín. Analysis of shock motion in shockwave and turbulent boundary layer interaction using direct numerical simulation data. *Journal of Fluid Mechanics*, 594:71–83, 2008.

T. Ye, R. Mittal, H. S. Udaykumar, and W. Shyy. An Accurate Cartesian Grid Method for Viscous Incompressible Flows with Complex Immersed Boundaries. *Journal of Computational Physics*, 156(2):209–240, 1999.

P. S. Zandonade, J. A. Langford, and R. D. Moser. Finite-volume optimal large-eddy simulation of isotropic turbulence. *Physics of Fluids*, 16:2255–2271, 2004.

O. C. Zienkiewicz and R. L. Taylor. *The Finite Element Method - Volume 1*. Butterworth-Heinemann, 2000a.

O. C. Zienkiewicz and R. L. Taylor. *The Finite Element Method - Volume 2*. Butterworth-Heinemann, 2000b.